

ulm university universität
uulm

Experimental Investigations of Microstructural Coarsening in 3D using X-Ray Microscopy

Dissertation

zur Erlangung des akademischen Grades

Doktor-Ingenieur
(Dr.-Ing.)

der Fakultät für Ingenieurwissenschaften, Informatik
und Psychologie der Universität Ulm

von

Jules Mullen Dake
aus Oregon, USA

Gutachter:	Prof. Carl E. Krill III, PhD
	Prof. Gregory S. Rohrer, PhD
Amtierender Dekan:	Prof. Dr.-Ing. Maurits Ortmanns

Ulm, 12. August 2019

In memory of my grandfather Lee Judd Dake

Abstract

Since the Stone Age, the development of new materials with enhanced properties has driven technological advancements and continually expanded the limits of human endeavor. Over the last century, improvements in the experimental characterization of materials have also revealed how decisively the microstructure—the structure of a material on the microscopic level—affects material properties. A modern engineer can control the temperature, pressure and time of various processing steps to set the desired microstructure of a material during production. At the same time, computer simulation has become an important tool for predicting the effect that these processing parameters will have on microstructural evolution, and although the physical phenomena underlying microstructural evolution are three-dimensional (3D) in nature, conventional metallographic characterization techniques only provide two-dimensional snapshots of a material's microstructure. In order to better optimize and verify computer simulations, which, thanks to exponential increases in computing power, can easily be performed in 3D, time-resolved 3D experimental data are required. Filling in this fundamental gap in our experimental knowledge of microstructural evolution was the motivation behind this doctoral thesis.

The advent of three-dimensional x-ray (3DXRD) microscopy created exciting new possibilities for the characterization of materials, and its inherently nondestructive nature allows for time-resolved studies of microstructure in 3D. Microstructural coarsening caused by heat treatments was studied in two aluminum alloys. The first was a single-phase Al-1 wt% Mg alloy, which coarsens by grain growth, and the second was a semisolid Al-5 wt% Cu alloy, for which Ostwald ripening is commonly assumed to be the dominant coarsening mechanism. Experiments were performed at the synchrotron radiation facility SPring-8 in Sayō, Japan. A box-beam implementation and optimized use of far-field and near-field x-ray detectors allowed for the rapid collection and reconstruction of 3DXRD data for a large sample volume, initially containing upwards of 1000 grains.

Reconstructions of the Al-Mg specimen revealed the presence of crystallographic texture, the preferred orientation of grains, with a distinct Cube component. Grains with similar crystallographic orientations were not found randomly distributed throughout the specimen but rather in clusters. This resulted in a nonrandom distribution of low and high-angle grain boundaries. The latter migrated on average about twice as fast as their low-angle counterparts. Although the mean grain size increased approximately linearly with the square root of the annealing time (as predicted by isotropic grain growth models), wide variations were measured in the growth rate of individual grains, and abnormally growing grains were observed at the boundaries between grain clusters. In the semisolid Al-Cu samples, the rigid-body rotation of grains was found to occur in parallel to coarsening by Ostwald ripening. Both the coarsening and rotation rates increased with increasing fraction of liquid phase. Two types of rotations were observed: (1) random rotations, associated with Brownian motion and the redistribution of the liquid phase during annealing, and (2) directed grain rotations, caused by the steep gradient in interfacial energy for low-angle grain boundaries. The non-standard coarsening mechanisms observed in both aluminum alloys demonstrate the necessity of studying microstructural evolution in 3D.

Contents

Abstract i

Contents iii

1 Introduction 1
1.1 Definition and importance of microstructure . . . 1
1.2 Basics of microstructural coarsening . . . 2
1.3 Experimental characterization of microstructure in 3D . . . 4
1.4 Open questions . . . 6
1.5 Preview . . . 7

2 Coarsening in Polycrystalline Materials 9
2.1 Interfaces in crystalline materials . . . 9
2.1.1 Crystallographic orientation and misorientation . . . 9
2.1.2 Structure and energy of grain boundaries . . . 14
2.2 Grain growth . . . 20
2.2.1 Curvature-driven boundary migration . . . 20
2.2.2 Normal grain growth . . . 21
2.2.3 Abnormal grain growth . . . 23
2.3 Ostwald ripening . . . 28

3 Microstructural Characterization by X-Ray Diffraction 31
3.1 Generation of x-rays . . . 31
3.1.1 Laboratory devices . . . 31
3.1.2 Synchrotron radiation . . . 33
3.2 Conventional x-ray diffraction . . . 35
3.2.1 Diffraction basics . . . 35
3.2.2 Single-crystal diffraction . . . 36
3.2.3 Polycrystal or powder diffraction . . . 37
3.2.4 Grain size determination . . . 37
3.3 Three-dimensional x-ray diffraction . . . 40
3.3.1 Basics of multigrain crystallography . . . 40
3.3.2 Postprocessing and grain tracking . . . 46

4 Grain Growth in a Single-Phase Al-Mg Alloy 49
4.1 Experimental details . . . 49
4.1.1 Material selection and sample preparation . . . 50
4.1.2 Collection and reconstruction of 3DXRD data . . . 51

4.2 Microstructural evolution . . . 53
4.2.1 Global growth parameters . . . 54
4.2.2 Local growth rates . . . 56
4.2.3 Grain morphology and topology . . . 58
4.3 Texture and misorientation . . . 63
4.3.1 Crystallographic texture components . . . 63
4.3.2 Distribution of boundary misorientations . . . 67
4.4 Discussion . . . 68
4.4.1 Excursions into the abnormal . . . 68
4.4.2 Average grain boundary velocities . . . 74
4.4.3 Spatial clustering of grains . . . 77
4.4.4 On the mechanism of abnormal grain growth in textured materials . 79
4.5 Concluding remarks on grain growth observed in single-phase Al-Mg . . . 83

5 Grain Rotations During Coarsening in a Semisolid Al-Cu Alloy 85
5.1 Theory of energy-driven grain rotation . . . 85
5.2 Experimental details . . . 88
5.2.1 Material selection and sample preparation . . . 88
5.2.2 Data collection . . . 90
5.3 Microstructural evolution . . . 91
5.3.1 Grain coarsening . . . 91
5.3.2 Grain rotation . . . 93
5.4 On the mechanisms of grain rotation . . . 97
5.4.1 Directed grain rotations . . . 97
5.4.2 Random grain rotations . . . 100
5.5 Concluding remarks on grain rotation in semisolid materials . . . 102

6 General Discussion and Conclusions 103
6.1 Practical suitability of 3DXRD microscopy for coarsening investigations . . 103
6.2 Applicability of isotropic models . . . 106
6.3 Alternative mechanisms of grain coarsening . . . 111
6.4 Conclusions . . . 112

Bibliography 115

List of Author's Publications 135

Acknowledgments 137

1

Introduction

Although many of the solid objects that we encounter on a daily basis appear to be singular, massive entities, inspection at the microscopic level often reveals the presence of a fine, cellular substructure. Notable examples include common technical materials, such as metals, ceramics and even some polymers, as well as many natural materials, such as rocks, glaciers and wood. The importance of this underlying cellular substructure—aptly termed microstructure—on material properties was pieced together around the dawn of the 20th century [1] and gave rise to the modern field of materials science. This thesis is concerned with the experimental investigation of microstructural coarsening in three dimensions and the implications of such measurements for the accurate modeling and simulation of growth phenomena.

1.1 Definition and importance of microstructure

In most solids the lowest-energy state is characterized by a periodic arrangement of atoms [2]. Such an atomic configuration is referred to as crystalline, and the average position of atoms in a crystal can be described by a three-dimensional point lattice. In a single crystal the regular ordering of atoms is uninterrupted throughout the entire volume. Perfect single crystals are, however, rarely found in nature (leading to their historic high valuation as gemstones) and must be produced with great care for industrial applications, e.g., large silicon ingots. It is much more common to find polycrystalline materials composed of many smaller crystalline domains [3]. The atomic ordering in each domain is still periodic but differs in orientation (lattice rotation) from neighboring domains, as illustrated in Fig. 1.1. Individual domains are referred to as crystallites or grains, and the interfaces separating two grains are commonly called grain boundaries. In multi-component materials similar boundaries may also exist between phases of different crystal structure or chemical composition. Both of these interfacial boundaries are planar defects and represent the most dominant feature of the microstructure in a polycrystalline material.

Point defects (vacancies and interstitial atoms) and linear defects (dislocations) are also components of the overall microstructure, but it is the network of planar defects that defines

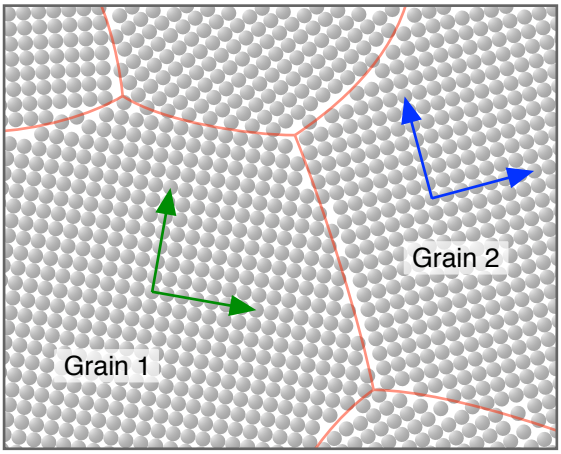

Figure 1.1: A planar section through a hypothetical polycrystal. Inside each crystallite, atoms are arranged periodically with identical spacing. While the spacing remains the same, the orientation with which atoms are arranged varies from grain to grain, as indicated by the green and blue coordinate systems. Grain boundaries—highlighted by red lines—exist wherever crystallites of differing orientation meet.

the cellular substructure and most decisively influences material properties [4]. Perhaps the foremost example is the effect of grain size on mechanical strength. In the 1950s Hall [5] and Petch [6] addressed the experimentally observed inverse relation between yield strength and the square root of grain size. The glide of dislocations—the phenomenon responsible for plastic flow in crystalline materials—is hindered at grain boundaries, and because the total grain boundary area increases as the average crystallite size decreases, a higher external stress must be applied to deform a material consisting of finer grains. Similarly, a high number of internal interfaces increases a material's electrical resistivity [7]. On the other hand, grain boundaries provide pathways of greater diffusivity for atoms moving along these planar defects [8]. Additional properties that depend on the size and distribution of grains in a polycrystalline bulk material include magnetic coercivity, optical scattering, and corrosion resistance [9, 10]. For these reasons the precise control of microstructure is highly desirable.

1.2 Basics of microstructural coarsening

The disruption in atomic ordering that occurs at grain boundaries results in an excess energy associated with these internal interfaces. To reduce a material's average grain size, which necessarily increases the total boundary area, work must therefore be expended. In the case of metals, this is most often achieved through deformation, such as a blacksmith hammering a piece of iron or the rolling of a thick steel slab into a thin sheet. The reduction of boundary area, on the other hand, is a spontaneous process, the kinetics of which are governed by an Arrhenius-type relation [11]. Given adequate thermal energy, the atoms of a polycrystal diffuse across grain boundaries such that the latter migrate toward their centers of curvature, and the average crystallite size increases. In a single-phase material, this coarsening phenomenon is referred to as grain growth, an example of which is given in Fig. 1.2. Here, an Al-Mg alloy was annealed at 350 °C for various time intervals, and after each step the sample was polished and etched to expose the internal microstructure [12].

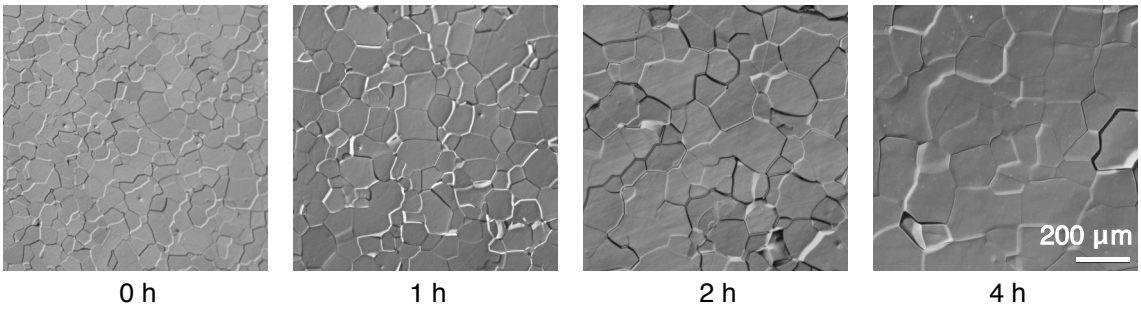

Figure 1.2: Optical micrographs illustrating grain growth in an Al-1 wt% Mg alloy. The samples were annealed at 350 °C for the indicated times, after which each specimen was ground, polished and etched to reveal its underlying microstructure. Owing to the destructive nature of this conventional method of microstructural examination, it is not possible to follow the growth and shrinkage of individual grains. Image adapted from Ref. [12] with kind permission by Anne-Catherine Probst.

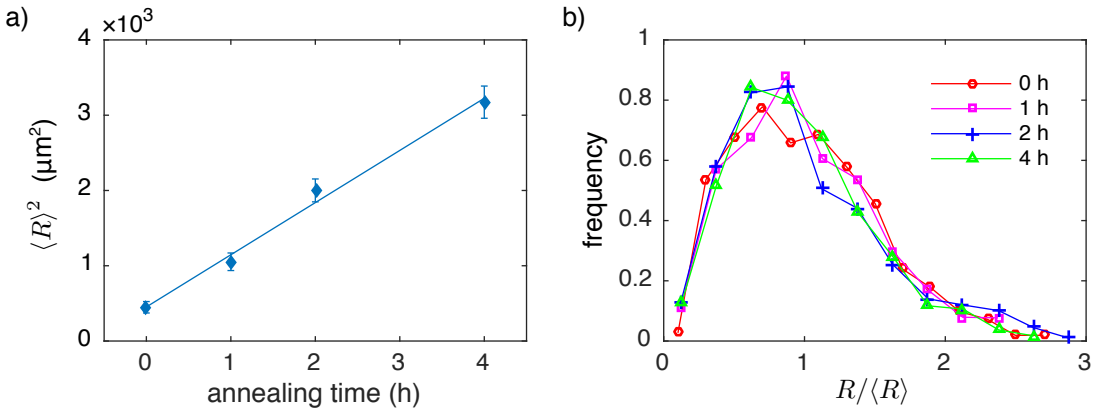

Figure 1.3: Characteristics of normal grain growth. Evolution of (a) the mean grain radius and (b) the grain size distribution in an Al-1 wt% Mg sample. Data from Ref. [12].

Through the application of stereographic identities [13], approximate grain sizes can be extracted from planar micrographs. This has been carried out for the polished cross sections of Fig. 1.2, and the results are displayed in the graphs of Fig. 1.3. The evolution of the mean grain radius is plotted next to the normalized grain size distribution of each time step. Two key features of grain growth have been identified in the literature [11, 14–16]: (1) a parabolic growth relation for the mean grain size ($\langle R\rangle^2 \propto t$), and (2) a self-similar grain size distribution, which is most often best fit by a lognormal function. When a sample undergoing coarsening displays both of these characteristics, it is said to be growing normally.

In 1965 the Swedish scientist Mats Hillert developed an analytical model for normal grain growth [16]. In this seminal paper, Hillert was able to predict both characteristic features described above, although the exact shape of his distribution function differed from the commonly observed lognormal distribution. To this day Hillert's mean-field model represents the most commonly cited theoretical description of grain growth; nevertheless, the model has several drawbacks that prevent its widespread application. First, because the model places all grains in the same average environment, it neglects the geometric and topological constraints imposed on a space-filling network of grains [14, 17]. Furthermore, variations in a grain's local neighborhood, which can facilitate the growth of smaller-than-average-sized grains or vice versa, are, by definition, not allowed. Finally, uniform values

are assumed for all boundary properties, i.e., grain boundary energy and mobility. These quantities, however, are known to vary in real polycrystalline specimens [18], and such variations can induce abnormal grain growth, a phenomenon that is characterized by the accelerated growth (and shrinkage) of a subpopulation of grains [11].

Over the last several decades computer-aided numerical modeling has become an important, if not the primary method for investigating microstructural evolution. Although early grain growth simulations were time consuming and practically feasible only for two-dimensional microstructures [19–22], the exponential increase in computational power in recent years now allows for the simulation of large, three-dimensional data sets containing tens of thousands to even millions of grains [23–28]. Various approaches have proliferated in the literature, including Monte Carlo Potts models [19, 29], phase-field models [23], front-tracking (or vertex) models [25] and cellular automata [30]. Each implementation has its strengths and weaknesses [31], but when performed correctly all models give nearly identical results, at least in the case of normal grain growth, as summarized by Krill and Chen [23]. The grain size distributions from simulated microstructures match experimental observations a good deal better than Hillert's analytical distribution, which should not be a surprise since the connectivity of space-filling grains is naturally captured in simulations.

With numerical models it is not only possible to simulate the idealized case of normal grain growth but also more complicated situations involving anisotropic boundary properties [22, 32, 33], solute drag [34] and Zener pinning [35]. The ability to easily tune simulation parameters, which are either directly or indirectly related to physical properties (stress, stored energy, boundary energy, etc.), has made computer simulation a powerful tool for investigating the physical phenomena behind microstructural coarsening. It promises to aid in the design of new materials and in the determination of their reliability under different operating conditions. However, as illustrated schematically in Fig. 1.4, the lack of time-resolved 3D experimental data prevents the validation and, consequently, more widespread application of computer simulations.

1.3 Experimental characterization of microstructure in 3D

Capturing the 3D shape of grains in a polycrystal is a very tedious endeavor, which is one reason why limited data exist in the literature. Historically, soap foams were used to model the microstructure of opaque crystalline materials [14]. Aqueous foams, which can be directly imaged with a light microscope, have space-filling configurations that are dictated by the balancing of surface tensions. Despite this topological similarity, several key differences exist with respect to polycrystalline solids. The first is the uniform pressure and, therefore, curvature of foam boundaries (made possible by the rapid motion of gas molecules), and the second is the isotropic nature of foam interfaces [36]. Both of these features are not shared by crystalline interfaces. Consequently, the coarsening kinetics observed in foams cannot be directly related to those in polycrystals.

Several destructive methods for determining 3D grain shapes have been developed. The most prominent is serial sectioning [37–44], but various grain separation techniques, such as selective grain boundary corrosion [45, 46] or liquid metal embrittlement [47], have been tested as well. Obviously, such investigations cannot provide kinetic data owing to their destructive nature, but they do yield valuable information on grain topology and size distributions. It is common practice to compare such static experimental data to the output of computer simulations to determine if microstructures generated by the latter produce reasonable results [23, 27, 48–55]

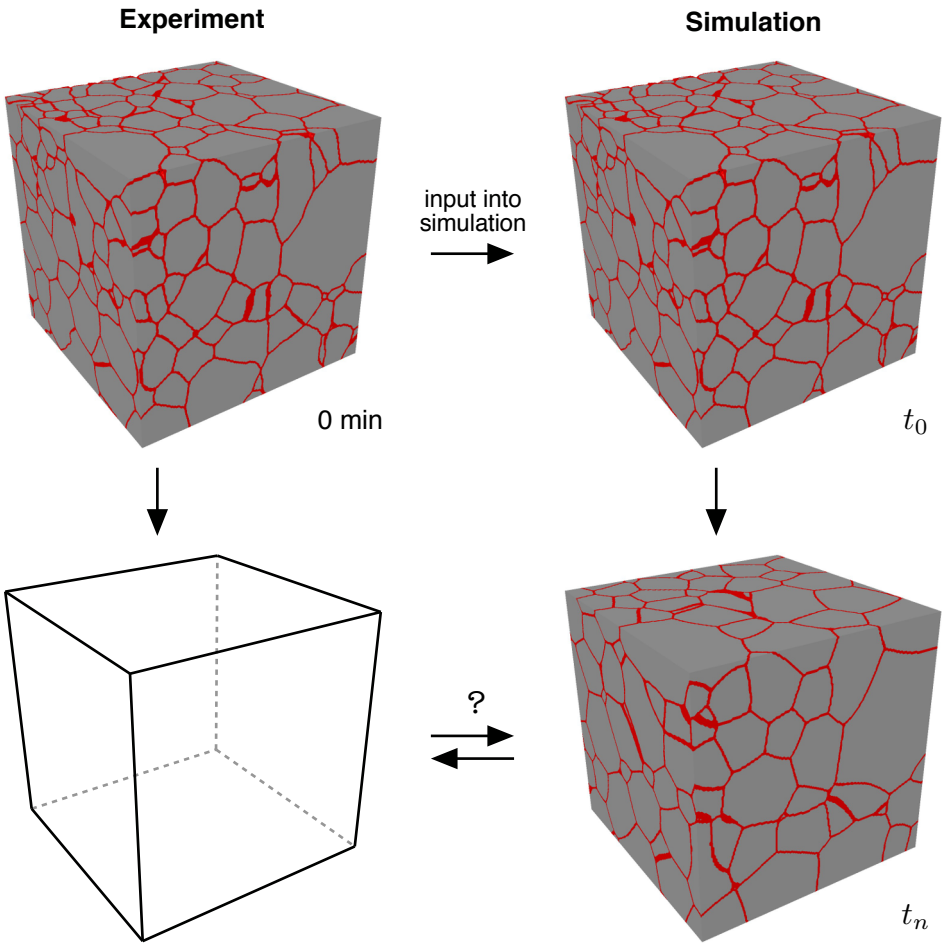

Figure 1.4: Gap in experimental coarsening data. 3D experimental data can be collected through conventional methods such as serial sectioning and then used as the initial state for 3D computer simulations. Owing to the destructive nature of such experimental methods, however, a direct validation of the simulation results at some later simulation time ($t_n > t_0$) against experiment is not possible.

Computed tomography (CT) provides a nondestructive means of capturing 3D data, but it requires absorption contrast to resolve microstructural features. Thus, grain boundaries need to be marked by an atomic species or phase having a higher or lower x-ray absorption coefficient than the bulk material (see for example [56]). However, marker species or phases that segregate to the grain boundaries of a polycrystal can significantly alter the properties of the original interfaces [11]. This experimental prerequisite effectively excludes investigations of grain growth using CT, but there are other coarsening phenomena that are well-suited to the technique. Microstructural evolution during sintering or various semisolid materials processing techniques has been investigated extensively using CT in recent years [57–63]. Although valuable 3D information on features like coordination number, neck formation and porosity has been obtained, segmentation errors and the lack of crystallographic orientation information often limit the conclusiveness of the observations.

In the early 2000s a team of scientists from Risø National Laboratory in Denmark achieved a significant breakthrough in the 3D characterization of microstructure [64–67]. Working together with beamline scientists at the European Synchrotron Radiation Facility (ESRF), they developed a nondestructive method for mapping grains of single phase materials. This new experimental technique, based on x-ray diffraction, was given the name

3D x-ray diffraction (3DXRD) microscopy. With a monochromatic x-ray beam of sufficient energy and brilliance, diffraction spots from the individual grains of a polycrystal can be captured with an area detector. If, in addition, the incident beam is parallel (i.e., displays minimal divergence), then the spots represent 2D projections of the diffracting grains. Typically, a polycrystalline specimen is rotated 360° during data acquisition, and hundreds of projections are recorded for each grain. From these projections grain morphologies can be reconstructed. Moreover, because the method is based on diffraction, the determination of crystallographic orientation is intrinsic to the reconstruction procedure.

3DXRD microscopy provides access to the coarsening data long sought after by materials scientists but previously thought to be unattainable. Not only can the evolution of bulk grains in opaque polycrystals be observed nondestructively, but growth rates can be related to features such as texture, misorientation and in some cases local elastic strain. Exciting proof-of-concept studies have been performed on a wide range of samples and phenomena, including the deformation of metals [68–70], recrystallization [67, 71], grain growth [72, 73], crack propagation [74], stress corrosion cracking [75], ferroelectrics [76] and more [77–81].

1.4 Open questions

A long-term goal in the field of materials science is predictive through-process modeling. With such a tool, an engineer could provide all forming and annealing steps of a given production line as inputs and then receive an accurate prediction of the microstructure and properties of the finished part [82, 83]. The time and cost of developing new products could be reduced dramatically. Although this vision is certainly somewhat utopian, it drives advancements in modeling and simulation of thermomechanical materials phenomena.

A key step in achieving predictive simulations of microstructure evolution is the collection of time-resolved 3D experimental data, against which simulations can be tested. Despite the promising initial studies listed above, surprisingly few 3DXRD investigations of coarsening in polycrystals have actually been reported. At the onset of the experimental work described in the subsequent chapters of this thesis, only one paper on grain growth had been published [72]. In their analysis, Schmidt *et al.* followed the evolution of 27 grains across one effective annealing interval. Although this study proved that grains in a polycrystal could be mapped and tracked from one time step to the next, the usefulness of the results was quite limited owing to poor time resolution. But the authors did provide suggestions for optimizing data acquisition during future experimentation.

The aim of this thesis was to collect statistically significant sets of microstructural data using 3DXRD microscopy and then to compare these data to standard coarsening models. The three overarching questions that guided this research were:

1. **Is 3DXRD microscopy well suited to the large-scale investigation of grain coarsening?**

   For over a decade now, 3DXRD microscopy has been in operation at various synchrotron facilities, some of which have beamlines with dedicated setups [77]. The lack of published data, however, indicates that 3DXRD studies of grain coarsening are not trivial. Previous attempts [84] have suffered from long acquisition and even longer data reconstruction times. As a consequence, grain growth experiments performed hitherto were carried out blindly, i.e., without feedback during the actual measurements. This often led to the microstructure changing either too little or too much between annealing steps. Over the coarse of this thesis, a substantial amount

of work went into the optimization and automation of 3DXRD for coarsening experiments. Thus, in answering this question, I will not only examine the theoretical limits of the technique but also consider the many practical aspects that contribute to successful experimentation.

2. **Do isotropic models of curvature-driven growth describe coarsening in real polycrystalline samples?**

   Although the anisotropic characteristics of special crystalline interfaces (e.g., symmetric twins) have been investigated in great detail [18], it is still commonly assumed that general high-angle grain boundaries—which make up the vast majority of boundaries in randomly oriented polycrystals—have relatively uniform properties. For this reason, isotropic coarsening models still form the basis of many growth simulations, and if isotropic models are able to capture the growth kinetics of a majority of grains, then the extra effort and computational power required for the simulation of more complicated anisotropic models would be unmerited. Thus, it makes sense to perform the first direct comparison of 3DXRD coarsening data against the predictions of isotropic simulations.

3. **Can non-standard coarsening mechanisms be detected by 3DXRD microscopy?**

   The excess energy ΔG associated with the interfaces of a polycrystalline sample can be expressed as

   $$\Delta G = \gamma A_{\mathrm{GB}}, \tag{1.1}$$

   where γ is the (average) boundary energy and A_{GB} the total interfacial area. If γ is constant, then the only way to lower ΔG is to reduce A_{GB}; indeed, a reduction in interfacial area is the basis of conventional coarsening models for normal grain growth in single-phase materials and Ostwald ripening in semisolid alloys. However, if γ is a function of boundary misorientation, inclination or any other variable, then it is conceivable that alternative thermodynamic paths exist to decrease ΔG. For example, the rigid-body rotation of a grain can reduce its boundary energy even if the boundary area remains the same [85]. Since 3DXRD microscopy provides the orientation of all grains in a reconstructed volume as well as their spatial extent, determining if variations in boundary misorientation contribute to microstructural evolution is rather straightforward.

1.5 Preview

In the following chapter, the basics of crystalline interfaces are explained before two of the most common forms of coarsening in polycrystals—namely, grain growth and Ostwald ripening—are reviewed. Chapter 3 details the generation of x-rays and how x-ray diffraction can be used to characterize microstructure. Emphasis is placed here on the reconstruction and processing of data sets acquired using 3DXRD microscopy. In Chapter 4, the first 3DXRD results are presented. The evolution of thousands of grains in a single-phase Al-Mg specimen is tracked over multiple time steps, allowing for both grain-by-grain and statistical analyses of grain growth rates. Coarsening in a two-phase Al-Cu alloy is investigated in Chapter 5. The ability to track grain orientations over time proved to be essential in understanding the full complexity of coarsening in this material, which was annealed in the semisolid state. In the final chapter of this thesis, the findings from both experiments are considered together to obtain answers to the open questions stated above.

2

Coarsening in Polycrystalline Materials

When the atoms of a polycrystalline solid are given enough thermal energy to diffuse through the material, there is a net positive flux of atoms from smaller to larger grains. The effect is that the smaller grains shrink, eventually disappearing, while the larger grains of the specimen grow. This is a spontaneous process and referred to in general as coarsening, since the average grain size increases with time. In this chapter I discuss the basics of microstructural coarsening, which will be built upon in later chapters.

2.1 Interfaces in crystalline materials

Two differently oriented crystallites that meet in space form a grain boundary, the structure and properties of which depend on the character of the interface. This section begins with a definition of crystallographic orientation and some of its most common representations before moving on to review low-angle, high-angle and some special coincidence site lattice grain boundaries.

2.1.1 Crystallographic orientation and misorientation

The orientation of an object describes its rotation relative to a given frame of reference. In order to quantify orientation, one must first define both a reference coordinate system and an object coordinate system—the latter is attached to the object and rotates with it. Typically, right-handed Cartesian coordinate systems are used for this purpose. In the case of crystalline objects, it is natural to establish the object coordinate system using crystallographic directions.

The entire periodic arrangement of atoms in a single crystal can be described by the translation of its basic building block, the so-called unit cell. For many common metals (Al, Cr, Cu, Fe, Mo, Ni, Pb, V, etc.) the unit cell is a perfect cube. A face-centered cubic (fcc) unit cell is sketched in Fig. 2.1 (a). Atoms are located at each of the cube's eight corners, as well as on the center of all six faces. The fcc arrangement results in the most dense packing of monodisperse spheres [86] and is the crystal structure of all Al alloys

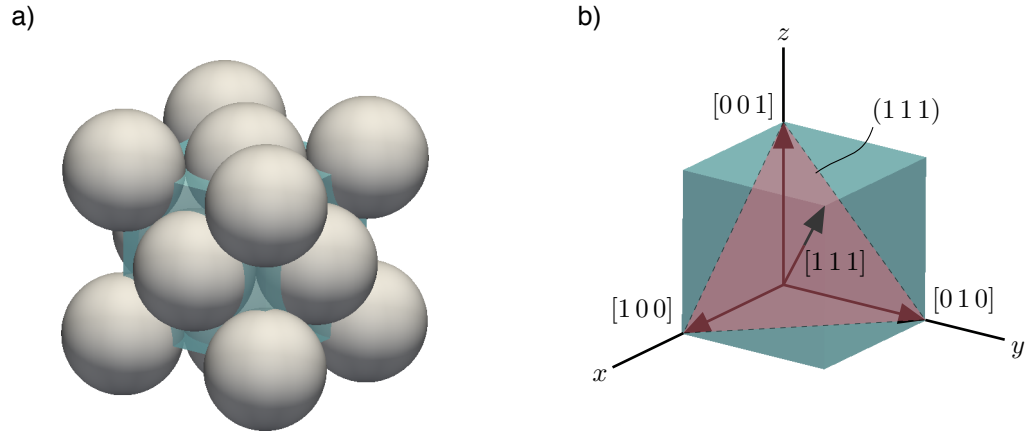

Figure 2.1: Unit cell and some crystallographic directions and planes for the face-centered cubic (fcc) lattice. (a) The hard-sphere model is a simple way to display the position of atoms in the closely packed fcc unit cell. (b) Here, the atoms are removed to reveal some of the more important crystallographic directions and planes. The Miller representation is used with directions in square brackets and planes parentheses. The (1 1 1) plane is the most densely packed plane.

investigated in later chapters. If we assign one corner of the unit cell to be the origin, the [1 0 0], [0 1 0] and [0 0 1] crystallographic directions are given by the three edges of the cell that intersect at the origin, as seen in Fig. 2.1 (b). These vectors are the crystallographic axes of the unit cell and, in the cubic case, are orthonormal (i.e., mutually perpendicular and of equal length). Accordingly, they are commonly used to define a coordinate system for fcc crystallites.

Having established the crystallite coordinate system, we can now determine the orientation of any grain in a polycrystalline specimen. A 3D orientation is expressed mathematically in its basic form as a 3×3 *rotation* or *orientation matrix* [87, 88]. This matrix, denoted here as U, rotates the reference coordinates through premultiplication onto the crystal coordinates:

$$U \cdot C_{\mathrm{Ref}} = C_{\mathrm{X}}, \tag{2.1}$$

where C_{X} and C_{Ref} represent the crystal and reference coordinates, respectively. One must be quite explicit in the definition of orientation, since its interpretation is easily beset by ambiguitiy. Thus, in the following list I emphasize the conventions used in this thesis:

1. All coordinate systems are right-handed.
2. The right-hand rule defines the direction of positive rotation.
3. The orientation matrix U actively rotates (alibi transformation) an object, vector or point in the reference coordinate system.
4. Vectors are represented as columns and are, accordingly, premultiplied by U.

To further elucidate these conventions an example rotation is given in Fig. 2.2. Here, the orientation of a given grain's cubic unit cell is seen in relation to the reference coordinate system. The crystallographic axes are labelled, and it is obvious that the orientation of the unit cell is represented by a pure rotation about the z-axis of the reference coordinate system. The angles α_1, β_1, and γ_1 describe the rotation of the [1 0 0] crystallographic axis relative to the x, y, and z axes of the reference coordinate system, respectively. The angles $(\alpha_2, \beta_2, \gamma_2)$ and $(\alpha_3, \beta_3, \gamma_3)$ between the [0 1 0] and [0 0 1] crystallographic directions and the x, y, and z axes can be calculated in the same fashion [88]. With these angles it is

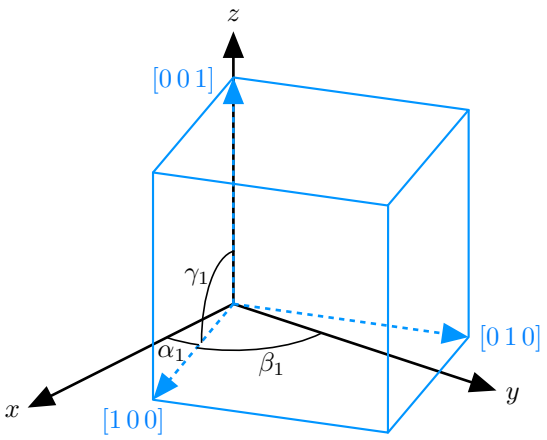

$$\alpha_1 = 20°,\ \beta_1 = 70°,\ \gamma_1 = 90°$$

$$U = \begin{pmatrix} 0.94 & -0.34 & 0 \\ 0.34 & 0.94 & 0 \\ 0 & 0 & 1 \end{pmatrix}$$

Figure 2.2: Orientation example. A unit cell (light blue box) is rotated 20°about the z axis of a reference coordinate system (black arrows). Direction cosines, shown graphically only for the [1 0 0] axis, are used to calculate the orientation (rotation) matrix U. A grain whose lattice is congruent with this rotated unit cell has the orientation defined by U.

possible to calculate the direction cosines and build the orientation matrix as

$$U = \begin{pmatrix} \cos\alpha_1 & \cos\alpha_2 & \cos\alpha_3 \\ \cos\beta_1 & \cos\beta_2 & \cos\beta_3 \\ \cos\gamma_1 & \cos\gamma_2 & \cos\gamma_3 \end{pmatrix}. \tag{2.2}$$

Because the crystallographic axes are unit vectors, the columns of the orientation matrix, from left to right, give exactly the x, y and z coordinates of the [1 0 0], [0 1 0] and [0 0 1] unit cell vectors (in this order) with respect to the reference coordinate system.

Although the orientation matrix contains nine values, only three are independent, since the rotation of 3D objects in Euclidean space is associated with three degrees of freedom. Thus, there exist more compact parameterizations of orientation, two of which are described below. The first is the so-called axis/angle notation. According to Euler's rotation theorem, if an object is rotated rigidly about its center of mass, there exist an axis that remains unchanged, i.e., this axis is not displaced [87]. Consequently, any rigid-body rotation can be described by an axis and an angle. The rotation axis is specified by the unit vector $\mathbf{n}$ and the angle of right-handed rotation by θ. Following this notation, the orientation of the unit cell in Fig. 2.2 is given by $\mathbf{n} = \mathbf{e}_z$ and $\theta = 20°$.

The axis/angle representation provides perhaps the most straightforward means of understanding 3D rotations, but it still utilizes four parameters to describe an orientation, one more than necessary. By relating the length of the rotation axis to the angle of rotation, we can reduce the number to three. Following Frank [89], this combination of parameters is most commonly carried out as

$$\mathbf{r} = \mathbf{n} \tan\left(\frac{\theta}{2}\right), \tag{2.3}$$

which defines the so-called Rodrigues vector $\mathbf{r}$. There are many advantages [3, 88–91] to this representation of orientation, perhaps the most valuable being the straight-line geometry of the 3D Rodrigues space. All rotations about a common axis lie along a straight line, and even when the origin is transformed, this property is retained, a fact

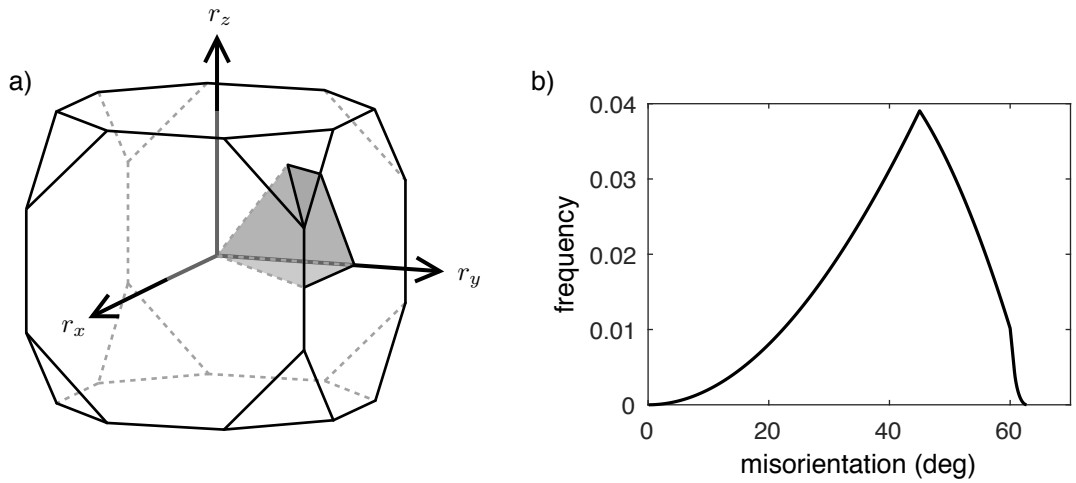

Figure 2.3: Orientation space and misorientation distribution for cubic crystals. (a) The fundamental zone in orientation space for cubic lattice symmetry is given by a truncated cube in the Rodrigues representation. The subsection shaded in gray amounts to 1/48th of the fundamental zone's entire volume and is the so-called Mackenzie cell in which all misorientations between cubic crystallites can be represented. (b) The Mackenzie distribution is a one-parameter function for the minimum misorientation angle between randomly oriented cubes.

utilized in the reconstruction of 3DXRD data (described in Section 3.3). Additionally, bounding surfaces introduced by crystal symmetries are always planar in Rodrigues space [90]. Therefore, a fundamental zone of unique rotations can be defined in Rodrigues space by a solid polyhedron.[1] For the case of cubic symmetry, the fundamental zone is a given by a truncated cube, and any orientation outside this volume can be represented by an equivalent point inside the fundamental zone. For example, a 50° rotation of a cube about its [0 0 1] axis results in the Rodrigues vector $\mathbf{r} = \langle 0, 0, 0.47 \rangle$. But this rotation is indistinguishable from a $-40°$ rotation about the same axis, and, accordingly, can be represented by the smaller but equivalent Rodrigues vector $\mathbf{r} = \langle 0, 0, -0.36 \rangle$ inside the fundamental zone. A final feature of convenience is the natural extension of the three components of a Rodrigues vector to a red-green-blue coloring scheme, which is utilized in subsequent chapters to color grains according to their orientations.

The orientation of a grain can also be visualized graphically with the help of pole figures, a type of stereographic projection. The construction of the {1 0 0} pole figure is illustrated in Fig. 2.4. This procedure can be implemented to visualize the orientation of any arbitrary set of crystallographic planes, but with materials of cubic crystal symmetry the {1 0 0}, {1 1 0} and {1 1 1} pole figures are most common [11]. Although the use of pole figures to represent a single grain's orientation is arguably excessive, the benefit of this visualization technique becomes clear when the orientation of multiple grains—all grains in a sample, for instance—is plotted simultaneously on the same projection. From the resulting distribution of points (the areal density), one learns the global distribution of grain orientations, also known as crystallographic texture. A helpful visual reference detailing the construction of pole figures is given by the e-learning tool AluMatter [92].

A grain's orientation is determined with respect to a somewhat arbitrarily chosen reference coordinate system.[2] In a polycrystalline sample one could just as well calculate a

[1] This is true for specimens with crystal symmetry greater than triclinic [89].
[2] Often the sample geometry is used to define the reference coordinates, but this need not be so.

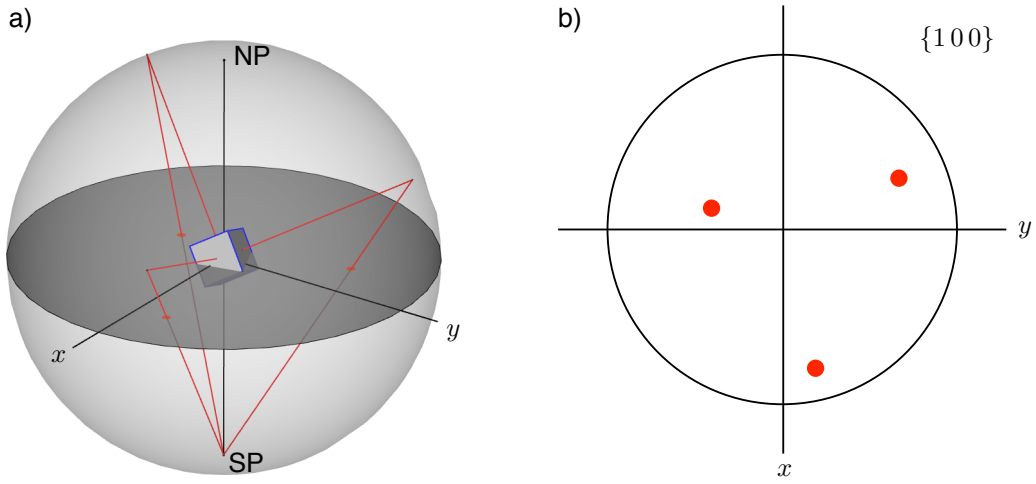

Figure 2.4: Graphical representation of orientation. (a) To construct the {1 0 0} pole figure, the unit cell of a grain of interest is placed at the origin of the reference coordinate system. Then a sphere, also centered at the origin, is drawn and the surface normals of the unit cell's {1 0 0} planes are extended to the sphere's outer surface. From here straight lines are drawn to the sphere's south pole (SP). (b) The points at which these lines intersect the equatorial plane of the sphere create the 2D projection of the {1 0 0} planes' orientation, referred to as {1 0 0} pole figure.

grain's orientation relative to another grain in the specimen. In this case, the term *misorientation* is used to emphasize that one is referring to a difference in absolute orientation between crystallites. If we choose one grain with orientation matrix U_A to be our reference grain, then the misorientation M between it and a second grain with orientation matrix U_B is defined as

$$M = U_B \cdot U_A^{-1}, \tag{2.4}$$

where U_A^{-1} is the matrix inverse of U_A. Obviously, the misorientation is exactly equal to the orientation if U_A is the identity matrix, that is, when grain A is perfectly aligned with the reference coordinates.

When calculating both the orientation and misorientation of grains, it is important to take their underlying crystal symmetry into account. There are 24 equivalent representations of the orientation of a cubic crystal—these can be found listed in various sources [18, 88]. Generally, the orientation with the smallest angular displacement is chosen from the list of equivalent rotations. Doing so ensures, as mentioned above, that the particular orientation lies in the fundamental zone. For the representation of misorientation between two cubic crystals, there are $24 \times 24 = 576$ possibilities [90], and since it is, for all practical purposes, irrelevant which of the two grains is considered the reference grain, this number doubles, which allows all misorientations to be represented in 1/48th of the fundamental zone in Rodrigues space for cubic orientations [91]. This subset is highlighted in Fig. 2.3 (a) and often referred to as the Mackenzie cell after the Australian scientist James Kenneth Mackenzie. His piecewise analytical function for the minimum misorientation—sometimes referred to as disorientation—distribution of randomly oriented cubes is reproduced in Fig. 2.3 (b) [93]. Despite the 3D nature of grain misorientations, often only the minimum misorientation angle is reported.

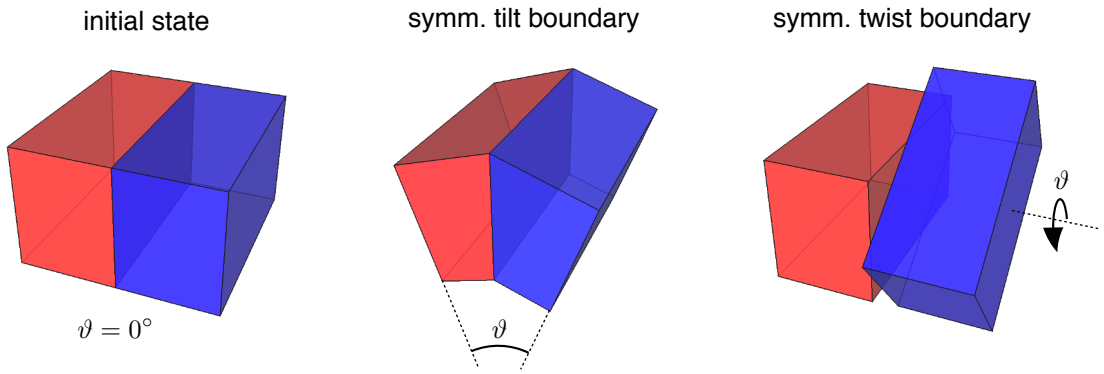

Figure 2.5: Tilt and twist boundaries of a theoretical bicrystal. In the initial configuration the two crystallites are perfectly aligned and no grain boundary exists. This configuration represents the hypothetical $\Sigma 1$ boundary, for which every lattice point is coincident. Rotating the crystallites about an axis in the grain boundary plane results in a tilt boundary, while a rotation perpendicular to the grain boundary plane leads to a twist boundary. Pure twist boundaries are by definition symmetric, but tilt boundaries are symmetric only if the two crystallites terminate at the same crystallographic plane. This is the case when each component grain is tilted by half of the total misorientation.

2.1.2 Structure and energy of grain boundaries

A difference in crystallographic orientation between neighboring grains of a polycrystal disrupts the local atomic ordering at and very near to the boundary separating the two grains, which in turn leads to an increase in the specimen's total free energy. The amount by which the free energy increases per unit area is termed (specific) grain boundary energy. Although no generally reliable geometric relation has been discovered between atomic arrangement and boundary energy (despite decades of intense investigation), some overarching trends exist [4, 11, 18, 94, 95]. In metals—the simplest 3D polycrystals—the interfacial energy is approximately inversely proportional to the packing density of atoms in the grain boundary; that is, the closer the density is to that of the perfect crystal, the lower the energy [94].

Traditionally, grain boundaries have been classified by their tilt and twist components [18, 96]. This classification is especially useful when investigating which type of dislocations are present in the boundary. Tilt boundaries can be constructed from arrays of edge dislocations, while screw dislocations are required to achieve twist. Examples of pure tilt and twist boundaries are given in Fig. 2.5 for an ideal bicrystal with a planar interface. A tilt between the two component grains occurs when the axis of rotation lies in the boundary plane. A twist boundary, on the other hand, results from a rotation about an axis perpendicular to the boundary plane. For either boundary type, the quantifier "symmetric" is added when the crystallographic planes of the two crystallites at the boundary are identical on both sides of the interface. Most grain boundaries have tilt and twist components, and the decomposition of these components is dependent on the method chosen to do so, since rotations do not commute. A typical approach is given in the introduction of Ref. [18].

Although symmetric tilt and twist boundaries are useful academic tools for describing the construction of grain boundaries, these interfaces are in fact rather rare in real polycrystals, especially since most boundaries are curved and not planar. To characterize general grain boundaries five macroscopic parameters are needed—three for the misorientation between neighboring grains and two for the orientation (also called inclination) of the boundary

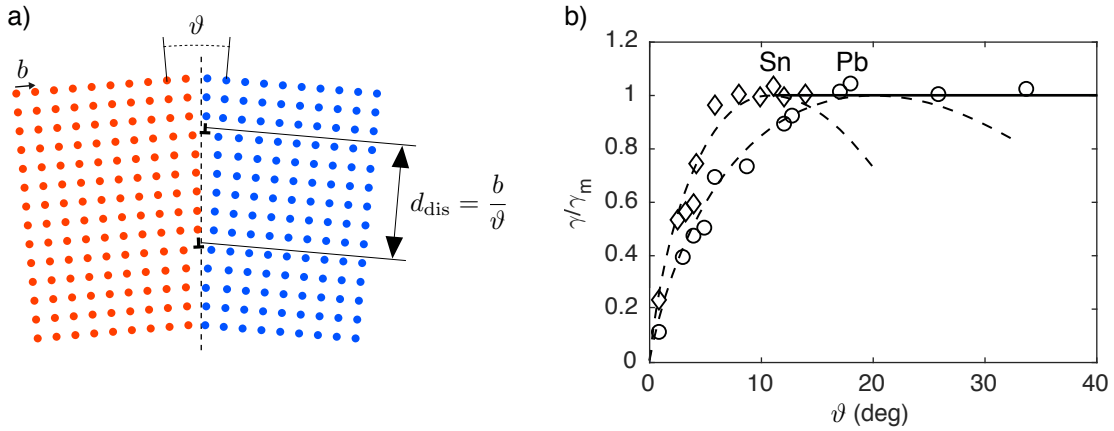

Figure 2.6: Read-Shockley model for low-angle grain boundaries. (a) A pure low-angle tilt grain boundary can be constructed from an array of uniformly spaced dislocations. The lattice planes that disappear to accommodate for the tilt angle end in edge dislocations. The distance d_{dis} between dislocations is simply the ratio of the Burgers vector magnitude b to the tilt angle ϑ. (b) Experimental values for the normalized boundary energy of Sn and Pb are plotted as a function of misorientation and fit by the Read-Shockley model (dashed lines) [4]. The fit is accurate only for low misorientations, after which the energy is approximately constant (solid line).

plane. The development of fast, automated electron backscattered diffraction (EBSD) mapping systems has greatly aided the experimental investigation of grain boundary types, and, utilizing this technique, researchers at Carnegie Mellon University have popularized what they refer to as the five-parameter grain boundary character distribution [36, 97–100]. In his review of grain boundary energy anisotropy [95], Rohrer shows that a very rough discretization of this 5D space in 10° intervals results in about 6000 different grain boundary types. While the grain boundary character does not reveal the atomic structure of an interface, an inverse correlation between the frequency and energy of boundary types has been observed [101].

Low-angle grain boundaries (LAGBs)

When the misorientation between adjacent grains is small, their mutual boundary can be represented by a spatial array of distinctly separated dislocations. The dislocation model of grain boundaries was first proposed by Burgers [102] and Bragg [103] and later used by Read and Shockley [104] to calculate energies for LAGBs. A cross section of a symmetric tilt boundary about an [0 0 1] axis is sketched in Fig. 2.6 (a). The edge dislocations—which, in this case, extend perpendicular to the plane of the page—define the grain boundary and are found at regularly spaced intervals. As the misorientation angle ϑ increases, the dislocation spacing d_{dis} decreases. In the small angle approximation, the relation between these two quantities is

$$d_{\mathrm{dis}} = \frac{b}{\vartheta}, \tag{2.5}$$

where b is the magnitude of the Burgers vector, which in most metals is equal to the interatomic spacing in the close-packed direction. Low-angle twist boundaries can be constructed similarly using screw instead of edge dislocations. Low-angle mixed tilt/twist boundaries require, accordingly, both types of dislocations.

From the dislocation line energy and approximate spacing (Eq. (2.5)), Read and Shockley

estimated the specific grain boundary energy γ as a function of misorientation ϑ. Their widespread and well-accepted model is formulated as

$$\gamma = E_0 \vartheta \left[A - \ln \vartheta \right], \tag{2.6}$$

where the parameters E_0 and A are independent of ϑ and depend on the elastic constants of the material [104, 105]. A normalized version of this equation is fit to measured boundary energies for Pb and Sn in Fig. 2.6 (b). Equation (2.6) predicts an initial increase in γ with misorientation, reaching a maximum at $\vartheta = \exp(A - 1)$, after which a steady decline in boundary energy should follow. However, a decrease in γ at larger misorientation angles is not generally observed experimentally [4, 11]. Read and Shockley addressed this discrepancy by applying Eq. (2.6) only to small ϑ, because the dislocation model breaks down at high misorientation angles, owing to its linear elastic assumption of dislocation stress fields and its treatment of dislocation cores [106]. The concept of a dislocation core was introduced to avoid a stress singularity at the center of a dislocation. Usually, a cut-off radius for the dislocation core is defined somewhere in the range of one to five times the Burgers vector [11]. Once the dislocation spacing becomes so small that core regions overlap, individual dislocations lose their unique identity, and the Read-Shockley model breaks down [105]. Although some researches [95, 107] restrict the validity of the Read-Shockley model to angles smaller than 6° (claiming that elastic dislocation-dislocation interactions are no longer negligible above this value), cut-off angles ranging from 10° to 30° can be found throughout the literature [18, 108, 109]. The most commonly cited value for this transition is, however, $\vartheta = 15°$.

High-angle grain boundaries (HAGBs)

The simplest model for HAGBs assumes a constant energy for all grain boundaries having a misorientation angle greater than the LAGB cut-off angle. A large body of experimentally determined data for general (also referred to as random) HAGBs show boundary energies scattered about a relatively constant value of γ, the magnitude of which varies depending on the material at hand [4, 11, 110]. This relative invariance of γ with ϑ at high angles leads to the common piecewise definition

$$\gamma = \begin{cases} \gamma_m \dfrac{\vartheta}{\vartheta_m} \left(1 - \ln \dfrac{\vartheta}{\vartheta_m} \right), & \text{if } \vartheta < \vartheta_m \\ \gamma_m, & \text{if } \vartheta \geq \vartheta_m. \end{cases} \tag{2.7}$$

The top portion of this equation is just the Read-Shockley model for LAGBs [105] (Eq. (2.6)), rewritten in terms of the maximum boundary energy $\gamma_m = E_0 \vartheta_m$ and the corresponding misorientation at this point $\vartheta_m = \exp(A - 1)$. Average boundary energies for a range of metals and alloys were tabulated by Murr [110] and found to be on the order of about $1\,\mathrm{J/m^2}$, which one can use as an estimate for γ_m; as mentioned above, ϑ_m is frequently taken to be 15°. Although this model for grain boundary energy is extremely simple, it is nevertheless useful when describing materials that do not easily form twin boundaries (e.g., Al and its alloys [110–112]) and routinely employed in simulations of grain growth [26, 29, 113].

There do, however, exist HAGBs with interfacial energies much smaller than γ_m, and more sophisticated models of the grain boundary energy landscape seek to incorporate the energy minima of such "special" grain boundaries. Arguably the most conceptually significant breakthrough in the study of HAGBs was the coincidence site lattice (CSL), the

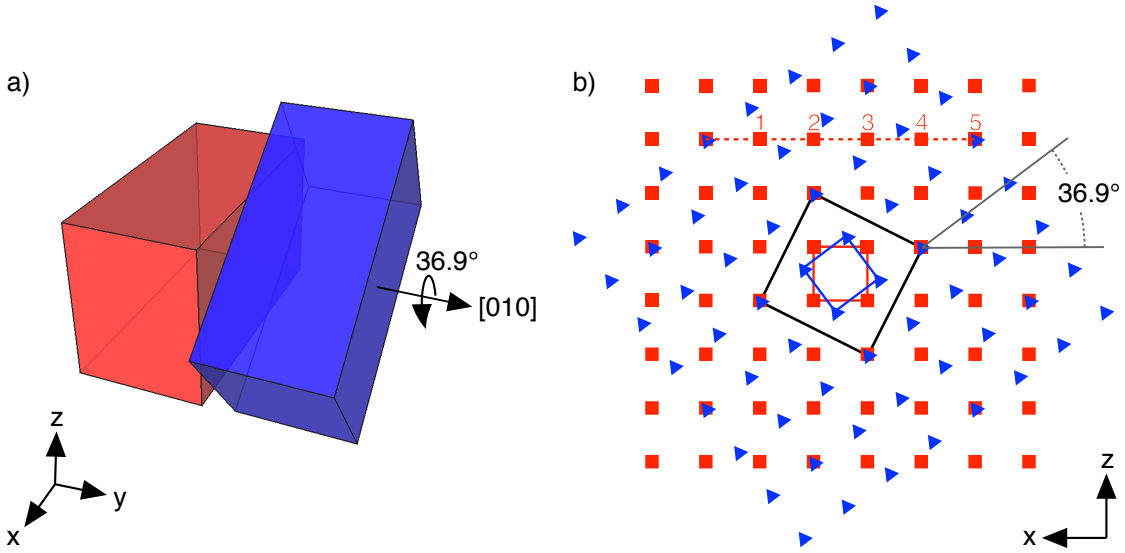

Figure 2.7: Example of a coincidence site littice (CSL) grain boundary in a cubic metal. (a) A twist by 36.9° about any ⟨1 0 0⟩ axis generates a Σ5 CSL boundary. (b) Every fifth atom in the boundary plane is coincident, and the {1 0 0} planes of the CSL lattice have an area that is five times that of the bicrystal's component grains. (In this illustration it is assumed that the 6 faces of the cuboidal grains are aligned with the 6 faces of their respective cubic unit cells.)

basic concepts of which are addressed here. The historical development of the CSL was summarized by Sutton and Balluffi [94] in their seminal review of the predictive power of geometric models in determining boundaries of low interfacial energy.

If, at the interface between two crystallites, points exist matching the lattices of both adjacent grains, these sites are coincident. One might expect misorientations with a high number of coincidence sites to lead to lower values of γ than random HAGBs with little or no coincidence. Of course, high-coincidence relations require exact misorientations (both axis and angle) between the two neighboring grains. The precise geometric requirements [114] and a list of misorientations [115] that fulfill them can be found elsewhere in the literature.

A common example of a CSL boundary is depicted by the bicrystal in Fig. 2.7. Here, the blue crystallite is rotated (twisted) by 36.9° about the [0 1 0] axis, and the boundary between the two grains is symmetric, since the terminating surface of both crystallites is a {1 0 0} plane. The atomistic detail of this example boundary is shown in Fig. 2.7 (b)—the red squares represent the unrotated atoms of the red grain, while the blue triangles symbolize the atoms of the rotated blue grain. The CSL is classified by its so-called Σ-value, which is defined as the reciprocal of the coincidence-site density. For example, following either grain's lattice (the red squares or blue triangles) in Fig. 2.7 (b), we can count five "normal" lattice sites per coincidence site. Taking the inverse of this linear density, we find $\Sigma = 5$. Likewise, the area of the square connecting the CSL (black box) is also five times that of a {1 0 0} surface of the grains' unit cell. The CSL is not restricted to a plane but can be thought of as hypothetical 3D lattice. If the red and blue grains of Fig. 2.7 (a) are made to occupy the same space, then one-fifth of the lattice sites in each will coincide throughout the entire volume, and all planes parallel to that of Fig. 2.7 (b) will show the same coincidence.

Although, for the purpose of visualization, it is easiest to explain the CSL concept using

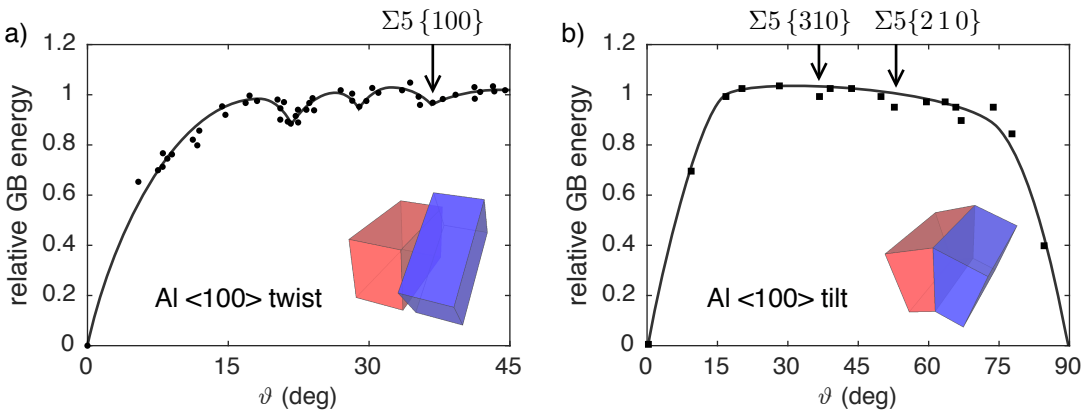

Figure 2.8: Experimental grain boundary energies of symmetric twist and tilt boundaries. While small cusps can be seen for (a) ⟨1 0 0⟩ twist boundaries in Al, a very flat plateau is observed for (b) ⟨1 0 0⟩ tilt interfaces. Locations of Σ5 boundaries are indicated in both plots. (The notation gives the Σ-value followed by the Miller indices of the grain boundary planes.) Noteworthy is the absence of a significant decrease in energy for the Σ5 boundaries, despite their relatively high degree of coincidence. Data taken from Refs. [18] and [120].

a symmetric boundary, this need not be the case. The interface between adjacent crystallites is considered a CSL boundary as long as the necessary misorientation relationship is satisfied between the two grains [115]. In other words, the inclination of the boundary is irrelevant in the determination of its Σ-value—this follows from the extension to interpenetrating 3D lattices mention above. However, the areal density of CSL points in a given grain boundary depends strongly on the inclination. One might assume, therefore, that a high planar density of coincidence sites corresponds to a low grain boundary energy, but the general predictive power of this argument is limited. In fact, in Sutton and Balluffi's review [94] they found no reliable geometric conditions for predicting the excess energy at crystalline interfaces. Nevertheless, the CSL construct provides a useful means of classifying grain boundaries and is ubiquitous in modern literature on boundary structure and properties [95, 116–119].

By limiting the choice of rotation axis and boundary inclination, we can reduce the five macroscopic degrees of freedom to one—namely, the rotation angle—and in doing so plot the boundary energy as a function of misorientation angle. This is most commonly done for symmetric twist and tilt boundaries. Even though the fraction of grain boundaries that can be represented in this manner is very limited [96], we can still garner useful information on interfacial properties, especially since most special, low-energy grain boundaries (e.g., the Σ3 coherent twins) are included in this subset. In the spirit of the example Σ5 CSL boundary above, experimentally determined interfacial energies are plotted in Fig. 2.8 for both ⟨1 0 0⟩ twist and tilt boundaries. The Σ5 boundary is present in both at an angle of 36.9°. For the case of symmetric twist, the interface remains a {1 0 0} plane for all rotation angles, while for symmetric tilt boundaries the plane changes continuously with ϑ. Despite the relatively high number of coincidence lattice sites for the symmetric Σ5 twist and tilt boundaries, the observed reduction in interfacial energy is minimal for both configurations.

In CSL notation, LAGBs are labelled Σ1 boundaries. As ϑ goes to zero, every lattice point becomes coincident, which means that the boundary and its associated excess energy vanish. The second deepest—and really the only other consistently significant—drop in interfacial energy in fcc materials occurs at Σ3 boundaries, to which the coherent twin belongs. In general, crystallographic orientations that are related by mirror symmetry are

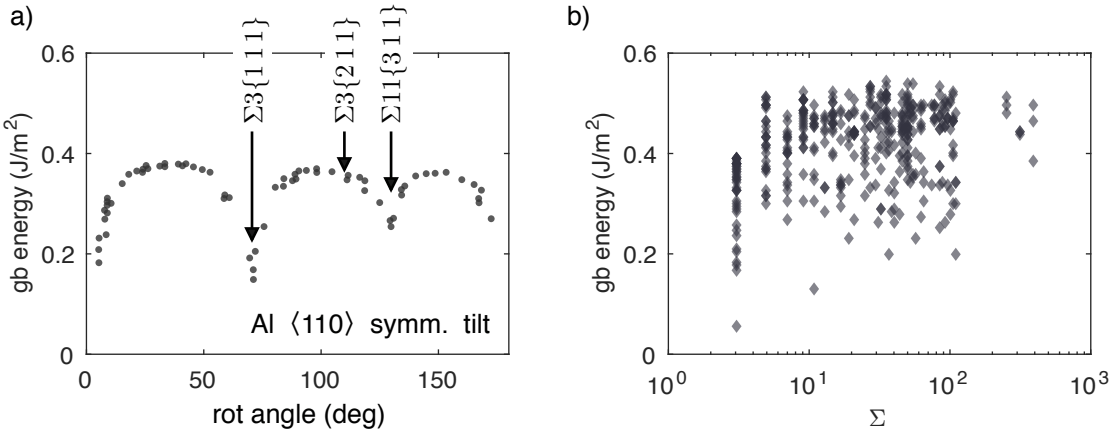

Figure 2.9: Energies of CSL grain boundaries. (a) Experimental grain boundary energies show variations in the depth of cusps at different Σ3 boundaries in Al [94]. (b) Calculated energies, based on the embedded-atom method, for Al grain boundaries are plotted against their Σ values [116]. Large variations in energy can be seen at identical values of Σ.

referred to as twins. Thus, all symmetric tilt boundaries can be considered twins [18]. The term coherent refers to complete matching of atoms at the interface. These conditions are fulfilled in fcc metals when {1 1 1} planes meet at a relative rotation of 60°.[3] In this case, the coherent twin boundary is equivalent to a stacking fault and commonly found in fcc metals with low stacking fault energies, such as copper and its alloys [11].

The sharp dip in interfacial energy for the coherent Σ3 twin can be seen when γ is plotted against the rotation angle for symmetric [1 1 0] tilt boundaries, as in Fig. 2.9 (a). (In fcc metals a 70.5° tilt about the [1 1 0] axis is equivalent to a 60° twist about the [1 1 1] axis.) Some measurements even show the boundary energy going all the way to zero at the coherent twin [121]. However, close observation of Fig. 2.9 (a) also reveals the danger of directly correlating a boundary's Σ-value with its interfacial energy. A Σ3 relation exists at a tilt angle of 109.5°, as well, but no significant reduction in γ is measured here. The difference is the boundary plane: in the former case the interface is a coherent {1 1 1} plane, whereas in the latter it is an incoherent {2 1 1} plane.

To better classify grain boundaries, researchers at Carnegie Mellon University developed the concept of the five-parameter grain boundary character distribution. For each misorientation a complete distribution of interfacial planes is considered. According to this scheme, a single curved grain boundary will have many different boundary segments (the exact number depends on the discretization interval used), all with differing character. From the distribution of grain boundary characters in a statistically significant sample set, the relative grain boundary energy distribution (GBED) can be estimated [101, 122]. The assumption here is that the frequency with which a certain boundary character appears is inversely proportional to its energy.

With the exception of Σ1 and Σ3 boundaries, the analysis of five-parameter character distributions reveal no obvious preference for high-coincidence interfaces [36]. Instead, the current consensus of the community actively investigating boundary character is that the excess energy of a given grain boundary depends more strongly on the surface energy (i.e.,

[3] Even though every atom in the boundary plane is coincident, when considering the hypothetical volumetric overlap that two interpenetrating grains with this misorientation relation would have, one can show that only every third {1 1 1} plane is perfectly aligned. Thus, Σ3 is the proper notation.

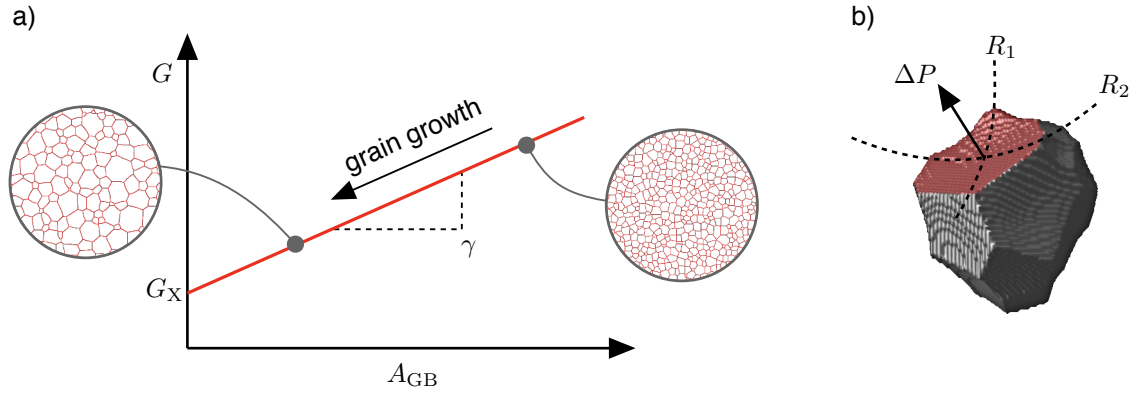

Figure 2.10: Driving force for grain boundary migration. (a) As the average grain size increases during grain growth, the grain boundary area A_{GB} decreases, thereby reducing the sample's free energy G. The mean boundary energy γ is given by the slope of this curve. (b) A finite value of γ results in a capillary pressure ΔP that acts on a curved grain boundary, shown here with the principal radii of curvature R_1 and R_2.

the inclination) of adjoining planes rather than coincidence of lattice sites [36, 95, 112, 119, 123]. This conclusion is supported by the simulated boundary energy data of Fig. 2.9 (b). A large spread in γ is observed not only for $\Sigma 3$ boundaries but for all higher Σ-values as well. On the other hand, $\{1\,1\,1\}$ twist boundaries have a relatively constant low interfacial energy across a wide range of CSL boundaries, presumably related to the low surface energy of densely packed $\{1\,1\,1\}$ planes in fcc metals [116].

2.2 Grain growth

When a polycrystal is heated, typically above about half its melting temperature, one observes an increase in the specimen's average crystallite size over time. The larger grains in the sample grow at the expense of their smaller counterparts. In a single-phase material this coarsening phenomenon is known as grain growth.

2.2.1 Curvature-driven boundary migration

The thermodynamic force driving grain growth arises from the excess energy associated with the grain boundaries in a polycrystalline sample. Accordingly, the lowest energy state for a crystalline material is that of a single crystal. This is exemplified by the schematic plot of free energy G versus grain boundary area A_{GB} in Fig. 2.10 (a). Assuming a uniform (or average) value of boundary energy γ, the free energy G varies linearly with A_{GB} according to

$$G = G_X + \gamma A_{GB}, \tag{2.8}$$

where G_X is the free energy of the single-crystalline state.

At the individual boundary level, a finite value of γ leads to an effective capillary pressure ΔP felt by a curved grain boundary in the direction of its center of curvature [18], as illustrated in Fig. 2.10 (b). (A planar boundary has a smaller area and thus smaller energy than a curved interface.) The velocity v_{GB} with which a curved boundary migrates is

directly proportional to ΔP and can be expressed as

$$v_{\mathrm{GB}} = M\Delta P = M\gamma\left(\frac{1}{R_1} + \frac{1}{R_2}\right). \tag{2.9}$$

The proportionality constant M is referred to as the grain boundary mobility, and R_1 and R_2 are the boundary's principal radii of curvature. The mobility depends strongly on temperature and is usually found to follow an Arrhenius-type relation

$$M = M_0 \exp\left(\frac{-Q_{\mathrm{mig}}}{k_B T}\right), \tag{2.10}$$

with temperature-independent prefactor M_0, activation energy Q_{mig}, Boltzmann constant k_B and absolute temperature T [4, 11]. The activation energy for boundary migration represents the energy barrier that an atom must overcome when hopping from one side of the crystalline interface to the other; its value typically lies somewhere between the activation energy for bulk lattice and grain boundary diffusion [4].

As with the energy γ of an interface, its mobility M is also thought to depend on grain boundary parameters, such as misorientation, inclination and Σ-value. However, significantly less is known about these correlations, and conflicting results are often found in the literature [117, 124]. The general lack of understanding is due not only to a scarcity of experimental data on mobility but also to the difficulty in interpreting such results [11]. From Eq. (2.9) it is evident that to determine the mobility of a given boundary, one must know its curvature and energy as well as the position of the interface as a function of time. Until recently, measurements of M were possible only on the polished surface of a polycrystal, but this method brings with it undesirable surface effects. At locations where grain boundaries intersect a specimen's free surface, thermal grooves form, which must be "dragged" along by the migrating boundary [4]. Additional factors complicating the accurate determination of M include the interaction of grain boundaries with impurity atoms (solute drag) [125, 126] and second-phase particles (Zener pinning) [127], as well as the strong dependence of mobility on temperature. In fact, the mechanism of boundary migration may change discontinuously at high homologous temperatures, as suggested by experimental results [11] and more recently by atomic-scale computer simulations showing a roughening transition [117, 128]. The complex interplay of factors affecting the grain boundary mobility emphasizes (again) the need for precise nondestructive characterization of microstructural evolution in 3D.

2.2.2 Normal grain growth

The modifier "normal" is not meant to describe the frequency with which this form of microstructural coarsening occurs but rather to indicate the special case of grain growth in which all boundary properties can be considered to be uniform and isotropic. Although the boundary energy γ and mobility M do, as discussed above, depend on misorientation, inclination, solute concentration, etc.; it may still be acceptable to assume that γ and M take on constant, average values in a specimen, as long as the material is homogeneous and devoid of significant crystallographic texture. Experiments [11] that most closely reproduce these conditions have found three notable features of normal grain growth: (1) a power-law evolution of the average grain size, (2) a unimodal lognormal distribution of grain sizes and (3) a quasi-stationary (time-invariant) distribution of normalized sizes. These attributes are summarized graphically in Fig. 2.11.

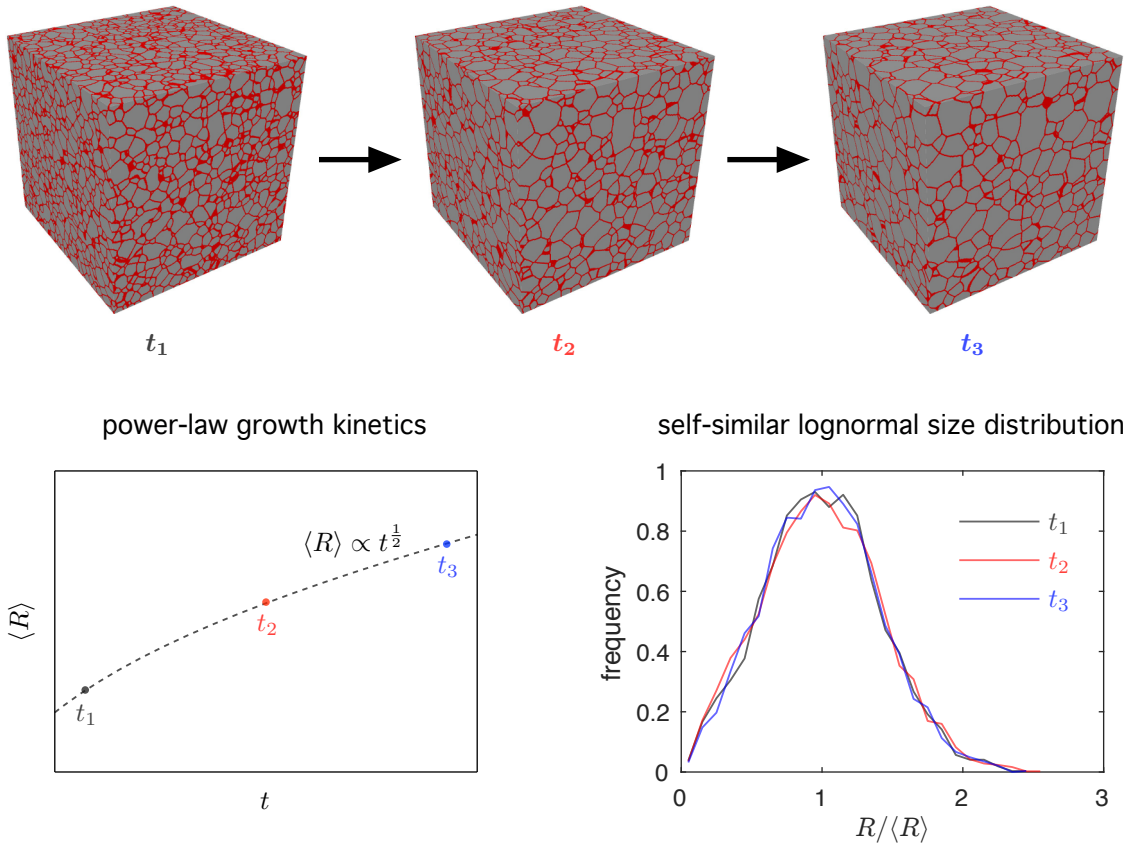

Figure 2.11: Characteristics of normal grain growth. Snapshots of a coarsening microstructure illustrate the decrease in grain boundary area and increase in grain size with time ($t_1 < t_2 < t_3$). The evolution of the mean grain size follows a power law, and the distribution of grain sizes is lognormal as well as time invariant when normalized by the mean grain size.

Based on such experimental observations, Burke and Turnbull [15] laid the foundation for a theoretical description of normal grain growth. Starting from the equation for the migration rate of a curved boundary, they made the simplifying argument that the mean boundary curvature $\frac{1}{2}(1/R_1+1/R_2)$, averaged over all grain boundaries in a polycrystalline specimen, can be approximated by the inverse mean grain radius $\langle 1/R\rangle$. In doing so they were able to rewrite Eq. (2.9) as

$$\frac{d\langle R\rangle}{dt} = \frac{2M\gamma}{\langle R\rangle}, \tag{2.11}$$

which can be directly integrated to obtain the classic parabolic grain growth law:

$$\langle R\rangle^2 - \langle R_0\rangle^2 = 4M\gamma t, \tag{2.12}$$

where R_0 is the mean grain radius at time $t = 0$. Parabolic growth of the average grain size has rarely been observed in metals, and when, then only in extremely pure samples annealed close to their melting points [11]. Therefore, it is common to write Eq. (2.12) in a more general form as

$$\langle R\rangle^n - \langle R_0\rangle^n = kt \tag{2.13}$$

with variable growth exponent n. The rate constant k also combines the terms M and γ with all other sample-specific properties affecting the boundary migration rate.

Although Burke and Turnbull achieved a significant breakthrough in the quantitative

description of grain growth, they did not consider topological constraints imposed by a space-filling ensemble of grains—e.g., when one crystallite becomes larger, the size and shape of its neighboring grains is directly affected. Smith [14] was the first to bring attention to this aspect of microstructural coarsening. He pointed out, for example, that when three grains meet at a triple juction, the local balance of interfacial tensions requires the dihedral angle between boundary planes th be 120°, which necessarily leads to curved boundaries (and thus coarsening) when grains of differing sizes meet.[4] Of course, the value of 120° stems from the assumption that all boundary energies are identical ($\gamma = \text{const.}$). If this is not the case, then curved boundaries can form even when the grain size is uniform.

In a classic paper on the theory of normal and abnormal grain growth, Hillert [16] was able to predict an analytic form for the quasi-static distribution of grain sizes. Assuming curvature-driven growth, spherical grains and the same mean environment for each grain in a polycrystal, he deduced the following relation for the time rate of change of an arbitrary grain with radius R:

$$\frac{dR}{dt} = \frac{M\gamma}{R}\left(\frac{R}{R_{cr}} - 1\right). \tag{2.14}$$

According to this equation, a grain with a radius smaller than a critical value R_{cr} will shrink, while the opposite is true of a grain with $R > R_{cr}$. For three-dimensional systems, the critical radius is slightly larger than the mean, $R_{cr} = (9/8)\langle R\rangle$. From Eq. (2.14) Hillert was then able to derive the quasi-stationary grain size distribution

$$\tilde{f}_H(u) = (2e)^3 \frac{3u}{(2-u)^5} \exp\left(\frac{6}{u-2}\right), \tag{2.15}$$

where u is the normalized grain size R/R_{cr}. Although Hillert's mean-field model is still to this day one of the most successful theoretical descriptions of normal grain growth, the shape of the grain size distribution he predicted is not consistent with experimental observations (displayed in Fig. 6.3 as part of the discussion at the end of this thesis).

2.2.3 Abnormal grain growth

Abnormal (or discontinuous) grain growth is characterized by the accelerated growth of a subset of grains in a sample and, contrary to the rarity implied in the name, is commonly found in many material systems [11, 124, 129–137]. Subtle cases of abnormal grain growth lead to a broadening of the grain size distribution, while more pronounced instances produce a clear bimodal distribution, as illustrated in Fig. 2.12 (d). Despite decades of intense research, our basic understanding of this phenomenon is still only rudimentary [138], leading some researchers to designate abnormal grain growth as one of the "perennially fascinating problems in materials science" [139]. It is here that variations in γ and M become relevant, and, because of the many factors affecting these two quantities, a plethora of mechanisms have been proposed to explain the origins of abnormal grain growth.

Typical cross sections through specimens undergoing abnormal grain growth are given in Fig. 2.12. Because this form of coarsening has unpredictable and often detrimental effects on a material, one usually tries to avoid its occurrence during production and processing. For example, aluminum alloys (Fig. 2.12 (a)) are frequently used to manufacture lightweight components for the aerospace and automobile industries [140, 141], but abnormal grain growth can significantly reduce the hardness and strength of such components.

[4] The more precise constraint is the number of facets (or faces), but the relative size of a crystallite is generally related to its total number of facets.

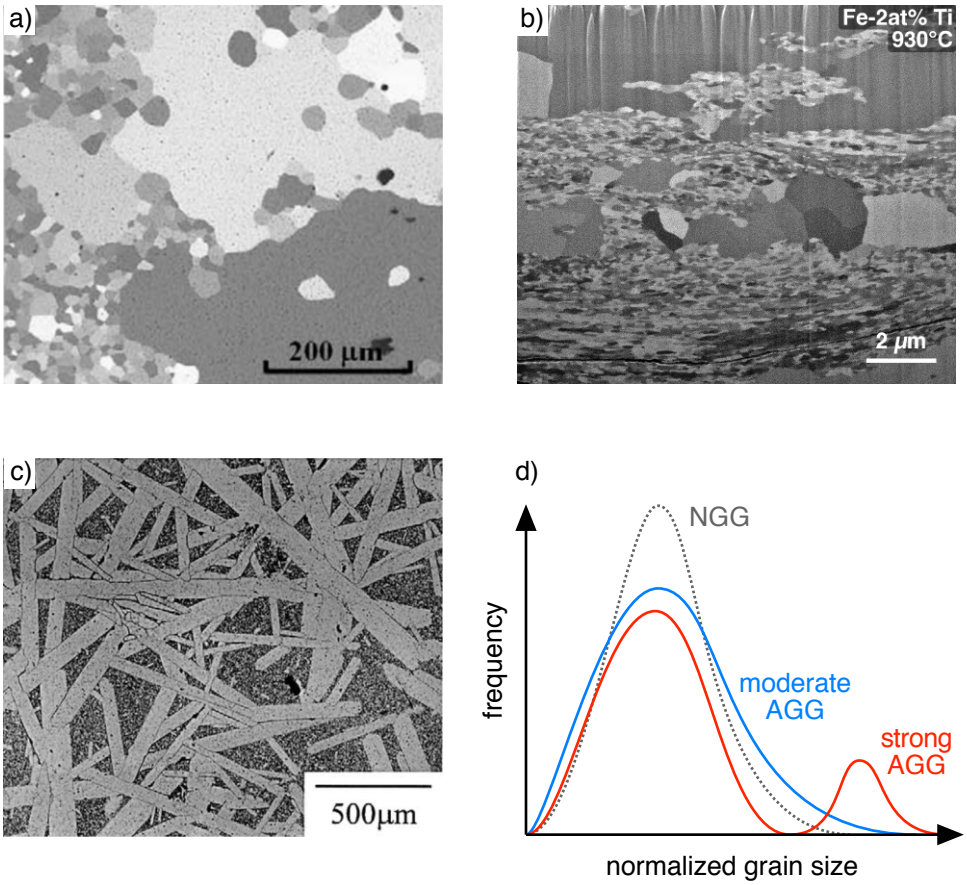

Figure 2.12: Examples of abnormal grain growth as seen in: (a) an Al-Cu alloy [142], (b) a nanocrystalline Fe-Ti alloy [133] and (c) alumina doped with TiO_2 and SiO_2 [130]. The grain size distribution of a normally coarsening specimen (NGG) is unimodal. Moderate instances of abnormal grain growth (AGG) lead to a broadening of the grain size distribution, while stronger occurrences—to which the examples in this image belong—result in fully bimodal distributions. See footnote for copyrights[5].

Similarly, the unique properties promised by nanocrystalline materials are lost when AGG sets in (Fig. 2.12 (b)). There are, however, some cases in which abnormal grain grain can be advantageous. In ceramics, elongated abnormal grains, as seen in Fig. 2.12 (c), can reduce crack propagation in otherwise brittle specimens. Grain-oriented electric steel that is produced for use in transformers is another example of purposefully induced abnormal grain growth. In either case—whether seeking to avoid or induce abnormal growth—a better physical understanding of the underlying mechanisms is desired.

Like normal grain growth, the growth of abnormal grains is driven by the reduction in excess interfacial energy, but for abnormal grain growth to occur, there must be a sustainable growth advantage for select crystallites. For an abnormally growing grain with

[5]Fig. 2.12 (a) was reprinted from Acta Materialia, 57 (15), J. Dennis, P.S. Bate and F.J. Humphreys, Abnormal grain growth in Al–3.5Cu, 4539–4547, Copyright © 2009 Acta Materialia Inc. Fig. 2.12 (b) was reprinted from Scripta Materialia, 66 (6), J.M. Dake and C.E. Krill III, Sudden loss of thermal stability in Fe-based nanocrystalline alloys, 390–393, Copyright © 2011 Acta Materialia Inc. Fig. 2.12 (c) was reprinted from Acta Materialia, 50 (19), O.-S. Kwon, S.-H. Hong, J.-H. Lee, U.-J. Chung, D.-Y. Kim, N.M. Hwang, Microstructural evolution during sintering of TiO2/SiO2-doped alumina: mechanism of anisotropic abnormal grain growth, 4865–4872, Copyright © 2002 Acta Materialia Inc. Published by Elsevier Ltd. All rights reserved., with permission from Elsevier.

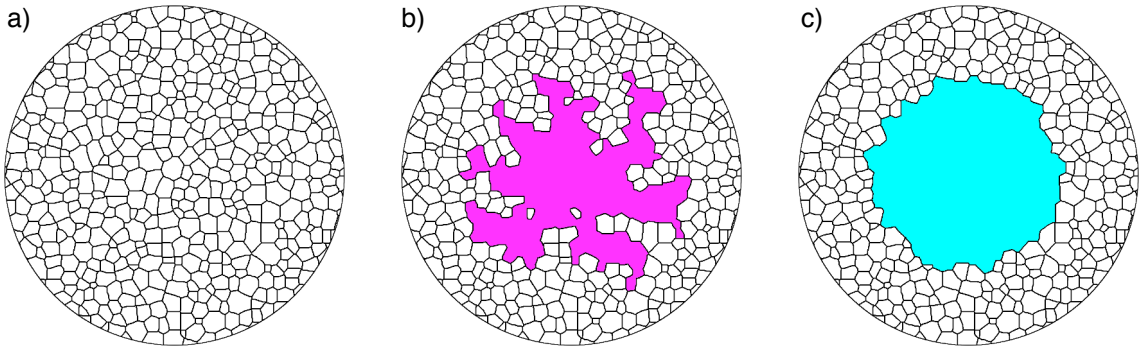

Figure 2.13: Illustrations of abnormal grain growth. Simulations have shown that when an arbitrary grain is given either an energy or a mobility advantage, it will evolve abnormally [22, 145, 146, 148, 151]. Illustrations of typical microstructures—inspired by these simulation results—are shown for (a) no abnormal grain, (b) an abnormally growing grain with an energy advantage and (c) an abnormally growing grain with an mobility advantage. An energy advantage produces abnormal grains with a fractal shape, while a mobility advantage yields more compact and more spherical abnormal grains.

radius R_{ab}, this criterion can be expressed mathematically as

$$\frac{d}{dt}\left(\frac{R_{\mathrm{ab}}}{\langle R_{\mathrm{m}}\rangle}\right) > 0, \tag{2.16}$$

where $\langle R_{\mathrm{m}}\rangle$ is the mean radius of the matrix grains. Abnormal grains are able to grow at an accelerated rate only as long as there are an adequate number of smaller matrix grains in their vicinity. Once abnormal grains begin to impinge upon each other, their growth advantage typically ceases. Thus, abnormal grain growth is almost always transient in nature, but when allowed to run its course (to full impingement), the result is often a microstructure with a mean grain size several orders of magnitude larger than the initial grain size.

In the same paper in which Hillert proposed his mean-field model of normal grain growth, he also discussed conditions for the appearance of abnormal grains [16]. He asserted that if the initial distribution of grain sizes is wide and there exist some grains larger than $2\langle R\rangle$, these will grow abnormally until all matrix grains (i.e., normally growing grains) are consumed. This description implies that a size advantage alone is enough to initiate abnormal grain growth, but later theoretical [11, 143] and numerical investigations [20] demonstrated that, given uniform boundary properties, such a mechanism is not sustainable, since larger-than-average grains always grow at slower relative rates than the mean and eventually rejoin the normal grain size distribution. On the other hand, simulations have repeatedly verified the assumption that an advantage in boundary energy or mobility can lead to abnormal growth [22, 24, 32, 144–151]. The arbitrary assignment of a low γ or high M to the boundaries of a chosen grain produces the respective microstructures shown in Fig. 2.13. The debate in recent literature and the focus of current research is to explain the origins of such growth advantages. Two well-accepted mechanisms are presented below.

Texture-induced abnormal grain growth

Many of the earliest appearances of abnormal grain growth were noted in recrystallized metals [11, 152], and because the kinetics are similar to recrystallization—both phenomena can be described reasonably well by the Johnson-Mehl-Avrami-Kolmogorov model—abnormal grain growth was historically called secondary recrystallization, a term still found in today's literature.

Following recrystallization, the newly formed strain-free grains often display a distinct crystallographic texture—i.e., a preferred orientation of crystallites. In aluminum and many other fcc metals, the recrystallization texture is the so-called "cube" texture[6] [153]. Since the presence of texture in a polycrystal leads to a high fraction of low-misorientation and thus low-energy grain boundaries, the driving force for grain growth is small. If, however, a few grains are present that deviate substantially from the primary texture component ($\vartheta \gtrsim 15°$), they will have high-energy and (presumably) high-mobility grain boundaries [154, 155]. Consequently, larger-than-average, off-texture grains can rapidly coarsen, consuming the textured regions of a specimen, where normal grain growth proceeds sluggishly. The presence of crystallographic texture is necessary for the sustainability of this mechanism, and, as one might expect, the more distinct the texture in a sample is found to be, the more pronounced are the observations of abnormal growth [156].

Although this mechanism is among the most well accepted, significant debate regarding the exact nature of the growth advantage continues to the present day. As new experimental methods (most notably electron backscatter diffraction) have allowed access to previously uninvestigated features, such as grain boundary characters at the normal/abnormal interface, new questions have arisen. In addition to speculation that large misorientations lead to a highly mobile grain boundaries [157, 158], other researchers have suggested that the mobility advantage my be restricted to certain CSL boundaries rather than being shared by all HAGBs [159, 160]. Still others contend that the relative boundary energy is more important than a mobility advantage, postulating that abnormal grains propagate through a process of "solid-state wetting" by which two LAGBs replace one HAGB because the sum of their individual interfacial energies is lower than that of the high-angle boundary [22, 146, 161]. In their short review of abnormal grain growth in Fe-Si alloys, Zaefferer and Chen [124] mention the wide variety of explanations put forth by the research community, pointing out that the authors generally do not prove their suggested mechanism but merely (and somewhat arbitrarily) assign special properties to a set of boundaries that best fit their individual results.

Further complicating the unambiguous identification of underlying processes during abnormal grain growth is yet again the effect of free surfaces. Owing to the lack of *in situ* 3D measurement techniques, scientists must infer the 3D coarsening behavior of abnormally growing grains from 2D cross sections; moreover, studies attempting to follow the time evolution of abnormally growing grains have until now always been performed on free surfaces, where the surface anisotropy of crystals may play a decisive role during coarsening. As noted by Morawiec [162], crystallites with a low surface energy could have a growth advantage in thin sheet metals, similar to abnormal grain growth in thin films [163].

[6] Cube texture can be written as: $\{1\,0\,0\}\langle 0\,0\,1\rangle$, where the $\{1\,0\,0\}$ planes are parallel to the sample surface and the $\langle 0\,0\,1\rangle$ directions parallel to the rolling direction (see also Fig. 4.13).

Pinning-induced abnormal grain growth

A dispersion of second-phase particles can slow and eventually stop the curvature-driven migration of grain boundaries by Zener pinning [127, 164]. Hillert [16] showed that under certain conditions microstructural coarsening can, nevertheless, continue via abnormal grain growth once normal grain growth has ceased. His argument has been refined by several later authors [11, 165, 166] but remains, in its essence, unchanged and is summarized here.

The Zener pinning pressure P_Z exerted by inclusions on a planar interface with energy γ is given by

$$P_Z = \frac{3\gamma f_V}{2r}, \tag{2.17}$$

where f_V is the volume fraction of randomly distributed spherical second-phase particles with radius r [11]. When P_Z is equal to the driving pressure on a curved boundary ΔP (cf. Eq. (2.9)), boundary motion comes to a halt. Assuming spherical grains and taking the mean grain radius $\langle R \rangle$ to be the mean radius of curvature, one can define a limiting grain size

$$\langle R_Z \rangle = \frac{2r}{3f_V} \tag{2.18}$$

above which normal grain growth is not possible [11]. According to Hillert a window for the initiation of abnormal grain growth exists when: the average grain radius is below $\langle R_Z \rangle$ and at least one grain "much" larger than $\langle R \rangle$ is present [16]. Because the curvature of boundaries at the normal/abnormal interface is typically greater than when two normal grains meet, the boundaries of anomalously large grains are able to overcome the pinning pressure P_Z and move in a manner that allows the crystallite to continue advancing into an otherwise pinned structure of smaller grains. Hillert argues that a grain large enough grain to grow abnormally will most likely not evolve out of the distribution of normal grains as the limit R_Z is approached. But a grain formed by some extraordinary process could grow abnormally in a pinned matrix of normal grains [16].

The coarsening and/or dissolution of the second-phase pinning particles is generally considered the most likely origin of abnormal grain growth in pinned microstructures [11, 16, 142, 165–167]. Not only do crystalline interfaces become mobile at elevated temperatures, but inclusions also begin to coarsen by Ostwald ripening. Moreover, the solubility of second phases frequently increases with temperature [166]. The combination of these effects can lead to discontinuous microstructural coarsening, either because the largest grains in a distribution are the first to break free from pinning forces and can grow abnormally, or because a nonuniform distribution of second-phase particles allows coarsening in particular regions of a sample.

It is often mentioned in the literature that second-phase pinning particles also play a role during abnormal grain growth in textured materials [124, 159, 168]. Proponents suggest that the pinning pressure is reduced for certain special interfaces (e.g., $\Sigma 9$ boundaries in Fe-Si steels [169] and $\Sigma 5$ boundaries in Al-Cu alloys [160]), which can then move with less resistance through the pinned matrix. Furthermore, owing to the presence of texture, the boundary's character does not change significantly as it encounters new neighbors during growth, remaining near its original $\Sigma 5$ or $\Sigma 9$ relation. This mechanism is, however, speculative in nature, and it is not clear why precisely these selected CSL boundaries should have special properties while others do not.

2.3 Ostwald ripening

Grain growth describes the process by which crystallites coarsen in a single-phase material. In multiphase materials, particles (or droplets) of a dispersed phase coarsen by Ostwald ripening. The eponym of this phenomenon is Wilhelm Ostwald, who was the first to systematically study the solubility of particles as a function of their size [170]. The thermodynamic driving force for Ostwald ripening is the reduction of interfacial energy, just as with grain growth; however, instead of atoms hopping from one side of a curved boundary to the other to migrate from a smaller to a larger grain, in the case of Ostwald ripening, atoms from a smaller particle must first diffuse through a second (matrix) phase before they can join a larger particle.

Ostwald ripening is a ubiquitous coarsening phenomenon not only in the realm of materials science but also our everyday lives. It contributes to the formation of rain droplets and ice particles in clouds [171]. Another—and usually less desirable—manifestation is the coarsening of ice crystals in ice cream [172]. Even if kept in a freezer, ice cream will, given time, transition from having a fine, creamy texture to one that is gritty and crunchy. In precipitation-hardened alloys, Ostwald ripening plays an important role during aging heat treatments [173]. As these examples indicate, Ostwald ripening can occur in many different multiphase systems. These can be liquid-vapor (rain droplets), liquid-liquid (emulsions), solid-solid (precipitation-hardened alloys), solid-vapor (pores in sintered materials) or solid-liquid (semisolid materials) systems.

During liquid-phase sintering, components of an eutectic alloy are heated into the semisolid temperature range. Once the liquid phase has formed, Ostwald ripening is generally assumed to be the dominant coarsening mechanism of the solid grains, certainly at later sintering times [174–176]. In Chapter 5 of this thesis, coarsening is investigated in a fully dense, semisolid Al-Cu alloy, which was selected as a model system for late-stage liquid-phase sintering. Consequently, this section focuses on Ostwald ripening as it occurs in binary semisolid systems, for which a typical example is given in Fig. 2.14. Here, a Sn-Pb alloy is annealed isothermally just above the eutectic temperature. A clear increase in the size of the Sn-rich particles is observed at longer annealing times.

The basis for Ostwald ripening lies in the dependence of the chemical potential on the curvature of a phase boundary [174, 177]. Given a semisolid binary alloy with components A and B, the concentration at the interface between the liquid α phase (the matrix phase) and the solid particles of the β phase (the coarsening phase) is described by the Gibbs-Thomson equation, which in its simplified form—assuming spherical particles with radius R, a dilute solution and isotropic interfacial energy—can be expressed as

$$C_B^{\alpha}(R) = C_B^{\alpha,\infty}\left(1 + \frac{2\gamma_{\alpha,\beta}\Omega_{\beta}}{k_B T} \cdot \frac{1}{R}\right), \tag{2.19}$$

where C_B^{α} is the concentration of B in the α phase, $C_B^{\alpha,\infty}$ is the equilibrium concentration at a flat interface (i.e., $R = \infty$), $\gamma_{\alpha,\beta}$ is the interfacial energy between the α and β phase, Ω_{β} is the average atomic volume in the solid β phase, k_B is Boltzmann's constant and T is temperature in Kelvin [177]. From this expression it is clear that C_B^{α} is higher for particles with smaller R, as illustrated in Fig. 2.15. If a dispersion contains particles of different sizes, then concentration gradients form that result in a net flow of atoms from the smaller to the larger particles in the system. This picture also indicates that the mean-field concentration of B in the matrix phase ($C_B^{\alpha}(R_{cr})$) depends on the whole ensemble of particle sizes. Thus, without knowledge of the size distribution—which determines the

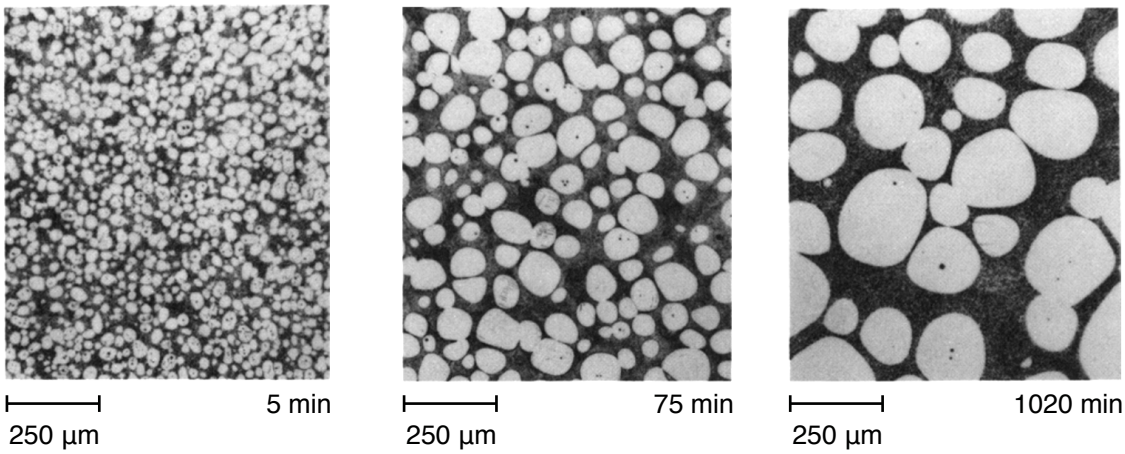

Figure 2.14: Example of Ostwald ripening occurring in a semisolid system. Sn-rich solid particles coarsen in a Sn-Pb liquid. This alloy was annealed at 185 °C (just above the eutectic temperature), resulting in a volume fraction of the solid phase of $V_V = 0.64$. Images taken from Ref. [175] and reprinted with permission from Springer Nature: Springer, Metallurgical Transactions A, 19 (11), Ostwald ripening in a system with a high volume fraction of coarsening phase, S.C. Hardy and P.W. Voorhees, 2713–2721, Copyright © The Metallurgical of Society of AIME 1988.

critical radius R_{cr}—one cannot solve the problem of ripening [177].

The first complete analytic solution for the kinetics of Ostwald ripening was given by Lifshitz and Slyozov [178] and later in an independent derivation by Wagner [179]. Their model is commonly referred to as the LSW theory, and, although it is valid only for vanishing volume fractions of the coarsening phase ($V_V \to 0$), it is the starting point for most subsequent theories of Ostwald ripening [174]. Furthermore, the existence of a time-invariant, self-similar grain size distribution—though not the exact shape of the distribution—and the temporal power law that were developed within the framework of the LSW theory still hold today [174, 180].

In developing their theory, Lifshitz, Slyozov and Wagner made the following simplifying assumptions: (1) the particle dispersion is infinitely diluted ($V_V \to 0$), (2) the coarsening phase is comprised of spherical particles and (3) the concentration fields are in steady state. The Laplace equation can then be used to calculate the concentration field outside of a particle, and, through application of mass balance at the matrix-particle interface, one can derive the growth rate equation

$$\frac{dR}{dt} = \frac{K}{R^2}\left(\frac{R}{R_{cr}} - 1\right). \tag{2.20}$$

In this expression, K is a temperature-dependent growth rate constant related to the diffusivity of solute atoms in the matrix phase, and R_{cr} is some critical grain size above which a grain grows and below which it shrinks [177]. With an asymptotic analysis in the long-time limit ($t \to \infty$), LSW were able to predict a steady-state normalized particle size distribution and show that $R_{cr} = \langle R \rangle$. The evolution of the mean particle size follows a power law with growth exponent 3:

$$\langle R \rangle^3 - \langle R_0 \rangle^3 = \frac{4}{9}Kt \quad [177]. \tag{2.21}$$

The full derivation of these equations is presented in the eloquent works of Voorhees and

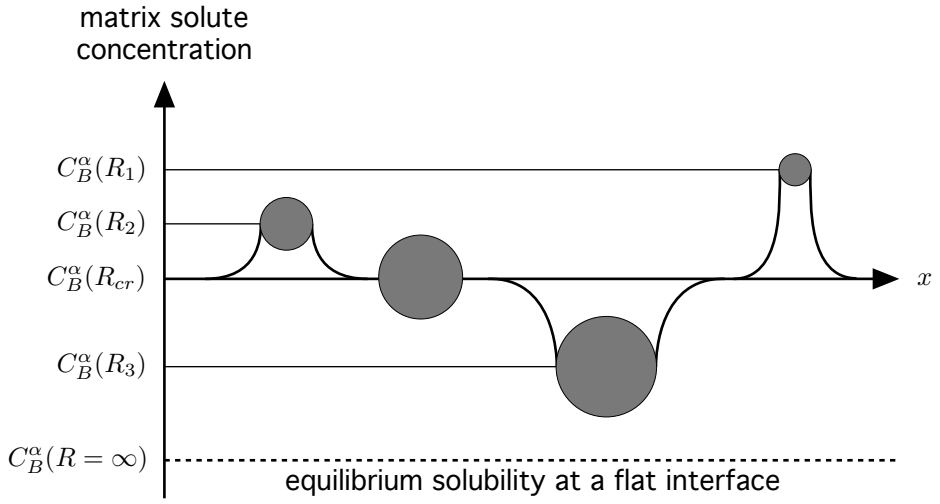

Figure 2.15: Concentration fields in a dispersion of second-phase particles surrounded by a matrix phase. The dependence of chemical potential on curvature (Gibbs-Thomson effect) leads to local variations in concentration at the boundaries of particles of different sizes. The mean concentration of excess solute ($C_B^\alpha(R_{cr})$) is set by the size distribution of all particles in the system. Lifshitz, Slyozov and Wagner [178, 179] showed that $R_{cr} = \langle R \rangle$. Based on Fig. 6.6 of Ref. [177].

Ratke, in which the LSW predictions are also compared against experimental coarsening data [174, 177, 181]. Although the LSW theory represented a significant breakthrough in our understanding of Ostwald ripening, the model's major limitation was the physically unrealistic zero-volume-fraction assumption, which allowed diffusive particle-particle interactions to be ignored (the mean-field assumption). Most subsequent treatments of Ostwald ripening have focused on determining the growth rate constant and the particle size distribution for finite volume fractions of the coarsening phase [181]. Some theories also seek to incorporate additional effects, such as particle motion, particle geometry, stress fields generated by particle-matrix misfit and anisotropic interfacial energy, all of which are presumed to be sources of error between theoretical Ostwald ripening models and experimental results [177]. More than 100 years after Ostwald's original paper and nearly 60 years after the publication of the LSW theory, the study of Ostwald ripening remains an active field of research with implications for a wide variety of material systems [177, 182].

3

Microstructural Characterization by X-Ray Diffraction

The experimental investigation of microstructural evolution in 3D requires a nondestructive characterization technique so that time-resolved data can be captured. In multiphase materials standard absorption or phase-contrast computed tomography may suffice, but in single-phase materials diffraction-based techniques are indispensable. X-ray scattering has long been used to characterize the crystal structure, chemical composition and various physical properties of materials. With the advent of 3DXRD microscopy x-rays can now be used to map grain morphologies in polycrystalline specimens as well.

3.1 Generation of x-rays

It was quite by accident that the German physicist Wilhelm Conrad Röntgen discovered x-rays in 1895. While studying the attenuation of cathode rays in metals, Röntgen noticed a glow coming from a fluorescing screen far removed from the Crookes tube he was operating [183]. For his discovery and initial experiments, Röntgen was awarded the very first Nobel prize in physics in 1901 [184]. Röntgen referred to these newly discovered rays as "x-rays" because their nature was unknown. Today we know that x-rays are a form of electromagnetic radiation, like visible light but with a much shorter wavelength.

3.1.1 Laboratory devices

In modern laboratory devices x-rays are generated in essentially they same way as in Röntgen's original experiments. A cathode ray (now known to be a beam of electrons) is directed at a metal anode in an evacuated tube—see Fig. 3.1 (a). The electrons, which are boiled off a heated filament,[1] are attracted to the anode by a large positive voltage. The resulting electric field established between the anode and filament in the evacuated tube accelerates the electrons until they collide with the anode at velocities normally greater than one-third the speed of light. The kinetic energy of most electrons arriving at the

[1] In his original device, Röntgen used a cold cathode, which requires the presence of a small number of air molecules in the Crookes tube to ignite the cathode ray.

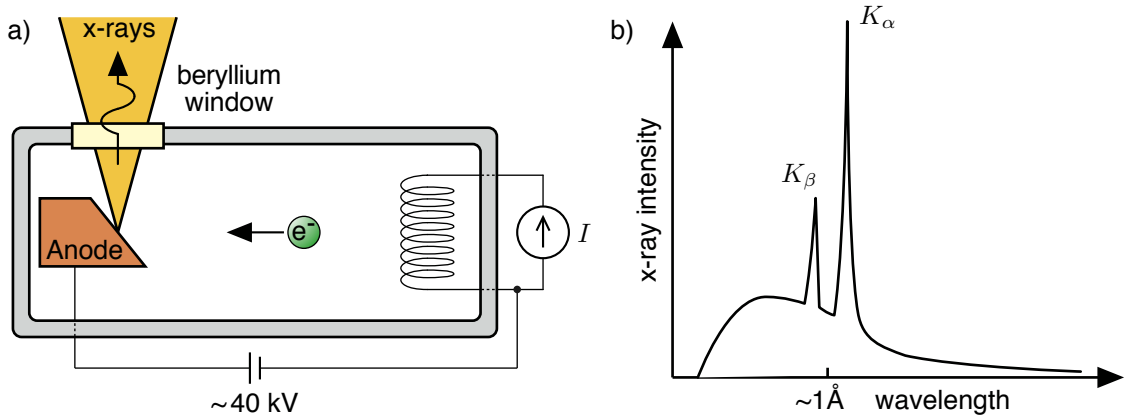

Figure 3.1: Generation of x-rays in a laboratory device. (a) X-rays are generated in an evacuated tube when high-energy electrons collide with a target anode. Electrons are extracted from a filament, heated by the current I, by applying a large accelerating voltage between the filament and anode. A beryllium window allows the x-rays to exit the tube. (b) A tube of this type will generate both Bremsstrahlung and x-rays characteristic of the elements in the target material. Electron transitions from the L to the K shell and from the M to the K shell result in K_α and K_β emission peaks, respectively. The observed x-ray intensity is the superposition of the Bremsstrahlung continuum with the discrete wavelengths that are characteristic of the anode material.

anode is lost as heat, with less than 1% of the energy being radiated in the form of x-rays [185].

Depending upon how the high-energy electrons interact with atoms of the target anode, x-rays are generated in two different ways. The first is known as Bremsstrahlung and results in a continuous energy spectrum. The origin of this type of radiation is the deceleration that the oncoming electrons experience when they collide with the target material. In order to conserve energy, the electrons emit photons of various wavelengths to compensate their losses in kinetic energy [185]. If an electron loses all of its energy in one interaction, a photon of maximum energy is emitted. This maximum x-ray energy is determined by the accelerating voltage between anode and filament. At this point, known as the short wavelength limit, the Bremsstrahlung goes to zero. The two sharp peaks of the x-ray intensity spectrum in Fig. 3.1 (b) are the result of characteristic radiation. This second type of radiation is generated when an incoming electron ejects a core electron from the K shell of an atom in the target material, and an electron from the atom's outer shells fills the resulting void. By falling to a lower quantum orbit, the electron reduces its energy and emits a photon equal to the difference in quantum energy between the two electron shells. Voids generated in the K shell are filled with highest probability by an electron from the very next shell, the L shell, resulting in the so-called K_α emission. If a K shell void is filled instead by an electron from the M shell, a photon of higher energy is emitted, referred to as K_β emission. Because the latter transition is less likely, the intensity of the K_β peak is lower [185, 186].

X-rays generated in laboratory devices are generally divergent and polychromatic, which, depending on application, may or may not be desired. For example, a divergent beam can be used to magnify an object placed in front of it, a feature often exploited in standard CT investigations. Polychromatic or "white" radiation is required when capturing Laue diffraction patterns, with which the precise orientation of a single crystal can be determined. However, for many applications of x-rays in materials science, monochromatic radiation is desirable: not only is it necessary for diffraction-based techniques used to determine crystal

structure, grain size, internal strain and texture, but an x-ray beam of a single wavelength can also enhance contrast during tomography by eliminating artifacts like beam hardening. The simplest and cheapest way to obtain a quasi-monochromatic beam is to filter out the K_β peak of the full source spectrum seen in Fig. 3.1 (b) by placing in the path of the beam a thin metallic foil that has an absorption edge lying between the K_α and K_β wavelengths [185]. A more effective monochromator can be made from a single crystal oriented to reflect K_α radiation [187].

3.1.2 Synchrotron radiation

50 years after Röntgen accidentally discovered x-rays with his cathode ray tube, a second method of generating x-rays was also stumbled upon. Scientists at General Electric's research laboratory in Schenectady, New York, had become interested in high-energy electron accelerators for use as x-ray sources[2] and built a 100 MeV betatron [188]. A betatron consists of a doughnut-shaped vacuum tube and a large electromagnet. Electrons in the vacuum tube are accelerated by varying the magnetic flux through the "doughnut hole" [189]. This manner of electron acceleration is much more practical than applying 100 megavolts between the anode and filament of a conventional x-ray tube. It was in their 100 MeV betatron that the engineers at GE first noticed the indirect effects of what we now call synchrotron radiation. The circular orbit of the high-speed electrons shrank with time due to radiative energy losses [188]. Work on betatrons would, however, soon came to an end, because in 1945 Veksler [190] and McMillan [191] described a new type of electron accelerator, the synchro-cyclotron or synchrotron. Both scientists independently proposed accelerating electrons by application of a radio frequency (RF) generator, synchronized in energy and phase to the orbiting electrons. In this manner, electrons out of sync due to, for example, radiative losses are automatically corrected. The new design was also much lighter (the large electromagnet varying the magnetic flux at the center of the ring was no longer necessary), more efficient and cheaper to construct [189]. The race to build the first operating synchrotron was on. GE was actually scooped by the British team of Goward and Barnes, who quickly built a small 8 MeV synchrotron [192]. A few months later GE finished construction of its 70 MeV synchrotron [193], which had a unique feature: a glass vacuum tube. During operation, a bright light was seen coming from this transparent tube, the color of which could be tuned by changing the electron energy [188]. Since then, the electromagnetic radiation emitted from charged particles moving at relativistic speeds has been referred to as synchrotron radiation [194]. A complete description of this new radiation was given by Schwinger in 1949 [195].

Although the engineers at GE were surprised to discover radiation coming from their electron accelerators [188], the theoretical groundwork explaining this effect had been laid long before by Maxwell in his 1873 treatise on electricity and magnetism and further developed for point charges traversing circular paths by Liénard [196], Wiechert [197] and Schott [198]. The acceleration of any charged particle will generate electromagnetic waves, like the radio waves coming from electrons oscillating in an antenna. In a synchrotron's storage ring, the electrons, which are traveling near the speed of light, can experience extremely large radial accelerations when they move through a magnetic field and thus emit very high-energy photons [194]. The latter is shown schematically in Fig. 3.2 (a).

The basic elements of a modern synchrotron source are shown in Fig. 3.2 (b). At the time

[2] General Electric (GE) planned to direct these extreme high-energy electrons at a metal target to generate Bremsstrahlung and characteristic x-rays as described above.

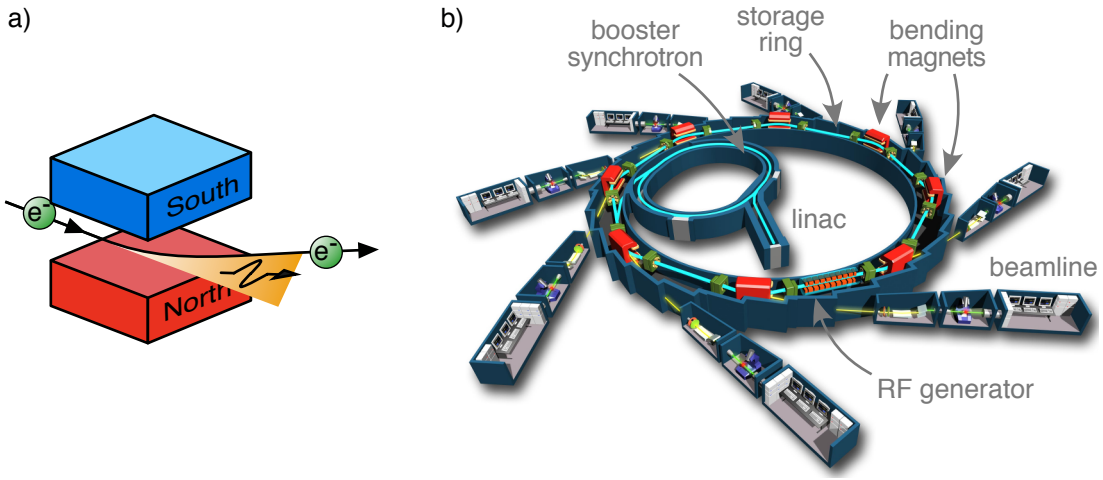

Figure 3.2: Generation of synchrotron radiation. (a) An electron is accelerated radially as it moves through a magnetic field, thereby emitting x-ray radiation. (b) The fundamental components of a synchrotron source include: a linear accelerator (linac), which feeds electrons into a booster synchrotron, where they are further accelerated until their energy is high enough to inject them into the main storage ring. The electrons in the storage ring are kept in the correct orbital path by bending magnets. The radiation produced during bending is used for experimentation at the various beamlines arranged tangentially along the storage ring. The RF generator synchronizes the electron speeds in the storage ring by adding the lost radiative energy back to the electrons. Panel (b) adapted with permission from Ref. [199], Copyright © EPSIM 3D/JF Santarelli, Synchrotron.

of its discovery, synchrotron radiation was an undesired effect, which limited the achievable end velocity in particle accelerators [188]. So-called first-generation synchrotron sources were conceived for high-energy particle physics but also allowed users access to the parasitic synchrotron radiation from beam bending. As interest in experimentation with these high intensity x-rays grew, the first dedicated (second-generation) synchrotron sources were soon built. The current state-of-the-art machines are referred to as third-generation sources and include most notably the European Synchrotron Radiation Facility (ESRF) in Grenoble, the Advanced Photon Source (APS) at Argonne National Laboratory in Chicago and the 8 GeV Super Photon Ring (SPring-8) in Japan.

In these new sources undulators are used as x-ray insertion devices to produce extremely brilliant x-ray radiation [200]. An undulator is essentially a long row of bending magnet pairs arranged so that the north and south poles of the magnets alternate. Thus, electrons traveling through an undulator oscillate back and forth, taking a sinusoidal path until they exit the undulator. If the strength of the magnetic field and distance between neighboring magnet pairs is set correctly, the resulting synchrotron radiation is nearly monochromatic, highly parallel and extremely intense [194]. This combination of properties allows materials scientists to study a wide range of phenomena nondestructively with simultaneously high temporal and spatial resolution. The experiments described in this thesis were performed at SPring-8 in Japan, which at the time achieved the highest electron energies of third-generation synchrotron sources [201].

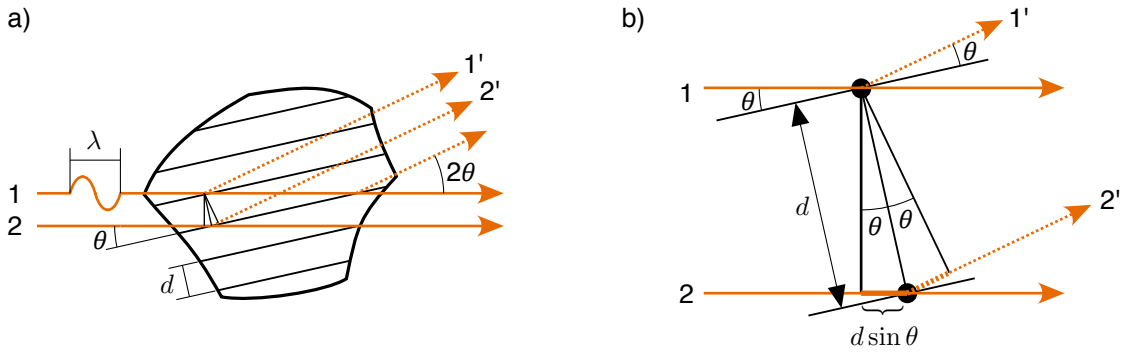

Figure 3.3: Diffraction in crystalline solids. (a) Rays 1 and 2 representing an incident x-ray plane wave approaching a set of lattice planes at an angle θ. If the condition for diffraction is fulfilled (Eq. (3.1)), then a portion of the incident beam's intensity will be diffracted at an angle 2θ. (b) Graphical representation of Bragg's law: Scattered waves will interfere constructively if the extra distance traveled by ray 2 ($2d\sin\theta$) is equal to a multiple of the incident beam's wavelength.

3.2 Conventional x-ray diffraction

3.2.1 Diffraction basics

The interatomic spacing in crystalline solids is of the same order of magnitude as x-ray wavelengths. Thus, the periodically arranged atoms act as a natural diffraction grating for x-ray radiation [185]. Max von Laue was the first to demonstrate this principle in 1912, thereby proving the wave nature of x-rays and giving birth to the field of crystallography [202]. Bragg would later develop a simple mathematical equation to describe the conditions necessary for diffraction. An x-ray beam incident with angle θ on a set of parallel crystallographic planes is scattered by the atoms defining these planes (Fig. 3.3 (a)) and will interfere constructively if the Bragg condition is fulfilled (Fig. 3.3 (b)). Examining rays **1** and **2** of Fig. 3.3 (b), we see they are scattered by parallel lattice planes with interplanar spacing d. The second ray travels the additional distance $d\sin\theta$ before and after being scattered by the second plane of atoms. If the total additional distance is equal to a multiple of the incident beam's wavelength, then the scattered rays **1'** and **2'** will interfere constructively. This relation is known as Bragg's law and written mathematically as

$$2d\sin\theta = n\lambda, \tag{3.1}$$

where λ is the wavelength of the incident x-ray radiation and n is an integer greater than or equal to 1.

The intensity of diffracted beams depends on many factors, such as the atomic scattering factor, crystalline structure, temperature, polarization, absorption, multiplicity, etc. For more information on these and other aspects, the reader is referred to the comprehensive and eloquent works of Cullity [185] and Klug and Alexander [203]. I will only emphasize here that the low-order $(h\,k\,l)$ planes of a crystal generally display the highest relative diffraction intensities and that not all planes are represented in diffraction patterns owing to systematic absences caused by destructive interference. From the unit cell structure one can calculate so-called selection rules that determine which sets of crystallographic planes will interfere constructively [185, 203]. In the fcc Al alloys of this thesis, diffraction can occur at angles where Bragg's Law is satisfied for planes that have either all odd or all even h, k, l indices. Thus, the first seven possible reflections, in order of increasing diffraction

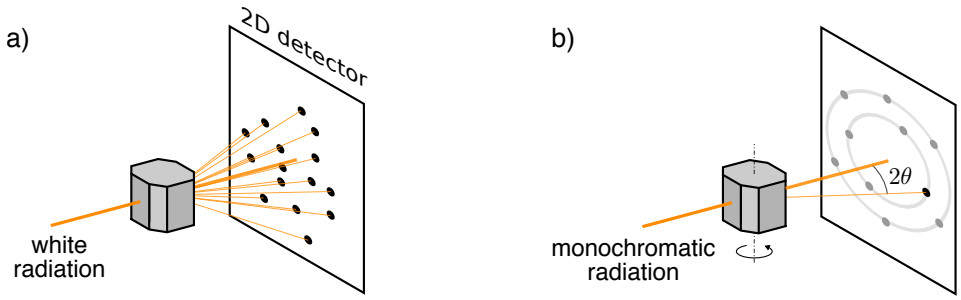

Figure 3.4: Single-crystal x-ray diffraction. (a) A single crystal that is illuminated with a white (polychromatic) x-ray beam produces many diffraction spots simultaneously. (b) When monochromatic radiation is used, the crystal must be rotated in order to collect more than one spot.

angle, stem from the {1 1 1}, {2 0 0}, {2 2 0}, {3 1 1}, {2 2 2}, {4 0 0} and {3 3 1} planes.

3.2.2 Single-crystal diffraction

When a single crystal is illuminated with a monochromatic x-ray beam, the chance that any of its lattice planes will fulfill the Bragg condition and diffract the incident radiation is relatively low. To acquire diffraction spots, one can either employ a polychromatic source or rotate the crystal. The former was the approach used by von Laue for his original diffraction experiments. The method is, however, by no means outdated: it is still widely used to solve the structure of chemical and biological molecules [200]. As illustrated in Fig. 3.4 (a), the Bragg condition is fulfilled for a large number of planes and many diffraction spots appear simultaneously when a single crystal is irradiated with a white beam. Owing to crystal symmetry, the intensity maxima appear along elliptical or hyperbolic paths, the origin of which are so-called zone axes [185]. A zone axis is used to define a set of planes that all contain this crystallographic direction. For example, if we choose the [0 0 1] axis to be our zone axis, then all planes in which the [0 0 1] axis lies (e.g., (1 0 0), (1 1 0), (2 1 0), etc.) are referred to as planes of the [0 0 1] zone. Accordingly, analysis of the Laue diffraction patterns provides very detailed information on crystal orientation and structure.

The second means by which to obtain multiple diffraction spots and thus more information on a single-crystalline specimen is the rotating-crystal method illustrated in Fig. 3.4 (b). In contrast to the Laue method, here the sample is illuminated with a monochromatic x-ray beam. Thus, for any given orientation of the sample, there will be few if any lattice planes that diffract. However, by rotating the crystal 180 °, all planes will satisfy the conditions for Bragg reflection at least once, and an analysis of the full diffraction pattern allows for comprehensive indexing of the lattice planes and determination of the underlying crystal structure. For this purpose the rotation method is the most powerful and most often used of the various diffraction methods [185, 204]. Because the wavelength and angle of the incident beam are fixed, all diffraction spots corresponding to a given set of lattice planes $\{h\,k\,l\}$ are located on the detector with the same radial distance to the transmitted beam. The circular paths along which related diffraction spots lie are called Deybe-Scherrer rings. For a single crystal, the number of spots found on each ring is determined by the multiplicity factor of each respective lattice plane.

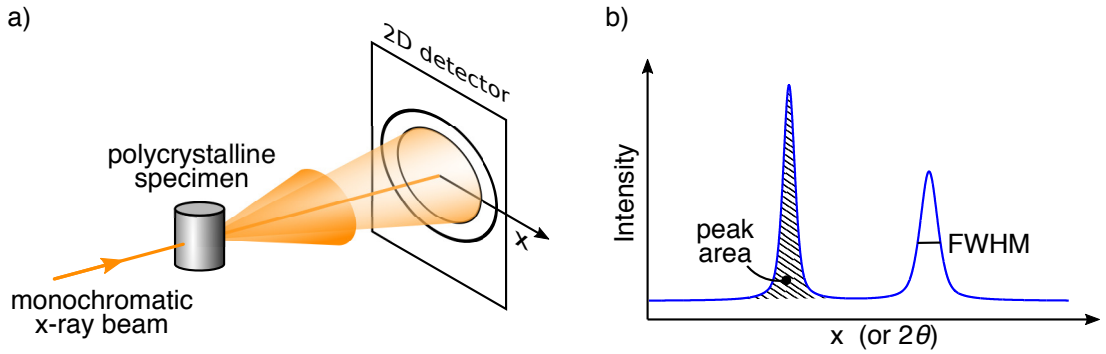

Figure 3.5: Powder diffraction method. (a) When a fine powder or polycrystalline sample is struck by monochromatic x-ray radiation, a portion of the incident beam's intensity is diffracted as a solid conical shell forming rings on a 2D detector. (b) A linear plot of intensity vs. position or 2θ reveals the intensity profile of the diffracted beams. The integrated intensity of each reflection is given by the area under the respective peak. The average grain size can be estimated from the peaks' full width at half maximum (FWHM).

3.2.3 Polycrystal or powder diffraction

When a fine powder or a polycrystalline sample consisting of small, randomly oriented grains is placed in a monochromatic beam, many of the constituent crystallites will, by chance, be oriented to diffract a portion of the incoming x-rays. This method is similar to the rotating-crystal method, except that the specimen need not be rotated, since one can assume that every possible orientation is already present in the polycrystal or powder. A further consequence of randomly oriented crystallites is that the diffracted beam takes on the shape of a solid conical shell, as seen in Fig. 3.5 (a). This feature can be understood by considering, for example, the $\{1\,1\,1\}$ lattice planes of a polycrystalline sample: not only will the $\{1\,1\,1\}$ planes of many individual crystallites be properly oriented for Bragg diffraction, but there are also an infinite number of possible rotations for the $\{1\,1\,1\}$ surface normals about the incoming x-ray beam [185]. Thus, instead of individual diffraction spots from a single crystal appearing on the detector (Fig. 3.4 (b)), the entire circumference of the Deybe-Scherrer rings are illuminated.

The intensity profile of the diffracted cones varies from reflection to reflection. If we examine a fixed length of the Deybe-Scherrer rings and plot the intensity versus position, we obtain a graph similar to Fig. 3.5 (b). Instead of using the position x here, it is more natural to plot 2θ on the horizontal axis, which allows for straightforward calculation of the lattice spacing d using Bragg's equation.

3.2.4 Grain size determination

In conventional research laboratories, powder diffractometers configured in Bragg-Brentano focusing geometry are quite possibly the most common setup, and from the diffraction patterns they produce one can gather a substantial amount of information regarding the nature of the illuminated material [185, 203]. The crystal structure and lattice parameters can be determined from the 2θ positions of the peaks. In multicomponent systems, concentrations can be estimated via Vegard's law [185], and in multiphase alloys the amount of each phase can be determined from the relative intensities of their respective x-ray peaks.

If the grain size is small enough, it can also be estimated from the width of diffraction

peaks, because a finite grain size—and thus a finite number of diffracting planes—leads to peak broadening [185, 203, 204]. The full width at half maximum (FWHM), seen in Fig. 3.5 (b), is often taken as the measure for peak width. With this value, one can approximate the average grain size of the diffracting material by applying the Scherrer equation [205]:

$$\mathrm{FWHM}\,(2\theta) = \frac{K\lambda}{L\cos\theta}. \tag{3.2}$$

The mean column length of the crystallites contributing to the Bragg peak is given by L, and the wavelength of the incident radiation by λ. The central angular position of the diffraction peak is denoted here by θ, and K is a constant close to unity (often taken to be 0.89 or 0.94) [204]. The column length L is the size of the diffracting crystal perpendicular to the scattering planes.

Due to the inverse relation between peak width and grain size, one can more accurately determine the peak broadening and, consequently, the size of smaller crystallites. Nanocrystalline materials are, therefore, well-suited for grain growth investigations by means of standard x-ray diffraction (XRD) [206]. Experiments performed at the beginning of this thesis work demonstrate both the capabilities and limitations of this method. Binary nanocrystalline Fe-Ti alloys were synthesized via high-energy ball milling and thereafter annealed *in situ* in a PANalytical X'Pert Pro diffractometer equipped with a Co source, position sensitive detector (PSD) and vacuum furnace. With this setup, shown schematically in Fig. 3.6 (a), isothermal anneals were performed at 930 °C while repeatedly scanning 2θ from 49° to 53° in Bragg-Brentano geometry. Typical results for a Fe-2 at% Ti sample are plotted in Fig. 3.6 (b). In the scanned 2θ range both (1 1 0) bcc and (1 1 1) fcc iron peaks can be found, and we see the effects of the α to γ phase transformation after about 20 minutes with the appearance of the (1 1 1) peak. Theoretically, from these two peaks one can calculate both the amount and average grain size of the two phases; however, the first limitation of this technique becomes apparent in Fig. 3.6 (c). Application of Eq. (3.2) shows that the bcc grains grew from about 44 nm to 86 nm in one hour, but the (1 1 1) fcc peak is so narrow that a grain size could not be resolved for this phase. Every diffractometer has a finite instrumental broadening, which represents the narrowest observable peak width. For the XRD setup used here, crystallite size broadening can no longer be separated from instrumental broadening when the grain size has reached about 150 nm. Thus, the grains of the fcc phase must have been on average at least 150 nm in size. In Fig. 3.6 (d), the electron micrographs of the annealed specimen do indeed show a bimodal distribution of grain sizes, as suspected from the diffraction data.

The second limitation is the statistical nature of the Scherrer and related analyses. Although millions of nanocrystalline grains can be probed simultaneously by XRD, there is no way to examine the evolution of individual grains. One is able to follow only changes in the mean grain size and, in some cases, the approximate width of the grain size distribution [204]. In general, however, XRD is not well suited to the analysis of crystallites with a broad or multimodal size distribution. Although the small grain size makes nanocrystalline materials good candidates for growth studies by XRD, abnormal grain growth is commonly observed in such samples [133, 137, 207–209] and relying on diffraction data alone is dangerous when characterizing such materials [209, 210]. Except for material systems that have an allotropic phase transformation tied to the occurrence of abnormal grain growth, the latter remains effectively invisible to XRD.

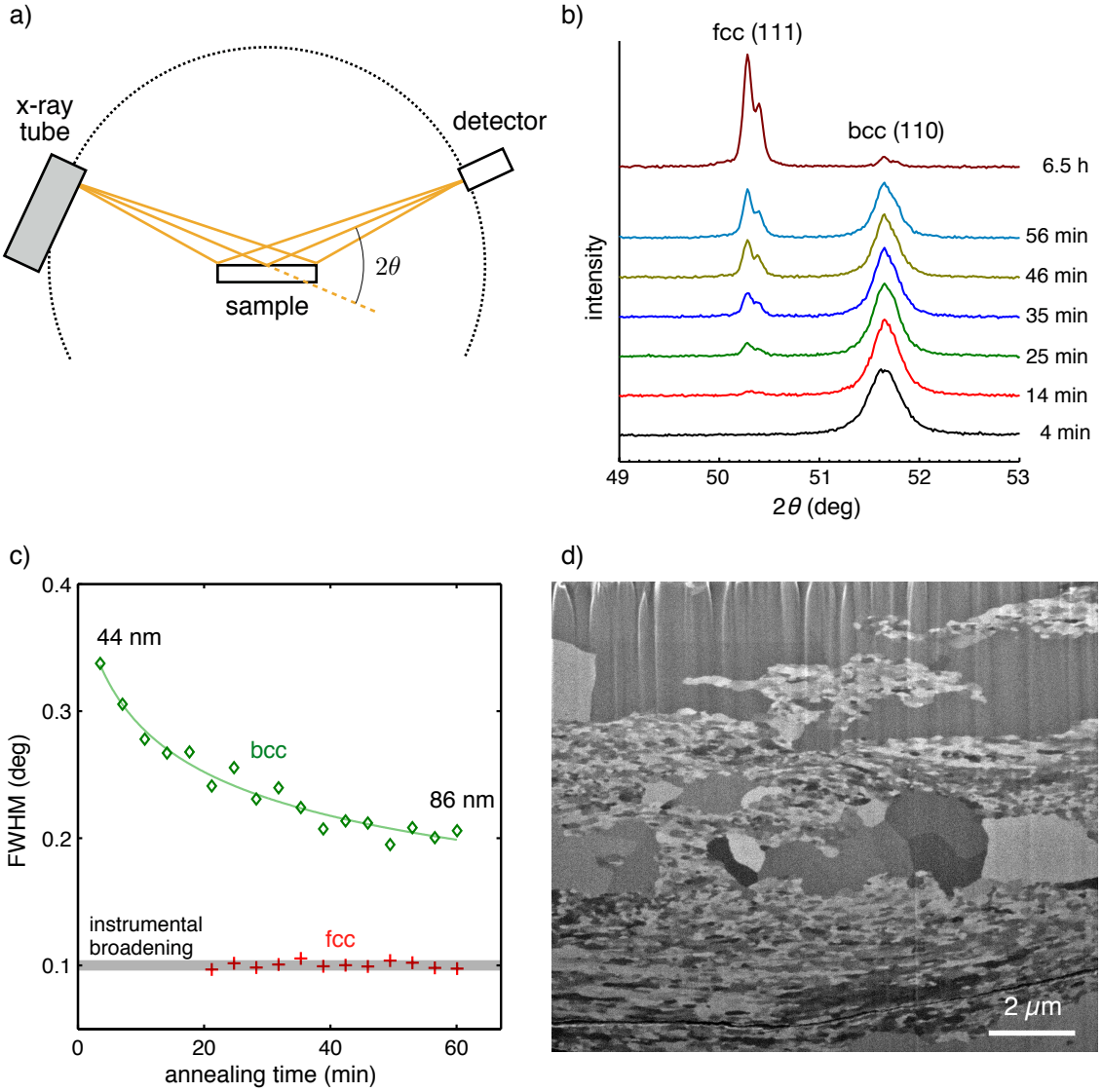

Figure 3.6: Grain growth studies in standard XRD. (a) The Bragg-Brentano geometry is the most common setup for powder XRD because it focuses the divergent incident beam onto the detector. (b) The growth of the fcc phase is clearly seen in diffraction patterns recorded during *in situ* annealing of an Fe-2 at% Ti alloy at 930°C. (c) The width of the bcc peaks show that this phase is nanocrystalline, but the average grain size of the fcc phase cannot be quantified since its peaks have widths equal to the instrumental broadening. (d) A cross section through a specimen that was taken out of the furnace after the fcc phase had grown to 50% shows a clear bimodal microstructure. Figure panels (b), (c) and (d) reprinted from Scripta Materialia, 66 (6), J.M. Dake and C.E. Krill III, Sudden loss of thermal stability in Fe-based nanocrystalline alloys, 390–393, Copyright © 2011 Acta Materialia Inc. Published by Elsevier Ltd. All rights reserved., with permission from Elsevier.

3.3 Three-dimensional x-ray diffraction

Diffraction experiments performed on conventional polycrystalline samples with micron-sized grains often lead to spotty, incomplete Scherrer rings. The diffraction pattern is something between that of a single-crystalline (Fig. 3.4 (b)) and a fine powder specimen (Fig. 3.5 (a)). Exactly how incomplete the rings are depends on the number of grains in the irradiated volume and their crystal symmetry. If the individual diffraction spots along the rings can be separated, then it is possible to determine precisely the orientation of each crystallite from which the polycrystal is composed. Furthermore, from the shape of diffraction spots, one can also reconstruct the morphology of grains to which the respective diffraction signals belong. Thus, a nondestructive mapping of single-phase materials in three dimensions is conceivable. This idea motivated the development of a new diffraction-based imaging technique that came to be called three-dimensional x-ray diffraction (3DXRD) microscopy [64, 65, 78].

3.3.1 Basics of multigrain crystallography

The reconstruction of 3DXRD data is a two-step process. First, the individual grains located within the irradiated volume of a sample are indexed, i.e., their crystallographic orientation and center of mass are determined. Next, the spatial extent of each grain is mapped back to the sample volume. After a short illustration of the experimental setup, both steps of the reconstruction procedure are described below.

Experimental setup

Because an intense monochromatic and parallel x-ray beam is a prerequisite for the technique, 3DXRD experiments are performed at synchrotron radiation facilities. A typical experimental setup is shown schematically in Fig. 3.7. Although a flat, planar beam was used throughout the development and early stages of 3DXRD, it is now common to use a box-beam to illuminate the sample. Individual grains in the irradiated volume diffract a portion of the incoming beam's intensity when their various atomic planes satisfy the Bragg condition, resulting in bright spots on a two-dimensional detector. In general, two detectors are employed: a high-resolution ($\sim$ 5µm pixel size) near-field detector and a lower-resolution ($\sim$ 50µm pixel size) far-field detector. The near-field detector is physically smaller than the far-field detector (the number of pixels is usually about the sample for both) and placed closer to the sample, so that the first four or five Bragg peaks can be captured. Obviously, the distance between diffracted and transmitted beams increases as they travel away from the specimen. If the near-field detector is too far from the sample, too few reflections are captured, and the quality of the reconstructed data suffers. If the near-field detector is too close to the sample, reflections begin to overlap, which also leads to lower-quality reconstructions. The far-field detector, on the other hand, can be placed much farther from the sample and still capture a large number of Scherrer rings because of its larger pixel size. The greater sample-to-detector distance allows for a more accurate determination of scattering angles and consequently grain orientations. Usually it is sufficient to capture 6 to 7 complete rings with the far-field detector. The specimen, which is typically cylindrical, is mounted on a tilt/translation stage for alignment purposes and rotated 360° during data acquisition to ensure that each grain comes into diffraction many times.

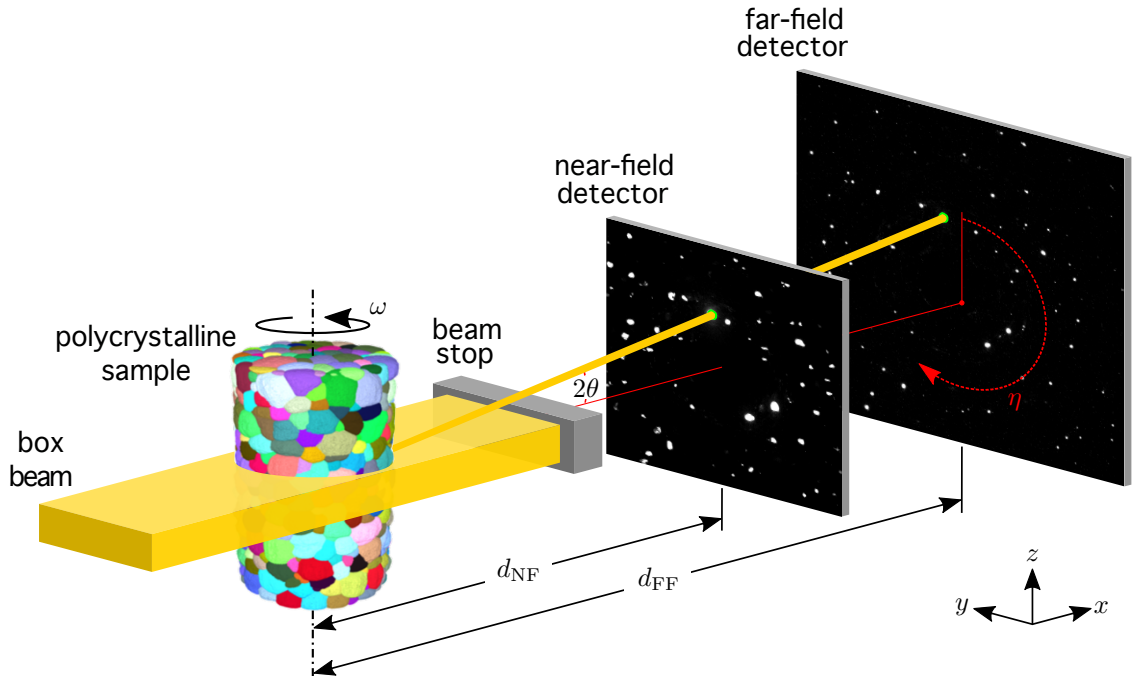

Figure 3.7: 3DXRD experimental setup. A polycrystalline sample is illuminated with a monochromatic x-ray beam and rotated up to 360° so that each grain fulfills the Bragg condition for diffraction multiple times. The diffraction spots at each angle of rotation ω are recorded on two detectors: (1) a high-resolution near-field detector placed a short distance d_{NF} from the sample and (2) a far-field detector with a coarser pixel size positioned at a greater distance d_{FF} from the specimen. The laboratory coordinates x, y and z are defined as shown, along with the diffraction angle 2θ and the angle η about the circumference of the Scherrer rings.

Grain indexing

From the diffraction data collected with the far-field detector, it is possible to determine the crystallographic orientation and location of each grain in a polycrystalline specimen. Thousands of individual far-field diffraction patterns are typically collected as the sample is rotated in small increments about an axis that is ideally parallel to the z-axis of the laboratory coordinate system (cf. Fig 3.7). The noisy raw diffraction images (Fig. 3.8 (a)) are filtered and binarized to enable identification of individual diffraction spots (Fig. 3.8 (b)). Each spatially separated area of diffracted intensity can then be assigned a set of coordinates $(y_{\mathrm{det}}, z_{\mathrm{det}}, \omega)$, where y_{det} and z_{det} are the positions of the peak's maximum intensity on the far-field detector, and ω is the sample rotation for the given diffraction image. In this manner, one is able to parameterize all diffraction spots originating from the grains of an illuminated sample volume. When the diffraction maxima $(y_{\mathrm{det}}, z_{\mathrm{det}})$ recorded across all values of ω are combined in a single scatter plot, an image with nearly complete Scherrer rings is the result—see Fig. 3.8 (c). Close inspection of this subfigure reveals the typical pattern of rings for fcc materials.[3] An alternative form for displaying the diffraction spots is presented in Fig. 3.8 (d). The diffraction angle 2θ of each maximum can be calculated by the simple trigonometric relation

$$2\theta = 2\arctan\left(\frac{\sqrt{y_{\mathrm{det}}^2 + z_{\mathrm{det}}^2}}{d_{\mathrm{FF}}}\right), \tag{3.3}$$

[3] All data in Fig. 3.8 originate from an fcc Al-5 wt% Cu alloy.

where d_{FF} is the distance from the sample to the far-field detector. By plotting η—the angle of rotation about the x-axis—vs. 2θ, we unroll the Scherrer rings, which now appear as vertical lines. The broadening of the Scherrer rings along the y-axis ($\eta = \pm 90\,^{\circ}$) is also clearly evident. This effect results from the use of a parallel incident beam and will be described in more detail in the following section.

Each diffraction spot represents a set of parallel lattice planes. If the lattice parameters and exact orientation of the sample's rotation axis relative to the detector are known, then the observed spots can be transformed into scattering vectors in reciprocal space. (For a complete mathematical description of this transformation, refer to Appendix A of Ref. [211].) In the diffraction-based imaging community, these scattering vectors are commonly referred to as g-vectors, a notation also adopted in this thesis.

The task of grain indexing is to determine which g-vectors belong to which crystallites. An efficient algorithm for doing so was developed by S. Schmidt [211] and made publicly available as the software package GrainSpotter [212]. Assuming each grain is a single crystal, its orientation is given by a specific point in orientation space. Individual g-vectors, however, provide only the orientation of a given set of lattice planes (i.e., the vector normal to the diffracting planes but not the crystal's rotation about this vector) and are, thus, mapped as lines (so-called geodesics) in the Rodrigues orientation space [211]. But the geodesics of all g-vectors corresponding to the same grain must pass through a single point defining that grain's 3D orientation. Consequently, by identifying locations in orientation space where a large number of geodesics intersect, one is able to establish the crystallite orientations present in the illuminated sample volume [211].

GrainSpotter performs the task of indexing iteratively, initially assuming that all grains are located at the center of the sample [211]. Analogous to the intersection of geodesics at a common point in orientation space, if we trace the diffracted rays belonging to a single grain from the detector back to the sample, they should all intersect at a common point in real (sample) space: namely, at their point of origin. Thus, at a grain's true location in the specimen, the spread of the back-traced rays is smallest. By minimizing the spread of these rays about a point in the sample volume [211], one can fit each grain's center-of-mass location. Of course, a grain's measured orientation and position are interrelated, since the g-vectors (scattering vectors) are determined from the direction of diffracted rays, which depend on the position of the grain relative to the detector. Through an iterative process of minimizing the spread of geodesics in orientation space and diffracted rays in real space, one can refine the position and crystallographic orientation of each grain. The final product of grain indexing is a set of "seed" grains for which the 3D center-of-mass positions (Fig. 3.8 (e)) and orientations (Fig. 3.8 (f)) are now known.

Described above is the indexing algorithm implemented by GrainSpotter, which was used during the reconstruction of all data sets presented in this thesis. Other strategies for grain indexing are summarized in Refs. [78, 79].

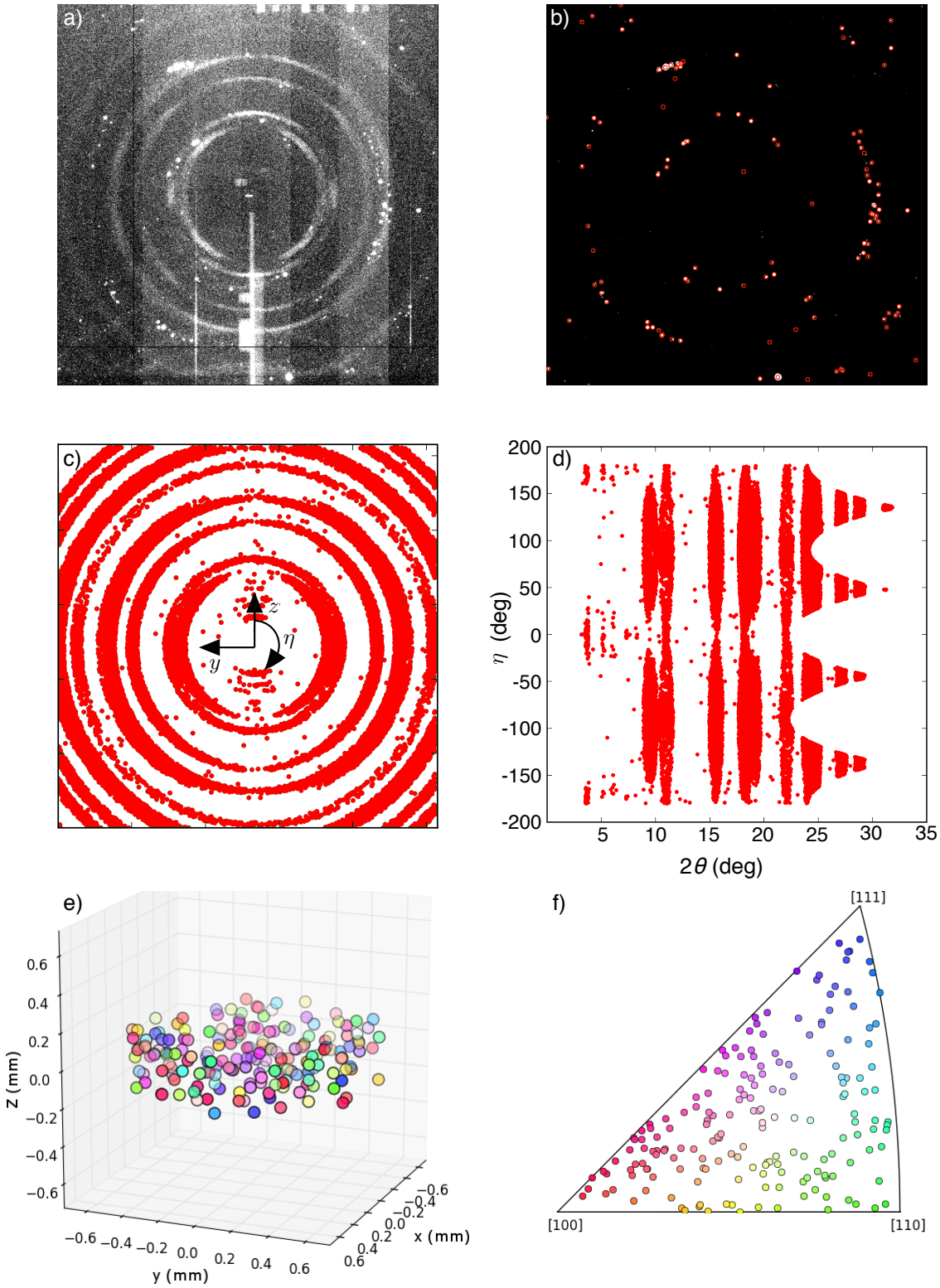

Figure 3.8: Grain indexing from far-field diffraction patterns: (a) raw diffraction signal, (b) filtered and binarized diffraction image showing detected peak positions, (c) combination of all diffraction peaks, (d) alternative representation of all diffraction peaks, (e) center-of-mass positions for indexed grains and (f) indexed grain orientations displayed on an inverse pole figure for cubic crystal symmetry.

Grain mapping

The second step in the reconstruction of 3DXRD data is the mapping of grain shapes. For this purpose the near-field diffraction images are utilized. Currently, there exist two separate classes of mapping algorithms: (1) forward-projecting and (2) inverse-problem methods [79, 213]. The latter are similar to approaches taken to reconstruct tomographic data. The application of such algorithms to 3DXRD data sets is computationally taxing owing to the considerable size and dimensionality of the reconstruction space—a six-dimensional combination of orientation and sample space [213, 214]. At the same time the total number of projections is limited, being determined by the experimental setup and the crystal symmetry. The inverse-problem methods for reconstructing 3DXRD data are, nevertheless, of great interest, since they yield, in theory, the highest-quality grain maps [213]. However, with forward-projecting algorithms it is possible to avoid much of the aforementioned complexity, while, under many circumstances, still achieving high-quality grain maps.

All 3D grain maps presented in this thesis were reconstructed with GrainSweeper, a second piece of software developed by S. Schmidt [213, 215]. The underlying principles of the program's forward-projecting algorithm are summarized in Fig. 3.9. When a polycrystal is illuminated with a parallel beam, the detected diffraction spots are 2D projections of its grains, as illustrated in Fig. 3.9 (a). To obtain multiple projections of each grain, the sample is typically rotated 360°. With the setup described here, it is common to detect more than 200 diffraction spots per fcc Al grain. Although the intensity of the diffraction spots contains information on the scattering volume, current implementations of GrainSweeper do not utilize this feature [216]. Instead, the algorithm relies solely on the area of the spots after filtering and binarization. Also evident in Fig. 3.9 (a) is the horizontal shift of the detected diffraction signal, briefly alluded to during the presentation of far-field data in the previous section. If, during rotation, a grain fulfills the Bragg condition and diffracts to the right while also positioned to the right of the sample's rotation axis, the resulting diffraction spot will be detected to the right of the given reflection's ideal Scherrer ring position.[4] The same effect causes the broad scattering of points about the Scherrer rings evident in Figs. 3.8 (c) and (d). The rings are typically wider in the y-direction because of the beam geometry. The so-called "box beam" is usually not square but rather rectangular, leading to this asymmetric distribution of diffraction spots.

The first step in the mapping process is division of the sample space into small subvolumes (voxels). Thereafter, the seed grains from GrainSpotter are imported. Although this step is not necessary, it generally improves the accuracy and runtime of GrainSweeper. Each seed grain can then be "grown" from its center of mass until the predefined sample volume is filled in, as illustrated in 2D in Figs. 3.9 (c) and (d). Because the orientation of each seed grain is known, the program projects, as it steps through sample space, a diffracted beam from the current voxel to the detector. If enough ($> 70\%$) pixels are illuminated at the expected locations on the detector, the voxel is assigned the assumed orientation. The ratio between the number of detected diffraction signals to the expected number defines a value referred to as the "completeness." It is a measure for the confidence with which each voxel is assigned. A map of the completeness is shown in Fig. 3.9 (e). White indicates 100% completeness, while darker shades of gray denote lower values. Large volumes of low completeness often indicate missing seed grains. In the vicinity of grain boundaries it is common for the completeness to fall off somewhat (similar

[4] The positions of the ideal Scherrer rings are the locations on the detector to which grains would diffract if they were all centered in the incident x-ray beam.

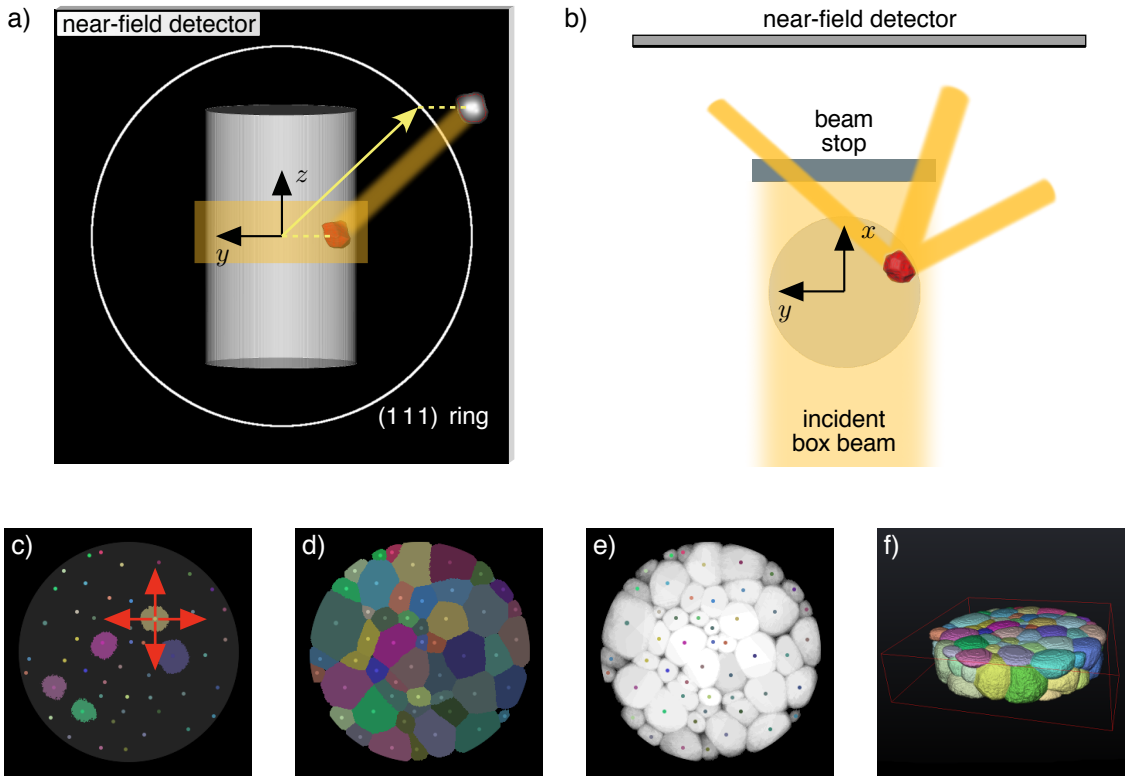

Figure 3.9: Mapping of grain shapes from near-field diffraction data. (a) A cylindrical sample is illuminated with a monochromatic, parallel box beam, incident in the $+x$ direction. The (1 1 1) planes of an interior grain fulfill the Bragg condition and diffract a portion of the incoming intensity, projecting the grain's shape onto the near-field detector. Because the grain is located right of center, the diffraction spot is shifted to the right of the (1 1 1) Scherrer ring. (b) As the sample is rotated (about the z-axis) many projections of the same grain are captured. (c) The projections are used to grow the seed grains—found during grain indexing and shown here as colored dots—into (d) a space-filling ensemble of crystallites. (e) The completeness of the diffraction signal for each voxel can also be mapped. (f) Final 3D reconstruction of the entire illuminated sample volume.

to the confidence index of electron backscatter diffraction maps). Also near boundaries, two solutions may exist for the same voxel. This can be caused by smearing effects [213], when strong diffraction signals bleed onto neighboring pixels on the near-field detector, and spots appear larger than they actually are. In such cases, the orientation with the highest completeness is selected. The final output of GrainSweeper is a 3D grain map (3.9 (f)), equal in volume to the intersection of the incident x-ray beam with the sample.

When neighboring grains have similar orientations, their diffraction spots may overlap on the near-field detector. This effect, in combination with detector inhomogeneities, can lead to segmentation errors at low-misorientation grain boundaries. Typical examples are shown in Fig. 3.10. Most grain boundaries, including the low-angle grain boundaries, are smooth and presumably well located. A few interfaces, however, have quite unphysical forms. The segmentation errors also vary from time step to time step, because samples were removed from the experimental hutch for annealing. This fluctuation in boundary position leads to an artifact during the analysis of average grain boundary velocities; low-angle grain boundary appear to migrate faster than they actually do, as seen later Fig. 4.21.

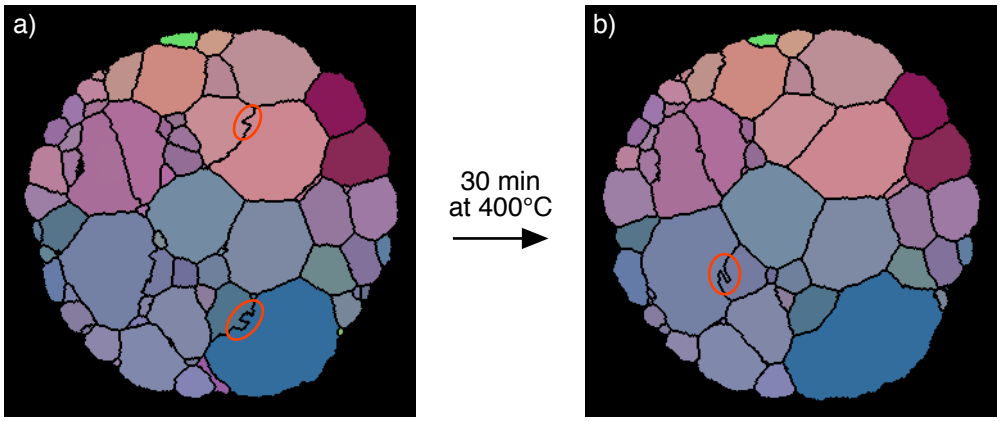

Figure 3.10: Example of a segmentation artifacts. Overlapping diffraction spots and detector inhomogeneities can lead to segmentation errors at low-angle grain boundaries, as indicated with red circles. A comparison of the same cross section from (a) an earlier to (b) a later time step reveals that this artifact appears irregularly from measurement to measurement.

3.3.2 Postprocessing and grain tracking

The sample volume that can be probed by a single 3DXRD measurement is limited by the number of crystallites contained therein, since both grain indexing and, to a lesser extent, grain mapping are most reliable when diffraction spots do not overlap. Under ideal conditions up to 1000 grains may be indexed simultaneously [78]. In more realistic specimens, however, this quantity is reduced by the presence of crystallographic texture and nonuniform grain size distributions. By adjusting the height of the incident box beam, one can easily control the number of grains being irradiated. During experiments on various Al alloys (described in the coming chapters), the cross-sectional area of the beam was set such that no more than about 400 crystallites were present in the beam's interaction volume with the specimen. A consequence of the reduced beam size is, however, a limited number of grains illuminated in their entirety—see 3.9 (f). To compensate, multiple, adjacent volumes can be individually recorded and reconstructed and then stitched together during the postprocessing of 3D image data.

The combination of five independently reconstructed sample volumes (layers) is illustrated in Fig. 3.11. Measurements were preformed such that a defined amount of overlap existed between each layer. Because the indexing of grains near the beam's edges is most prone to failure, overlap is necessary to ensure a final reconstructed volume free of artificial voids. But this also means that, in the regions of overlap, there exists two solutions for many voxels (see highlighted areas in Fig. 3.11 (c)). Often, the exact orientation and contour of grains that are split across layers do not correspond completely with one another, owing to the experimental accuracy with which slight differences in the intensity, position and shape of diffracted beams can be measured. Thus, when stitching, a decision must be made regarding how to assign voxels in doubly indexed regions. Here, the completeness value can again be used to make this choice. However, the orientation of a grain spanning two layers may still vary discontinuously at the stitching interface. To avoid over-segmentation, grains that overlap in this manner are assigned the same orientation (either that of the larger half grain or an average of both), if their misorientation of two overlapping grains in the stitching region is less than a given threshold value, usually in the range of 0.5° to 1°.

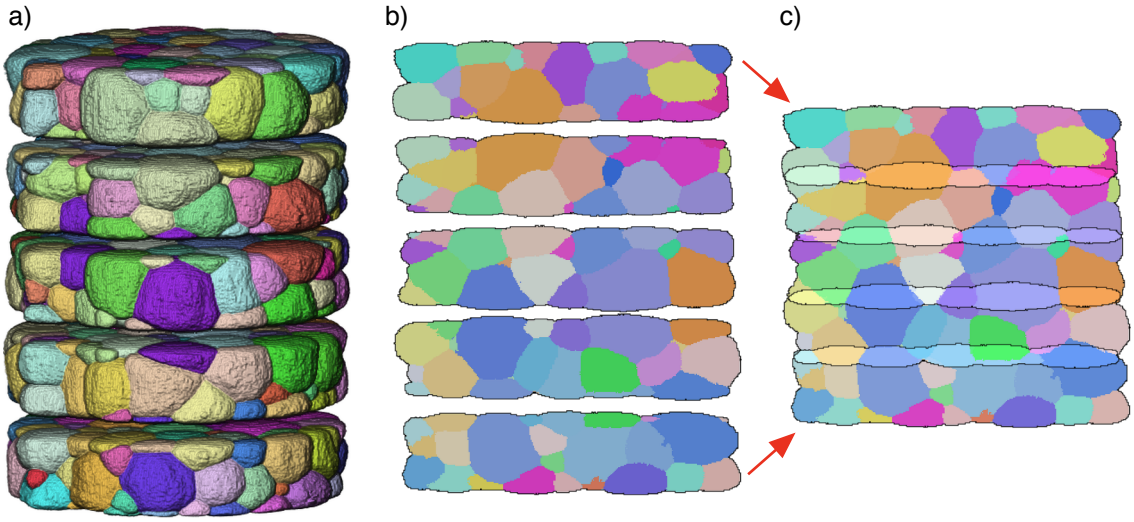

Figure 3.11: Stitching of 3DXRD layers. (a) Individually reconstructed layers of a cylindrical sample are merged to obtain a large 3D data set. Vertical sections along the cylinder's longitudinal axis demonstrate how (b) 5 separate layers are shifted in the vertical direction and united to form (c) the complete reconstruction. Areas of overlap, where the stitching occurs, are highlighted.

After multiple reconstructed layers have been stitched together, one has acquired a sample volume that contains a statistically relevant number of grains, providing a basis for performing meaningful analyses of microstructural parameters, such as the distribution of grain sizes, shapes and orientations. This same information is, however, attainable from serial-sectioning methods [42, 217]. The truly unique feature of 3DXRD microscopy is its nondestructive nature, which allows the study of time-resolved coarsening phenomena in 3D. In the context of 3DXRD investigations, samples are often annealed in an external furnace because of space and temperature restrictions in the experimental hutch [72, 218]. Thus, between successive measurements, specimens are removed, annealed and remounted, which inevitably leads to global translations and rotations (that affect the positions and orientations of all grains equally). Of course, the goal of time-resolved data collection is to track changes in microstructure; therefore, such global transformations must be removed, which is why a registration of data sets is preformed during postprocessing.

The differences before and after registration are displayed in Fig. 3.12 with the help of axial cross sections through 3D reconstructions of a cylindrical sample. Positioning errors introduced when remounting a specimen result most frequently in a rotation about the z-axis (which corresponds to the sample rotation axis, cf. Fig. 3.7), as is evident in Figs. 3.12 (a) and (b). Close inspection of these images also reveals the switching of several grains' colors. Because the coloring scheme is derived from the crystallographic orientation, which in turn is defined relative to laboratory coordinates, global sample rotations change the measured orientation of all grains.[5] Thus, we can calculate the difference in sample orientation by averaging individual changes in crystal orientation and, by applying the inverse of this transformation, remove the global rotation. This correction, however, does not fix sample translations between time steps. Positional changes in x, y and z can be accounted for using newer versions of MATLAB's Image Processing Toolbox™ [219] to

[5]The three components of the Rodrigues vector notation for orientation are used to index each grain's red, green and blue (RGB) values. Due to crystal symmetry some grains may hit the edge of the so-called fundamental zone in Rodrigues space when the sample is rotated, causing such vectors to "wrap around," hence the drastic change in some grains' color.

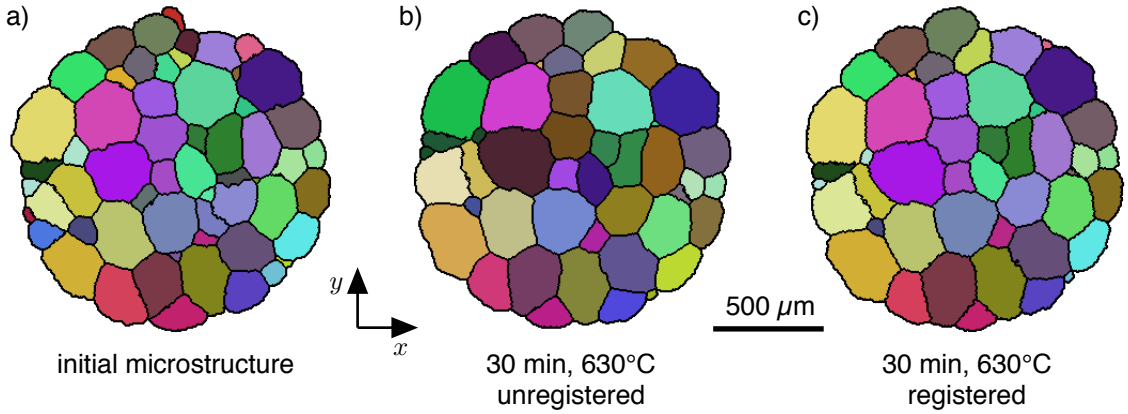

Figure 3.12: Registration of data sets. Because the specimen is remounted after each annealing time step, its global position and orientation change slightly between measurements, as demonstrated by cross sections through (a) the initial and (b) a later reconstruction. The most obvious difference is a rotation about the z-axis and changes in some of the grain colors. (c) Proper registration removes both of these artifacts.

register time steps, as was carried out with the data sets presented in the coming chapters. This translational registration was performed on the specimens' internal network of grain boundaries after binarization.

The final step in postprocessing the reconstructed 3DXRD data sets—before microstructural evolution can be temporally resolved—is the tracking of grains from time step to time step. It is generally safe to assume that no new grains form during the heat treatment of a fully recrystallized material [11], the one exception being the nucleation of annealing twins [220]. But the latter are neither expected [221] nor were they observed in the Al alloys under investigation. Thus, all grains present in a sample at any annealing interval ($t > t_0$) can be tracked back to the original grains in the sample at the initial time ($t = t_0$).

Two criteria are used to track grains from one time step to the next: (1) the fraction overlap in grain volume and (2) difference in orientation $\Delta\theta$. By superimposing two registered reconstructions, the first quantity can be calculated as $(V_{X,t_n} \cap V_{i,t_{n-1}})/V_{X,t_n}$, where $V_{i,t_{n-1}}$ is the volume of the grain with label i in the previous time step t_{n-1} and V_{X,t_n} is the volume of an unknown (not yet tracked) grain X in the current time step t_n. If this fraction is greater than some threshold (usually chosen to be 0.5), a potential match is noted, and the algorithm proceeds to test a second criterion—namely, the difference in orientation (i.e., the misorientation). If the misorientation angle between two candidate grains is also less than a certain threshold (typically 1°), then the label of the known grain is assigned to the unknown grain. This tracking algorithm was always applied to the reconstruction of the current time step and that of the time step immediately before it, so as to minimize the difference in microstructure. Tracking efficiencies greater than 95% were commonly achieved, and grains that were not tracked were manually inspected. Most of these untracked grains were located at the very top or bottom of the complete (ten-layer) reconstructed volume and often corresponded to crystallites growing into this volume, which was possible because the entire sample was not irradiated (see, for example, Fig. 4.2). After successful grain tracking, the evolution of individual grains in a polycrystal can be studied in 3D.

4

Grain Growth in a Single-Phase Al-Mg Alloy

Understanding microstructural evolution is a key step toward controlling a wide range of material properties, and for this reason materials scientists have devoted much effort over the last century to the investigation of grain growth. Many theories [15, 16, 222–226] have been developed to describe this coarsening phenomenon, and more recently focus has shifted from analytic to computational investigations [23–25, 28, 53, 54, 227, 228]. But one essential piece of the puzzle has remained absent throughout the years of study: namely, time-resolved three-dimensional measurements of grain growth. Until the development of 3DXRD microscopy, such data were unattainable in single-phase materials.

The 3D coarsening behavior observed in a single-phase Al-1 wt% Mg alloy is presented in this chapter. Although before-and-after snapshots of 3D microstructures undergoing grain growth have been reported previously [72], only a handful of grains were identified in the respective data sets, making it difficult to draw meaningful conclusions concerning the underlying coarsening mechanisms. The results here are extracted from thousands of grains across multiple time steps, allowing for a unique examination of the evolution of grains in their natural environment, i.e., without boundary marker phases [56] or the influence of free surfaces [229, 230]. The effect of local neighborhood and misorientation on changes in grain size and shape are investigated. A comparison of current findings with conventional normal and abnormal grain growth theories is also carried out.

4.1 Experimental details

The 3DXRD technique is far from standardized, and feedback from each experiment continues to flow into the development of better instrumentation and reconstruction algorithms. It took nearly one year to successfully reconstruct three data sets from the first measurements performed in 2012, whereas data sets collected during a third trip to the same beamline in 2015 were reconstructed live on site, i.e., during the beamtime.

For a successful 3DXRD experiment, care must be taken during sample selection and preparation. Likewise, the beam parameters (energy, intensity, illumination time, etc.), detector placement and annealing intervals require precise planning. These details and

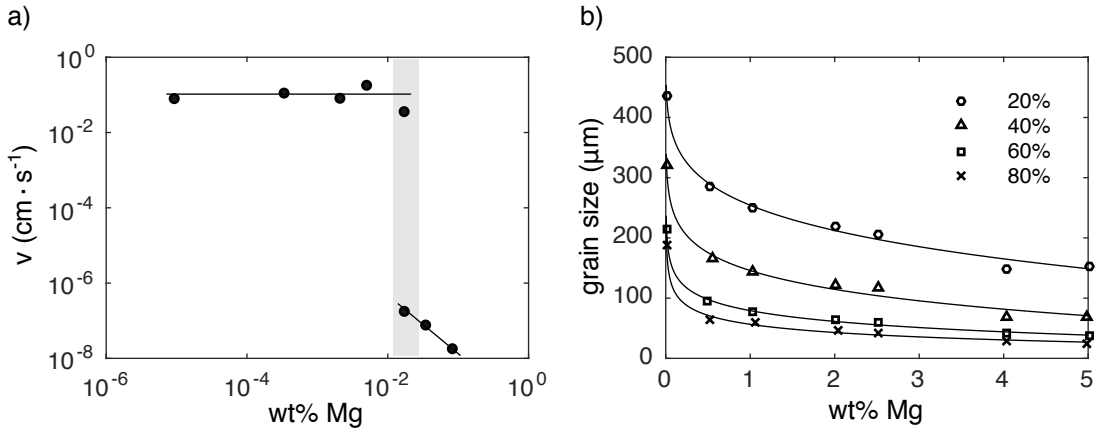

Figure 4.1: The influence of magnesium on (a) the growth rate of recrystallized grains in aluminum [11] and (b) recrystallized grain size after various degrees of deformation [232].

practical notes on the experiment at hand are given below.

4.1.1 Material selection and sample preparation

The ideal specimen for 3DXRD experiments has a low to moderate x-ray absorption coefficient and relatively simple crystal structure. The internal stress state and distribution of impurities in the material are equally relevant. For grain growth experiments, strain energy should be minimized so that the reduction of grain boundary area is the primary driving force for microstructural coarsening. Additionally, the presence of second-phase particles, which can have a significant impact on growth kinetics but are generally below the spatial detection limit of 3DXRD, should be avoided. Low crystallographic texture[1] is also advantageous, since it otherwise leads to overlapping diffraction spots, making an unambiguous indexing of grains difficult.

Many of these criteria are fulfilled by the low-density metal aluminum. Its low x-ray absorption coefficient allows for relatively large sample sizes containing a considerable number of internal crystallites. In pure metals grain growth proceeds rapidly, making interrupted coarsening experiments tricky. One way to slow grain growth is to add atoms of a second species. This effect is demonstrated by the plot in Fig. 4.1 (a) of boundary velocity vs. weight-percent magnesium in aluminum. According to the Al-Mg phase diagram [231], the solubility of Mg in Al is about 1 wt% at 100 °C, increasing rapidly to 7 wt% at 300 °C; yet very small amounts of Mg (beyond a plateau value of about 0.02 wt%) can significantly reduce the boundary migration rate. The addition of a small amount of Mg also leads to a smaller initial grain size following recrystallization, as evident in Fig. 4.1 (b). To maximize the number of grains included in a limited sample volume (typical specimen diameters are on the order of 1–2 mm) and thus enhance statistics, a small initial crystallite size is advantageous.

At 1 wt% Mg in Al, second-phase pinning particles are not expected to form, and the reduced coarsening rate accommodates the capture of intermediate stages of microstructural evolution. Given an adequate reduction in sample thickness during cold rolling, an initial

[1] Texture refers to a non-random distribution of crystallographic orientations. In a specimen with high texture, many grains have similar crystallographic orientations (i.e., the misorientation between individual grains in this subpopulation is small).

grain diameter less than 100 µm can be achieved for this concentration (cf. Fig. 4.1 (b)). Thus, Al-1 wt% Mg was chosen as a well-suited material. Specimens were prepared with the help of Dmitri Molodov from the RWTH Aachen. Elemental Al (99,9999+%) and Mg (99.99+%) metals were melted under argon (6.0) in an induction furnace and cast to form a 20 mm-thick plate. After a homogenization heat treatment (24 hours at 300℃), the plate was cold-rolled and the overall thickness was reduced stepwise by 90% to a final value of 2 mm. Cylindrical specimens with a diameter of 1.4 mm and height of 6 mm were cut via spark erosion from the rolled alloy. The longitudinal axis of the cylinders was chosen to lie in the rolling direction. Following a recrystallization heat treatment developed by A.-C. Probst [12], samples were annealed for 75 min at 350 ℃, producing an initial grain radius of about 45 µm for the start of growth experiments.

One of the Al-1 wt% Mg samples prepared in this manner was found to exhibit relatively low crystallographic texturing and mosaicity,[2] two qualities that improve the chances of successful 3DXRD mapping and the observation of normal grain growth. For these reasons all coarsening experiments were performed on the same Al-1 wt% Mg specimen. During previous unsuccessful attempts to characterize this same sample,[3] it was annealed for a total of 190 min at 350 ℃. This time is in addition to the 75 min recrystallization treatment. As a result of the extensive annealing history, the grains grew beyond an average radius of 45 µm, and we can be certain that the specimen is completely recrystallized.

4.1.2 Collection and reconstruction of 3DXRD data

Diffraction experiments were performed at beamline BL20XU of the synchrotron radiation facility SPring-8 in Sayō, Japan. BL20XU is a medium-length beamline designed for micro-tomography experiments [233]. The source is a planar undulator with a periodic length of 26 mm. By means of a double Si-crystal monochrometer, beam energies from 7.6–113 keV can be selected. During acquisition of the 3DXRD data presented here, a box beam with an energy of 32 keV (monochromated to $\Delta\lambda/\lambda = 10^{-4}$) and dimensions 1600 µm × 300 µm (width × height) was used to irradiate the cylindrical Al-1 wt% Mg specimen as it was rotated about its longitudinal axis.

As described theoretically in Section 3.3, two separate CCD detectors were used to capture diffraction spots. The far-field detector (Hamamatsu C7942CA-22) with a 50 µm pixel size was located 60 mm downbeam from the specimen's axis of rotation, while the near-field detector (Photron SA2) with a 4.56 µm pixel size was placed 12 mm behind the sample. The near-field detector not only had a higher resolution than the far-field detector but also a greater number of pixels (2048 × 2048 compared to 1024 × 1024).

Before the first heat treatment and after each successive anneal, 10 layers of both far-field and near-field data were collected *ex situ*, that is, at room temperature outside of the annealing furnace. Illustrations of the irradiated volume of the Al-1 wt% Mg specimen and the annealing procedure are given in Fig. 4.2. The height of each layer was 300 µm, and an overlap of 50 µm was used between adjacent layers to ensure that the final reconstructed volume would be free of gaps. For each layer, 750 far-field and 750 near-field images were recorded while the sample was rotated 360° at a constant speed. This translates to one diffraction image per 0.48°, and over this angular interval the intensity of photons reaching

[2] Mosaicity is a measure of the orientation spread inside individual crystallites. Low mosaicity means that the crystallographic orientation is approximately constant throughout the entire volume of each individual grain. Stress fields associated with dislocation networks can lead to increased mosaicity.

[3] The sample was given the nickname "Black Hole" because of the large number of photons it had absorbed without producing any publications.

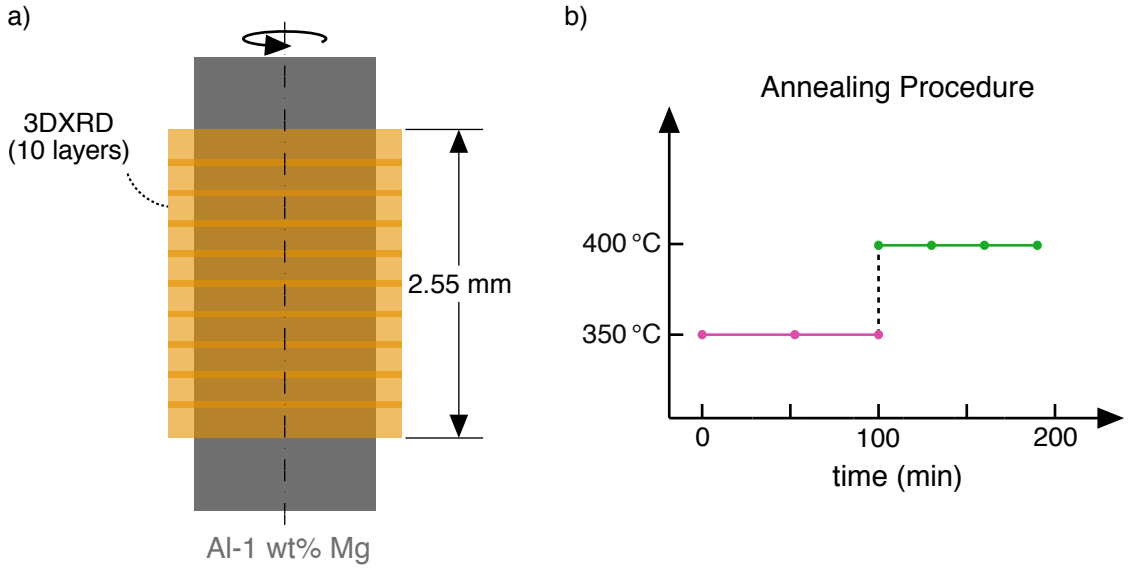

Figure 4.2: Measurement schematic and annealing procedure of the Al-1 wt% Mg specimen. (a) Ten overlapping layers of 3DXRD data (far-field plus near-field) were recorded at each point in the annealing protocol depicted in (b). Initial annealing intervals of 50 minutes were used at 350 °C, which were later reduced to 30 minutes when the temperature was increased to 400 °C.

the CCD detectors is integrated.

Details on the layer-by-layer reconstruction of 3DXRD data can be found in Section 3.3. Here, only the specifics related to reconstruction of the Al-1 wt% Mg specimen are described. As we will see shortly, this sample manifests crystallographic texture, despite precautions taken during sample preparation to avoid the occurrence of such. Because texture leads to an overlapping of diffraction spots, a multilevel thresholding of the far-field images was implemented. A high threshold allows separation and segmentation of the overlapping spots, and a subsequent low threshold ensures that the low-intensity diffraction spots from high index planes and/or smaller crystallites are not lost. Thus, by combining the intensity maxima from both the low and high-threshold segmentations into one large peak file, one is able to optimize the diffraction information used for subsequent grain indexing.

Even with multilevel thresholding, however, not all seed grains were identified with one run of GrainSpotter, an aspect revealed by incomplete final grain maps. Therefore, an iterative implementation of GrainSpotter was developed. It began with stringent conditions (called *cuts* in the software) on how much the fit parameters were allowed to vary. The grains indexed during initial runs were the easiest to identify—larger grains near the sample center—and their corresponding diffraction spots were removed from the master peak file. The execution of GrainSpotter was repeated until no more "good" seed grains (those with, for example, at least 100 diffraction spots) were found with the restrictive cuts. The limits on the indexing parameters were then relaxed and the process repeated. Through this procedure of iterative grain indexing, 3D reconstructions of the Al-1 wt% Mg specimen were obtained with virtually no internal voids (i.e., missing grains). This method of seed grain identification has now been incorporated into the standard 3DXRD reconstruction software [234].

Using the set of seed grains from GrainSpotter, grain maps for individual layers were reconstructed with GrainSweeper [215]. The 10 layers of each time step were then stitched

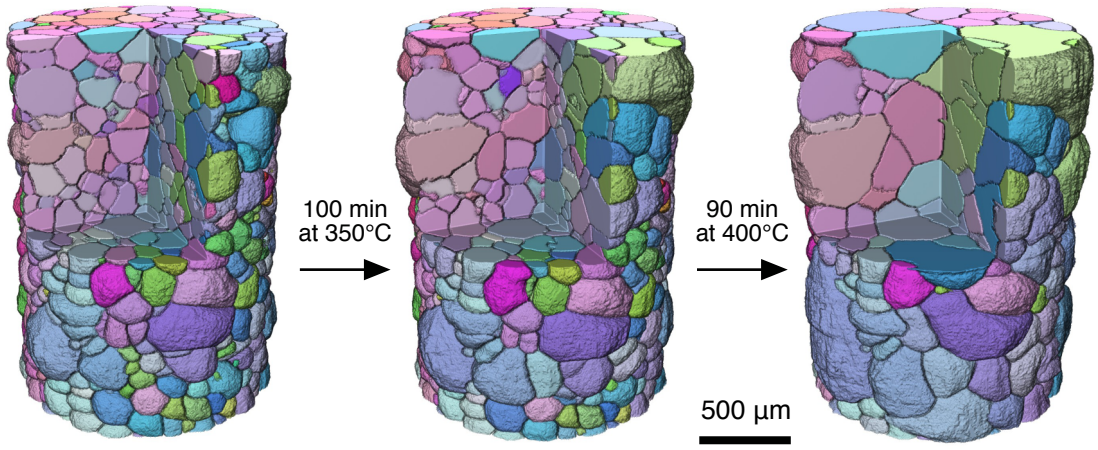

Figure 4.3: Microstructural evolution in Al-1 wt% Mg. During 100 minutes of total annealing at 350 °C, the average grain radius increased from 64.9 µm to 73.3 µm, while the number of grains decreased from 1619 to 1207. The growth rate was much higher after the temperature was raised to 400 °C, and after 90 minutes at this temperature the number of grains dropped to 571, with a final average grain radius of 82.4 µm. A wedge-shaped portion of the cylindrical sample has been cut out to reveal internal grain boundaries.

together with algorithms developed in MATLAB. A stitching threshold of 1° was employed for the Al-1 wt% Mg specimen, meaning that grains occupying the same space in the overlapping regions were combined into a single grain if their misorientation was less than 1°. The registration of measurements across annealing intervals and grain tracking was performed as described in Section 3.3. More than 98% of all grains were tracked from time step to time step.

4.2 Microstructural evolution

With time-resolved 3D data in hand, we can analyze the changes in grain size and shape that occurred during successive heat treatments. Illustrating the coarsening observed in the specimen under investigation, Fig. 4.3 shows 3D reconstructions before and after the cumulative heat treatments at 350 °C and 400 °C. In this figure a section of the sample has been removed to reveal internal grain boundaries. Microstructural changes appear to be more dramatic after annealing for 90 minutes at 400 °C compared to the previous 100 minutes at 350 °C. Since grain growth is a thermally activated process, this observation comes as no surprise. The RGB color values for the grains shown in this figure, as well as in subsequent images, are indexed according to each grain's orientation via the three components of the Rodrigues vector (as defined in Section 2.1.1).

4.2.1 Global growth parameters

The destructive nature of conventional grain growth investigations [11, 37–44] allows for only a statistical description of the coarsening behavior. Measurable quantities include the number of grains, the mean grain size and in some cases the grain size distribution. We begin our analysis in this section by looking at these same parameters. A notable difference, however, between previous studies and this work is that all values herein are determined nondestructively. Consequently, grain size distributions and their corresponding mean values are calculated from the same set of grains throughout the entire coarsening experiment, making this global analysis quite unique—certainly on the micrometer length scale.[4]

3DXRD reconstructions return grain volumes, quantified in terms of voxels. In the literature, however, one most commonly finds the size of grains specified by their radius or diameter rather than volume. A simple method of conversion is to calculate the equivalent radius R of a sphere whose volume V is equal to the experimentally determined grain volume, i.e.,

$$R = \sqrt[3]{\frac{3V}{4\pi}}. \tag{4.1}$$

In this and all subsequent chapters, grain sizes are reported in equivalent radii.

As expected and evident in Fig. 4.3, the number of grains decreases with annealing duration, as this eliminates boundary area and reduces the Al-Mg specimen's excess free energy. The reduction in the number of grains is displayed graphically in Fig. 4.4 along with the corresponding increase in average grain radius $\langle R \rangle$. Instead of directly plotting the mean, we look at $\langle R \rangle^2$ because for normal grain growth this quantity is expected to vary linearly with annealing time (Section 2.2.2). A straight-line fit to the data points seems to validate this assumption, but only three data points go into the fit for each temperature. (Although there are four measurements for $\langle R \rangle$ at 400 °C, the final point is excluded because a large fraction of grains (65%) intersects the sample's free surface, a condition known to retard growth [229, 230].)

When growth experiments are carried out for the same material at different temperatures, it is also possible to estimate an activation energy. Assuming a growth exponent $n = 2$, we can write Eq. (2.13) as

$$R^2 - R_0^2 = kt, \tag{4.2}$$

where R_0 is the initial grain radius and t the annealing time. The growth rate k combines all factors affecting the (average) boundary migration rate into one term, which is generally assigned an Arrhenius-type dependence on temperature, i.e., $k = k_0 \exp(-Q_{\mathrm{mig}}/(k_B T))$. From the straight-line fits of k in Fig. 4.4, an activation energy $Q_{\mathrm{mig}} = 0.51\,\mathrm{eV}$ was determined. Generally, one expects to find an activation energy for grain growth similar in magnitude to that of grain boundary or lattice diffusion. For Al this would be somewhere between 0.87 and 1.47 eV [11]. Although the experimentally determined value is lower than anticipated, this discrepancy may be caused by the Al-1 wt% Mg sample's high fraction of low-angle grain boundaries, the energy and mobility of which may manifest less sensitivity to changes in temperature than is typical of high-angle grain boundaries [4, 236].

The evolution of the grain size distribution is presented for both annealing sequences in Fig. 4.5. Most notable is the dissimilarity between Hillert's prediction and all of the

[4] The grain size of nanocrystalline materials ($\langle R \rangle < 150\,\mathrm{nm}$) can be measured nondestructively by standard x-ray diffraction [235].

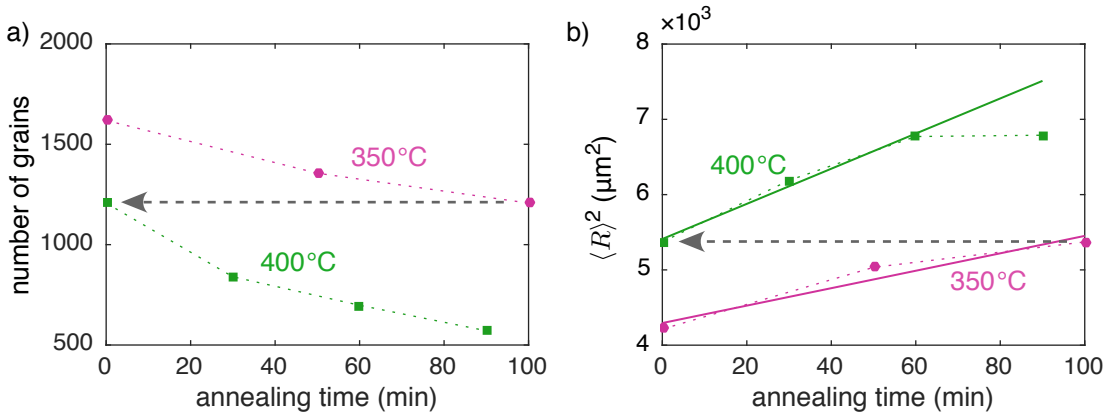

Figure 4.4: Global grain statistics. (a) The number of grains and (b) the squared mean grain radius versus annealing time. Linear fits (solid lines) in (b) correspond to conventional grain growth models (Eq. (4.2)), which predict a linear increase in $\langle R\rangle^2$ with annealing time. The last measurement of $\langle R\rangle^2$ at 400 °C was excluded from the fit, because at this point the fraction of surface grains reached 0.65.

measured distributions. According to Hillert's model, no grains with $R > 2.25\langle R\rangle$ should exist during self-similar (normal) grain growth. But we observe a non-negligible fraction of grain sizes well above this theoretical maximum and even individual grain radii up to 4 times the mean radius. Despite the discrepancy with theory, the general shape (broadness) of the measured distributions does remain about the same during annealing, giving at least the impression of self-similar growth having taken place. Analyses of real [40, 43, 46] and simulated [23, 28, 237] microstructures commonly find grain size distributions broader than Hillert's and more similar to the ones presented here.

When examining nuances in the shape of the grain size distributions, we find minimal differences over the course of the 350 °C anneal (except for an initial depression near $R = \langle R\rangle$). Raising the temperature to 400 °C, however, induces changes in the frequency with which some grain sizes are observed. Again, we see a suppression in the fraction of grains with sizes near $R/\langle R\rangle = 1$, but this time the dip in frequency becomes more prominent with increasing annealing time. Because the total area under each distribution is normalized (equal to unity), changes in one region must be compensated by changes of equal total area and opposite sign elsewhere. This aspect is identified in Fig. 4.5 (b) by arrows. A steady rise in relative frequency is observed for the smallest grains in the specimen as well as for those with a radius approximately 2.5 times the mean. Though it is not possible to obtain information on the exact mechanism(s) behind these changes in the distribution of grain sizes, such observations are certainly indicative of some form of abnormal grain growth occurring during annealing at 400 °C.

Note: in the remaining sections of this chapter we will consider only the growth sequence recorded at 400°C. Not only do these data have a greater dynamic range, but having a constant annealing temperature and interval also greatly simplifies the analysis. Furthermore, because we are examining grain growth in a fully recrystallized, single-phase material, a modest change in annealing temperature should affect only the speed with which the specimen coarsens and not the underlying growth mechanism(s).

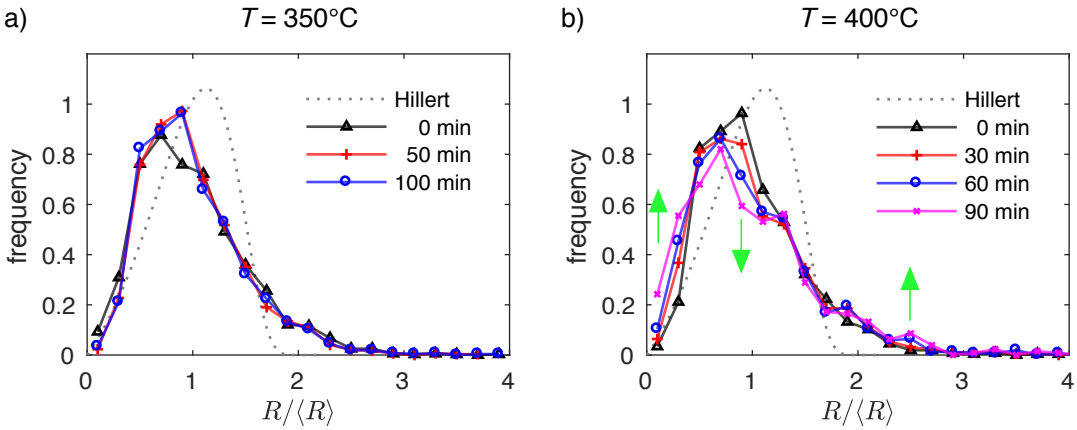

Figure 4.5: Changes in grain size distribution after annealing at different temperatures. (a) Except for a small dip near $R/\langle R\rangle = 1$, the relative distribution of grain sizes remains nearly identical during annealing at 350 °C. (b) At 400 °C changes in the grain size distribution become obvious: green arrows mark various trends with increasing annealing time. Prominent in both plots is the discrepancy between Hillert's mean-field prediction (dotted gray line) and the measured distributions.

4.2.2 Local growth rates

In addition to evaluating global measures of grain growth, we can, with spatially resolved 3D data, also examine the evolution of crystallites on an individual, grain-by-grain basis. An example of such an analysis is given in Fig. 4.6. Here, the evolution of five internal grains—i.e., crystallites not in contact with the sample surface—is displayed over the course of three 30-minute anneals at 400°C. Grain size trajectories can be generated by calculating the equivalent radius for each grain (Eq. (4.1)) and plotting these values against time. In this plot the sample's global mean grain radius $\langle R\rangle$ is represented by the thick black line. Initially, all five grains have larger-than-average equivalent radii; hence, one would intuitively assume that all five grains should grow. But the dark green grain in the middle of this cluster shrinks rapidly, even crossing the trajectories of two of its smaller neighbors and disappearing entirely after the second annealing interval (between the 30 and 60 minute mark). Such behavior represents a significant deviation from mean-field models for grain growth, suggesting that the assumption of uniform boundary properties is not valid at the local level.

This same analysis is extended in Fig. 4.7 (a) to include the trajectories for half of the grains[5] (selected at random) present in the specimen at the beginning of the 400 °C annealing sequence. The evolution of mean grain radius is again drawn as a thick black line. Close examination of the grain trajectories reveals that many crystallites with radii above $\langle R\rangle$ shrink, despite their presumed size advantage. In fact, these grains often disappear even faster than grains with initial sizes $R < \langle R\rangle$. On the other hand, there are almost no smaller-than-average size grains that grow. These observations are also clearly discernible in Fig. 4.7 (b), a scatter plot of the grains' scaled growth rate $R\Delta R/\Delta t$ against their normalized grain size. The points in this graph are calculated by computing the central difference of each grain trajectory. Through a process of averaging, the central difference estimates the slope of discretized data more accurately than a simple forward (or backward) difference. The downside, however, is a reduction in data range, which becomes apparent

[5] When all the grains are included it is even more difficult to distinguish individual trajectories.

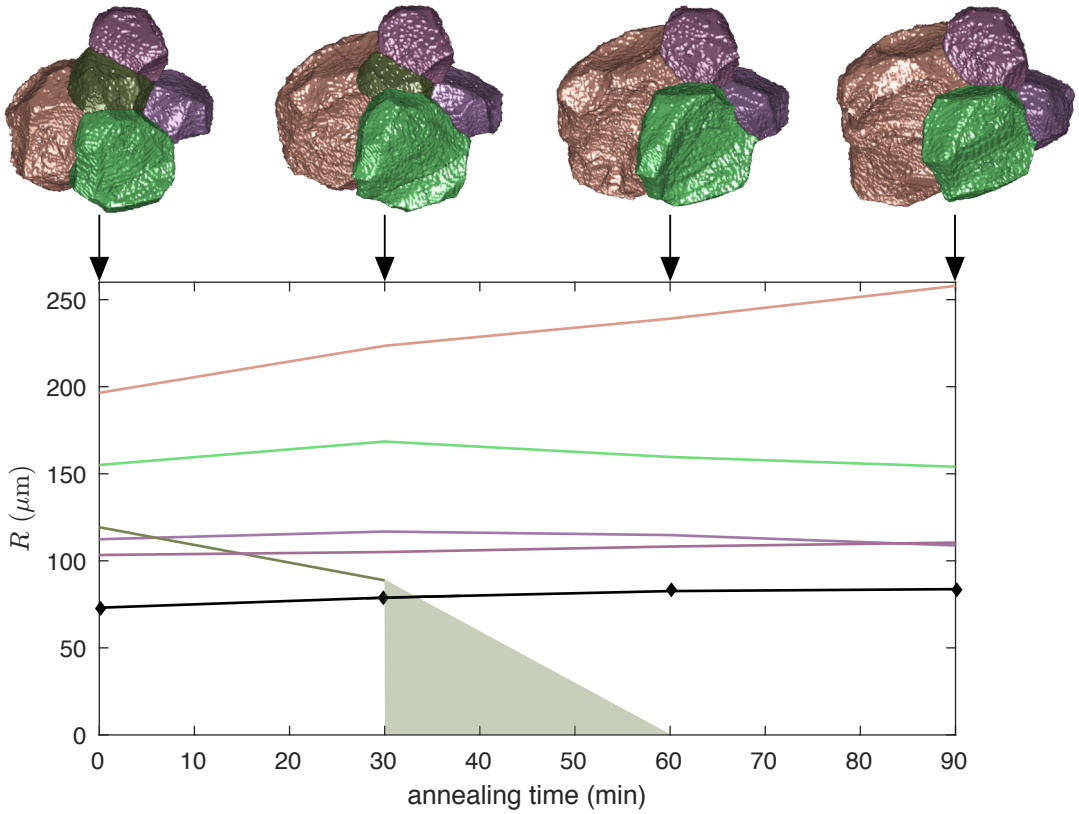

Figure 4.6: A cluster of five neighboring grains is shown as it evolves in 3D. The corresponding grain size trajectories (coloring is consistent) are given below the 3D representations. Initially, the equivalent radius of all grains is above the average value $\langle R \rangle$, which is given by the thick black line. Over the course of 90 minutes at 400 °C, the salmon-colored grain grows continuously, while the two purple and one light green grain fluctuate around the same value. The dark olive-colored grain shrinks despite being larger than average. Its trajectory ends after 30 minutes because this grain is not found in the sample following the next annealing interval (at 60 minutes). The shaded region indicates upper and lower bounds on the hypothetical path that this grain's trajectory could have taken, but the shrinkage rate cannot be determined precisely.

when the equation to calculate the central difference is examined. For a given measurement interval n, values for both the previous (R_{n-1}) and future (R_{n+1}) grain radius are required. Mathematically, the central difference is expressed as

$$\frac{\Delta R_n}{\Delta t_n} = \frac{\frac{R_{n+1}+R_n}{2} - \frac{R_n+R_{n-1}}{2}}{\frac{t_{n+1}+t_n}{2} - \frac{t_n+t_{n-1}}{2}} = \frac{R_{n+1} - R_{n-1}}{t_{n+1} - t_{n-1}}, \tag{4.3}$$

where t_n is the annealing time at the start of interval n. Thus, for any given grain, a maximum of two growth rates—determined at the 30 and 60-minute marks of the 400 °C annealing sequence—can be computed.

Grains that vanish (shrink to zero) over the course of a given annealing interval are included in Fig. 4.7 (b) as gray points. As evident in the case of the dark olive grain in Fig. 4.6, the shrinkage rate of such grains cannot be determined unambiguously, because the exact time at which they disappear is unknown. However, a *slowest case* scenario, which assumes that these grains disappear exactly at the end of the respective annealing interval, can be implemented. Accordingly, most of the gray data points in the scatter plot

(Fig. 4.7 (b)) will underestimate the true values of $|R\Delta R/\Delta t|$, which we would expect to find further down (more negative) on the vertical axis. In other words, an excluded area in the growth rate diagram (defined by the parabola $-R^2/\Delta t$) is introduced by the discrete time sampling of the specimen's microstructure.[6] The gray points are not found exactly on the perimeter of this parabola because the central difference is used and the mean grain size also changes from time step to time step.

A fit of the growth rates in Fig. 4.7 (b) provides an estimate for the average reduced mobility ($M\gamma$) of the grain boundaries in the Al-Mg specimen. Multiplying both sides of Eq. (2.14) by R and inserting $R_{cr} = (9/8)\langle R\rangle$, we can rewrite Hillert's growth equation as

$$R\frac{dR}{dt} = M\gamma\frac{8}{9}\left(\frac{R}{\langle R\rangle} - \frac{9}{8}\right). \tag{4.4}$$

A simple linear regression returns a value of $M\gamma = 59.0 \pm 5.79\,\mu\text{m}^2/\text{min}$. Fitting begins at $R/\langle R\rangle = 0.5$, because below this value the fit would otherwise enter the parabolic excluded region described above. Prediction bounds, containing 90% of the fitted data points, are drawn above and below the fit as dashed red lines. The large spread of the data points leads to rather wide bounds. It is interesting to examine the points that lie outside of the 90% prediction bounds. Many of the largest grains in the sample grow at rates far above the values expected for their respective sizes. This finding is yet another indication for the occurrence of abnormal grain growth.

4.2.3 Grain morphology and topology

Instead of using the equivalent radius—which is essentially the same as fitting a sphere to each grain—to characterize the crystallites of a sample, we can also fit each grain with an ellipsoid. In doing so one obtains information about the grain shape. An example of an ellipsoidal fit can be seen in Fig. 4.8. Here, the three semi-principal axes of the ellipsoid are labelled R_a, R_b and R_c. We can now define an aspect ratio for each grain by dividing the minimum axis by the maximum. The more spherical a grain is, the larger its aspect ratio is—a value equal to unity describes a perfect sphere. The aspect ratio of the grains in the Al-Mg sample for the 400 °C annealing sequence is presented in Fig. 4.9. The mean aspect ratio of all grains decreases slightly during annealing from an initial value of 0.53 to 0.50, which implies that there exists a significant deviation across all time steps from the sphericity of grains assumed by Hillert's mean-field model. On average, the aspect ratio is larger for bigger grains, but this increase appears to level off, approaching 0.6 for the largest grains (Fig. 4.9 (b)). No correlation was observed, however, between this aspect ratio and the growth rate of grains.

Because of the plane-strain conditions during cold rolling, grains are often extremely elongated in the direction of rolling [11]. Consequently, one might expect to find grains still elongated after recrystallization, which could potentially influence the subsequent coarsening behavior by producing large boundaries of low curvature. Defining the term *grain shape orientation* by the direction of the longest semi-principal axis (R_a in Fig. 4.8 (c)), we can confirm, however, that the grains in this Al-Mg specimen are not preferentially aligned in any particular direction. The intersection of each grain's longest semi-principal axis with a unit sphere is plotted in Fig. 4.10 (a). Projecting these points onto a plane through the sphere's equator (Fig. 4.10 (b)), we see that they are quite uniformly distributed. Thus, despite a considerable degree of shape anisotropy—grains are on average

[6] When plotted against the normalized grain radius this expression becomes $-\langle R\rangle^2(R/\langle R\rangle)^2/\Delta t$.

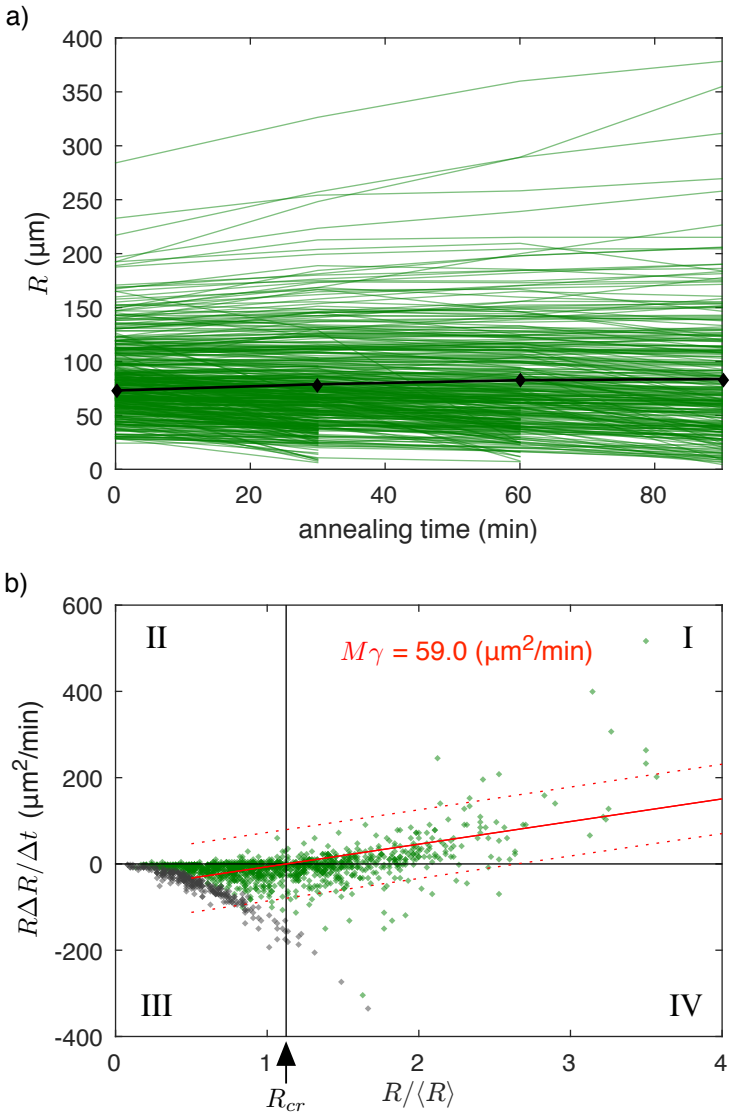

Figure 4.7: Growth rate analysis. (a) Growth trajectories for half of the initial grains (chosen at random) reveal how the grain size evolves during annealing at 400 °C. The growth rates in (b) are calculated by taking the central difference in grain size at the 30 and 60-minute marks. (Note that all grains are included in this scatter plot.) The shrinkage rates for grains that vanish between measurements are plotted in gray and lie approximately along a parabola defined by $-R^2/\Delta t$. A straight-line fit through $(R_{cr},0)$ is drawn in red with the 90% prediction interval indicated by the dashed red lines. Because the discrete annealing interval $\Delta t = 30$ min hinders an accurate determination of $R\Delta R/\Delta t$ for the smallest grains in the sample, fitting begins at $R/\langle R\rangle = 0.5$. The slope of this fit provides an estimate for the reduced mobility $M\gamma$, averaged over all of the grain boundaries. Four quadrants defined by the intersection of the lines at $R\Delta R/\Delta t = 0$ and $R/\langle R\rangle = R_{cr}$ are labelled with Roman numerals.

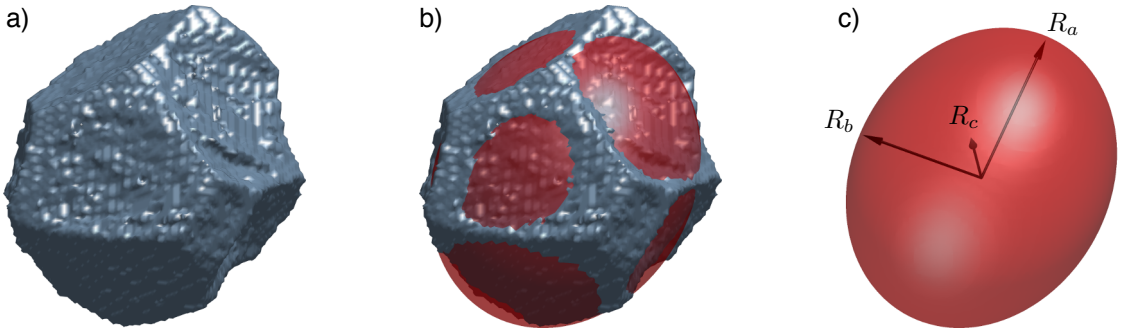

Figure 4.8: Ellipsoidal fitting of grains. The experimentally determined grain volume in (a) is fit by an ellipsoid in (b). The semi-principal axes R_a, R_b and R_c of the ellipsoidal fit are shown in (c).

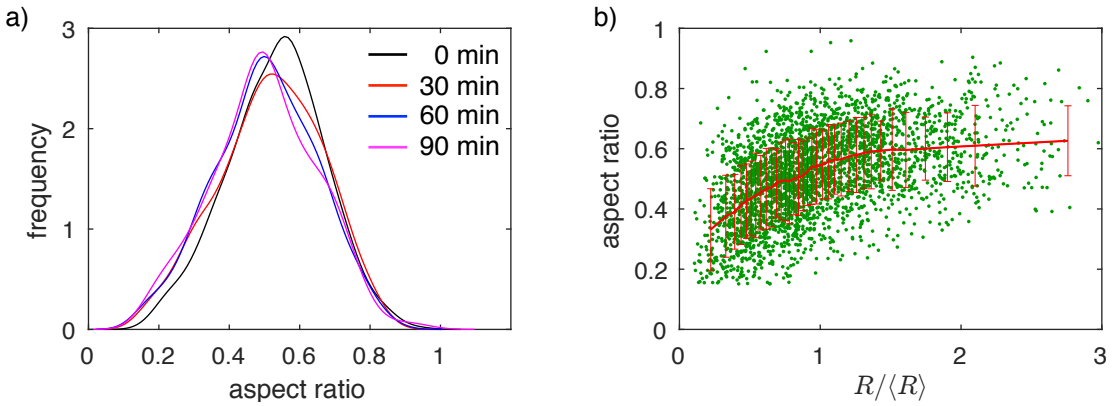

Figure 4.9: Grain shape evolution. (a) The aspect ratio is defined as the minimum semi-principal axis of the ellipsoidal fit divided by the maximum. Over the course of 90 min at 400 °C, the mean grain aspect ratio decreases from 0.53 to 0.50. (b) Plotting the individual ratios against the normalized grain size, we see that after rising initially the aspect ratio approaches an average value of about 0.6 for the larger grains in the Al–Mg specimen. The mean aspect ratio is drawn as the solid red curve and is determined at various intervals along $R/\langle R\rangle$ such that the same number of data points enter into each calculation. The standard deviation is shown as vertical bars.

twice as long as they are wide—it is presumably safe to conclude that the effects of this feature on microstructural evolution are limited, since there is no preferential orientation of the elongated grains.

In addition to the morphological aspects described above, a 3D network of interconnected domains has topological features that include corners (quadruple points), edges (triple lines) and faces (grain boundaries). Of these, the latter are perhaps the most dominant and certainly the most investigated feature [23, 43, 50, 238, 239]. Under the assumption that all interfacial properties are uniform, the evolution of domains in 2D depends entirely on their topology, namely the number of sides. Domains with more than 6 sides will always grow, and those with fewer than 6 will invariably shrink [222]. Accordingly, a perfectly hexagonal structure of domains (e.g., the honeycomb structure) is entirely stable and will not coarsen. In 3D the boundaries between the domains of a cellular structure are faces; however, no purely topological relation exists to describe the coarsening of 3D boundary networks [225]. Nevertheless, correlations can be drawn between the rate at which 3D grains coarsen and their number of faces [240].[7]

[7] A note on terminology: The number of grain faces is synonymous with and equivalent in value to the

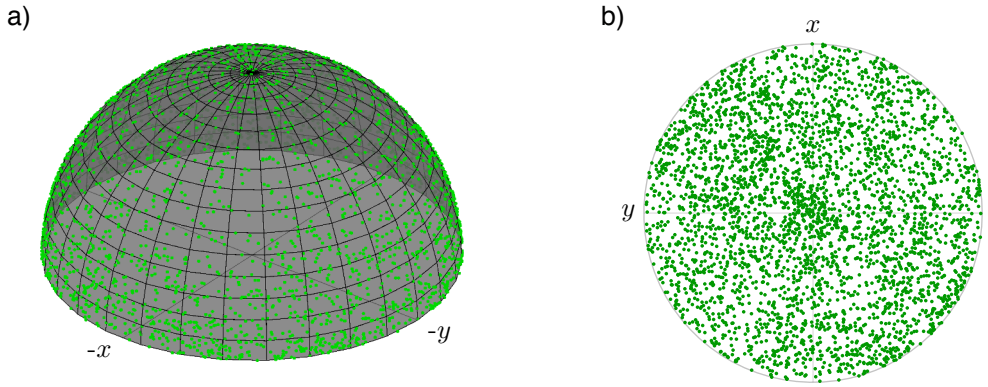

Figure 4.10: Distribution in orientation of grain shapes. (a) The intersection of the longest semi-principal axis of each ellipsoidal fit with the unit sphere reveals a relatively homogenous distribution of grain shape orientations. (b) A stereographic projection of these points displays the same information in a form similar to a pole figure. To enhance visualization only the grains of the initial microstructure (0 min at 400 °C) are included here, but the random distribution of grain shape orientations remains the same for all subsequent time steps.

A monotonic relation between the size of a grain and its number of faces is expected, since larger grains tend to have more neighbors. In Fig. 4.11 (a) experimentally determined histograms of the number of faces per grain F are given for grains in the 400 °C annealing sequence as well as for the subset of internal grains. Both histograms display a lognormal shape. The mean number of faces $\langle F \rangle$ for all grains is 11.3, and when surface grains are excluded this value increases to 12.3. Values reported in the literature range from 11 on the low end to 15 at the upper limit [52], with 13.7 commonly reported for simulations of ideal grain growth [23, 25, 241]. Because large grains are preferentially removed when surface grains are excluded,[8] it is likely that the value reported here for $\langle F \rangle$ is an underestimate of the true value. If we plot the normalized grain size of the internal grains against F (Fig. 4.11 (b)), we find an approximate linear relationship between the two quantities up to about 25 faces per grain, after which the slope levels off. A decreasing slope at higher values of F is consistent with previous characterizations of 3D microstructures [43, 50]. An interesting quantity is the number of faces expected for a grain of average size. This number can be extracted from the intersection of the fit in Fig. 4.11 (b) with the horizontal line at $R/\langle R \rangle = 1$ and is found to be 12.6, slightly above the value of $\langle F \rangle = 12.3$. Although the mean follows an approximately liner relation up to $F = 25$, the scatter of the individual data points is noteworthy. Some grains with fewer than 10 neighbors have above-average grain radii, while others with nearly 20 faces are nevertheless smaller than $\langle R \rangle$.

Large grains usually have smaller neighbors [242–244], but if, for example, a large grain with large neighbors exists, it would not have many faces and could still shrink despite being above the global average in terms of size. Thus, one might expect the number of grain faces to be a better indication of whether a grain will grow or shrink than its normalized size. All growth rates $R\Delta R/\Delta t$ are plotted in Fig. 4.12 against the number of faces F. A straight-line fit (starting from $F = 7$) to the data of Fig. 4.12 is drawn in dark red and crosses the horizontal axis at $F = 15.8$. Analogous to the critical grain radius R_{cr} (cf. Fig. 4.7), this value will be referred to as the critical number of grain faces F_{cr}, below which most grains shrink and above which most grow. If we use the linear fit in

number of grain boundaries of a given grain and the number of nearest neighbors.

[8] The larger a grain, the greater the chance that it intersects the sample's free surface.

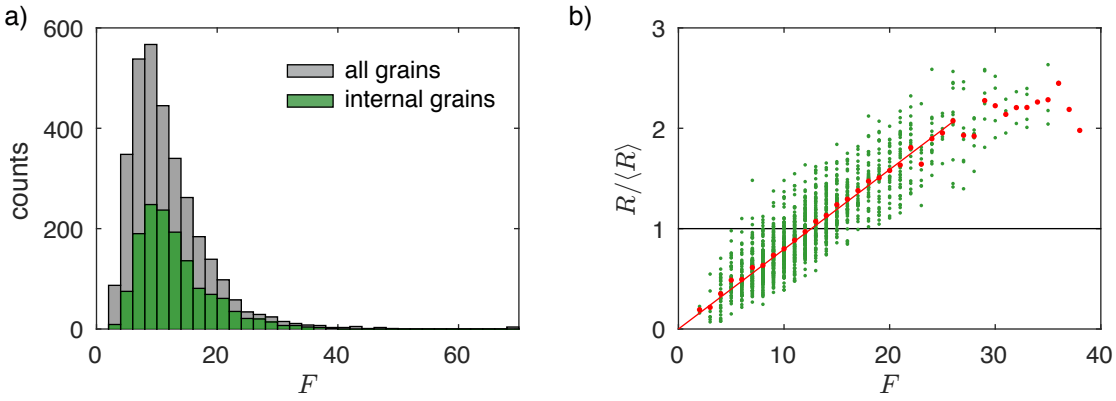

Figure 4.11: Grain face attributes. (a) The number of grain faces per grain F is distributed log-normally, similar to the grain size distribution. When all grains are included in the distribution (gray histogram), the mean value is found to be 11.3 faces per grain; this number increases to $\langle F \rangle = 12.3$ when surface grains are excluded from the calculation (green histogram). (b) A correlation between grain size and number of faces is observed up to about $F = 25$, as indicated by the linear fit (red line) to the mean normalized grain size for each value of F (red dots).

Fig. 4.11 (b) to predict the number of faces for a grain with $R = R_{cr}$, we find $F(R_{cr}) = 14.2$. (This discrepancy essentially indicates that, in comparison to Fig. 4.7 (b), growth rates are preferentially shifted to the left, from quadrants I and IV into quadrants II and III, when plotted against F.)

In both Figs. 4.7 (b) and 4.12 we see substantial scatter, and at first glance the predictive power of F does not seem to be any better than that of $R/\langle R \rangle$. However, a more detailed inspection of individual points reveals some interesting aspects. For example, the three grains shrinking fastest in Fig. 4.12 are all below F_{cr}, despite having equivalent radii that lie considerably above R_{cr}. It seems, as postulated above, that these crystallites have a limited number of even larger neighbors, which consume the former at a very high rate. Using the horizontal line at $R\Delta R/\Delta t = 0$ and the vertical lines at either $R/\langle R \rangle = R_{cr}$ or $F = F_{cr}$ to define quadrants of the growth rate plots, we can perform a semi-quantative comparison of Figs. 4.7 (b) and 4.12. All growing grains are expected to appear in quadrant I, while shrinking grains should be found in quadrant III. According to mean-field theories [16, 245], no data points are expected in either quadrant II or IV. However, the space-filling constraints imposed on real microstructures inevitably lead to some scatter, as clearly observed in simulations of isotropic grain growth [239, 240]. Nevertheless, comparing the fraction of points found in quadrants II and IV, we can get an idea of how well a given parameter (e.g., $R/\langle R \rangle$ or F) predicts whether a grain grows or shrinks. When the growth rate is plotted against the normalized grain size (see Fig. 4.7 (b)), we find that a total of 21.6% of the data points lie in quadrants II and IV. One the other hand, only 16.2% of the data points fall in these same quadrants in Fig. 4.12.

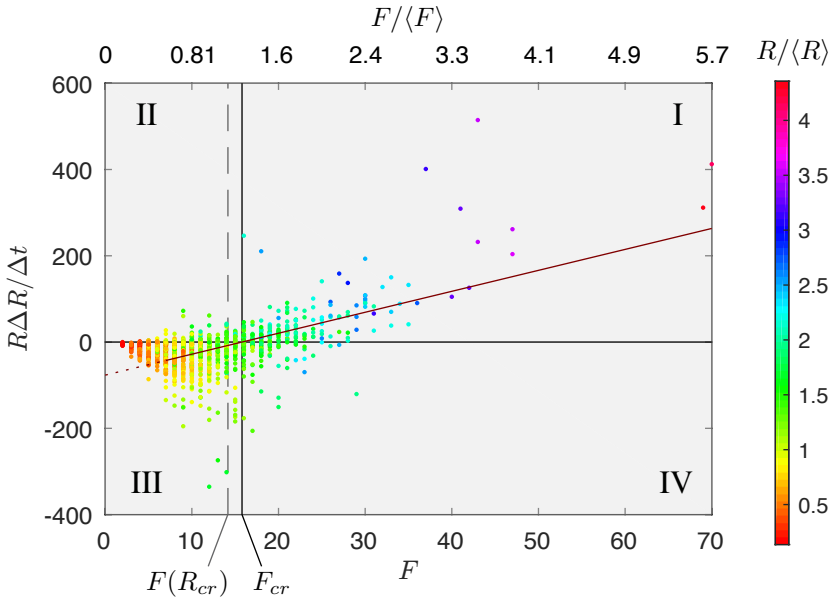

Figure 4.12: The growth rate of each grain is plotted against its number of faces. The color scale on the right is used to indicate the relative grain size. A liner fit to these data, starting at $F = 7$, is drawn in dark red. The fit line intersects the zero growth rate at $F = 15.8$, and this position is defined as the critical number of grain faces F_{cr}. For comparison, the number of faces for the critical grain size, $F(R_{cr})$—extracted from Fig. 4.11 (b)—is indicated by the dashed vertical line. Four quadrants are defined with respect to the lines $F = F_{cr}$ and $R\Delta R/\Delta t = 0$.

4.3 Texture and misorientation

4.3.1 Crystallographic texture components

In the materials science sense of the word, texture refers to a preferred crystallographic orientation of grains in a polycrystal. Plastic deformation is a ubiquitous step in the processing of metallic materials and almost inevitably leads to some form of texture [11]. The most common textures have been given names (such as Cube, Copper, Brass, Goss) and are defined by crystallographic planes and directions [246]; for example, the Cube texture is denoted as $\{1\,0\,0\}\langle 1\,0\,0\rangle$. In this notation there is an implicit relation between the crystallographic directions and the material's reference coordinate system. Because the study of texture is so intertwined with mechanical deformation, the reference directions of a specimen are typically defined by its respective forming process. This convention is illustrated in Fig. 4.13 for a sheet of rolled metal. In the rolling process, metal plate material is fed through one or more sets of parallel rollers, which reduce the thickness of the specimen while elongating its length and (if unconstrained) width, similar to the rolling of pizza dough. The direction in which the material is fed is called the rolling direction (RD). Perpendicular to the RD and parallel to the longitudinal axis of the cylindrical rollers is the transverse direction (TD). The normal direction (ND) is, as the name implies, normal to the plane spanned by RD and TD. In general, these three orthogonal directions are used to define the specimen axes (when speaking of a rolled material), and with them one can interpret the notation with which textures are represented.

In the example of the Cube texture given above, the first term in curly braces indicates that $\{1\,0\,0\}$ crystallographic planes are found parallel to the surface of the sheet, i.e., the

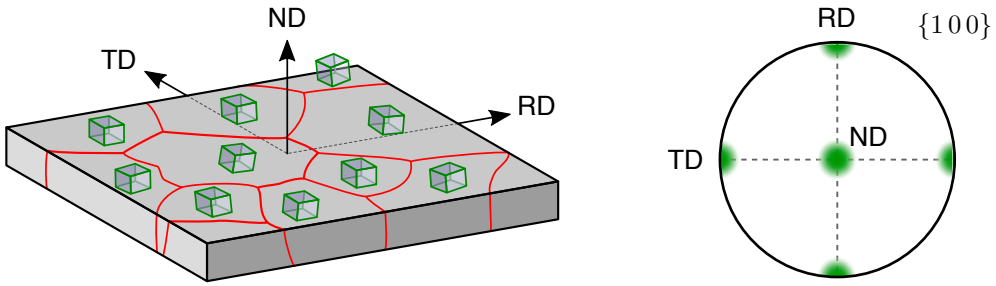

Figure 4.13: Example of the Cube recrystallization texture. This texture is often found after the recrystallization of cold-rolled fcc materials. Independent of grain size and shape, the unit cell axes of the individual crystallites tend to be aligned with the orthogonal processing directions, i.e., the rolling (RD), transversal (TD) and normal directions (ND). Consequently, when the {1 0 0} pole figure is plotted, maxima in the frequency of {1 0 0} poles are observed at the RD, TD and ND.

plane defined by RD and TD. The second term gives the set of crystallographic directions that lie in the direction of rolling, in this case ⟨1 0 0⟩. This means, for the Cube texture, that the axes of a cubic unit cell are aligned exactly with the axes RD, TD and ND. In reality there is a finite amount of spread in the orientation of crystallites about the directions of any specific texture, and the strength of the texture component is inversely proportional to this spread. A strong texture is characterized by a very narrow distribution of grain orientations, while a weak texture displays a broad distribution.

The Cube texture is commonly found in recrystallized Al alloys [247–249], and the Al-1 wt% Mg sample under investigation here is no exception. The pole figures of Fig. 4.14 show a clear Cube texture that remains relatively constant during annealing at 400 °C. Although the sample's x-, y- and z-coordinate axes are not aligned with the rolling, transverse and normal directions—while mounting the sample before experimentation, only the rolling direction was unambiguously identifiable since it was parallel to the z-axis of the cylindrical specimen—the Cube texture is still easily recognized by the distinctive cross pattern formed by the {1 0 0} poles.

On the left-hand side of Fig. 4.14 the poles of individual grains (cf. Fig. 2.4) are depicted as dots, the areal density of which is displayed on the right-hand side. For a perfectly untextured sample—one with randomly oriented grains—the distribution of poles would be uniform. In this specimen, however, we find a peak in the pole figure near x, showing that it is eight times more likely to find a pole at this position; and if we assume that this dominant peak in the orientation distribution marks the normal direction (since the sample is compressed in this direction during rolling, it seems reasonable to assume that the grains are preferentially aligned with respect to the normal direction), then we can locate the approximate positions of all three processing directions, as indicated in the figure.

Texture components are sometimes more easily visualized in orientation space, since each point represents the orientation of a single grain. In Fig. 4.15 all grain orientations present in the initial microstructure are plotted in Rodrigues space relative to the surmised rolling, transverse and normal directions. In Rodrigues space, a grain with an ideal Cube orientation is now depicted as a point at the origin. Although a larger number of grain orientations are located near the origin, they are not evenly distributed, but rather tend to be concentrated along the normal direction r_{ND} slightly above and below zero. Other orientations are found in smaller clusters farther away from the origin. Based on these observations seven different texture components were defined, and each was assigned a unique color.

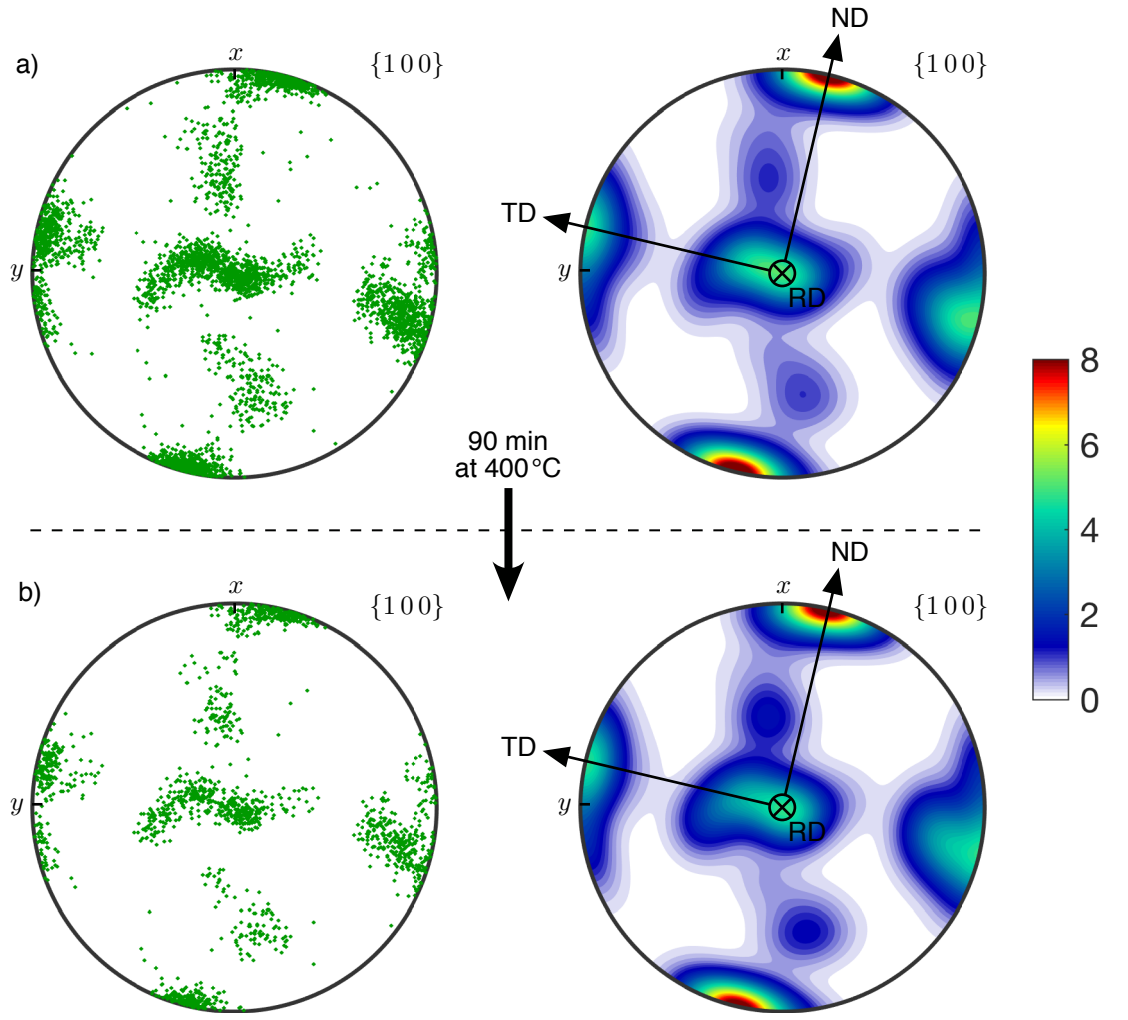

Figure 4.14: Evolution of crystallographic texture. The (a) initial and (b) final {1 0 0} pole figures of the Al-1 wt% Mg specimen show a clear Cube texture that remains relatively constant during heat treatment at 400 °C for 90 min. On the left-hand side, the individual {1 0 0} poles of all grains are plotted as green dots. The color-coded contour plots on the ride-hand side depict the areal density of the {1 0 0} poles in multiples of a random distribution. The x and y specimen axes are indicated, as well as the presumed normal (ND), transverse (TD) and rolling (RD) directions. All images were generated with the MTEX toolbox [250].

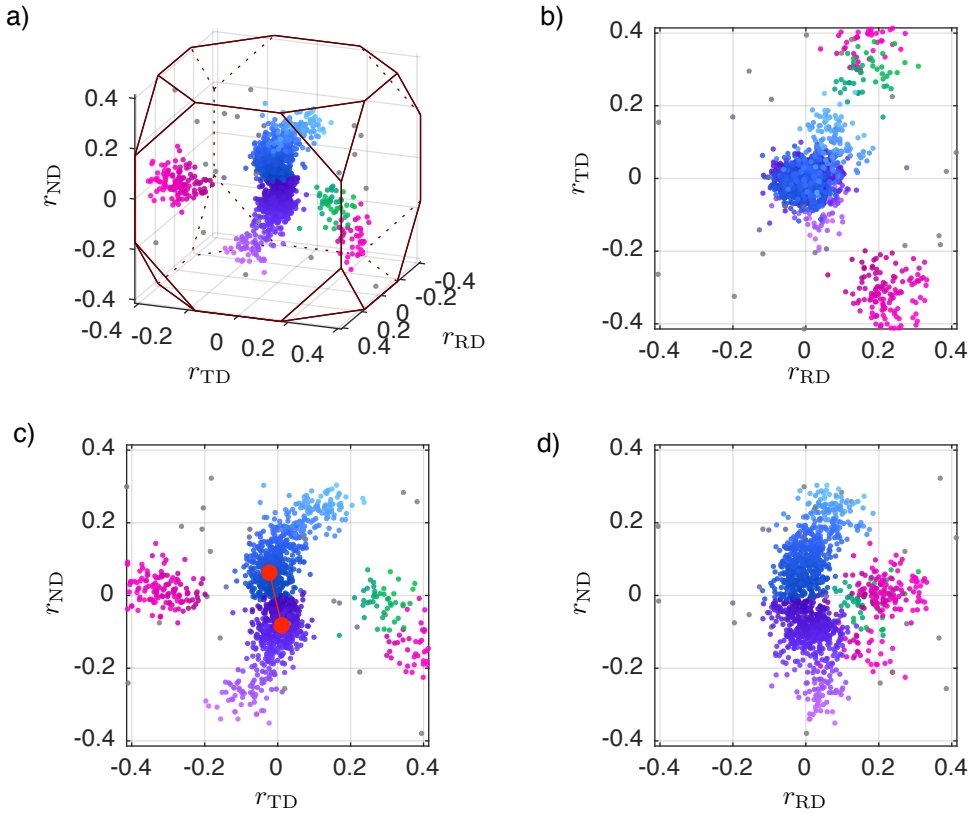

Figure 4.15: Representation of texture components in orientation space. (a) All grain orientations present in the initial microstructure are plotted in the Rodrigues fundamental zone against the rolling (r_{RD}), traverse (r_{TD}) and normal (r_{ND}) directions. Seven different texture components are identified and assigned unique colors. Projections from the (b) top, (c) front and (d) side are seen in the remaining panels of the figure. Two dense orientation clusters, marked by red dots in (c), are located slightly above and below the origin.

The vast majority of grain orientations lies along what appears to be an S-shaped line that passes through the origin, above and below which the density of points is highest, as indicated by the red dots in Fig. 4.15 (c). These heavily concentrated clusters of near-Cube orientation define the first two texture components; they are shaded dark blue if their Rodrigues vector component in the normal direction is positive, or dark purple if it is negative. The centers of the dark blue and purple lobes are separated by a rotation angle of nearly 20°.

Along the upper and lower tails of the S-shaped distribution, the color changes from dark to light blue or purple, respectively, once the orientations differ by more than 20° from the center of mass of the corresponding dark lobes. These tail regions are the next two texture components and, as the color indicates, are almost certainly related systematically—through the cold-rolling deformation process—to their darker counterparts. The remaining orientations are denoted by three additional colors. Grains with orientations near $\mathbf{r} = (0.168, 0.286, -0.016)$ are shaded green, while those close to $\mathbf{r} = (0.221, -0.347, 0.016)$ are given a magenta hue. Crystallites with orientations that deviate by more than 20° from all previously defined orientations are colored gray. The small number of gray points in the figure indicates that there are very few randomly oriented grains in the specimen.

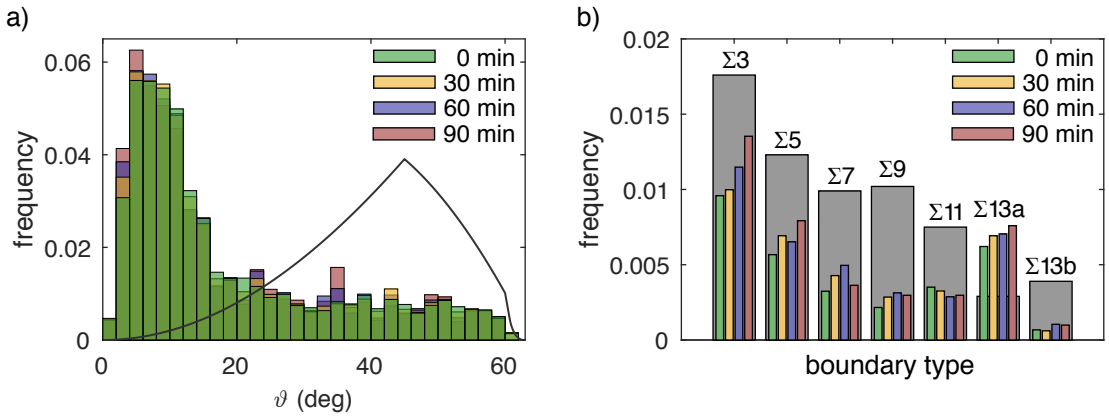

Figure 4.16: Grain boundary misorientation distributions. (a) Area-weighted grain boundary misorientations show a large peak at low misorientation angles and very little variation with annealing time. Across all time steps approximately 67% of the total boundary area is included in the interval $\vartheta < 20°$. The Mackenzie distribution for randomly orientated cubic crystals is drawn as a solid black line. (b) The frequencies of the first seven CSL boundaries are compared to their expected fractions in a random cubic polycrystal (wide gray bars). Except for Σ13a interfaces, a lower fraction for all CSL boundaries is observed.

4.3.2 Distribution of boundary misorientations

Crystallographic texture can have a dramatic impact on material properties [82, 251], but the presence or lack of texture does not adequately describe a microstructure at the boundary level. In fact, Miodownik *et al.* [252] demonstrated that vastly different misorientation distributions can be generated from the same set of randomly orientated grains; indeed, because grain growth proceeds by the migration of individual boundaries, their character and distribution is perhaps more relevant than is texture to investigations of grain coarsening.

From the 3D reconstructions in Fig. 4.3 it is already apparent that a large number of low-angle grain boundaries must exist in the Al-1 wt% Mg sample, since, in these snapshots, the color of a crystallite is related to its orientation, and we find large clusters of similarly shaded grains. This initial observation is confirmed by the misorientation histograms of Fig. 4.16. Given a random distribution of cubic crystallites, one would expect the fraction of low-angle grain boundaries (defined here as $\vartheta < 20°$) to be about 5.4% in accordance with the Mackenzie distribution [93]. In all reconstructions of the Al-1 wt% Mg sample, however, low-angle boundaries make up about 67% of the total internal interfaces. Apparently, the grains of the various texture components defined above are not distributed randomly throughout the sample but rather tend to be correlated spatially.

Perhaps the most striking consequence of Figs. 4.14 and 4.16 is the invariability of both the distribution of grain orientations and of misorientations. These two distributions remain essentially unchanged despite the large dynamic range of the data—the number of grains decreases by more than one half. Thus, we can conclude that not only do grains in the various texture components disappear at about the same relative rate, but also the misorientations between surviving grains remain nearly constant. The only somewhat noticeable changes in the area-weighted grain boundary distributions of Fig. 4.16 (a) are the slight increase in frequency of interfaces with $\vartheta < 10°$ and the emergence of a small peak near 35°. As we will see in the coming section, both effects are related to the growth of grains in clusters of similarly oriented grains.

Similar to low-angle grain boundaries, cusps in the energy landscape at coincidence site lattice (CSL) misorientations can lead to an increase in their population during thermomechanical processing [253], and special properties, such as exceptionally high or extraordinarily low mobilities, are often ascribed to these boundaries [100, 124, 135, 160, 254]. The most common experimentally observed CSL boundaries in Al alloys are $\Sigma 3\{1\,1\,1\}$, $\Sigma 7\{1\,1\,1\}$ and $\Sigma 11\{3\,1\,1\}$ interfaces [100]. As revealed in Fig. 4.16 (b), however, no peaks in frequency at these positions are observed. In fact, the populations of CSL boundaries are in general much lower than one would predict even in a material with randomly oriented grains. One exception is the frequency of $\Sigma 13$a boundaries, but their fraction still much lower than expected for specimens with Cube texture.[9] Garbacz and Grabski [255] report fractions of $\Sigma 13$ boundaries near 5% for Cube-textured materials, whereas fewer than 1% of the grain boundaries in the present sample manifest $\Sigma 13$ character. Thus, for the Al-Mg specimen under investigation, we may infer that the influence of CSL boundaries on grain growth is insignificant, especially when compared to the considerable fraction of low-angle grain boundaries.

4.4 Discussion

The standard theory of texture-induced abnormal grain growth was explained briefly in Section 2.2.3. This model predicts a higher growth (or shrinkage) rate for a grain when its crystallographic orientation deviates from that of the dominant texture component(s). Moreover, if the size of such a "deviant" grain is greater than the mean, then it is expected to grow abnormally, since its growth advantage is sustainable and self reinforcing. Two examples of grains that fulfill the prerequisites for abnormal growth are considered below, after which the findings are generalized and, finally, modifications/extensions of the conventional texture-induced model for abnormal grain growth are discussed.

4.4.1 Excursions into the abnormal

Case I: The abnormal shrinkage of grain 661

The yellow grain in Fig. 4.17, given the label 661 during tracking, has a crystallographic orientation substantially different from that of its neighbors, which, for the most part, belong to the near Cube texture components of the Al-1 wt% Mg specimen. Before the initial 400 °C anneal, this grain is also quite a bit larger than the average grain size ($R_{661} = 1.6\langle R\rangle$). Thus, according to the texture-induced abnormal growth model, this grain should grow rapidly and consume its neighbors, which are essentially pinned by their low-energy grain boundaries. But exactly the opposite behavior is observed. After 30 minutes grain 661 has shrunk slightly to a relative size of $1.5\langle R\rangle$. Upon further annealing the negative growth rate is amplified, and grain 661 vanishes completely sometime before the end of the next 30-minute heat treatment.

The pole figures on the right-hand side of Fig. 4.17 demonstrate just how markedly the orientation of grain 661 differs from the orientation of all of its neighbors. The 2D cross sections through the cylindrical specimen at grain 661's center of mass give the impression

[9] CSL boundaries with a $\langle 1\,0\,0\rangle$ misorientation axis include $\Sigma 5$, $\Sigma 13$a, $\Sigma 17$a and $\Sigma 25$a boundaries. Of these, the $\Sigma 13$a boundary has the lowest misorientation angle (22.62°). Thus, a higher fraction of $\Sigma 13$a boundaries is expected in materials with Cube texture, for which the $\langle 1\,0\,0\rangle$ misorientation axis is prevalent between neighboring grains.

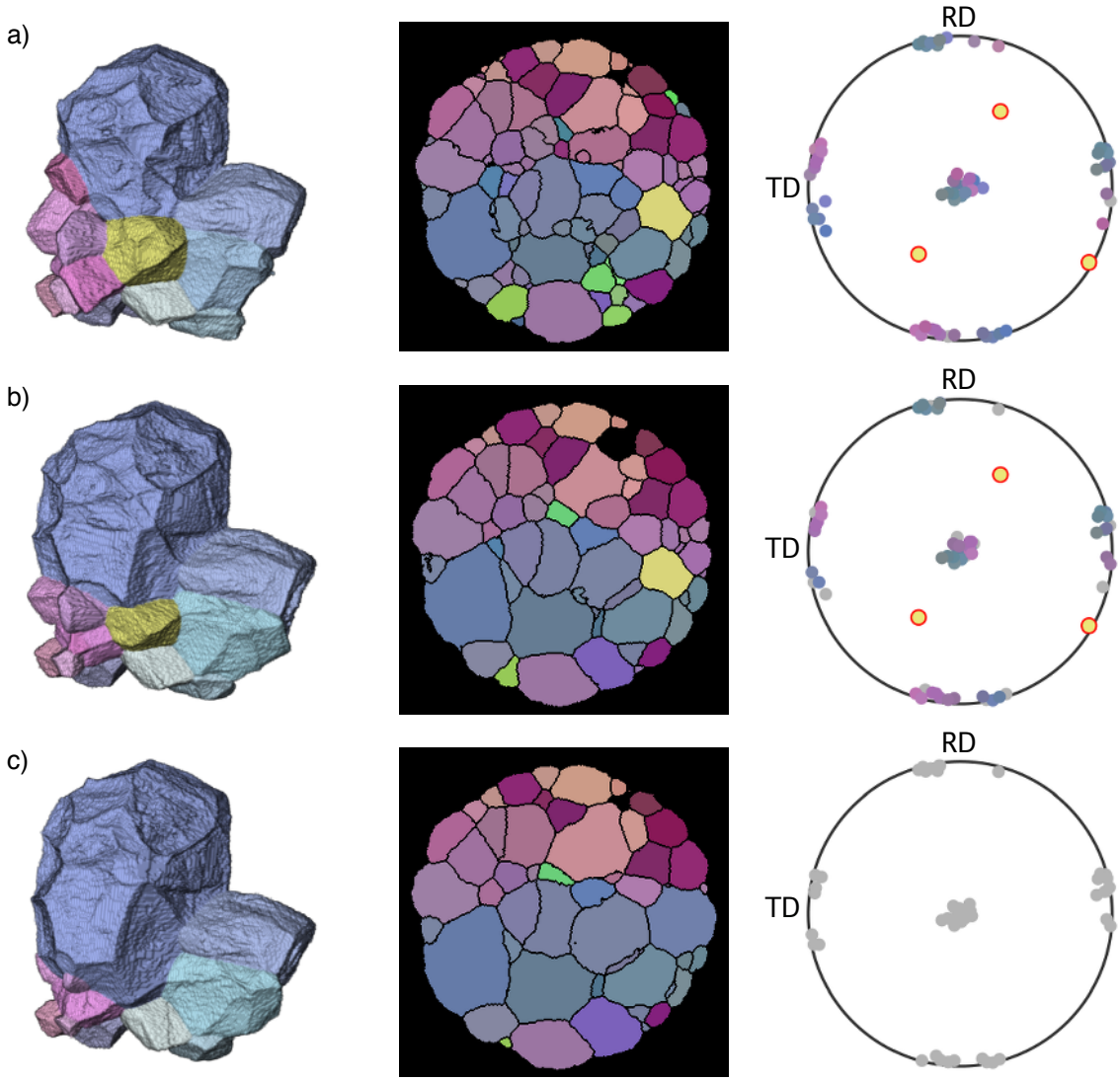

Figure 4.17: Case I: The evolution of the yellow grain 661 is tracked during annealing at 400 °C from (a) 0 min to (b) 30 min and finally (c) 60 min. For each time step a 3D map of the grains surrounding grain 661 is shown on the left next to a 2D cross section through the yellow grain's center of mass in the middle column. On the right-hand side, {1 0 0} pole figures show the orientation of grain 661 in relation to all of its direct neighbors. (Orientations of the grains that are present in the current time step and either were or will become nearest neighbors are shaded gray in the pole figure.) After 60 minutes grain 661 has completely vanished, despite being larger than the mean grain size at the beginning. An artifact of the reconstruction and tracking algorithms—a missing grain—is seen in the upper right-hand corner of the 2D cross sections.

Table 4.1: Some characteristic values for grain 661.

time (min)	$\frac{R\Delta R}{\Delta t}$ (μm^2/min)	$R/\langle R\rangle$	F	$R/\langle R_{\mathrm{nn}}\rangle$	$R/\langle R_{\mathrm{nn}}\rangle_{\mathrm{area}}$	$\langle\vartheta_{\mathrm{nn}}\rangle$	$\langle\vartheta_{\mathrm{nn}}\rangle_{\mathrm{area}}$
0		1.63	22	1.22	1.02	52.6°	54.1°
30	-206	1.51	16	0.97	0.71	52.9°	54.9°

that this grain should grow. In these images the grain appears larger than its neighbors and its grain boundaries are curved outward. Only with 3D reconstructions does the full story of what happened to grain 661 become evident. Our yellow grain of interest is bounded on its upper border by a large bluish grain, which is more than twice the size of grain 661. As annealing proceeds, the interface between these two grains becomes larger. At this boundary, the bluish grain, thanks to its larger relative size, has a local growth advantage and is able to push its way through grain 661, consuming the majority (71.2%) of the yellow grain's volume.

Although the boundaries of grain 661 do migrate at an elevated rate—consistent with the mechanism of texture-induced abnormal grain growth—no comparisons of this grain's properties with global averages (grain size, number of faces or texture) are able to foretell its ultimate demise. Obviously, these global values do not adequately represent the local environment of grain 661, as assumed by mean-field models. If, on the other hand, we compare the size of grain 661 to the mean radius of its direct neighbors $\langle R_{nn}\rangle$, the effect of having adjacent crystallites larger than our grain of interest becomes evident by a reduction in the normalized size. Initially, $R_{661} = 1.22\langle R_{nn}\rangle$ before dropping to just $0.97\langle R_{nn}\rangle$ after the first 30-minute anneal. This effect is more convincing when the size of grain 661's neighbors are weighted by their contact (grain boundary) area. The area-weighted mean neighbor radius can be calculated as

$$\langle R_{\mathrm{nn}}\rangle_{\mathrm{area}} = \frac{\sum A_i^{\mathrm{GB}} R_i}{\sum A_i^{\mathrm{GB}}}. \tag{4.5}$$

Similarly, the area-weighted average misorientation angle is defined as

$$\langle\vartheta_{\mathrm{nn}}\rangle_{\mathrm{area}} = \frac{\sum A_i^{\mathrm{GB}} \vartheta_i}{\sum A_i^{\mathrm{GB}}}. \tag{4.6}$$

The different normalizations of grain 661's radius are summarized in Table 4.1 along with values for the mean misorientation to its nearest neighbors. In light of these local averages, the decline of grain 661 is less surprising.

This example emphasizes the importance of considering a grain's local environment when predicting its coarsening behavior. Although a simple comparison of migration rates between the low and high-angle boundaries of this grain is not possible (since grain 661 has only high-angle grain boundaries), the high shrinkage rate is at least consistent with the assumption that boundaries between highly misoriented grains are very mobile.

One final piece of insight to be gleaned from the abnormal evolution of grain 661 is the inadequacy, and even deceptiveness, of using 2D cross sections to analyze the inherently 3D phenomenon of grain growth. 2D cross sections often give a false impression of which grains will grow and which will shrink. To truly understand microstructural coarsening,

Table 4.2: Characteristic values for grain 1017.

time (min)	$\frac{R\Delta R}{\Delta t}$ (μm^2/min)	$R/\langle R\rangle$	F	$R/\langle R_{nn}\rangle$	$R/\langle R_{nn}\rangle_{area}$	$\langle\vartheta_{nn}\rangle$	$\langle\vartheta_{nn}\rangle_{area}$
0		2.63	36	2.34	1.47	32.0°	20.8°
30	401	3.15	36	2.38	1.38	32.9°	20.2°
60	515	3.50	42	2.67	1.49	31.9°	20.4°
90		4.24	47	2.92	1.80	32.3°	21.9°

3D characterization is indispensable.

Case II: The abnormal growth of grain 1017

The second grain that we will examine in detail is one of the fastest growing grains in the entire Al-Mg specimen. The highest two points along the vertical axis in Fig. 4.7 (b) both belong to grain 1017, which grows much faster than the Hillert fit predicts for a grain of its size. The evolution of grain 1017 can be seen in Fig. 4.18, and although it should be colored light green according to its orientation, in the 3D view, as well as in the 2D cross sections, our grain of interest is given a red shading to differentiate it from similarly oriented neighbors. Pole figures also display grain 1017's orientation relative to the rolling and transverse directions of the specimen, and it is plain to see that grain 1017 does not belong to the dominant near-Cube texture components.

Like grain 661 above, grain 1017 is initially larger than the mean grain size ($R_{1017} = 2.6\langle R\rangle$) of the specimen. Grain 1017 also has a neighbor even larger than itself—by a factor of at least 1.4. (The larger neighboring grain is not completely contained within the illuminated sample volume and thus the exact factor is unknown.) Unlike the previous case, however, the large neighboring grain here has an orientation very close to that of the grain of interest. The misorientation between grain 661 and the large bluish neighbor that consumes it was 60.5°, while the misorientation between grain 1017 and its neighbor of greater relative size is only 4°. Consequently, the boundary between the latter grains is most certainly a low-energy grain boundary, which means that the driving force for its migration should be small. Examination of this interface (seen in the 2D cross sections of Fig. 4.18 on the lower right side of grain 1017) verifies that it is essentially stationary over the entire course of the 400 ℃ heat treatment.

Values summarizing the size and local neighborhood of grain 1017 are given in Table 4.2. Although the mean misorientation to its neighbors is not exceptionally large—according to the Mackenzie distribution [93] a value of about 42° would be expected on average for a grain with randomly oriented neighbors—grain 1017 still manages to grow at a highly accelerated rate. The area-weighted mean misorientation is substantially less than the simple number average, confirming that this grain shares large boundaries with similarly oriented grains.

To understand exactly how grain 1017 increases its size so dramatically, it is necessary to examine the migration of individual grain boundaries. In the cross sections of Fig. 4.18 it is apparent that not only does the interface on grain 1017's lower right remain rather stationary, but so do all boundaries with light green-shaded neighbors. On the other hand, boundaries between the grain of interest and its bluish/purplish neighbors on the upper side

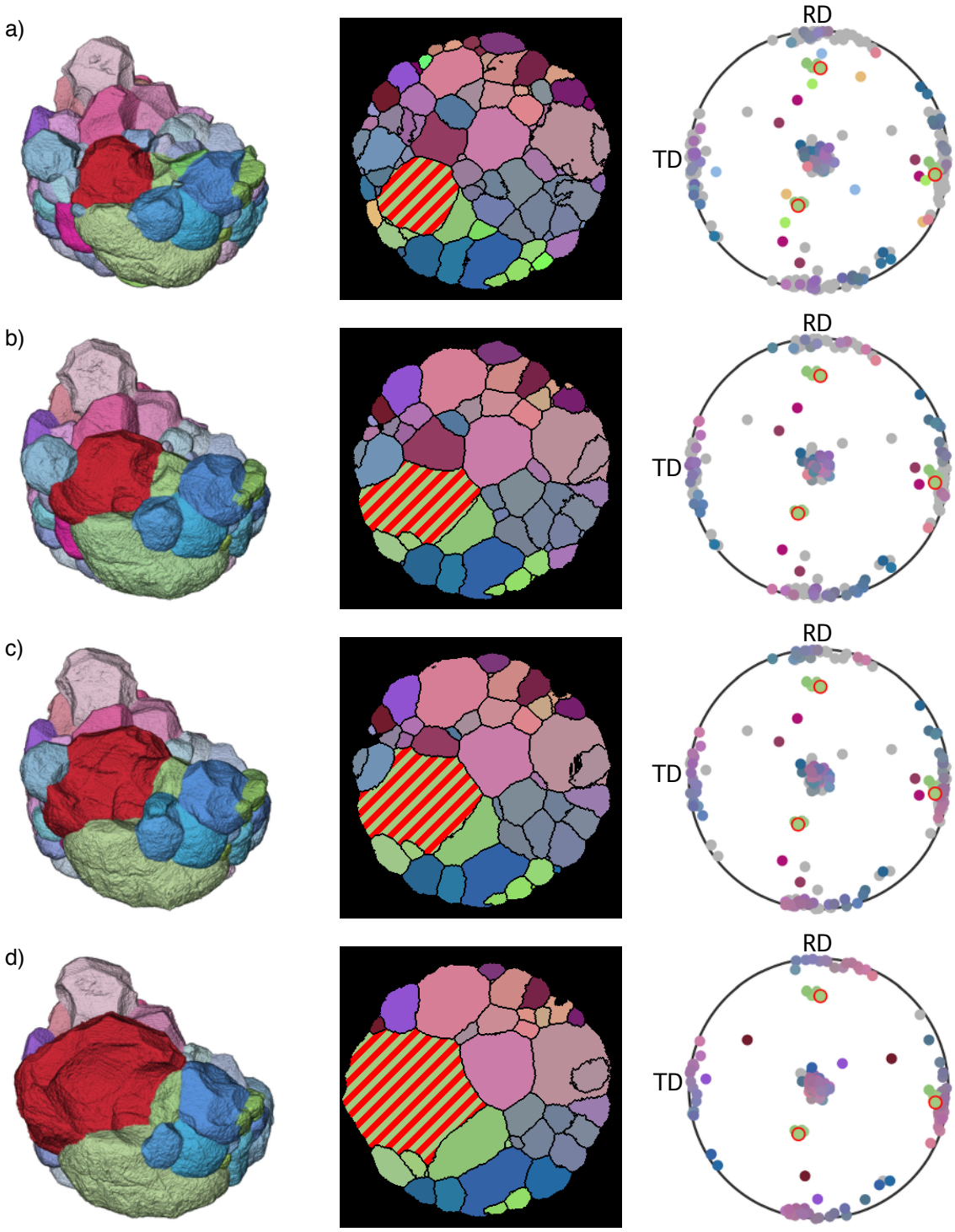

Figure 4.18: Case II: The evolution of grain 1017 is tracked across the annealing intervals of (a) 0 min, (b) 30 min, (c) 60 min and (d) 90 min at 400 °C. Grain 1017 is shaded red in the 3D images on the left and given red stripes in the 2D cross sections to separate it from its similarly colored neighbors. The {1 0 0} pole figures on the right show how close the orientations of the greenish grains are to each other. Here, again, the orientation of grain 1017 is identified by the red outline. (Orientations of the grains that are present in the current time step and either were or will become nearest neighbors are shaded gray in the pole figure.)

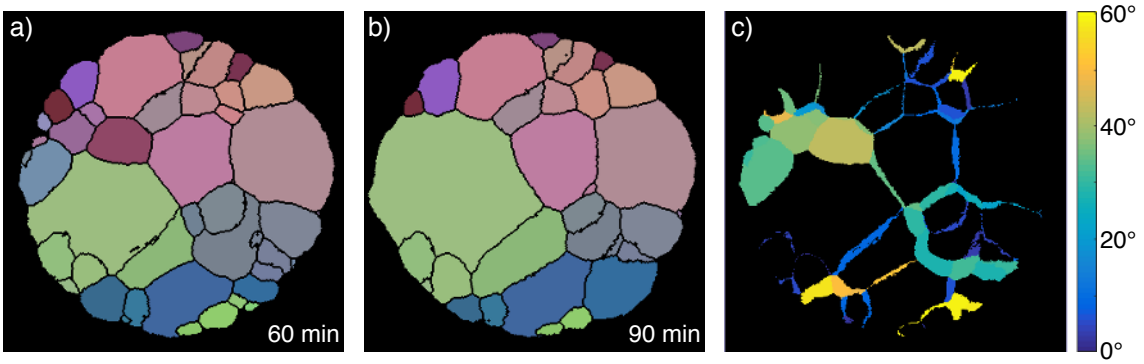

Figure 4.19: Visualization of the exchanged volume ΔV. Cross sections through grain 1017 are shown at the (a) 60-minute and (b) 90-minute annealing marks. (c) The individual voxels that changed grain assignment from time steps (a) to (b) are colored according to the misorientation angle from their previous to current orientation. The non-zero voxels represent the volume swept by migrating grain boundaries and will be referred to as the exchanged volume ΔV.

migrate rapidly as grain 1017 expands in this direction. Figure 4.19 displays this aspect in greater detail. Cross sections through grain 1017 before and after the final 30-minute anneal are reproduced in Figs. 4.19 (a,b), and the corresponding change in orientation between the two time steps is shown in Fig. 4.19 (c). If the orientation of a voxel does not change between the 60 and 90-minute measurements, it is colored black in this mapping. We see here that grain 1017 grows almost exclusively at the cost of its high-misorientation neighbors.

The distribution of grain 1017's boundary area as a function of misorientation is plotted in red in Fig. 4.20 (a). The height of each bar represents the total area of grain 1017's boundaries that fall within each 1° bin, as determined from the 3D reconstruction at the 60-minute annealing mark. At this time step there are 42 total boundaries but only 22 bins with nonzero areas. Obviously, some bins contain more than one grain boundary. A similar distribution is plotted in blue for all voxels that are either added to or subtracted from grain 1017 during the subsequent 30-minute anneal—i.e., the voxels whose atoms have taken on a new crystallographic orientation. These voxels are extracted from the before-and-after 3D reconstructions by applying an XOR filter and then calculating their relative misorientation from one time step to the next. Knowing the voxel size (a cube with side length 5 μm), we can calculate a volume in μm^3. This quantity will be referred to henceforth as the exchanged volume and given the symbol ΔV.[10]

Taking the quotient on a bin-by-bin basis of the two histograms ($\Delta V / A_{GB}$) in Fig. 4.20 (a) and dividing by the annealing interval of 30 minutes, we obtain an estimate for the average grain boundary velocity $\langle v_{GB} \rangle$ as a function of ϑ for the interfaces of grain 1017. These values are approximate, depending not only on the binning but also on neighbor switching events, among other effects. Nevertheless, the bar graph of $\langle v_{GB} \rangle$ in Fig. 4.20 (b) clearly displays larger migration rates for grain 1017's high-angle grain boundaries.

Although grain 1017 and grain 661 were initially both larger than average, their evolution could hardly be more dissimilar. It appears that the deciding difference between these two crystallites is the makeup of their local neighborhoods. While grain 661 was completely isolated in terms of crystallographic orientation, a large fraction of grain 1017's perimeter

[10] Regardless of whether a given grain grows or shrinks, all voxels that change orientation contribute positively to the count of ΔV.

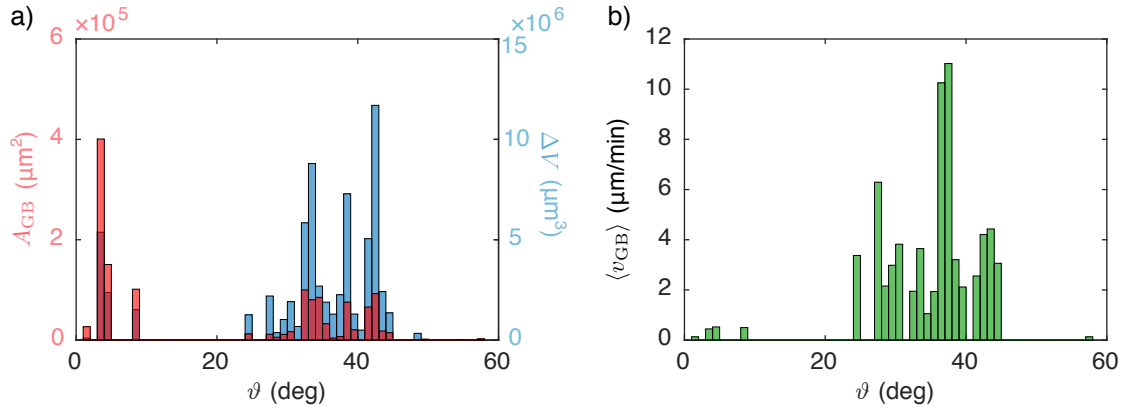

Figure 4.20: Average grain boundary velocities for grain 1017. (a) Grain 1017's boundary area and exchanged volume are calculated for the final annealing interval and indexed to the corresponding misorientation angle ϑ (1° bins). (b) Average values for the grain boundary velocity can be estimated from the previous quantities.

is made up of very low-angle grain boundaries. Grain 1017 and its similarly oriented light green neighbors operate almost as if they were a single unit, providing grain 1017 an advantage when competing for the atoms of its high-misorientation neighbors, to which grain 1017 effectively appears larger than it actually is.

4.4.2 Average grain boundary velocities

In both of the case studies above, high-angle grain boundaries tend to migrate more rapidly than low-angle interfaces. But is this behavior generally true?

To answer this question an analysis of average boundary velocities similar to that of Fig. 4.20 was performed for the entire irradiated sample volume and the results displayed in Fig. 4.21. Frequencies of boundary area and exchanged volume are plotted against misorientation angle in Fig. 4.21 (a) for the initial growth interval (from 0 to 30 minutes at 400 °C), and in the bar graphs of Fig. 4.21 (b) mean velocities, calculated per bin, are given for all three annealing intervals. We see here that $\langle v_{\mathrm{GB}} \rangle$ initially increases with misorientation angle, before reaching a plateau between 25–45°. Somewhat surprisingly, the average velocity then drops back to values comparable to those of low-angle grain boundaries as misorientation increases further.

Most models of grain boundary energy (and by extension grain boundary velocity) assume a constant value for general high-angle grain boundaries [108, 154, 256]. But recent embedded atom simulation results reported by Olmstead *et al.* [116] show a bell curve, somewhat similar in shape to the trend line plotted in Fig. 4.21 (b). To the knowledge of the author, there are no current models that predict a drop in energy or velocity for general high-angle grain boundaries above a misorientation of 45°.[11] However, the results presented here seem to confirm the conclusion in [116] that the high-angle grain boundary energy cannot be treated as a single-valued parameter.

[11] Peaks in boundary migration rates near $\vartheta = 40°$ have been reported for Al and other fcc materials, as summarized by Humphreys and Hatherly [11], but these observations are connected to specific misorientations, which most often correspond to particular CSL relations (e.g., $40° \langle 1\,1\,1 \rangle \approx \Sigma 7$). However, I have not found any literature detailing a peak in boundary migration rates for general high-angle grain boundaries, although the Ni grain boundary energies simulated by Olmsted *et al.* seem to show a peak at $\vartheta = 40°$ (cf. Fig. 2 in [116]).

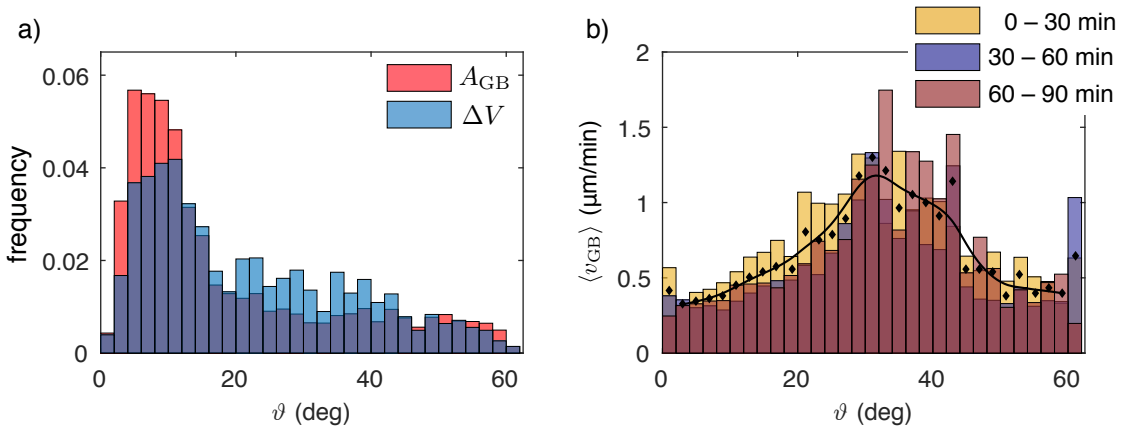

Figure 4.21: Average grain boundary velocities for all grains. (a) Normalized histograms of boundary area and exchanged volume for the initial microstructure allow for a direct comparison of the two quantities. At misorientation angles where the blue volume bars extend beyond the red area bars, we expect to find the highest boundary velocities. (b) $\langle v_{GB} \rangle$ takes on a similar shape across all annealing intervals, with the highest values forming somewhat of a plateau at about 1 µm/min between 25° – 45°. Average values for each of the 2° bins are displayed as black diamonds with a spline fit connecting them. Artifacts in the reconstruction and discrete time sampling are responsible for the apparent peaks at the lowest and highest misorientation angles.

At the extreme ends of the velocity plot in Fig. 4.21 (b), there appear to be two spikes in magnitude. Segmentation artifacts at the boundary of similarly oriented contiguous grains is responsible for spurious exchanges of volume that are then converted into systematic larger values of $\langle v_{GB} \rangle$ for the lowest misorientation angles (see Fig. 3.10). The origin of the apparent spike at the highest value of ϑ is not immediately obvious. The cause appears also to be primarily an artifact—this time an effect of the discrete sampling of the microstructure. During annealing, some of the faster growing grains can grow through several layers of neighboring grains, i.e., they consume parts or all of grains with which they had no contact in the previous grain mapping. This leads to a misrepresentation of A_{GB}, which, in the extreme case, can be zero. On the other hand, as long as a voxel is indexed in both time steps before and after the annealing interval, there is always a finite value for the exchanged volume ΔV. (An example of exactly this situation can be seen in Fig. 4.20 (a) near $\vartheta = 50°$.) This error should average out when many grain pairs for a given misorientation angle are present in the analysis; however, very few boundaries go into the calculation of $\langle v_{GB} \rangle$ at angles above 60°, leading to the large scatter and uncertainty for the final data point of Fig. 4.21 (b).

Although an underrepresentation of CSL boundaries in this particular Al-1 wt% Mg sample has already been established, one might suspect—especially after seeing the peak in $\langle v_{GB} \rangle$ near 60° (the misorientation angle of Σ3 boundaries)—that the limited fraction of such interfaces could still have an influence on the overall coarsening behavior. Thus, for the sake of completeness, these boundaries are examined here, as well. In Fig. 4.22 (a) the average grain-boundary velocities of the first seven lowest-indexed (and most common) CSL boundaries are compared to the mean values for low and high-angle boundaries. From this figure it appears that boundaries can be sorted into one of two populations: slow or fast-moving interfaces. The Σ3, Σ11 and Σ13b boundaries are slow-moving interfaces that migrate at about the same average speed as low-angle grain boundaries. On the other hand, the Σ5, Σ7, Σ9 and Σ13a boundaries all migrate at higher average velocities, similar to those of general high-angle grain boundaries. Since there are no distinct differences

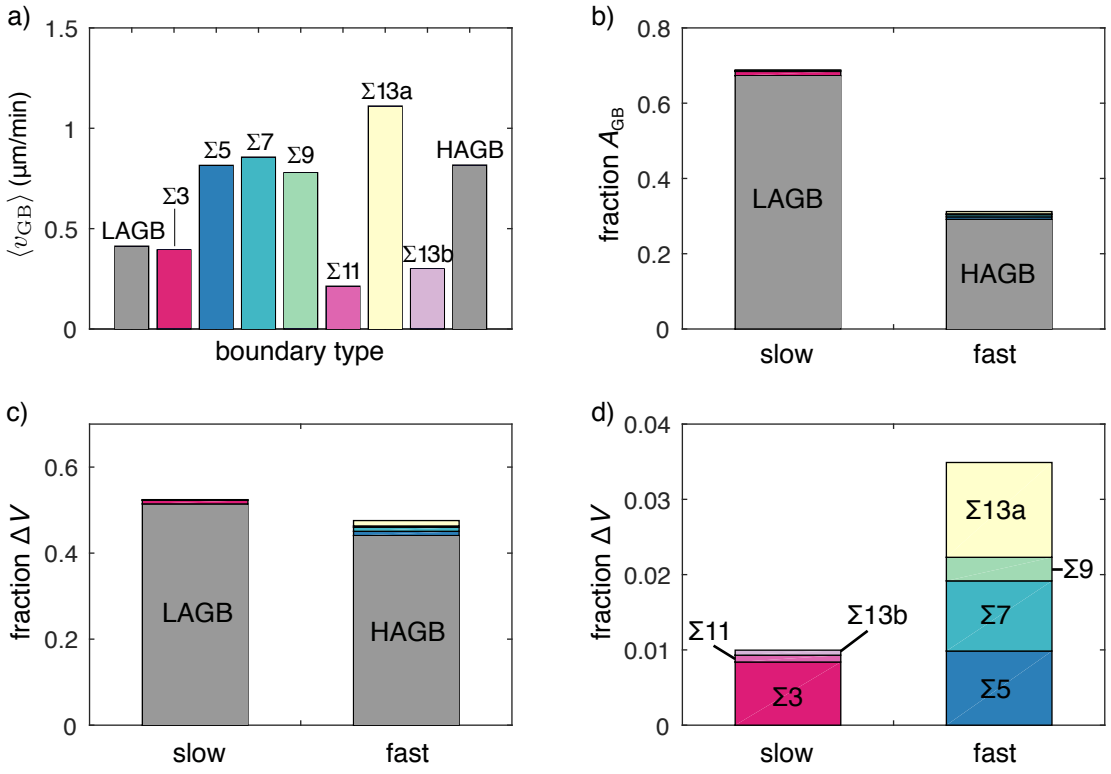

Figure 4.22: Velocities and relative fractions of CSL boundaries. (a) The average velocities of the lowest-indexed CSL boundaries are compared to the mean values for general low and high-angle grain boundaries (LAGB and HAGB, respectively). From this plot interfaces are classified either as slow ($\langle v_{GB} \rangle < 0.5\,\mu m/min$) or fast (the rest) moving boundaries. Population-specific bar graphs of (b) grain boundary area and (c) exchanged volume—shown in higher magnification in (d)—reveal the small relative fractions of CSL boundaries present in the Al-1 wt% Mg specimen. Average velocities from all time steps are included in this analysis. The colors assigned to the different Σ-values in (a) are used consistently in the remaining bar graphs.

in velocity compared to the majority populations of low and high-angle grain boundaries, CSL interfaces should not significantly affect coarsening behavior.

A look at the relative fractions of boundary area (Fig. 4.22 (b)) and exchanged volume (Fig. 4.22 (c)) reinforces the insignificance of CSL boundaries: their fractions in both bar diagrams pale in comparison to those of the low and general high-angle grain boundaries. In the end, including CSL interfaces in the grain boundary velocity analysis marginally increases the population of slow-moving boundaries, since the Σ3, Σ11 and Σ13b interfaces, owing to their misorientation angles greater than 20°, would otherwise be grouped with high-angle grain boundaries. Furthermore, on an individual grain level, a detailed examination of the boundaries surrounding grains 661 and 1017 (case studies I and II above) reveals that none of the exceptionally fast-moving boundaries manifest CSL character. The fact that grain 661 was consumed by a neighbor with a misorientation angle of approximately 60° appears to be merely coincidental; moreover, from the $\langle v_{GB} \rangle$ data presented here we would not expect a Σ3 boundary to migrate rapidly.

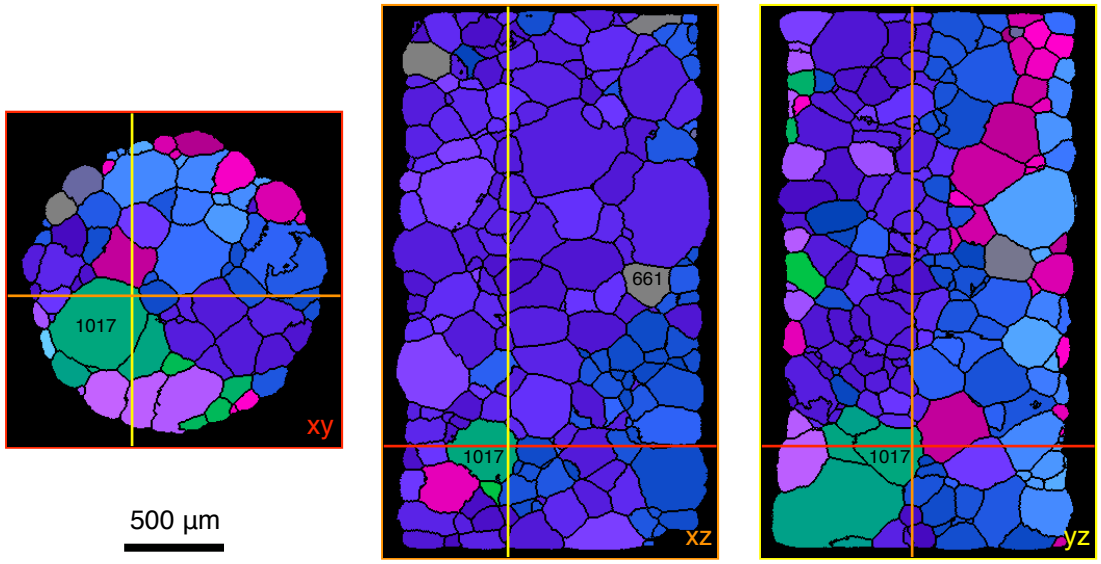

Figure 4.23: Clustering of grains with similar crystallographic orientations. In these three orthogonal sections, grains are colored according to the texture component to which they belong (see Fig. 4.15). The intersecting lines in each section indicate the position of the other two slices. These sections through the microstructure at the beginning of the 400°C anneal were chosen to reveal the positions of grains 661 and 1017, which were investigated in detail above.

4.4.3 Spatial clustering of grains

The reader may have noticed in the various cross sections above (Figs. 4.17 – 4.19) that grains of like color are often found in close proximity to each other. By applying the texture component-based coloring scheme—developed for the Rodrigues plots of Fig. 4.15—to spatial grain mappings, the clustering of like-oriented grains becomes even more evident. Three orthogonal sections through the initial microstructure are shown in Fig. 4.23. The high spatial correlation between grains of similar orientation is perhaps most clearly visible in the yz-section. Here, we observe a separation of the two near-Cube orientations along the z-axis of the cylindrical specimen. (The z-axis is parallel to the rolling direction.) On the right-hand side of the yz-section, the dark blue grains located along the center line are gradually replaced by lighter blue and magenta crystallites as we move radially outwards to the right. This behavior is mirrored on the left-hand side; near the center we observe a high frequency of dark purple grains, which give way to lighter purple and green grains at the left edge of the sample.

To further investigate the inhomogeneous radial distribution of grain orientations, the rotation angle (relative to the ideal Cube texture) of individual grains is plotted against the distance of each grain's center of mass from the sample's z-axis in Fig. 4.24 (a). The points of the resulting scatter plot are colored according to the same texture component-based coloring scheme as in Fig. 4.23. Since the volume of a cylinder increases linearly with the square of its radius, the specimen radius squared is used to define the horizontal axis. Therefore, each interval of given length along the horizontal axis represents an equal volume of sample, and, assuming a uniform distribution of grain sizes throughout the sample, the number of grains in each interval should also be approximately equal. As expected from the cross sections above, we observe an increase in the average rotation angle from 12° near the specimen center to 27° at its outer edge. Using color to represent frequency, the bivariate frequency plot (Fig. 4.24 (b)) overcomes the ambiguity of overlapping points in

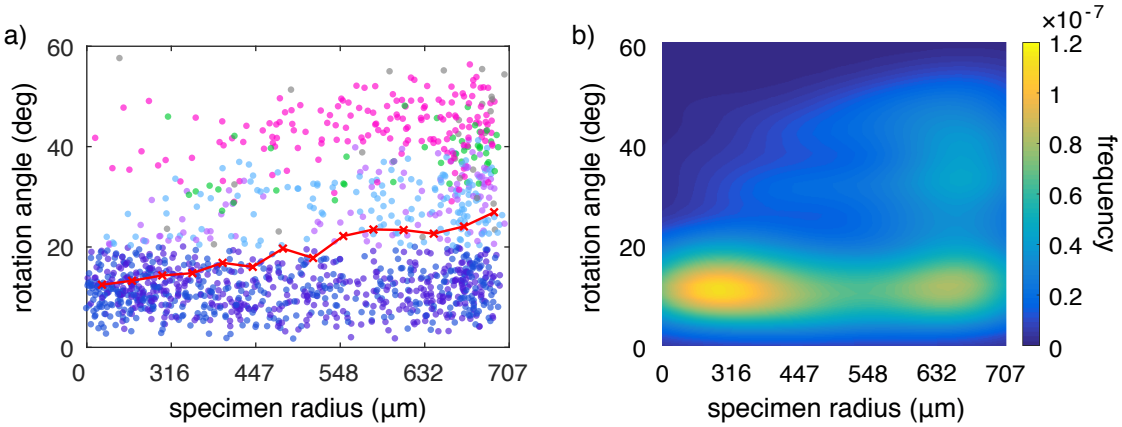

Figure 4.24: Radial distribution of grain rotation angles in the initial microstructure. (a) The angle of rotation between the ideal Cube orientation and each grain's experimentally determined orientation is plotted as a function of the grain's radial position. Each dot in this plot represents a single grain, the texture component of which is identified by its color. The red line connects average values calculated at intervals marked by red x's. (b) Maxima in frequency are more clearly visualized in a bivariant frequency plot of the same data. In both plots the square of the specimen radius is used to define the horizontal axis so that the volume increases linearly.

the scatter plot, thereby displaying some trends in the data more clearly.

This nonrandom spatial distribution of similarly oriented grains is undoubtedly related to the specimen's processing history. Face-centered cubic metals with moderate to high stacking fault energies, such as Al, deform by slip, and the high (plane) straining that occurs during cold rolling commonly leads to large bands of similarly oriented material [11]. Familiar deformation textures in Al alloys are the so-called Copper, Brass and S textures [251]. Although none of these textures were observed in our recrystallized Al-1 wt% Mg specimen, the microstructure of the deformed state appears, nevertheless, to have been retained to some degree even after recrystallization through the clustering of grains with similar orientations in the bands or cells of the previously deformed material. Such observations are not unusual in recrystallized metals, and the causes are assumed to be related to inhomogeneous distributions of strain energy as well as to preferential nucleation and growth of recrystallized grains inside deformation bands or at their boundaries [11, 257].

Regardless of its precise origin, the clustering of like-oriented grains has a noticeable impact on the distribution and migration of grain boundaries. To establish the spatial extent of any particular grain cluster, we can make use of the texture components defined in Section 4.3. Grains that are in direct contact with each other and belong to the same texture component belong to the same grain cluster. Consequently, the boundaries between grains of the same cluster are almost exclusively low-angle boundaries, while most high-angle grain boundaries are found at borders between clusters. With this definition of a grain cluster, we can examine the migration of grain boundaries with respect to their classification as either intra or inter-cluster boundaries. In Fig. 4.25, misorientation distributions of exchanged volume as well as average velocities are displayed for both boundary types. Given that the latter are made up of mostly low or mostly high-angle boundaries, it comes as no surprise that inter-cluster boundaries migrate on average at about twice the speed of intra-cluster boundaries. Inevitably then, we expect the microstructural coarsening in the Al-Mg specimen to be dominated by the migration of high-angle, inter-cluster boundaries.

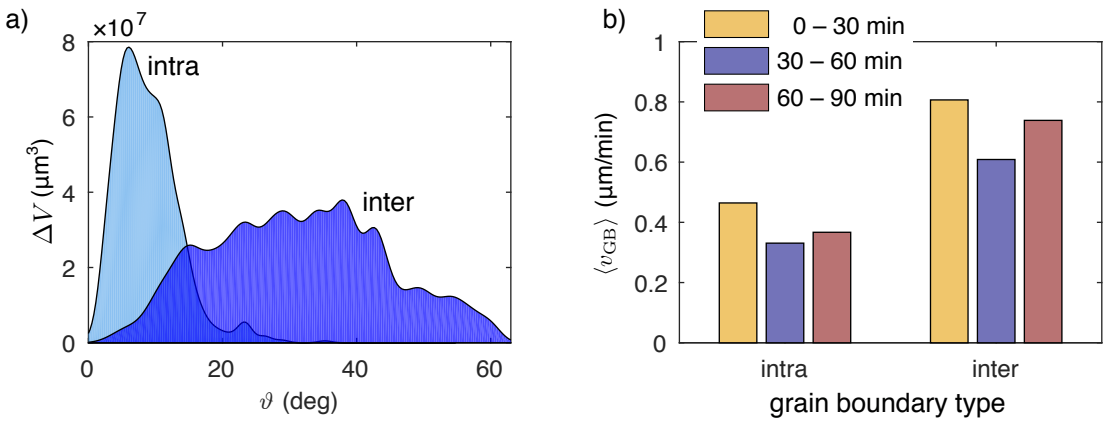

Figure 4.25: Intra versus inter-cluster boundary migration. Grouping contiguous crystallites of the same texture component into grain clusters, we compare the behavior of grain boundaries that separate grains in the same cluster (intra-cluster boundaries) with those that define borders between clusters (inter-cluster boundaries). Even though the total area of intra-cluster boundaries outweighs that of inter-cluster boundaries (55% vs. 45%), significantly more volume is exchanged across inter-cluster grain boundaries, as shown in the plots of (a) summed across all time steps. Consequently, the average boundary velocities, displayed for individual annealing steps in (b), are also considerably higher for inter-cluster boundaries.

4.4.4 On the mechanism of abnormal grain growth in textured materials

In the case studies presented at the beginning of this section, we saw that abnormal growth and shrinkage occurred through the rapid migration of high-angle grain boundaries. We then analyzed all boundaries of the specimen and found that high-angle grain boundaries move on average about twice as fast as their low-angle counterparts, while also establishing a lack of significance for the limited fraction of CSL boundaries. Finally, we determined that grains of the same texture component are not randomly distributed throughout the sample but tend to form clusters of similarly oriented grains.

The effects of clustering on grain growth kinetics are highlighted in the cross sections of Fig. 4.26. By blending out the intra-cluster grain boundaries, an overarching network of mostly high-angle boundaries becomes visible; and although the constituent grains of the various clusters do coarsen upon annealing, the most significant microstructural changes are associated with the migration of high-angle, inter-cluster grain boundaries. Several CSL boundaries are also seen in these cross sections, but their only impact on coarsening appears to be through the slightly retarded motion of $\Sigma 3$ interfaces. Because a global threshold was used to define each texture component in orientation space, it is possible for clusters to meet at low-angle grain boundaries. These boundaries are colored black in the right-hand column of Fig. 4.26 and, like the $\Sigma 3$ interfaces, they appear to be rather sluggish.

In the competitive process of grain growth, the clustering of similarly oriented grains seems to result in a strength-in-numbers phenomenon, and grains that belong to a cluster enjoy two advantages. First, owing to the reduced migration rates of low-angle grain boundaries, the coarsening of grains inside clusters proceeds slowly. This means that the internal grains of a cluster (even the very smallest) are able to survive longer than they otherwise would if isolated, i.e., if located in a randomly oriented neighborhood. This effect is sometimes referred to as orientation pinning [157], and it explains the low growth rates for many of the grains in the Hillert plot (Fig. 4.7).

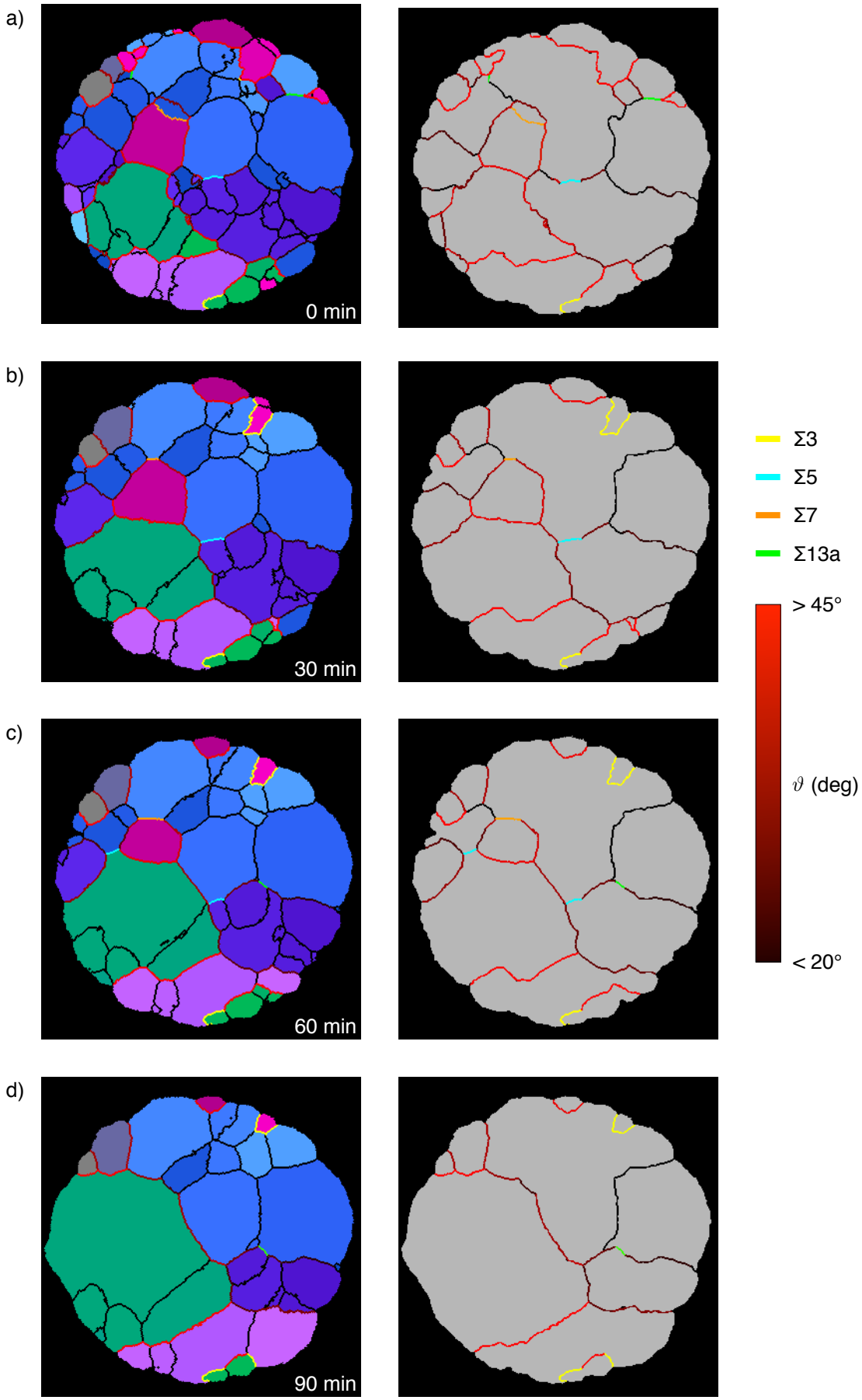

Figure 4.26: Visualization of grain clustering. Grains on the left are colored according to their respective texture component. On the right, all intra-cluster boundaries are blended out.

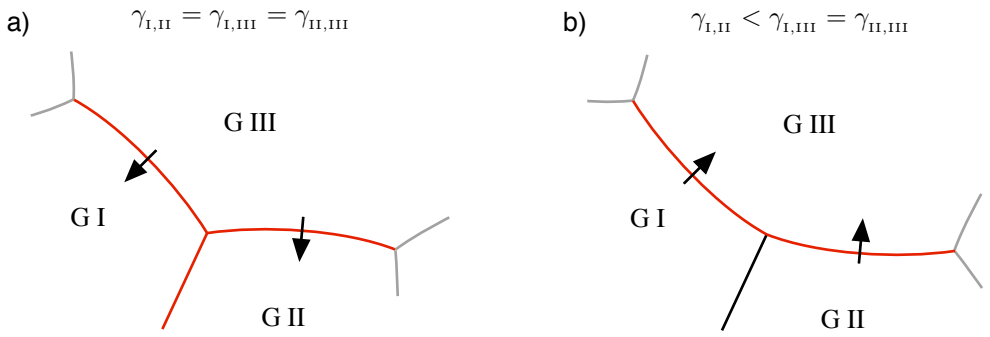

Figure 4.27: Dihedral angles for a theoretical arrangement of grains at a triple junction. (a) Assuming uniform boundary energies, equilibrium dihedral angles of 120° form at the triple junction where grains G I, G II and G III intersect. (b) If the boundary energy between grains G I and G II ($\gamma_{I,II}$) is lower than the energy of the other two boundaries, the dihedral angle opposite to the low-energy grain boundary will open up to maintain equilibrium of interfacial tension at the triple junction. In this case, boundary curvatures can flip direction, and grains G I and G II can grow into G III despite both being individually smaller than grain G III.

The second advantage that grains of a cluster enjoy pertains to those on its outer perimeter. If two neighboring grains from the same grain cluster also form a contiguous boundary with a third grain from a foreign cluster, the former can work together to overwhelm and consume the third grain, even if it is bigger than either of the first two. A hypothetical intersection of three grains at a triple junction is shown in Fig. 4.27. If the crystallographic orientation of all three grains is random (Fig. 4.27 (a)), then the interfaces between each pair of grains are, in all likelihood, general high-angle grain boundaries. Assuming a uniform energy for such random high-angle grain boundaries, the tension applied by each boundary at the triple junction is equal, and dihedral angles of 120° will form in equilibrium [4]. If, however, grains G I and G II belong to the same grain cluster (Fig. 4.27 (b)), they have a small misorientation, resulting in a low-energy grain boundary at their common interface. To compensate for the lack of tension applied by this boundary to the triple junction, the angle between boundaries G I-G III and G II-G III opens up, approaching 180° as $\gamma_{I,II}$ goes to zero. Consequently, the curvature of these two boundaries may—depending on the exact energy and size ratios—flip direction, leading to the cooperative growth of grains G I and G II. Close inspection of the cross sections of Fig. 4.26 does indeed reveal similar situations.

While 2D cross sections and 3D images of individual grains are helpful in visualizing coarsening phenomena, they provide a limited glimpse into the evolution of the overall microstructure. To better understand the effects of grain clustering on the general coarsening behavior, statistical evaluations of the slowest and fastest evolving grains in the Al-1 wt% Mg specimen are compared directly in Fig. 4.28; although segmentation issues affect the determination of both grain and cluster boundaries, we can still gain valuable insight from the trends found in these graphs. Both populations were extracted from the Hillert plot of Fig. 4.7 by applying thresholds at the extreme limits of the plot. The slowest evolving grains were selected as those growing or shrinking at an absolute velocity less than 1.6 μm^2/min, while the fastest evolving grains are those found outside the 90% prediction bounds of the Hillert fit. These limits result in an equal number of grains (73) for both populations.

As one would expect by now, the slowest evolving grains have fewer inter-cluster grain boundaries—i.e., they are more likely located toward the interior of grain clusters—while the opposite situation is observed for the fastest evolving grains. These trends are dis-

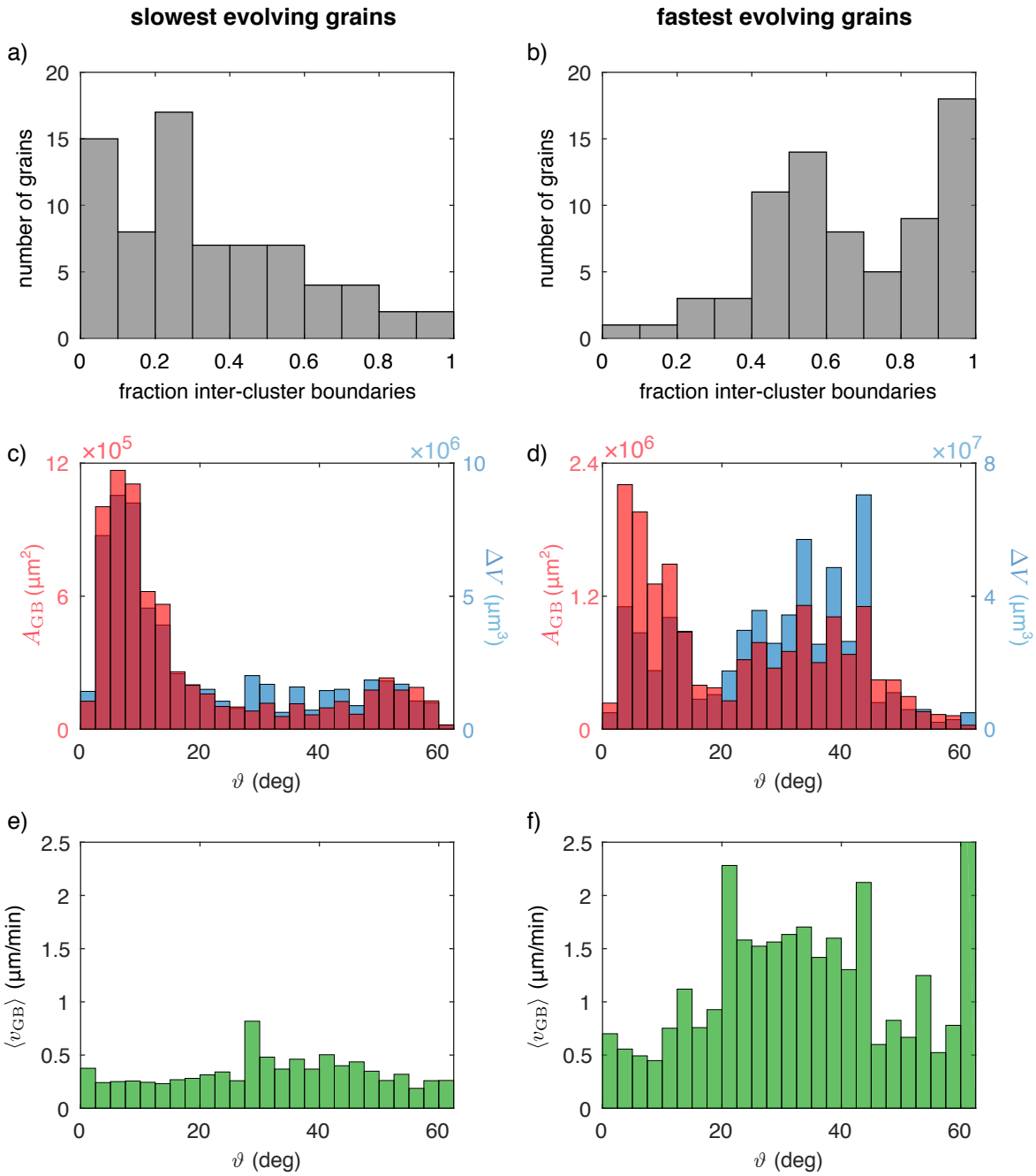

Figure 4.28: Examination of the slowest and fastest-evolving grains in the Al-1 wt% Mg specimen. (a) The slowest-evolving grains tend to have fewer inter-cluster grain boundaries, while (b) the opposite is true of the population of fastest-evolving grains. Distributions of grain boundary area A_{GB} and exchanged volume ΔV are markedly different for the two populations. A single peak at low misorientations is seen for (c) the slowest-evolving grains, while a bimodal distribution is observed for (d) the fastest-moving grains. Consequently, average boundary velocities also differ strongly. Other than a slight increase in $\langle v_{GB} \rangle$ for mid-ranged misorientations, the average velocities associated with the boundaries of (e) the slowest-growing grains are very low and essentially constant. Perhaps the few high-angle grain boundaries present in this population are pinned by the preponderance of low-angle grain boundaries. (d) The fastest-evolving grains show higher average velocities all around, but also a clear plateau at misorientation angles between 20° and 45°. The shape of this distribution is similar to one for all grain boundaries (Fig. 4.21), likely because these grains dominate the coarsening that occurred in the specimen.

played graphically in the histograms of Figs. 4.28 (a, b). A few grains are found to have a high fraction of inter-cluster boundaries but still remain quite stagnant. Detailed examination of these grains reveals that they are small surface grains with a small number of neighbors. The pinning of grain boundaries at free surfaces is a known phenomenon [229], which is apparently responsible for some of the low growth rates in this population. In the graphs of grain boundary area and exchanged volume versus misorientation (Figs. 4.28 (c, d)), the most obvious difference between the two populations are the peaks in both A_{GB} and ΔV for the fastest-evolving grains at misorientations between 20° to 45°. Because ΔV disproportionately outweighs the boundary area in this range, a peak in the average boundary velocity derived from the ratio of ΔV to A_{GB} is observed for the population of fastest growing grains (Fig. 4.28 (f)). This plateau is similar in shape and position to that of Fig. 4.21 (b)—which was determined from all grain boundaries in the Al-1 wt% Mg specimen—but somewhat more pronounced in magnitude. For the population of fastest-evolving grains, boundaries with $\vartheta > 20°$ account for only about half of the total area, yet 70% of the volume consumed or surrendered is exchanged across these high-angle boundaries. Not all grains with high-angle boundaries evolve abnormally, but those that do, do so through accelerated migration of high-misorientation interfaces.

Although an abnormally growing grain implies that at least some of its neighbors shrink abnormally fast and vice versa, it is nevertheless interesting to examine the differences between these two subsets of fastest-evolving grains. The entire population is comprised of 73 grains,[12] of which 12 grow and 61 shrink abnormally. The most definite difference is grain size. Most abnormally growing grains are larger than their shrinking counterparts. But the latter are still nearly all larger than average. In the range of normalized grain sizes from 2.0 to 2.5, there are exactly five data points from abnormally growing and five from abnormally shrinking grains. The primary difference between these grains is the average misorientation with respect to their nearest neighbors. While the abnormally growing grains share on average 50% of their total boundary area with similarly oriented grains from the same texture component, rapidly shrinking grains have a much lower average fraction of intra-cluster boundaries at only 27%. When averaged over all grains of both the abnormally growing and the abnormally shrinking subsets, this relative difference in the fraction of intra-cluster boundaries remains approximately the same. It seems that in order to enjoy a sustainable growth advantage, grains must not only be large and have some high-angle boundaries, but it also helps if they belong to a cluster of similarly oriented grains. These observations lend further support to the strength-in-numbers hypothesis developed above.

4.5 Concluding remarks on grain growth observed in single-phase Al-Mg

High-quality 3DXRD grain maps of an Al-1 wt% Mg sample were obtained through the iterative application of peak-finding and seed-refinement algorithms. These reconstructions revealed the presence of a fairly strong Cube texture, which was subdivided into seven separate components (Fig. 4.15). The grains of each component manifested a high spatial correlation—except for those of the final component, which was populated by the few randomly oriented grains in the sample. Consequently, grains of similar orientation were found in clusters throughout the sample, and this clustering had a pronounced influence on how the specimen coarsened. Grain boundaries located within clusters were nearly all low-angle grain boundaries ($\vartheta < 20°$), and they migrated at about half the average speed of

[12] It would be more accurate to speak of data points. Grains can show up twice, once for each time step.

the grain boundaries that defined the border between neighboring clusters. This difference in migration rate highlights the non-uniformity of grain boundary properties, and a full analysis of average boundary velocity against misorientation angle (Fig. 4.21) revealed a plateau of high boundary velocities at angles from 20° to 45°. The drop in average velocity for interfaces with $\vartheta > 45°$ has not been observed previously, and it will be interesting to see whether future experiments confirm the generality of this result, or if it is instead connected to this particular specimen and/or its processing history.

Not surprisingly, Hillert's normal grain growth model, which assumes uniform boundary properties, does a poor job of predicting growth rates for individual grains. Several of the largest grains in the sample grew much faster than expected according to Hillert, while other grains—even some larger than the mean grain size—shrank very rapidly. This behavior was caused by the abnormal growth and shrinkage of crystallites located at the outside edge of grain clusters. Although abnormal grain growth is not uncommon in textured samples, it is usually explained by the presence of highly mobile CSL grain boundaries and the growth of one texture component at the expense of another [124, 154, 159, 160]; however, neither of these two features were observed in the present study. Grains that grew abnormally had three common traits: they were initially large ($R > 2\langle R\rangle$), they expanded primarily through the migration of high-angle inter-cluster boundaries, and they had large low-angle intra-cluster boundaries. In contrast, grains that shrunk abnormally were typically isolated in terms of orientation.

At the onset of this investigation the goal was to collect 3D experimental data of "ideal" normal grain growth. Obviously, this objective was not achieved, and it is revealing to consider what went wrong. The selection of Al-1 wt% Mg as a good candidate material was based on preliminary studies that established an optimized recrystallization treatment and annealing temperature [12]. Relevant results from this earlier work were reproduced in Figs. 1.2 and 1.3 of the introduction. Growth curves and grain size distributions were derived from conventional 2D metallographic sections and displayed all the traits of normal growth. The sample's crystallographic texture, the clustering of similarly oriented grains and the true distribution of grain shapes and sizes were not uncovered until the first 3DXRD data sets were reconstructed. The discrepancy between 2D and 3D characterizations of samples from not only the same alloy but also the same physical plate of cold-rolled Al-1 wt% Mg clearly emphasizes the necessity of studying the 3D phenomenon of grain growth in 3D.

5

Grain Rotations During Coarsening in a Semisolid Al-Cu Alloy

Scientists studying coarsening in polycrystalline materials have long speculated that rigid-body grain rotation may occur as an alternate path of coarsening in parallel to the standard mechanism of boundary migration through atomic diffusion. The rotation of isolated spherical grains on single-crystalline substrates has previously demonstrated that the dependence of grain boundary energy on misorientation can indeed drive rotations; however, doubt has remained whether such rotations actually take place in bulk materials.

In this chapter three-dimensional x-ray diffraction (3DXRD) microscopy was employed to study coarsening in a fully compact, semisolid Al-5 wt% Cu alloy. Not only were significant grain rotations observed, but an evaluation of relative changes in misorientation between low-angle grains revealed that these rotations are in fact biased by the reduction of boundary energy. The results of this study—portions of which have been published in Ref. [218]—emphasize the importance of including orientation information in coarsening models of polycrystalline solids, particularly in the case of sintering.

5.1 Theory of energy-driven grain rotation

As explained in Chapter 2, the spatial extent of individual grains in a polycrystalline specimen is determined by their crystallographic orientation, which changes discontinuously upon crossing a boundary to an adjacent grain or phase. The boundaries between grains form a network of total interfacial area A_{GB} that spans the sample and raises its Gibbs free energy by the amount

$$\Delta G = \gamma A_{\mathrm{GB}}, \tag{5.1}$$

where γ denotes the boundary energy per unit area. As a result, all polycrystalline materials find themselves away from thermodynamic equilibrium, since a reduction in A_{GB} or γ would take the sample into a state of lower free energy. One need only supply sufficient thermal energy to witness the consequences of this thermodynamic instability: once atomic diffusion sets in, the area term in Eq. (5.1) begins to decrease over time, as during

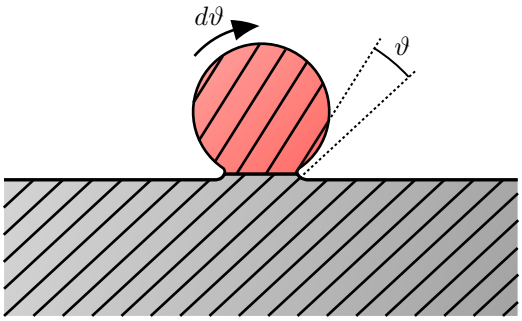

Figure 5.1: A spherical grain on a single-crystalline substrate of the same material. The hypothesis originally proposed by Shewmon [258] states that the dependence of grain boundary energy on misorientation ϑ can lead to a grain boundary torque and subsequent rotation $d\vartheta$ of the spherical crystallite in a direction that reduces the boundary energy.

the phenomena of grain growth [11, 15] and Ostwald ripening [170, 177]. In both of these processes, atoms tend to diffuse from smaller to larger crystallites, resulting in the growth of larger grains at the expense of their smaller neighbors. Each time one of the latter vanishes, the average volume of the remaining grains increases and the total boundary area decreases, thereby reducing the sample's free energy.

It is often assumed that γ is constant [16, 23, 25, 28, 54, 223, 225], in which case ΔG varies linearly with A_{GB}, making a reduction in A_{GB} the only possible means of minimizing the excess free energy. However, near low-angle and CSL grain boundaries γ is known to depend strongly on the misorientation ϑ [18, 104], with deep cusps in the energy landscape frequently appearing near such boundary configurations (see Section 2.1.2). In this case, a second mechanism for reducing the Gibbs free energy is conceivable: namely, the rigid-body rotation of entire grains to lower-energy boundary configurations.

In 1966 P. G. Shewmon was the first to consider grain rotations under the influence of a grain boundary torque [258]. He envisioned that a spherical grain sintered to a planar single-crystalline substrate of the same material—as depicted in Fig. 5.1—could rotate about an axis in the boundary plane, lowering the free energy by

$$dG = A_{\mathrm{GB}} \left(\frac{d\gamma}{d\vartheta} \right) d\vartheta. \tag{5.2}$$

Initial experiments confirming Shewmon's hypothesis were performed a decade later by Gleiter's group in Saarbrücken [85]. Thousands of randomly oriented single-crystalline Cu balls (~100 μm in diameter) were deposited onto single-crystalline Cu plates with surface orientations matching either (1 0 0), (1 1 0) or (1 1 1) planes. The decorated plates were then heated to 1060 °C for various times, and pole figures before and after annealing were captured by XRD. Not only were the authors able to prove through these novel "ball-on-plate" experiments that grains can rotate to reduce their boundary energy, but by analyzing the maxima of the pole figures, they were also in a position to estimate the relative energies of the observed CSL boundaries. (The lowest-energy boundaries presumably have the deepest cusps in the energy landscape and are, accordingly, the most stable and most frequently observed after grain rotation has ceased.)

In a later set of similar experiments, Chan and Balluffi were the first to directly observe

the rotation of nanometer-sized Au spheres on a thin gold plate in a transmission electron microscope [259, 260]. This study also provided insight into the mechanism behind such grain rotations: tilting occurred by the climb of grain boundary dislocations and twisting by the glide of screw dislocations. The most recent ball-on-plate experiments were performed again with Cu spheres, using electron-backscatter diffraction (EBSD) to track orientational changes of individual grains [261]. Interpretation of the rotation trajectories led to the conclusion that the energy landscape is likely asymmetric, with possible shallow cusps superimposed on deeper ones and flat-bottomed energy minima.

Although the above experiments provided validation that variations in the boundary energy landscape could indeed induce grain rotations, skepticism has remained whether this phenomenon actually occurs in technically relevant bulk polycrystalline systems, in which a given grain may have anywhere from 5 to 20 or more immediate neighbors [23, 262, 263]. Nevertheless, scientists studying both liquid-phase [264–266] and solid-state sintering [267–269] have long speculated on the possibility of grain rotation-induced coalescence of crystalline particles, especially during the early stages of sintering, where particle rearrangement and neck formation dominate the densification of more loosely packed green-body compacts. The primary basis for this speculation was the observation of elongated, non-equilibrium particle morphologies following sintering [264–266, 270]. However, researchers were quick to admit the indirect nature of such evidence and acknowledged that the direct observation of such rotations may not be feasible [264].

Recently, the arguments for boundary-induced rotations were bolstered by the first direct 3D tomographic observations of grain rotation taking place during the solid-state sintering of Cu spheres, which were marked by pits etched with a focused ion beam [61]. To quantify the motion of spherical particles in this study, Grupp *et al.* defined two modes of rearrangement: rolling and rotation. Here, *rolling* was used to denote the revolution of one sphere around the perimeter of another, while *rotation* described the revolution of a particle about its own center of mass. The primary driving force for sintering loose powder compacts is the reduction of excess free surface energy [268]. For this reason researchers imagined that the rolling of particles to close pores and gaps between particles would be preferred to rotations about a particle's center, as the latter do not necessarily serve to reduce the free surface area. Contrary to this assumption, however, Grupp *et al.* found the magnitude of grains rotating about their centers to greatly outweigh that of grains rolling—on average the difference was three times greater. The reduction of boundary energy at inter-particle contacts was considered the most plausible explanation for the observed rotations. Even so, the lack of crystallographic orientation information prevented a direct link from being made.

The unique ability to capture both spatial and orientation data nondestructively makes 3DXRD microscopy ideally suited to assess the role that grain rotations play during the sintering and coarsening of bulk, polycrystalline materials. Measured variations in grain orientation provide a direct means for quantifying the rotation of individual grains. This information, in combination with full 3D grain maps, allows us to detect correlations between rotating grains and their local neighborhoods and draw conclusions regarding the underlying mechanisms.

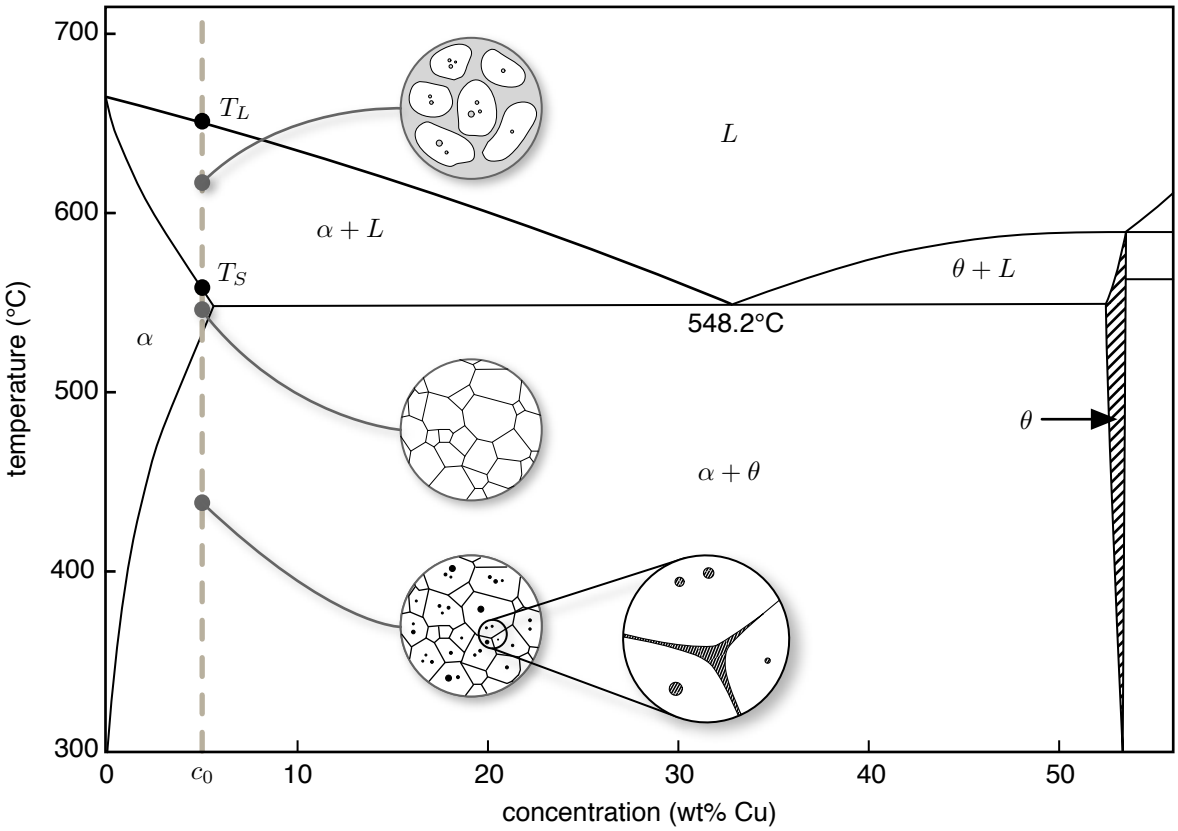

Figure 5.2: Al-rich side of the equilibrium Al-Cu phase diagram. Typical microstructures are illustrated for the different regions of the phase diagram at 5 wt% Cu. The location of the liquidus T_L and solidus T_S temperatures at this composition are also indicated. Phase boundaries are based on the data of Ref. [277], and the figure was adapted from Ref. [182] with kind permission by Thomas Werz.

5.2 Experimental details

5.2.1 Material selection and sample preparation

A unique combination of properties—low density, high strength, good ductility and corrosion resistance—make aluminium alloys attractive for the automotive and aeronautic industries [271–273]. The ability to produce Al alloys by powder metallurgy is especially appealing, since it would simultaneously increase the ease of production while reducing costs. However, Al has an extremely stable oxide, which makes conventional sintering of Al powders problematic [271, 274]. To overcome this difficulty, a liquid phase is often employed that reacts with and disrupts the powder particles' outer oxide shell. The presence of a liquid phase has the additional advantage that higher densification can be achieved in shorter sintering times [271, 275]. Possible additives for formation of a liquid phase include zinc, tin, magnesium, silicon and copper [274, 275]. Small amounts of Cu (< 5 wt%) can significantly increase the strength of pure Al through precipitation hardening [276], and Al-Cu alloys are arguably the most extensively studied and certainly the most widely produced powder metallurgical Al alloys [274]. For these reasons, Al-Cu was chosen as a model system in which to investigate the role of grain rotation during processing in the semisolid state.

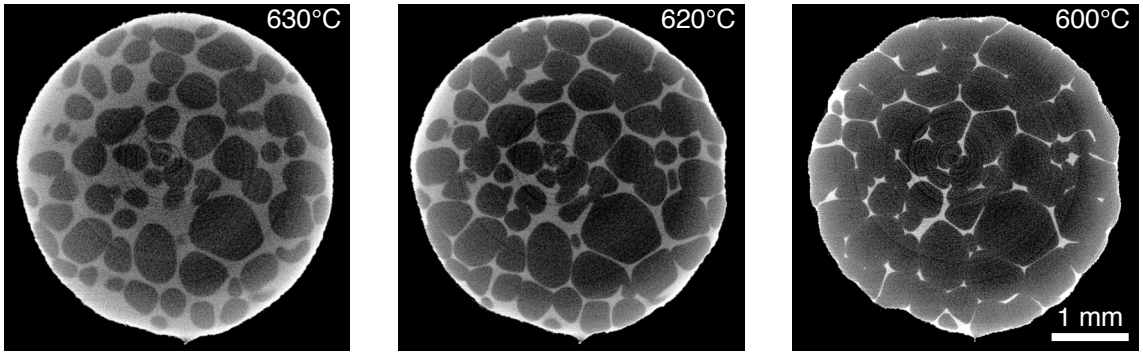

$V_V \approx 0.70$ $V_V \approx 0.81$ $V_V \approx 0.91$

Figure 5.3: Two-phase Al-Cu microstructures. *In situ* x-ray micrographs of an Al-5 wt% Cu alloy, being cooled slowly through the semisolid region, demonstrate the distribution of liquid phase at various volume fractions.

The aluminum-rich side of the Al-Cu phase diagram is depicted in Fig. 5.2. The low solubility of Cu in the α-Al phase and the existence of a eutectic composition between Al and the intermetallic θ phase (Al_2Cu) at 54 wt% are two important characteristics that make liquid-phase sintering possible with this alloy [274, 278]. At a composition of 5 wt% Cu, the liquid phase begins to form in equilibrium at the temperature $T_S = 563\,°C$ and increases in fraction up to 100% at $T_L = 649\,°C$. By varying the temperature in this range, one can effectively set the volume fraction of the solid phase V_V according to the lever rule [276]. This effect is demonstrated in Fig. 5.3, which shows cross sections through a cylindrical Al-5 wt% Cu specimen that was slowly cooled from 630 °C to room temperature while being scanned *in situ* at the Swiss Light Source (SLS) synchrotron radiation facility [182]. Consequently, it is possible, with samples of the same alloy, to investigate the influence of differing amounts of liquid phase on coarsening behavior and grain rotations.

Samples were provided by Dmitri Molodov of the Institute of Physical Metallurgy and Metal Physics, RWTH Aachen. A high-purity Al-5 wt% Cu melt was cast in an argon atmosphere into a 17 mm thick plate and subsequently homogenized for 24 hours at 500 °C. Following a thickness reduction of 50% via cold rolling, electric discharge machining was employed to cut out small cylinders 1.4 mm in diameter and 8 mm in length. The longitudinal axis of the samples was chosen to be parallel to the direction of rolling. After spark erosion and before the start of coarsening experiments, the specimens were heat treated in the semisolid state at 640 °C for 20 minutes. This final anneal was performed to recrystallize the Al-rich grains, while also ensuring that they are adequately wetted. Preliminary studies showed that this pretreatment reduced crystallographic texture in the samples as well.

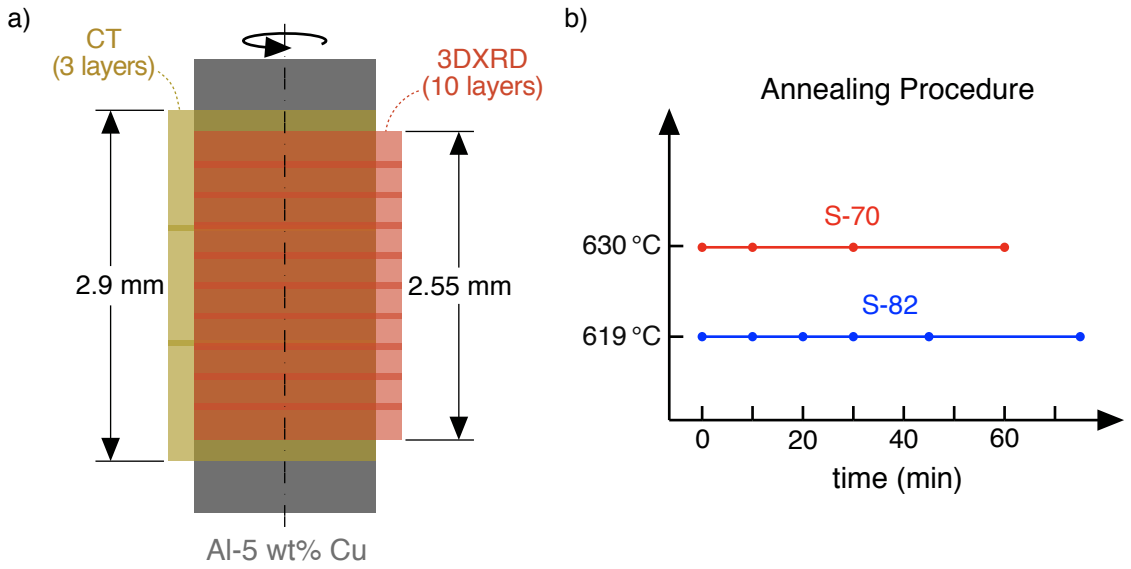

Figure 5.4: Measurement and annealing procedures. (a) 10 layers of 3DXRD and 3 layers of CT data (all with an overlap of 50 µm) were captured at room temperature before/after each annealing interval. (b) The sample S-70 was heat treated at 630 °C and scanned after cumulative annealing times of 0, 10, 30 and 60 minutes. Sample S-82 was annealed at 619 °C and scanned at the 0, 10, 20, 30, 45 and 75-minute marks.

5.2.2 Data collection

Microstructural evolution in Al-5 wt% Cu was investigated at two different volume fractions of the solid phase (V_V). One specimen was annealed at 630 °C and a second at 619 °C. A modified lever rule described by Werz *et al.* [62] was used to determine volume fractions, which were estimated to be $V_V = 0.70$ at 630 °C and $V_V = 0.82$ at 619 °C. Using the volume fraction to label the samples, I will refer to the respective specimens as S-70 and S-82 henceforth.

To capture microstructural changes in these samples, nondestructive CT and 3DXRD measurements were performed at the SPring-8 radiation facility in Japan. Beam settings and detector arrangements were nearly identical to those described in Section 4.1.2, the one exception being the additional collection of CT data.

During each measurement sequence, the same specimen volume was mapped first by CT and then by 3DXRD. For both experimental techniques a parallel, monochromatic (32 keV) box beam, with slight adjustments to its size and intensity, was used to irradiate the samples. To limit the number of diffraction spots and thereby facilitate their unambiguous assignment to individual grains, a reduced beam height is preferred when recording 3DXRD data. This constraint is irrelevant for the collection of standard absorption-contrast images; therefore, during CT scans, beam dimensions were set to the maximum values of 1.0 mm × 1.6 mm (height × width). For each CT scan 1800 images were captured over 360° with a high resolution (1 µm) Hamamatsu CCD detector. As shown schematically in Fig. 5.4 (a), three adjacent layers of CT data were recorded with an overlap of 50 µm between layers. The flux density for these scans was approximately 10^{12} photons/(s·mm^2).

For the collection of 3DXRD data, the beam height was reduced to 300 µm, while its intensity was increased to 10^{13} photons/(s·mm^2). Ten overlapping layers of both far-field (Hamamatsu C7942CA-22 detector with 50 µm pixel size) and near-field (Photron SA2

detector with 4.56 µm pixel size) diffraction data were recorded while continuously rotating the specimen 360°. One image was captured per 0.48°, and the total specimen volume indexed by 3DXRD was centered inside the volume captured by CT.

After the collection of both data sets, which took about three hours in total, the sample was removed from the experimental hutch and annealed in a muffle furnace in air. The duration of the individual anneals ranged from 10 to 30 minutes. Sample S-70 was annealed three times in total: first for 10 minutes, then for 20 and finally for 30 minutes. Sample S-82 was initially annealed three times for 10 minutes, followed by single 15 and 30-minute anneals.[1] Figure 5.4 (b) summarizes the heat treatment of samples, which were annealed on top of brass stubs. To accelerate cooling, the base of the stubs were submerged in water directly following their removal from the furnace. After annealing, samples were then remounted in the experimental hutch, and the entire measurement sequence was repeated. The procedures used to reconstruct, register and track grains from one time step to the next are described in Section 3.3.

5.3 Microstructural evolution

The reconstructions of Fig. 5.5 exemplify the amount of coarsening that occurred during annealing of Al-Cu samples. Just as with the 3DXRD reconstructions in Chapter 4, the crystallographic orientation of each grain is encoded in its RGB color value; therefore, grains of similar color have comparable crystallographic orientations. Because the specimens were scanned at room temperature, the true extent of the liquid phase was not captured. During heat treatment, however, it is safe to assume that most grains were separated from their neighbors by a liquid layer (cf. Fig. 5.3). The remnants of the liquid phase are visible in high-resolution CT but not typically resolved in 3DXRD reconstructions. Thus, grains in Fig. 5.5 appear to be in direct contact with each other. Also evident in these reconstructions is the removal of grains from the top and bottom surfaces of the cylindrical sample volume. These grains were not fully contained in the irradiated volume of the specimen and were therefore removed from subsequent analyses.

5.3.1 Grain coarsening

Growth trajectories of 100 crystallites selected at random from samples S-70 and S-82 are traced in Fig. 5.6 next to plots of their respective mean grain radii and total number of grains. For sample S-70, the mean grain radius increases from 96 µm to 113 µm, while the number of grains decreases from 682 to 418. Similarly, in sample S-82, the mean radius grows from 99 µm to 112 µm, while the number of grains drops from 637 to 431. Accordingly, the size and dynamic range of both data sets are more than adequate to ensure a statistically significant evaluation.

When interpreting these growth data, one should bear in mind that grain sizes are exaggerated since they are determined from room-temperature measurements; and although mean grain sizes appear to be about the same in both samples, the grains of specimen S-70 must be smaller on average when heated to 630 °C, owing to the higher fraction of liquid phase. We may assume, however, that the repeated heating and cooling does not

[1] During configuration and testing of the experimental setup, sample S-82 was annealed once at 619 °C for 10 minutes before the first set of data was recorded. Thus, the two specimens do not have the exact same annealing history at the zero-minute mark of this study.

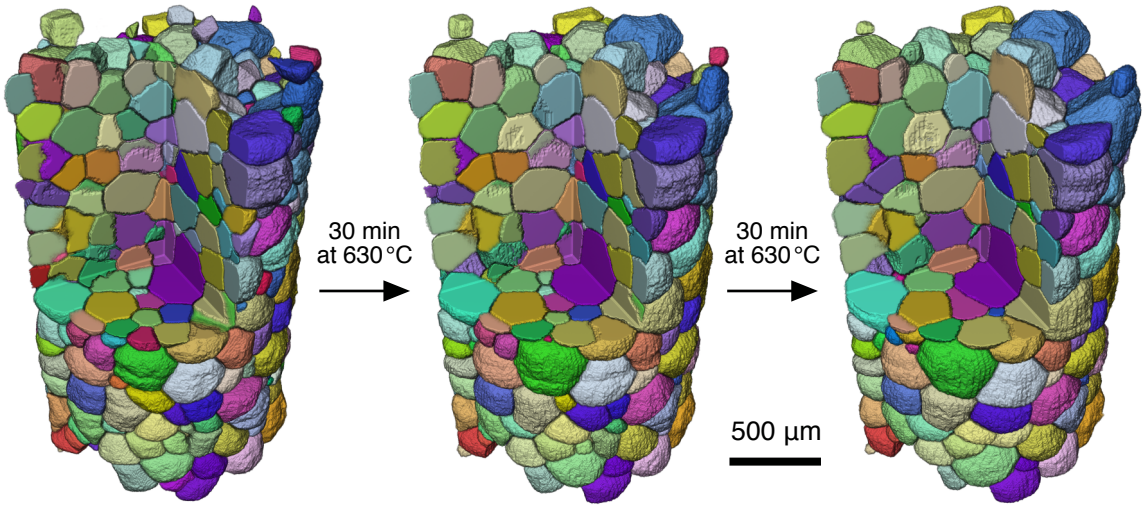

Figure 5.5: 3DXRD reconstructions of sample S-70. The size and distribution of grains is visible, and since grain colors are related to crystallographic orientation, an estimate of texture is also possible (cf. Fig. 4.3). The 3D microstructures of samples S-70 and S-82 appear qualitatively similar on this scale. Grains at the top and bottom of the sample were not completely captured and removed from the reconstructions.

introduce artifacts that significantly alter grain sizes between measurements. In other words, a grain that (apparently) increases in size because of solidification during cooling, returns to its previous size upon subsequent heating to the semisolid state. This is a safe assumption since the samples spend little time in the single-phase region during heating and cooling, which does not allow the Cu concentration to equilibrate. Instead, the higher fraction of Cu in the liquid phase freezes to form a dendritic structure of α and θ phases [62]. Thus, on the macro-scale, the distribution of Cu in the specimens remains essentially the same, and upon subsequent annealing the liquid phase will form most readily at its previous location. The smooth paths of the grain trajectories confirm this conjecture as well. Consequently, relative changes in grain size from one time step to the next are useful in describing coarsening kinetics.

From Fig. 5.6 (d) it appears that growth in sample S-82 was beginning to stagnate after three successive 10-minute anneals, and increasing the annealing interval, first to 15 and then to 30 minutes, seems to have accelerated the coarsening rate. The underlying cause of this behavior is most likely related to the transient effects associated with heating and cooling, which can lower the effective annealing temperature when intervals are short. Thus, the apparent acceleration in $\langle R \rangle$ for S-82 is more likely a return to the true coarsening kinetics that would otherwise govern if the sample were held at 619 °C without interruption. Such stagnation was not observed in sample S-70, probably because the annealing duration was increased with each successive heat treatment.

Ostwald ripening [170, 177] is conventionally assumed to be the dominant mechanism of coarsening during liquid-phase sintering. In 1961, Lifshitz, Slyozov and Wagner (LSW) developed a theoretical model to describe Ostwald ripening [178, 179], and although the LSW theory is valid only for vanishing volume fractions of the coarsening phase ($V_V \to 0$), it is still the standard analytic model for coarsening in two-phase systems, and it serves as a standard against which the present experimental data can be compared.

Growth rates calculated for the grains of samples S-70 and S-82 are plotted in Fig. 5.7

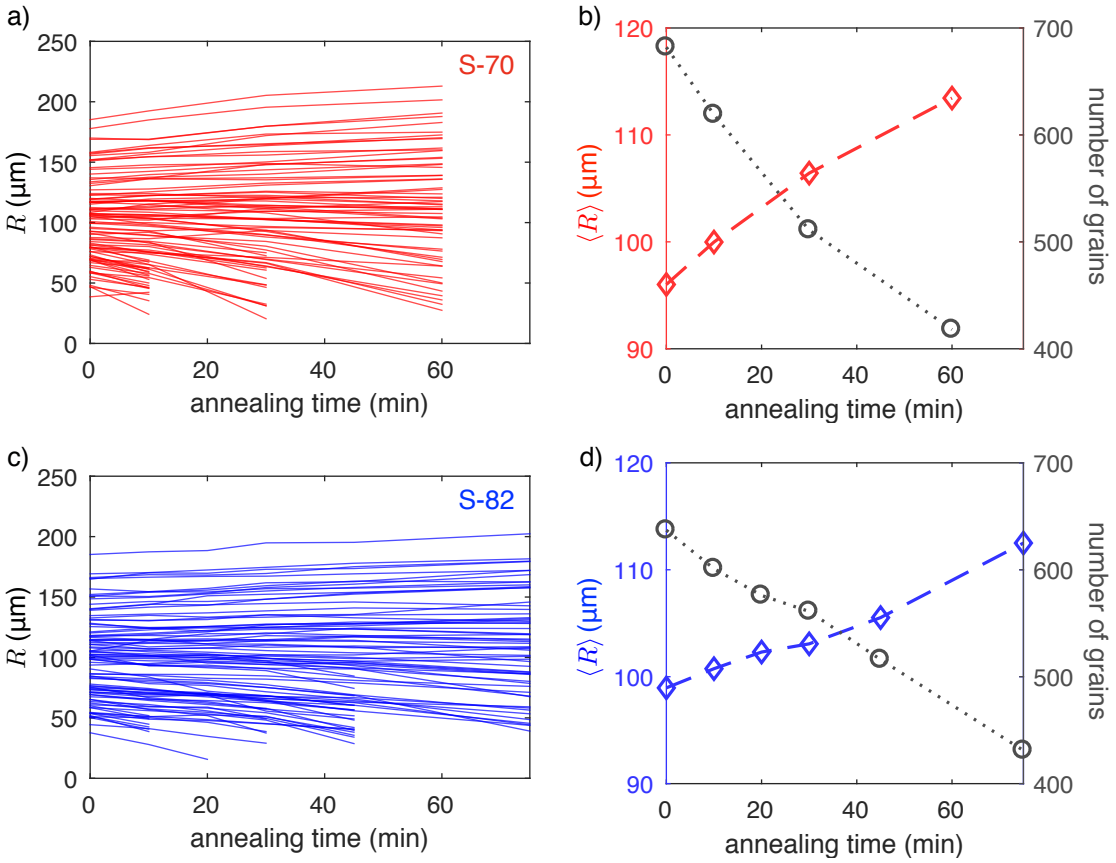

Figure 5.6: Coarsening in samples S-70 (red) and S-82 (blue). Growth trajectories are plotted for 100 grains chosen at random from (a) S-70 and (c) S-82. The evolution of the mean grain radius and number of grains is also given for (b) S-70 and (d) S-82.

against their normalized sizes. Fits of Eq. (2.20) to both data sets indicate that coarsening occurs about 1.6 times faster in S-70 than S-82. For both experiments, however, the straight-line fits do not appear to accurately model the dependence of growth rate on grain size. Contrary to the prediction of LSW, there is an upward curvature to the cloud of data points for both samples. Furthermore, the LSW theory predicts an upper limit of 1.5 for the distribution of normalized grain sizes. Obviously, there are many grains larger than this value in both specimens. Qualitatively similar deviations have been observed in experiments [62] and simulations [180, 279] for Ostwald ripening at higher volume fractions of the coarsening phase.

5.3.2 Grain rotation

Making use of the orientation data inherent to the 3DXRD technique, we can follow changes in grain orientation between annealing intervals, just as we did with the grain size. After a global registration of the data sets, any change in a particular grain's crystallographic orientation between time steps represents a rigid-body rotation of the grain that must have occurred during annealing.

To distinguish clearly between the similar quantities of rotation, orientation and misorientation, it is worthwhile to define the specific symbols that will be used to denote these quantities in this chapter. The orientation of any crystalline grain is given by the transfor-

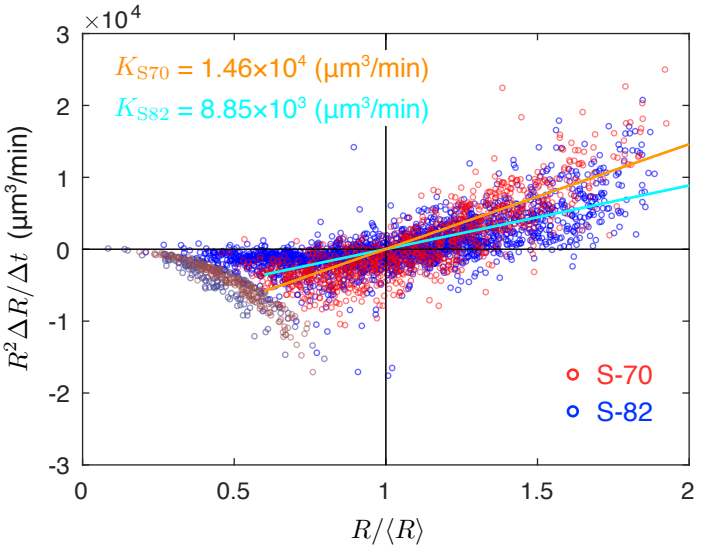

Figure 5.7: Growth rates vs. normalized grain size. According to the LSW theory, coarsening rates scaled by the grain size squared should display a linear relation when plotted against the normalized grain size. The actual scatter plots of $R^2\Delta R/\Delta t$ against $R/\langle R\rangle$ show a large amount of scatter and a slight upward curvature for both Al-Cu specimens. Fits of Eq. (2.20) to the data points indicate that the grains of sample S-70 coarsen on average slightly faster than do those of S-82.

mation required to rotate the axes of a reference coordinate system into the unit cell axes of the grain. In the axis-angle representation, the rotation angle of such a transformation is denoted by the symbol θ, which is inherently greater than or equal to zero. Grain rotations are determined by calculating changes in grain orientation from an earlier time step t_{n-1} to the next t_n and can also be described in axis-angle notation, but in this case the symbol $\Delta\theta$ is used to denote the (usually small) rotation angle. Again, this quantity is nonnegative. In a similar manner, the misorientation between two grains can be described as a rotation of the unit cell axes of one grain into those of the other. To distinguish orientation and misorientation relations, the latter are denoted by the rotation angle ϑ and changes in misorientation by $\delta\vartheta = \vartheta(t_n) - \vartheta(t_{n-1})$. Unlike $\Delta\theta$, the quantity $\delta\vartheta$ can take on positive or negative values.

The rotation $\Delta\theta$ (in degrees) from time step to time step for each grain in samples S-70 and S-82 is plotted against annealing time in Fig. 5.8 (a). All trajectories begin at zero, and, after each annealing step, $\Delta\theta$ is calculated relative to a grain's alignment at the end of the previous anneal, i.e., the current orientation θ_{t_n} is always compared to the previous $\theta_{t_{n-1}}$. Thus, a grain that rotates during the first annealing step and then retains exactly this new orientation following the next annealing interval, would have a trajectory with an initial positive slope that subsequently returns to zero. Careful inspection of the measured rotation trajectories, however, reveals that such stoppages in rotation rarely occur. Typically, a grain that begins to rotate continues rotating upon further annealing, often even accelerating.

Fluctuations in the measured grain orientations of a third, single-phase Al-1 wt% Mg sample (from Chapter 4) are also plotted in Fig. 5.8 (a) as the green rotation trajectories. This sample was scanned during the same beamtime with identical parameters for the 3DXRD experimental setup, and the same algorithms were used for its reconstruction,

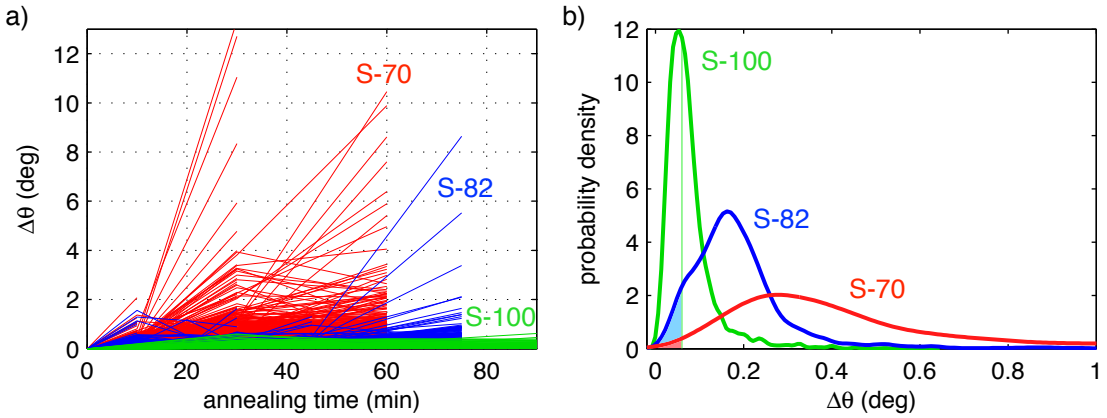

Figure 5.8: Trajectories and distributions of orientation changes. (a) Grain rotation trajectories, which are generated by plotting a grain's relative change in orientation $\Delta\theta$ after each heat treatment, show rotations up to 12°. The green trajectories, labelled S-100, are from the single-phase Al-1 wt% Mg sample discussed in Chapter 4; they provide a measure of the experimental accuracy. (b) Empirical probability densities of $\Delta\theta$ for all three samples reveal that the majority of rotations in the semisolid specimens S-82 and S-70 lie well above the experimental uncertainty.

registration and analysis. The grains of the Al-1 wt% Mg specimen (referred to as S-100, meaning 100% solid) are, however, not expected to actually rotate during annealing, since: (1) there is no liquid phase, (2) the grains are relatively large ($R \sim 100\,\mu$m) and (3) it was annealed at a moderate temperature of 400 °C (about 72% the melting temperature) [280, 281]. Thus, variations in grain orientation observed in this sample represent a measure for the accuracy with which crystallographic orientation can be determined repeatedly during *ex situ* annealing experiments. The median $\Delta\theta$ measured for S-100 was 0.06°, marked by the green vertical line in Fig. 5.8 (b). In this figure the experimental probability density of $\Delta\theta$ is plotted with the help of a normal kernel density estimator, and it is evident that the vast majority of rotations in both semisolid samples are substantially larger than the 0.06° detection limit. The median rotation is 0.17° for S-82 and 0.37° for S-70. Shaded in light blue and light red is the fraction of total rotations less than 0.06° in these two specimens. At values of $\Delta\theta$ higher than 0.06°, the possibility of measuring a false rotation, i.e., a non-zero $\Delta\theta$ for a grain that did not rotate, decreases rapidly, and we can confidently conclude that the majority of grain rotations observed in S-82 and S-70 are indeed true rotations.

To determine if measured rotations are greater than the experimental uncertainty, one must examine their absolute magnitude, but the better quantity with which to compare rotations between samples is the rate of rotation, since this quantity compensates for variations in the duration of the annealing intervals. The rotation trajectories above are, therefore, displayed again in Fig. 5.9 (a) as rotation rates. The trajectories of sample S-82, which initially underwent three short 10-minute anneals, are consequently magnified in this plot. By summing each rotation (as a rate) from smallest to largest, we obtain the cumulative probability functions of Fig. 5.9 (b). This graph shows a clear increase in the rate of grain rotation with greater amount of liquid phase.

We can also compare the rate of rotation to the normalized grain size as shown in Fig. 5.10. For both samples, there is somewhat of a constant background, seen as the horizontal cloud of points across all grain sizes. As expected, these so-called background rotations are somewhat greater for sample S-70, the sample with the more liquid phase. If,

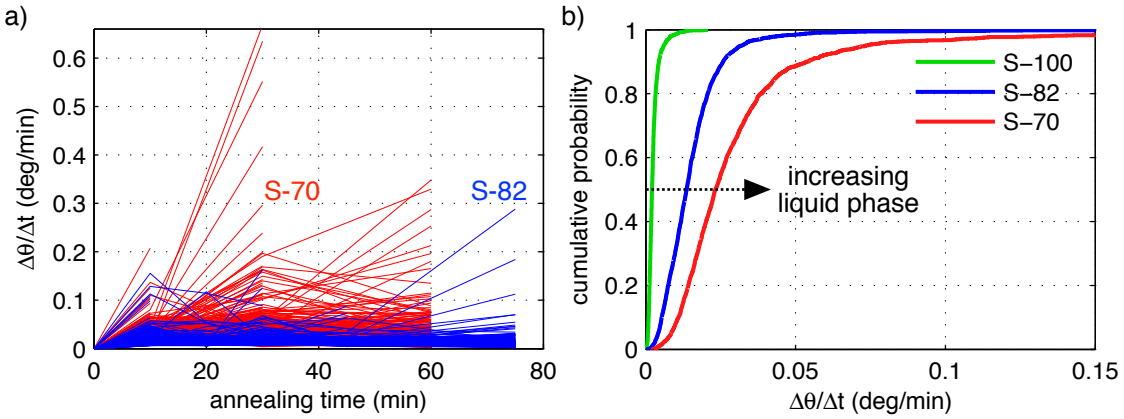

Figure 5.9: Grain rotation rates. (a) Plotting $\Delta\theta/\Delta t$ against annealing time normalizes differences in the duration of annealing intervals and helps to isolate the effects of the volume fraction on grain rotation. (b) The increase in rotation rate with the amount of liquid phase is clearly visible in the cumulative probability distributions of $\Delta\theta/\Delta t$.

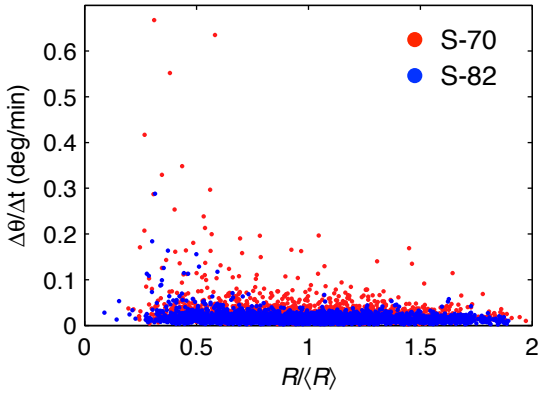

Figure 5.10: Rotation rates vs. normalized grain size. There appears to be a constant level of background rotations that are independent of $R/\langle R\rangle$ but increase with the amount of liquid phase. For values that deviate from this background, an inverse relationship exists between rotation rate and grain size.

however, we focus on the data points that deviate from the background level (above about 0.1°/min), we recognize that the vast majority of larger rotations is associated with grains that are smaller than the mean size. Apparently, a large rotation is more likely to occur the smaller a grain is. This inverse relation is not entirely unexpected—smaller grains have fewer direct neighbors to constrain their motion, are more spherical and typically have more liquid phase in their immediate vicinity [182]. These are all factors that encourage larger-than-average rotations. A detailed comparison of Fig. 5.9 (a) and Fig. 5.10 reveals that small grains experience a large rotation just before they cease to exist. Trajectories that terminate prematurely represent grains that have vanished from the sample. The largest three trajectories of sample S-70 correspond to the highest three red dots in Fig. 5.10; the associated grains were no longer present in the sample after the next 30-minute anneal.

5.4 On the mechanisms of grain rotation

5.4.1 Directed grain rotations

To shed light on the physical mechanisms behind the observed rotations, we begin by examining how grains rotate relative to their immediate neighbors. If gradients in grain boundary energy are responsible for rotations, then we can expect to find changes in misorientation ($\delta\vartheta$) that correspond to reductions in γ. The interfacial energy at the boundary between crystalline grains is a complex function of temperature, chemistry, orientation and the exact character of the interface [18]; surprisingly, although the topic represents a hot area of current research in materials science [95, 116, 118, 134, 282–285], there is no accepted model with which to estimate γ directly. The one notable exception is the deep cusp in energy at low-angle ($\Sigma 1$) boundaries, for which the analytic Read-Shockley dislocation model [104] is generally accepted and found to agree well with experimental data (see Section 2.1.2). Gradients in boundary energy also exist near some special twist and tilt boundaries [94, 96], and the former could certainly induce grain rotations in our samples, as well. But the exact shape (width and depth) of such cusps is not well understood, and some may even disappear completely at elevated temperatures [18, 94, 95, 261]. The following discussion is, therefore, limited to an analysis of grain rotations near low-angle boundaries.[2]

An example of a grain that undergoes a large rotation and also has a low-misorientation neighbor is displayed in Fig. 5.11. During the final 30-minute anneal of specimen S-70, the lower grain of the two depicted in this image rotates by 5.4°, thereby reducing its misorientation with respect to the upper grain by 2.7°. It seems likely that a reduction in boundary energy was at least partially responsible for this rotation. The plausibility of this explanation, however, hinges on the presence of a solid/solid interface between the two grains, since a liquid layer would effectively neutralize any dependence of γ on ϑ. In other words, two grains must first come into contact with each other before they can experience a rotational torque. A "dry" boundary can form when the excess energy of the solid-solid interface is smaller than the energy required for two solid-liquid interfaces. The CT micrograph in Fig. 5.11 (c) reveals the distribution of the Cu-rich phase at the shared boundary. The Cu-rich phase, which appears light gray to white in this image, decorates most of the boundaries. The boundary denoted by red arrows is the common boundary between the two green grains shown in Fig. 5.11 (a,b) and is only partially delineated by the solidified liquid phase. Although not completely conclusive (because the CT data were captured at room temperature and not 630 °C), it is certainly plausible that the two grains remained in contact upon heating and the reduction in boundary energy influenced the rotation.

To substantiate the conjecture that the gradient in boundary energy near low-angle misorientations can drive grain rotations, we now look at similar grain pairs throughout the entire volume of both specimens. Because effects related to repeated melting and solidification tend to convolute the analysis, only rotations from the final 30-minute anneals are included. (This constituted the longest annealing interval and equal in duration for

[2] In the previous chapter the cutoff angle between low and high-angle grain boundaries was set at 20°. The choice of this value was based on the distribution of orientations and misorientation in the Al-1 wt% Mg specimen. In the literature, values ranging from 10° to 30° can be found for the cut-off, but 15° is by far the most common [18, 29, 109]. The Al-5 wt% Cu specimens exhibit only a weak Cube texture and have misorientation distributions that are similar to the Mackenzie distribution. Therefore, in this chapter I use the conventional 15° limit.

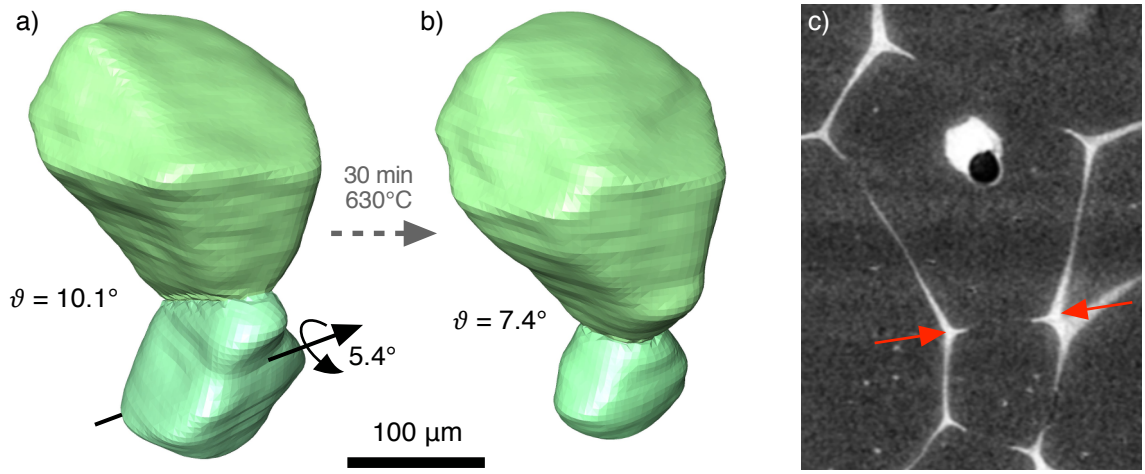

Figure 5.11: Example of rotating grain in sample S-70. During the 30-minute anneal at 630 °C, the lower grain in (a) rotates 5.4° about the specified axis to its final position in (b). A CT micrograph through the two grains in (c) reveals that their common boundary, denoted by red arrows, is not entirely decorated by the solidified Cu-rich liquid phase. Author's own figure from Ref. [218], Copyright © 2016 National Academy of Sciences.

both specimens.) In sample S-70 there are 72 unique pairs of grains with a single low-ϑ neighbor that remains after annealing, i.e., the grains of these pairs are nearest neighbors both before and after the final heat treatment. Similarly, 65 grain pairs with $\vartheta < 15°$ are included in the analysis of sample S-82. A clear reduction in misorientation is observed for both samples, as seen in the histograms of $\delta\vartheta$ in Fig. 5.12 (a,b). Since the change in misorientation is calculated as $\delta\vartheta = \vartheta_{\text{final}} - \vartheta_{\text{initial}}$, a negative value indicates that the misorientation between a pair of neighboring grains has gotten smaller. For S-70 the average value of $\delta\vartheta$ is -0.25°, while for S-82 the mean is -0.067°. If misorientation relations are ignored and grain pairs selected at random, much more symmetric distributions of $\delta\vartheta$ are found (Fig. 5.12 (c,d)). Apparently, most rotations are just as likely to increase the misorientation as they are to decrease it between neighboring grain pairs.

The significance of the negative skew of $\delta\vartheta$ can be determined by applying the Student's t-test [286]. If we assume that the two symmetric histograms of 500 plus randomly selected grain pairs represent the respective parent populations, the Student's t-test gives the probability of generating the histograms of low-ϑ grain pairs through a process of random selection from the respective parent population. This statistical test is defined as

$$t = \frac{\bar{x} - \mu}{SD/\sqrt{N}}, \tag{5.3}$$

where $\bar{x}$ is the sample mean, μ is the expected mean, SD is the sample standard deviation and N is the number of samples. For S-70, the test returns $t = -3.14$, which translates to a probability of 0.1%. Thus, the null hypothesis—the assumption that the 72 low-ϑ grain pairs have the same mean as the parent population—can be rejected with 99.9% certainty. The null hypothesis can also be rejected with comparable certainty (99.3%) for S-82.

Evidently, grain pairs with a misorientation less than 15° do, on average, rotate to reduce the misorientation at their common interface. This observation provides compelling evidence for the existence of energy-induced grain rotations, but it accounts only for the direction of rotation and not the rate of rotation, which we can also examine. Similar to how the migration rate of a curved grain boundary depends on capillary pressure (see

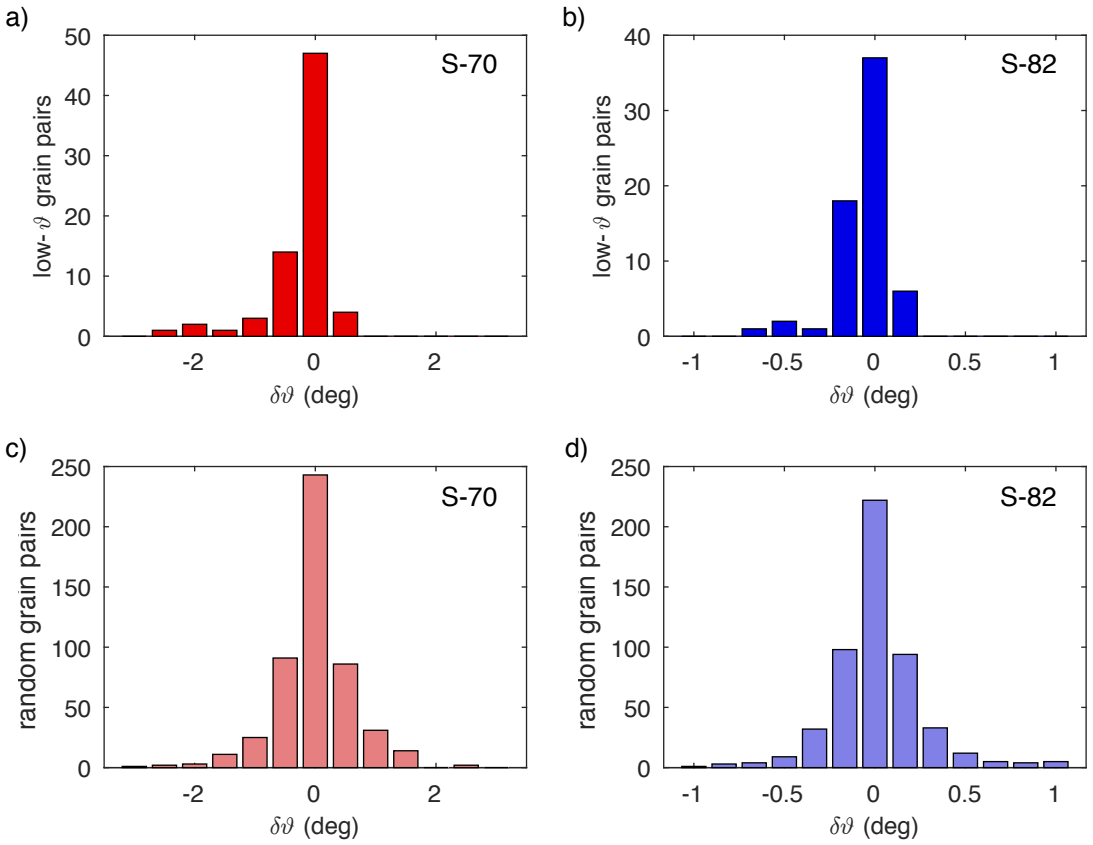

Figure 5.12: Distribution of misorientation changes for low-ϑ and randomly selected grain pairs during the final 30-minute anneal. The distribution of $\delta\vartheta$ for the low-misorientation grain pairs in (a) sample S-70 and (b) sample S-82 reveals a skew to negative values. These grain pairs tend to rotate so as to reduce their misorientation. On the other hand, when grain pairs are selected at random, the distributions of $\delta\vartheta$ are symmetric and centered at zero for both (c) S-70 and (d) S-82.

Eqn. (2.9)), the rate at which a grain rotates is directly proportional to the net torque acting at its perimeter [287]. For a grain with multiple solid-solid contacts, the net torque is the sum of all torques that arise at each grain boundary. In a randomly textured single-phase material, the average net torque is expected to be close to zero, since the individual contributions are randomly aligned and thus tend to cancel each other out. However, in the semisolid Al-Cu specimens under investigation here most grain boundaries are wet by the liquid phase (cf. Fig. 5.3), and since the grain pairs considered in our analysis have exactly one low-misorientation neighbor, it is plausible that these low-ϑ boundaries are the only dry boundaries of each pair. Under this assumption, the torque τ at the dry interface simplifies to

$$\tau = A\frac{d\gamma}{d\vartheta}, \tag{5.4}$$

where A is the boundary area and $d\gamma/d\vartheta$ the energy gradient. The rotation rate is then given by

$$\frac{d\vartheta}{dt} = M_r\tau = M_r A\frac{d\gamma}{d\vartheta}, \tag{5.5}$$

with the proportionality constant M_r denoting the rotational mobility. Shewmon derived an analytic expression for M_r for the case of a spherical grain forming a single grain boundary with a plate of the same material (Fig. 5.1) [258, 288]. He assumed that any change in free energy resulting from $d\vartheta$ goes into moving atoms across the common boundary by

lattice diffusion so that a crack does not open up during rotation. Shewmon's sphere-on-plate model is directly transferable to the case of two spherical grains in contact with each other, and, with his expression for M_r, Eq. (5.5) can be rewritten as

$$\frac{d\vartheta}{dt} = \frac{8 D_L \Omega}{k_B T a^3} \frac{d\gamma}{d\vartheta}, \tag{5.6}$$

where D_L is the lattice diffusion constant, Ω the atomic volume, k_B the Boltzmann constant, T the absolute temperature in Kelvin and a the radius of the contact area.

As a first approximation for the energy gradient, we can assume that γ increases linearly from 0 mJ/m^2 at 0° to 460 mJ/m^2 at 15° [116], which returns a value of $d\gamma/d\vartheta \approx 30.7$ mJ/(m^2 deg). Quantities for the diffusion constant and atomic volume at $T = 630\,$℃ can be taken from the literature [289], and a is estimated to be about 30 µm from examination of the grains pairs in the CT reconstructions. With these values, the application of Shewmon's model predicts a rotation rate of 0.003°/min for sample S-70. Thus, during the 30-minute anneal, we would expect low-angle grain pairs to reduce their misorientation by 0.09°, which is less than half of the observed value of −0.25°/min. The same calculation can be repeated for sample S-82 by replacing D_L and Ω with their respective values at 619 ℃. In this case the theoretical (-0.07°) and mean measured (-0.067°) rotations over 30 minutes are nearly identical. Given the difficulty in accurately estimating the contact radius from room temperature CT data and the strong dependence of $d\gamma/d\vartheta$ on a, the agreement between theory and experiment is remarkably good for both specimens.

5.4.2 Random grain rotations

The previous analysis indicates that the boundary energy landscape plays an instrumental role in driving grain rotations in semisolid Al-Cu alloys. However, this mechanism applies only to grains near steep gradients in γ. Most grains do not have nearest neighbors with misorientations near cusps in γ, and most rotations are just as likely to result in an increase as in a reduction in misorientation with respect to any given neighboring grain (see histograms in Fig. 5.12 (c,d)). These aspects suggest the presence of an additional random component to the observed rotations.

One obvious source of random rotations is the repeated melting and solidification associated with interrupted annealing experiments. Upon heating an Al-5 wt% Cu alloy into the two-phase region, small pockets of liquid form, which, given time, eventually coalesce and spread throughout the specimen (until equilibrium volume fractions of solid and liquid phases are achieved). This expansion and flow of liquid induces capillary forces that can cause grain rotations [290]. Likewise, heterogeneous nucleation and asymmetric neck formation during solidification are capable of giving rise to fluctuations in grain orientation [267]. Furthermore, because samples are removed from the furnace in the semisolid state, vibrations from handling may also cause a slight rearrangement of grains.

All of the above effects are time invariant in the sense that they depend only on the number of transitions from the solid to the semisolid state (and vice versa) and not on the duration of annealing intervals. For this reason it was somewhat surprising to see the distribution of random grain rotations broadening with annealing time (Fig 5.13). After each annealing interval, the change in misorientation for all nearest-neighbor grain pairs can be calculated and used to generate a histogram of $\delta\vartheta$, like those seen in Fig. 5.12 (c,d). Although the mean of each distribution is centered at zero, they become wider as the duration of heat treatments increases. This effect is visualized in Fig 5.13, where the

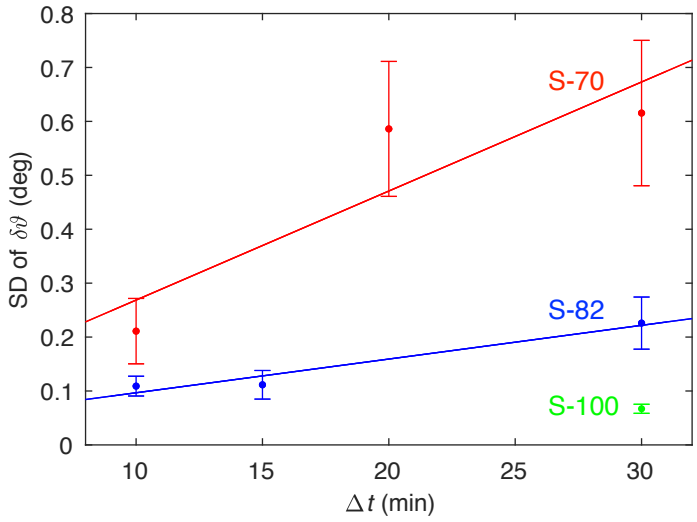

Figure 5.13: Standard deviation (SD) of $\delta\vartheta$ plotted against the duration of annealing intervals. After each heat treatment, the change in misorientation for all neighboring grain pairs is calculated and used to calculate histograms of $\delta\vartheta$, similar to those of Fig. 5.12. Although these distributions remain centered at zero, their width increases with the length of the annealing interval, indicating that a time-dependent mechanism must be responsible for at least some of the random rotations. (All rotations from the three 10-minute anneals are included in the first data point for S-82.)

standard deviation (SD) is used to quantify distribution widths. Evidently, there must also be at least one time-dependent mechanism, generating progressively larger grain rotations during isothermal annealing.

Random grain rotations may well be an inherent side effect of microstructural coarsening in semisolid specimens. For example, when a grain vanishes the liquid that once wet its boundaries can be redistributed throughout the specimen. This process is likely associated with a slight rearrangement of the solid-phase grains, similar to the rearrangements that occur during the early stages of liquid-phase sintering, but smaller in magnitude [264, 291]. Neighbor switching events that cause perturbations in capillary pressure—which among other things depends on wetting angle, grain size and interparticle spacing [292]—are also capable of altering the local arrangement of grains. Likewise, the reduction in residual porosity [293] and/or the escape of liquid trapped in grain interiors (the latter was observed in *in situ* experiments by Werz [182]) can bring about temporary imbalances in capillary pressure. In systems where the density difference between solid and liquid phases is large, a sedimentation or hydrostatic uplifting of the solid grains results in a repacking of grains [278, 294, 295]. This phenomenon, often referred to as slumping in the liquid-phase sintering community, is not expected to be relevant in Al-5 wt% Cu samples, since density differences are minimal (about 1% at 630 °C [296]). Furthermore, because of the way in which $\delta\vartheta$ was calculated—from each neighboring pair of grains—this quantity is not sensitive to a collective movement of grains.

Brownian motion is another factor capable of contributing to random fluctuations in grain orientation. Although this phenomenon is most commonly used to describe the motion of molecules, macromolecules and colloids on the submicron and micron scales [297–299], there are no fundamental physical reasons that it could not apply to the relatively large grains ($R \approx 100\,\mu\text{m}$) of these two Al-Cu samples as well. In fact, translational

Brownian motion has often been cited as a mechanism behind the formation of particle contacts during semisolid materials processing [278, 300]. The only prerequisite is that observation times are much greater than the characteristic time constant $\tau = I/\zeta$. In this case, a suspended particle's interactions with the liquid medium can be described stochastically [301]. ζ is the viscous drag coefficient for a particle rotating in a liquid medium and, assuming spherical grains, calculated as $\zeta = 8\pi\eta R^3$, where η is the viscosity of the liquid phase [298]. Values of η from the literature [302] allow us to estimate a time constant τ of about 1 ms for both Al-5 wt% Cu samples. Thus, with annealing intervals of 10 to 30 minutes, rotational Brownian motion could certainly play a part in random grain rotation.

5.5 Concluding remarks on grain rotation in semisolid materials

The results presented in this chapter confirm the hypothesis that gradients in grain boundary energy are capable of driving grain rotations during the sintering of bulk crystalline materials. In the case of semisolid samples (representative of liquid-phase sintering), such rotations are observed at grain pairs that share a low-angle boundary. The steep gradient in γ at small misorientation angles ($\vartheta < 15°$) generates a torque that leads to further reduction in misorientation through rigid-body grain rotation. Mean rotation rates observed at such grain pairs are consistent with the theoretical predictions of Shewmon [258]. This mechanism is presumably facilitated by the presence of a liquid phase, which wets most grain boundaries and reduces the number of solid-solid grain contacts. But the liquid phase does more than enable directed rotations: it also generates random fluctuations in grain orientation. This second mode of grain rotation appears not only to be connected to phenomena associated with coarsening but also quite to Brownian motion. The random variations in grain orientation are more constrained at high volume fractions of the solid phase, but they increase in magnitude with the amount of the liquid phase. The two modes of grain rotation—directed and undirected—are interrelated to the extent that random rotations allow a grain to sample more of its orientation space, thereby promoting the formation of the low-energy grain boundaries that are conducive to energy-driven rotations.

Both of the semisolid Al-Cu samples of this investigation were fully compact and displayed only minimal crystallographic texture. In the earlier stages of sintering, where densities are significantly lower and particle rearrangements quite common, energy-driven rotations are expected to be more prevalent. Likewise, in samples with high crystallographic texture (a feature that promotes the formation of low-misorientation grain boundaries as we saw in Chapter 4) the magnitude and frequency of energy-driven rotations might also be higher than those observed above. Among metals, Al is characterized by rather moderate variations in boundary energy. Much deeper cusps in γ have been found, for example, in Cu and Ni-based alloys [118]. Consequently, larger torques and higher rotation rates would be expected in the latter cases. With the importance of sintering and semisolid materials processing on the rise—in applications such as additive manufacturing [303, 304] and the production of materials for energy storage [305, 306]—the need for accurate sintering models is also increasing. Evidently, to achieve this objective, the rigid-body rotation of grains is a phenomenon that will have to be taken into account.

6

General Discussion and Conclusions

As is often the case with technical innovations, humans were using microstructure to enhance material properties long before the cellular nature of crystalline solids and the existence of grain boundaries were discovered. Well-known examples include steel swords forged in the Middle Ages [307] and porcelain sintered in ancient China [275]. Much more important than the raw iron or clay materials used for the production of these materials were the thermomechanical methods used to modify their microstructures, and the crafts behind these empirically developed processing techniques were carefully guarded trade secrets, meticulously passed down from one generation to the next.

Today, despite decades of research, the characterization and control of microstructure remain hot topics of scientific research, because as our knowledge of microstructure has grown, so has our understanding of its decisive influence on a broad range of physical and mechanical properties. Analytic theories have been developed to describe the migration of grain boundaries and the evolution of microstructure in two and three dimensions. Likewise, numerous algorithms have been written to simulate coarsening phenomena on a computer. However, one aspect of the investigation of microstructure has remained elusive: namely, the experimental characterization of coarsening in 3D. Closing this particular gap in our understanding of microstructural evolution served as the motivation for my work, and, with the knowledge gleaned from the preceding chapters, I now answer the three general questions posed in the Introduction.

6.1 Practical suitability of 3DXRD microscopy for coarsening investigations

The promise of 3DXRD microscopy is straightforward: it enables single-phase polycrystalline materials to be characterized nondestructively. Through repeated application of this measurement technique, one obtains dynamic 3D data with full spatial and orientation information. Such data sets provide researchers an opportunity to study the migration of individual grain boundaries in their native environment, i.e., away from free surfaces and without marker phases. But, like all experimental methods, 3DXRD microscopy also has

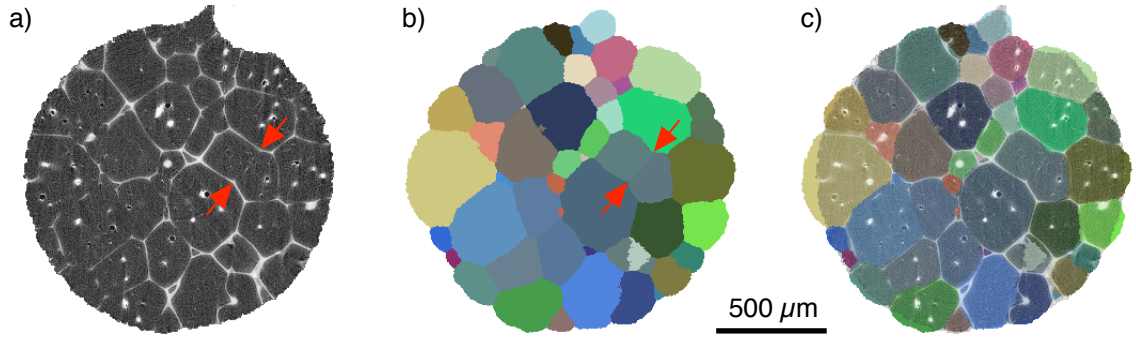

Figure 6.1: Comparison of CT and 3DXRD reconstructions. Registered cross sections through (a) CT and (b) 3DXRD reconstructions of the Al-Cu sample S70 are compared side by side. Red arrows indicate a low-angle grain boundary that was not clearly marked in CT but accurately located in the 3DXRD grain map. (c) The overlay of both slices confirms the good overall agreement between the two methods. Pores and second-phase inclusions are not detected by 3DXRD.

its own practical limitations. For this reason I first give a pragmatic answer to the question:

Is 3DXRD microscopy a suitable technique for experimental investigations of grain growth?

The minimum spatial resolution of a 3DXRD data set is given by the pixel size of the detector that is used to capture near-field diffraction images (4.56 µm for the data sets in this thesis). This denotes the lower limit for the voxel size, but it does not necessarily tell us how accurately the interfaces between grains are located. During the reconstruction procedure many different thresholds and cut-offs are applied, all of which affect the accuracy of the final reconstructed volume to various degrees. For single-phase materials there is no method other than 3DXRD to map the 3D microstructure of a polycrystal nondestructively. However, the two-phase Al-Cu alloys of the previous chapter can be mapped by both 3DXRD and standard CT, since the liquid phase wets most grain boundaries and provides absorption contrast. By comparing the outputs of these two methods, we not only learn about the accuracy of grain boundary placement in 3DXRD reconstructions but also about some of the strengths and weaknesses of the method itself.

Cross sections from registered CT and 3DXRD reconstructions are compared side by side in Fig. 6.1. The higher concentration of Cu in the θ-phase that decorates most of the Al grain boundaries is visible as the light gray to white regions in Fig. 6.1 (a). In the context of James Cole Shatto's master thesis [308], much effort was invested into a statistical comparison of CT and 3DXRD reconstructions. The original idea was to use the CT reconstructions as a control against which 3DXRD reconstructions could be tested. Ultimately, this attempt proved unfruitful, owing to the difficultly of segmenting the CT data. Many obvious over and under-segmentations were observed. An example of an under-segmented grain is indicated by the red arrows in Fig. 6.1. Triple junctions are discernible near the tips of the arrows, but the low-misorientation boundary that is actually present here is not wetted by the θ-phase and is therefore not present in the segmentation of the CT data. On the other hand, all of the boundaries marked by the θ-phase were also observed in the 3DXRD reconstruction, and the overlay of both cross sections shows that the locations of internal boundaries in the two reconstructions are essentially identical. In the end, it was determined qualitatively that 3DXRD reconstructions provide a much more accurate segmentation of the grains in these data sets than do watershed-based algorithms applied to CT reconstructions.

A few artifacts of the 3DXRD reconstruction are, however, visible in the superimposition of Fig. 6.1 (c). First, the size of some surface grains is larger in the 3DXRD reconstruction.[1] These expand into the empty space beyond the perimeter of the specimen. This artifact is the result of the relatively low completeness threshold (0.7) chosen during the execution of GrainSweeper, but when higher thresholds were used, the reconstructions were no longer fully compact. Evidently, this artifact does not impair the placement of internal grain boundaries, since the orientation with the highest completeness value is always assigned when two crystallites compete for the same voxel in the reconstructed volume. At the edges of the sample there is no competition between grains; consequently, surface grains tend to appear larger than they actually are.

The second discrepancy in the superimposed image (Fig. 6.1 (c)) is the lack of inclusions in the 3DXRD reconstruction, which are clearly visible as white spots in the CT cross section. Because these inclusions belong to the θ-phase, they were neither indexed by the 3DXRD peak-searching algorithms, which were calibrated to only consider diffraction peaks from the Al lattice, nor mapped as separate grains. The intensity of a diffracted signal is proportional to the scattering volume. Thus, grains with inclusions larger than the resolution limit will have local minima in their corresponding diffraction spots. However, diffraction images were binarized during the reconstruction procedures, and, as a result, even large inclusions did not appear in the final reconstructions. For the investigation of single-phase materials, this complication is naturally irrelevant, but it does highlight a weakness of 3DXRD microscopy: it is difficult if not impossible to detect small, second-phase particles (including voids) using the technique. Although not necessarily the case here, the main problem in detecting second-phase particles or voids is that they are simply too small. Both crystalline and amorphous second-phase particles are frequently added to commercial alloys to slow grain growth [309], but these inclusions are often one or more orders of magnitude smaller in size than the primary grains of the material. With the box-beam realization of 3DXRD microscopy and the reconstruction algorithms developed for this thesis, small inclusions or voids will not be detected.

This discussion brings us to the more general topic of detectable grain sizes. Hard limits are given by the detector resolution on the lower end and by the beam width on the upper end. These limits apply to 3DXRD configurations with parallel-beam geometry. (Although resolutions as low as 150 nm have been achieved with focusing geometry [310], such setups are extremely tedious to align and are able to scan only individual grains, underming their usefulness for statistical studies of grain growth.) In the experience of the author, grains can be mapped reliably when their diameters are at least 3–4 times the detector's pixel size. Of course, this value will vary depending on experimental equipment, but for the equipment at SPring-8's beamline BL20XU, the criterion translates to a minimum grain diameter of 15 to 20 µm. The average size of a (lognormally distributed) grain ensemble should be approximately twice this minimum value to ensure that the majority of grains are detectable. Thus, $\langle D \rangle = 40\,\mu\text{m}$ can be taken as the lower practical limit on the mean grain diameter. At the upper end of the grain size spectrum, there are no technical restrictions on mapping large grains or even single-crystalline samples. When the grains of a specimen become too large, however, it becomes irrational at some point to conduct coarsening experiments. One could argue that this point is reached when a majority of a specimen's grains make contact with a free surface. Assuming spherical grains and a cylindrical sample, the 50% threshold is reached when the mean grain radius is about one-tenth the sample radius, as demonstrated in Fig. 6.2. Using the setup at BL20XU again as a reference, 1.6 mm is the maximum beam width, which also determines the maximum sample

[1] This effect is more prominent with larger grains because these tend to oversaturate the detector.

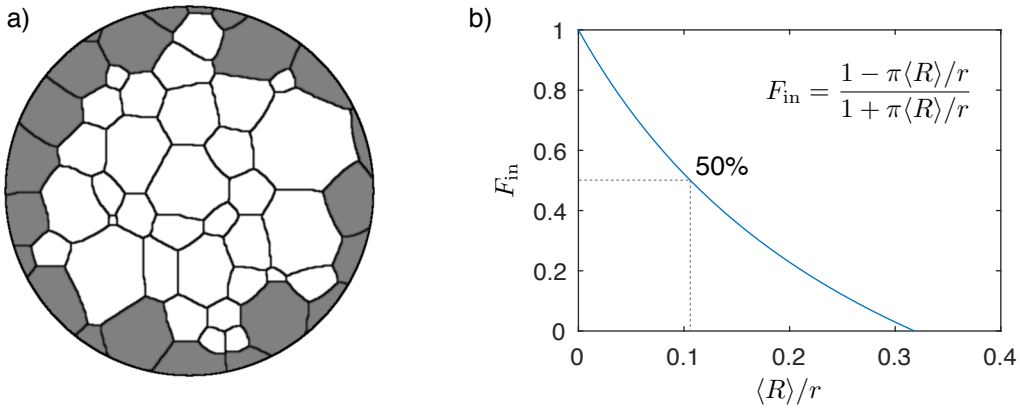

Figure 6.2: Fraction of internal grains. (a) Grains that are in contact with free surfaces (shaded gray here) can alter the coarsening kinetics and should not dominate the population of total grains. (b) When the ratio of the mean grain radius $\langle R\rangle$ to the sample radius r has reached $1/(3\pi)$, the fraction of internal grains is about 50%. At $\langle R\rangle/r = 1/\pi$, all of the grains are expected to be surface grains.

diameter. If one desires to stay below the 50% surface-grain threshold, the maximum grain diameter is about 160 µm. When this limit is exceeded, as in Fig. 4.4 (b), growth rates can slow significantly owing to the pinning of grain boundaries at free surfaces. Still, a broad size range ($40 < \langle D\rangle < 160$ µm) is available for coarsening investigations.

In summary, 3DXRD microscopy is well suited for experimental studies of grain growth. With the box-beam implementation of this technique, it is possible to map a large number of grains in a relatively short time over a considerable range of grain sizes. Stitching overlapping reconstructed layers together allows one to characterize thousands to tens-of-thousands of contiguous grains in a single coarsening experiment. A repetitive indexing and refinement scheme proved effective in mapping low to moderately textured materials. For more highly textured materials, precautions should be taken to reduce the overlap of diffraction spots. With multi-phase materials CT can be employed to obtain complementary characterizations of the microstructure. Moreover, for multi-scale investigations, 3DXRD is ideally suited to finding grain boundaries of interest, which can be examined subsequently by high-resolution electron microscopy techniques. As 3DXRD continues to mature, exciting studies of microstructure evolution will most certainly follow.

6.2 Applicability of isotropic models

In 1961 Lifshitz, Slyozov [178] and Wagner [179] developed a mean-field model to describe Ostwald ripening in two-phase materials. Using this theory as a starting point, Hillert [16] derived his mean-field model for grain growth four years later. Hillert's theory was able to predict the growth rate of individual grains as well as the shape of a grain size distribution that evolves in a self-similar manner. In 2007, MacPherson and Srolovitz [225] achieved a significant breakthrough in the analytic description of microstructural evolution when they managed to extend the von Neumann-Mullins relation [222, 223] from two to three dimensions. Parallel to the development of analytic theories, computer simulations became a powerful tool for the investigation of grain coarsening. The latter development was greatly aided by advances in numerical methods and computing power, but it also came about out of necessity, since access to 3D experimental data was practically nonexistent. With

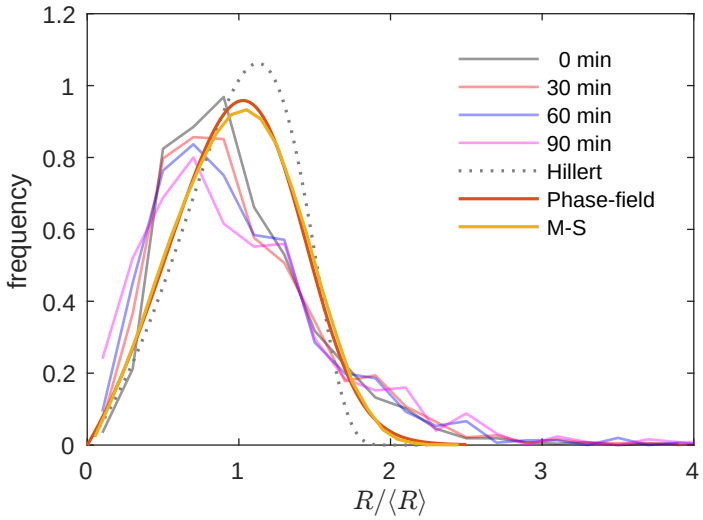

Figure 6.3: Comparison of experimental grain size distributions against those predicted by isotropic models/simulations. Four experimental grain size distributions from the 400 °C annealing sequence of the Al-1 wt% Mg specimen are plotted alongside the Hillert distribution [16] as well as the grain size distributions from a large-scale isotropic phase-field simulation [28, 311] and from a front-tracking simulation optimized to match the MacPherson-Srolovitz (M-S) relation [25, 237]. Although the experimental data agree with the simulated distributions slightly better than they do with the Hillert distribution, none of the predictions fit the measured data well.

the 3D experimental data presented in the preceding chapters, we can now compare the predictions of established theories and simulation algorithms to coarsening data obtained from real specimens. This brings us to the second question posed in the Introduction:

Do isotropic growth models describe coarsening in real polycrystalline samples?

The anisotropy of grain boundaries in crystalline materials is well established [18, 95] and also apparent in the results of this thesis (cf. Fig. 4.21). Nevertheless, isotropic growth models are ubiquitous, and the microstructures produced by such models form the canonical basis for 3D microstructural investigation [237]. One measure of microstructure that is easy to conceptualize is the distribution of grain sizes. In Fig. 6.3 experimental grain size distributions obtained for the single-phase Al-1 wt% Mg specimen presented in Chapter 4 are compared to the Hillert distribution as well as to the output of two isotropic computer simulations. The first is a phase-field simulation [28], and the second is a front-tracking method that was optimized to fit the MacPherson-Srolovitz relation [237]. The grain size distributions of the two simulations are very similar to each other, generating noticeably wider distributions than Hillert's model, yet the discrepancy with respect to the four experimental distributions is still significant.

Hillert's model, which assumes that each grain is embedded in the exact same mean environment, ignores topological constraints imposed on the grains of a space-filling polycrystal [14]. Therefore, we should not be surprised that his distribution of normalized grain sizes shows the largest deviation. On the other hand, both the phase-field and front-tracking methods do capture the full shape and local neighborhood of all grains included in the simulation volume, but their distributions match the experimental data only slightly better than Hillert's. It is important to note here that the grain size distributions of the two simulation methods are taken from the steady-state coarsening regime, where geometrical

and topological measures of microstructure remain statistically similar as the mean grain size increases. The experimental distributions are obviously not time invariant: the relative frequencies of both small and large grains increase over the course of the 400 °C annealing sequence. It is a somewhat unexpected finding that the experimental grain size distributions move away from—rather than toward—the steady-state prediction. Depending on the initial microstructure, however, isotropic simulations may also exhibit a transient regime, in which grain distributions vary with time [311]. Thus, the more fair comparison between experiment and simulation would be to start from the same initial grain configuration in both cases. Because we now have access to time-resolved 3D data, we can do exactly this!

In Fig. 6.4 a slice through the experimentally determined Al-1 wt% Mg microstructure is juxtaposed with the same section through two different phase-field simulations [312, 313]. The first is an isotropic simulation with completely uniform grain boundary properties, whereas the second implements a simple approximation for the anisotropy of grain boundary energies. The energy of high-angle grain boundaries is the same in both simulations ($\gamma = 1\,\mathrm{J/m^2}$). The difference between the two models arises at low misorientations ($\vartheta < 20°$). In the isotropic case, the grain boundary energy remains constant, but it follows a Read-Schockley relation (Eq. (2.6)) in the anisotropic simulation. Discrepancies between the experimental microstructure and the output of both simulations become more apparent at longer annealing times. Although neither simulation is able to reproduce the experimental data accurately, the simple anisotropic model performs noticeably better.

A comparison of growth trajectories and rates from the different simulations is also revealing. The plots in Fig. 6.5 (a,b) reproduce the experimental data presented in Chapter 4. Below each graph are the results of the isotropic (Fig. 6.5 (c,d)) and anisotropic (Fig. 6.5 (e,f)) simulations. The simulations have been rescaled so that the simulation times match the annealing intervals, and, to make the comparison fair, the growth rates were calculated exactly like they were for the simulation, i.e., at 30-minute intervals using the central difference. Although the growth trajectory plots are quite crowded, there is almost no intersection of trajectories in the isotropic case, while trajectory crossings occur much more frequently in the anisotropic case. The effect of this behavior can be observed in the scatter of the growth rate plots. A Hillert fit with prediction bounds (90% confidence) is added to each scatter plot to aid in comparison. The anisotropic simulation results in grain growth rates that show much more scatter about the Hillert prediction than do than those of the isotropic simulation. When this result is viewed in combination with the micrographs of Fig. 6.4, we can confidently conclude that the anisotropic simulation does a significantly better job of reproducing the actual coarsening that occurred in the real Al-Mg polycrystal.

In answering this second question, I have focused on grain growth in a single-phase Al-Mg sample, but the conclusions can be readily extended to the semisolid Al-Cu samples as well. Although the liquid phase present in the latter acts to equalize variations in interfacial properties, grains with boundaries that were not wetted by the liquid tend to coarsen with significantly different kinetics (generally much slower). Werz [182] addressed this feature in detail as part of his thesis work, in which he used micro-CT to capture time-resolved *in situ* mappings of microstructures from the same Al-Cu alloy that was investigated in Chapter 5. When directly comparing his experimental results to an isotropic phase-field simulation for Ostwald ripening, Werz found the largest discrepancies at grains that were in direct contact with one or more neighboring grains, i.e., at unwetted boundaries. Evidence for the occurrence of unwetted grain pairs was also found in this thesis (cf. Figs. 5.11 and 6.1). At higher volume fractions of the coarsening phase, the chance that neighboring grains come into direct contact with each other increases, and this effect, which is not

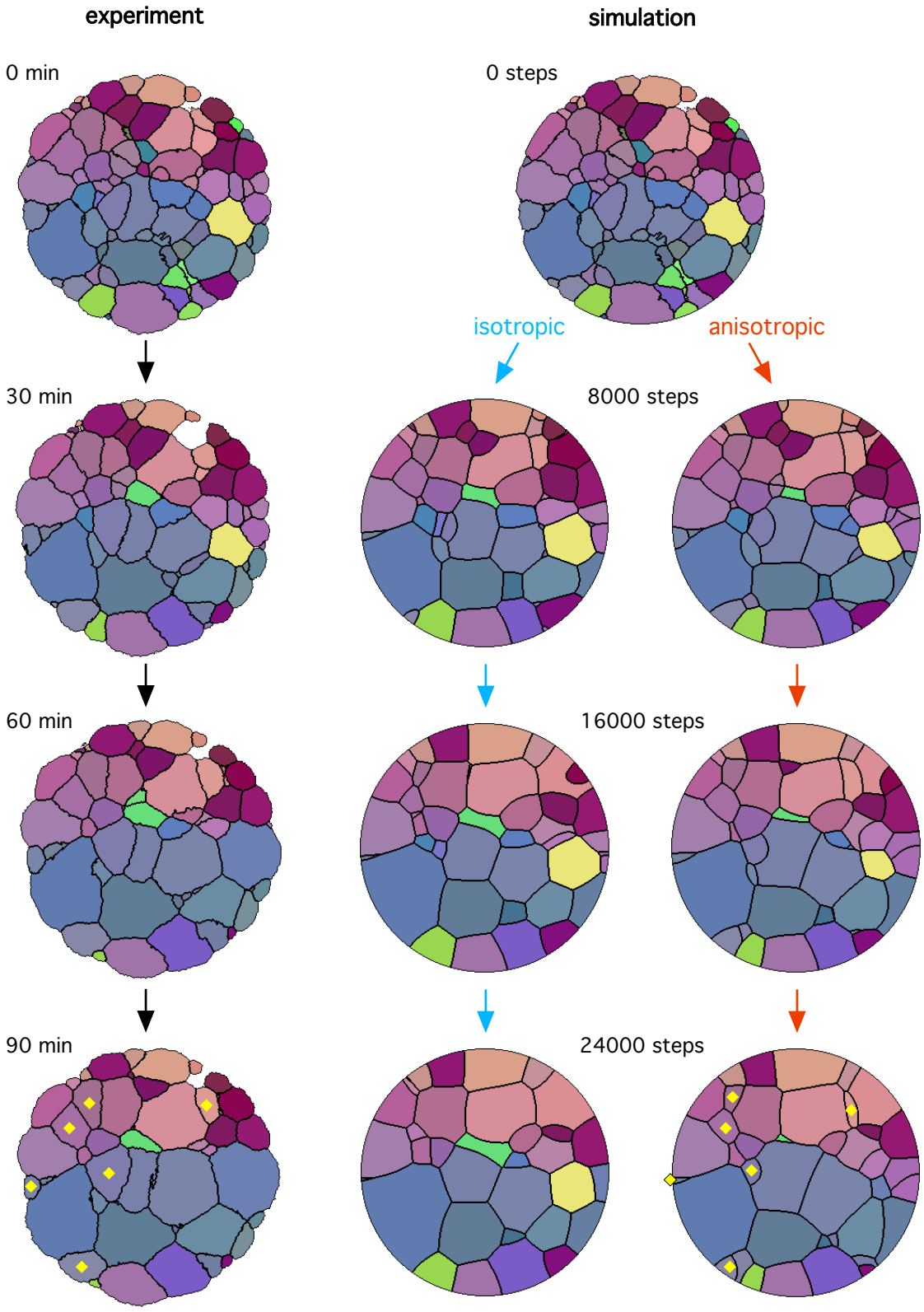

Figure 6.4: Experimental versus simulation results. Using the same starting configuration, the results of an isotropic and an anisotropic 3D phase-field simulation are compared to the experimentally determined microstructure. The most obvious difference between the two simulations is the evolution of the large yellow grain, the true growth behavior of which is better captured by the anisotropic model. In the final row of images, yellow diamonds indicate several surviving grains where the agreement between experiment and anisotropic simulation is also better. (A segmentation error in the experimental data caused some deviation in the upper right-hand corner of the sample.)

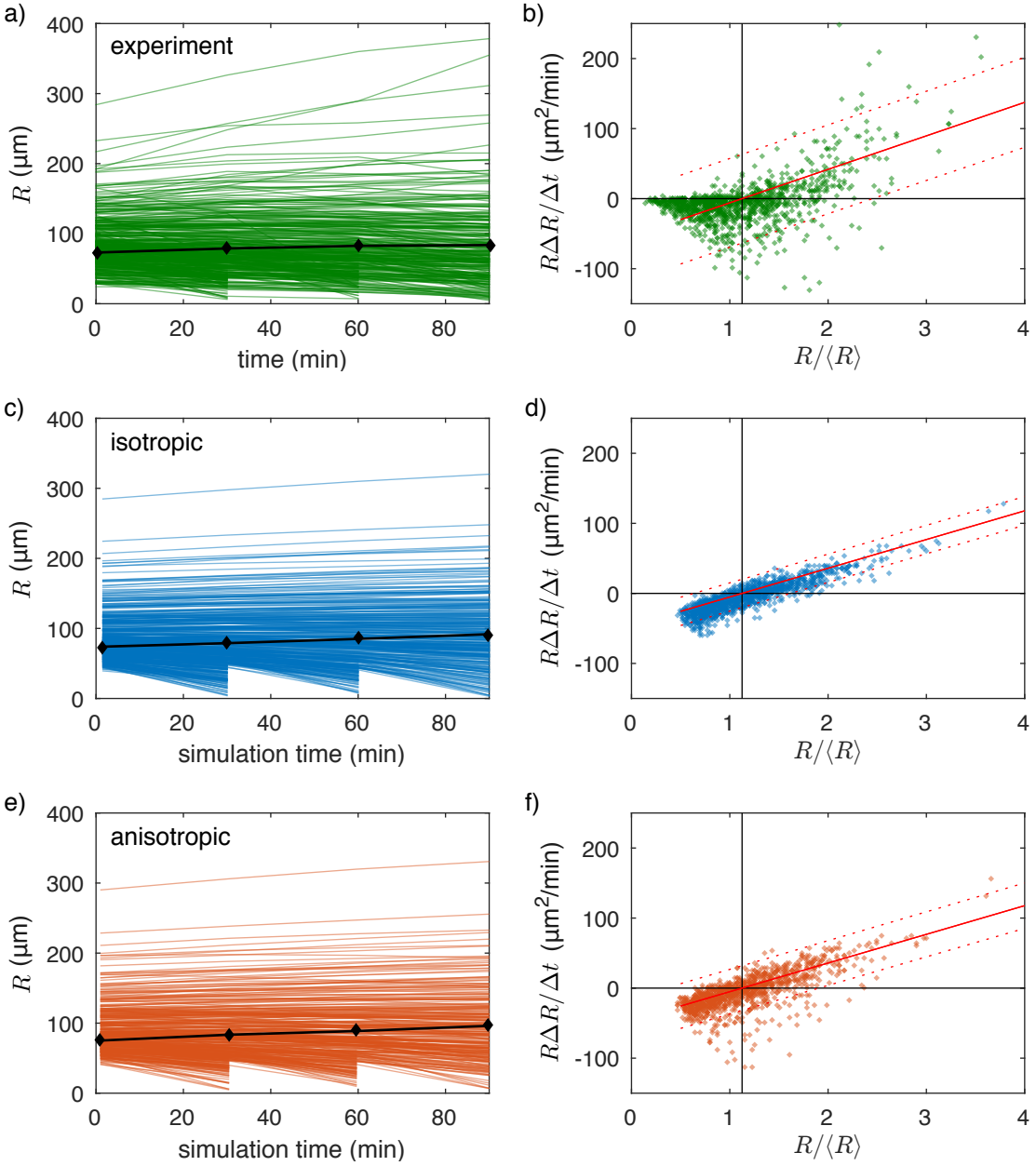

Figure 6.5: Grain size trajectories and growth rates from (a,b) experimental Al-1 wt% Mg data, (c,d) an isotropic simulation and (e,f) an anisotropic simulation. The latter simulation incorporated a Read-Schockley relation (Eq. (2.7)) for the interfacial energy of low-angle grain boundaries and, in so doing, was able to better predict features of the experimental results such as intersecting trajectories and larger scatter in growth rates.

accounted for in isotropic Ostwald ripening models, limits their usefulness in simulating real-world processing technologies, such as liquid-phase sintering.

The boundaries of some cellular structures (foams, for example) are isotropic, and for such systems isotropic models are able to accurately describe coarsening [225, 314]. Despite the anisotropic nature of crystalline interfaces, the same models are commonly extended to grain growth in polycrystals. The deficiencies in this approach, however, are clearly evident in the Al-Mg coarsening data presented in this thesis. This specimen's crystallographic texture and the corresponding large population of low-angle grain boundaries most certainly contributed to the poor agreement between the isotropic phase-field and experimental results. Most real-world samples are formed through various thermomechanical processing techniques, which frequently leads to the generation of recrystallization textures. In a similar 3D coarsening study published during the preparation of this thesis, the authors found that even in a weakly textured iron sample the growth rates of individual grains were not able to be accurately predicted by isotropic models [73]. Thus, it appears that anisotropic models are a prerequisite for reliably simulating grain growth in real polycrystals.

6.3 Alternative mechanisms of grain coarsening

Curvature-driven growth is the foundation of conventional coarsening theories, and for isotropic materials curvature is the only variable that differs from boundary to boundary. But, as we just established above, isotropic models do not capture the true microstructural evolution of polycrystalline materials—at least not in those investigated in this thesis, and probably not in other crystalline materials either, owing to the intrinsic anisotropy of grain boundary properties. 3DXRD data sets provide new possibilities for examining coarsening behavior, because they deliver not only the spatial extent of the grains inside the irradiated region of a sample but also the grain orientations. With such data sets in hand, we can delve into the third question raised in the Introduction:

Are there nonstandard paths by which microstructural coarsening may proceed?

In the first set of 3DXRD experiments, grain growth was investigated in a single-phase Al-1 wt% Mg alloy. This material was selected because previous 2D metallographic studies suggested that it displayed ideal normal grain growth. Not until the first sets of 3DXRD data were reconstructed and analyzed did the specimen's crystallographic texture and spatial clustering of similarly oriented grains come to light. The consequence of this grain configuration was the slow coarsening of crystallites located inside such clusters and the fast, sometimes abnormal growth of grains situated at the boundary between clusters. Grains that were randomly oriented and had no "allies" disappeared even though they were sometimes quite large (c.f. Fig. 4.17). The observed form of abnormal growth differs from the conventional model of textured-induced abnormal grain growth in two ways. First, CSL boundaries play no special role, and second, the relative strength of texture components remains approximately constant, i.e., one component does not grow at the expense of another.

In the second set of experiments, Al-5 wt% Cu samples were heat treated in the semisolid state. The presence of a liquid phase allowed the remaining crystalline grains of the solid phase to rotate. This effect was demonstrated in Chapter 5 at two different volume fractions of the solid phase ($V_V = 70\%$ and $V_V = 82\%$). Although most rotations were random in nature, some appeared to be directed by the reduction of grain boundary energy. The phenomenon was clearly observed at low-misorientation grain pairs, which tended to rotate

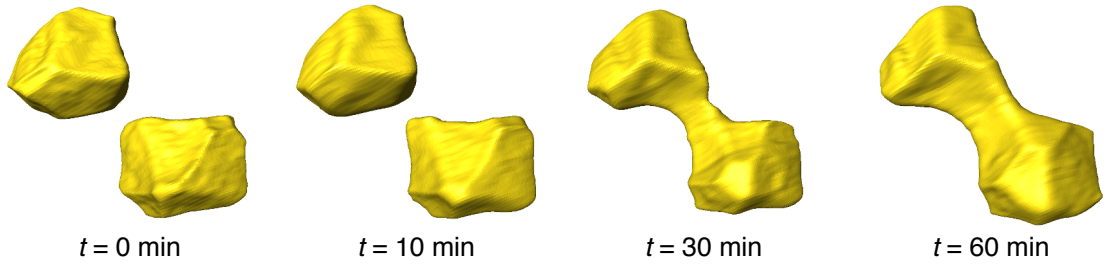

Figure 6.6: Example of a coalescence event in the Al-Cu specimen annealed at 630 °C. Two grains with an initial misorientation of 1.21° are located close together but are not touching. At some point between 10 and 30 min, they come into contact through a neighbor switching event. By the end of the annealing sequence, they have taken on exactly the same orientation—i.e., the two grains have become one elongated grain.

so as to further reduce their misorientation. The end result of such rotations is coalescence: when the misorientation between neighboring grains goes to zero, the boundary between them vanishes and the two become one larger grain. A coalescence event was actually observed in the specimen with $V_V = 70\%$ and is displayed in Fig. 6.6. At the beginning of the annealing sequence two similarly oriented grains are physically separated, but after a neighbor switching event, which occurred at some point between 10 and 30 minutes into the anneal, the two grains came into contact with each other and rotated so that their crystal latices were perfectly aligned ($\vartheta = 0°$). This unique form of coarsening can have a significant impact on the coarsening kinetics of nearby grains, as the newly formed/enlarged grain strives to take on a more compact, spherical shape. Direct observation of such a coarsening phenomenon was hardly imaginable before the development of 3DXRD microscopy.

Nonstandard forms of coarsening were detected in both Al alloys investigated by 3DXRD. In the single-phase Al-Mg specimen, a form of abnormal grain growth induced by the clustering of similarly oriented crystallites was discovered. In the two-phase Al-Cu samples, grain rotations and even the coalescence of low-angle grain pairs were observed. Both modes of coarsening were unexpected and discovered unintentionally during data analysis. They reveal how complex and sometimes nuanced coarsening in real polycrystals can be but also why the complete characterization of microstructure in 3D is so important to unlocking the mysteries of coarsening in crystalline materials.

6.4 Conclusions

3DXRD microscopy is a relatively new, still maturing experimental characterization technique, and the early portions of this work were focused on optimizing the setup and reconstruction procedures for grain coarsening experiments. To accelerate data collection, a box-beam was employed instead of a planar beam, which had previously been standard practice [72, 77]. During each measurement interval, diffraction images were collected with two separate detectors: a high-resolution near-field detector and a large-area far-field detector. A two-step reconstruction process was developed to make optimal use of the information contained in each set of images. First, seed grains were found by iteratively searching the far-field data. With seed grains in hand, high-quality grain maps were then reconstructed from the near-field data. This approach allowed not only for the efficient mapping of large sample volumes but also real-time reconstruction. The latter proved to be essential for successful experimentation at synchrotron beamlines, since specimens no

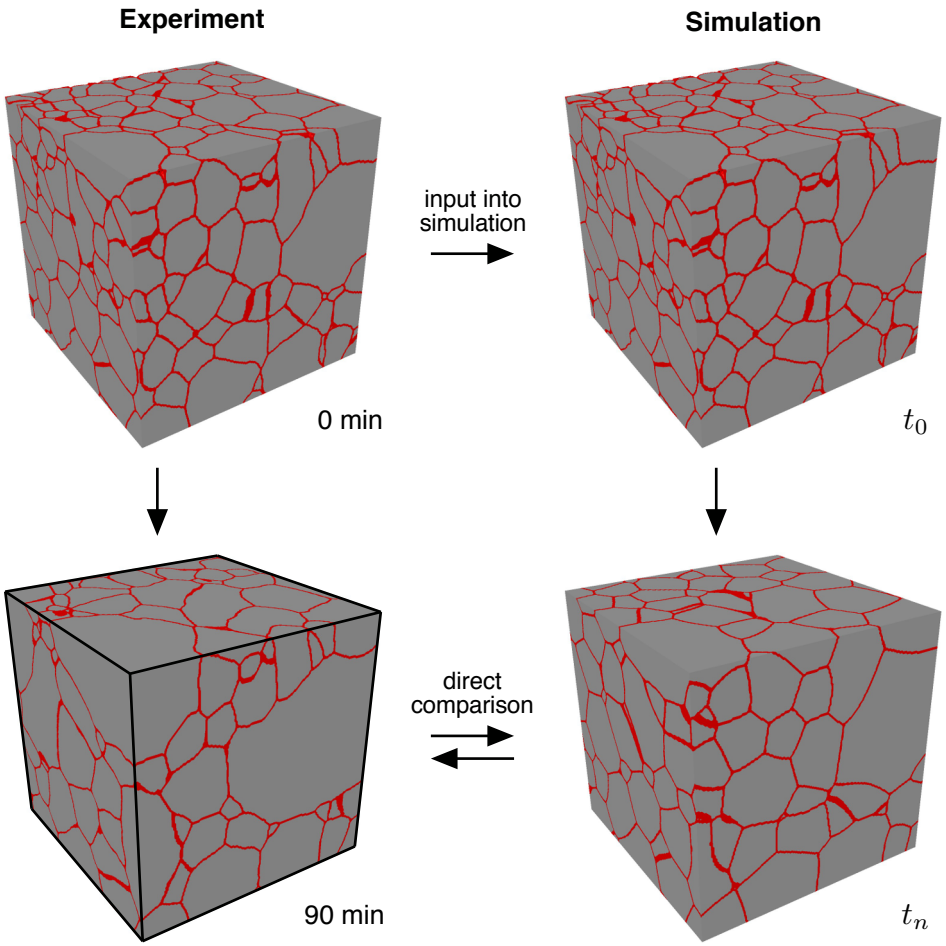

Figure 6.7: 3DXRD microscopy closes the gap in the 3D characterization of microstructure. The empty box on the lower left is now filled (cf. Fig. 1.4), and coarsening in real polycrystals can be compared directly to the output of grain growth simulations.

longer had to be annealed blindly. The optimized reconstruction and post-processing algorithms developed as part of this thesis are now included in the standard software for 3DXRD microscopy and used at beamlines around the world [234].

Since coarsening is a 3D phenomenon, it is essential to study the evolution of microstructure in 3D to gain a complete understanding of the underlying mechanisms. In two large-scale studies of different Al alloys, 3DXRD microscopy provided access to unique coarsening data. The growth and orientation of individual grains were tracked in 3D, and it was demonstrated how decisive the local neighborhood is for grain evolution. With these data sets, we can finally begin filling in the gaps in our experimental knowledge of coarsening. Fig. 6.7 reproduces Fig. 1.4 shown in the Introduction, but here the left-hand side is filled in with experimental data. Now, models can be adapted and tuned to fit real data so that predictive simulations of microstructural evolution may one day become a reality.

In a sense, the characterization of materials by x-rays has come full circle with the development of 3DXRD microscopy. Shortly after the discovery of x-rays, their application in diffraction experiments allowed researchers to solve the crystal structure of many solid materials. The experiments by von Laue were so convincing that the debate on the atomic nature of matter was finally settled [315]. Interestingly, Wilhelm Ostwald, whose theory of Ostwald ripening was discussed above, was one of the last major critics of atomism.

Later, x-rays were used to determine material characteristics, such as texture, mean grain size and microstrain, but only on a global scale. With 3DXRD it is now possible to follow the local evolution of grains and even track the migration of individual grain boundaries. As this technique matures, it will be exciting to see what new findings follow, now that coarsening phenomena can be observed in their native 3D environment.

Bibliography

[1] J. Czochralski. Geschichtlicher Beitrag zur Frage der Rekristallisation. Zeitschrift für Metallkunde 19 (1927) 316–320.

[2] R. S. Swalin. *Thermodynamics of Solids*. Wiley, 2nd edition, 1972.

[3] A. P. Sutton, E. P. Banks, and A. R. Warwick. The five-dimensional parameter space of grain boundaries. Proceedings of the Royal Society of London A 471 (2015).

[4] G. Gottstein and L. Shvindlerman. *Grain Boundary Migration in Metals: Thermodynamics, Kinetics, Applications*. CRC Press, 2010.

[5] E. O. Hall. The Deformation and Ageing of Mild Steel: III Discussion of Results. Proceedings of the Physical Society B 64 (1951) 747.

[6] N. J. Petch. The cleavage strength of polycrystals. Journal of the Iron and Steel Institute 174 (1953) 25.

[7] A. F. Mayadas and M. Shatzkes. Electrical-Resistivity Model for Polycrystalline Films: the Case of Arbitrary Reflection at External Surfaces. Physical Review B 1 (1970) 1382–1389.

[8] G. Knöner, K. Reimann, R. Röwer, U. Södervall, and H.-E. Schaefer. Enhanced oxygen diffusivity in interfaces of nanocrystalline ZrO2.Y2O3. Proceedings of the National Academy of Sciences 100 (2003) 3870–3873.

[9] C. Suryanarayana. Structure and properties of nanocrystalline materials. Bulletin of Materials Science 17 (1994) 307–346.

[10] C. C. Koch. *Nanostructured Materials*. William Andrew Publishing, Norwich, NY, 2nd edition, 2007.

[11] F. J. Humphreys and M. Hatherly. *Recrystallization and Related Annealing Phenomena*. Elsevier, Oxford, 2004.

[12] A.-C. Probst. Auf der Suche nach einem Modellsystem zum Verständnis der Korrelationseffekte beim normalen Kornwachstum. Master's thesis, Universität des Saarlandes, 2004.

[13] E. E. Underwood. *Quantitative Stereology*. Addison-Wesley series in metallurgy and materials. Addison-Wesley Pub. Co., 1970.

[14] C. S. Smith. Grain shapes and other metallurgical applications of topology. In *Metal Interfaces*, pages 65–133. American Society for Metals, Cleveland, OH, 1952.

[15] J. E. Burke and D. Turnbull. Recrystallization and grain growth. Progress in Metal Physics 3 (1952) 220–292.

[16] M. Hillert. On the theory of normal and abnormal grain growth. Acta Metallurgica 13 (1965) 227–238.

[17] C. S. Smith. Some elementary principles of polycrystalline microstructure. Metallurgical Reviews 9 (1964) 1–48.

[18] A. P. Sutton and R. W. Balluffi. *Interfaces in Crystalline Materials.* Clarendon Press, Oxford, 1995.

[19] M. P. Anderson, D. J. Srolovitz, G. S. Grest, and P. S. Sahni. Computer simulation of grain growth—I. Kinetics. Acta Metallurgica 32 (1984) 783–791.

[20] D. J. Srolovitz, G. S. Grest, and M. P. Anderson. Computer simulation of grain growth–V. Abnormal grain growth. Acta Metallurgica 33 (1985) 2233–2247.

[21] G. S. Grest, D. J. Srolovitz, and M. P. Anderson. Computer simulation of grain growth–IV. Anisotropic grain boundary energies. Acta Metallurgica 33 (1985) 509–520.

[22] A. D. Rollett, D. J. Srolovitz, and M. P. Anderson. Simulation and theory of abnormal grain growth—anisotropic grain boundary energies and mobilities. Acta Metallurgica 37 (1989) 1227–1240.

[23] C. E. Krill III and L. Q. Chen. Computer simulation of 3-D grain growth using a phase-field model. Acta Materialia 50 (2002) 3059–3075.

[24] K. Janssens, G. Frans, D. Raabe, B. Nestler, E. Kozeschnik, and M. A. Miodownik. *Computational Materials Engineering: An Introduction to Microstructure Evolution.* Elsevier, 2007.

[25] E. A. Lazar, J. K. Mason, R. D. MacPherson, and D. J. Srolovitz. A more accurate three-dimensional grain growth algorithm. Acta Materialia 59 (2011) 6837–6847.

[26] J. Hötzer, M. Jainta, A. Vondrous, J. Ettrich, A. August, D. Stubenvoll, M. Reichardt, M. Selzer, and B. Nestler. Phase-Field Simulations of Large-Scale Microstructures by Integrated Parallel Algorithms. In W. E. Nagel, D. H. Kröner, and M. M. Resch, editors, *High Performance Computing in Science and Engineering, '14*, pages 629–644. Springer International Publishing, 2015.

[27] W. Xue, H. Wang, G. Liu, L. Meng, G. Ma, and M. Feng. Analysis on topological grain forms via large-scale serial sectioning experiment and Monte Carlo simulation. Materials Letters 174 (2016) 171–174.

[28] E. Miyoshi, T. Takaki, M. Ohno, Y. Shibuta, S. Sakane, T. Shimokawabe, and T. Aoki. Ultra-large-scale phase-field simulation study of ideal grain growth. npj Computational Materials 3 (2017) 25.

[29] E. A. Holm and C. C. Battaile. The Computer Simulation of Microstructural Evolution. JOM 53 (2001) 20–23.

[30] Y. Liu, T. Baudin, and R. Penelle. Simulation of normal grain growth by cellular automata. Scripta Materialia 34 (1996).

[31] M. A. Miodownik. A review of microstructural computer models used to simulate grain growth and recrystallisation in aluminium alloys. Journal of Light Metals 2 (2002) 125–135.

[32] M. Upmanyu, G. N. Hassold, A. Kazaryan, E. A. Holm, Y. Wang, B. Patton, and D. J. Srolovitz. Boundary Mobility and Energy Anisotropy Effects on Microstructural Evolution During Grain Growth. Interface Science 10 (2002) 201–216.

[33] K. Chang and N. Moelans. Effect of grain boundary energy anisotropy on highly textured grain structures studied by phase-field simulations. Acta Materialia 64 (2014) 443–454.

[34] S. G. Kim and Y. B. Park. Grain boundary segregation, solute drag and abnormal grain growth. Acta Materialia 56 (2008) 3739–3753.

[35] A. Harun, M. A. Miodownik, M. P. Clode, and E. A. Holm. Modelling Zener Pinning: A Comparison of Different Computer Simulation Methods. Materials Science Forum 467-470 (2004) 1033–1038.

[36] G. S. Rohrer, D. M. Saylor, B. El Dasher, B. L. Adams, A. D. Rollett, and P. Wynblatt. The distribution of internal interfaces in polycrystals. Zeitschrift für Metallkunde 95 (2004) 197–214.

[37] R. T. DeHoff, E. H. Aigeltinger, and K. R. Craig. Experimental determination of the topological properties of three-dimensional microstructures. Journal of Microscopy 95 (1972) 69–91.

[38] F. N. Rhines, K. R. Craig, and R. T. DeHoff. Mechanism of steady-state grain growth in aluminum. Metallurgical Transactions 5 (1974) 413–425.

[39] J. E. Spowart, H. E. Mullens, and B. T. Puchala. Collecting and analyzing microstructures in three dimensions: A fully automated approach. JOM 55 (2003) 35–37.

[40] C. Zhang, M. Enomoto, A. Suzuki, and T. Ishimaru. Characterization of Three-Dimensional Grain Structure in Polycrystalline Iron by Serial Sectioning. Metallurgical and Materials Transactions A 35 (2004) 1927–1933.

[41] M. Groeber, B. Haley, M. Uchic, D. Dimiduk, and S. Ghosh. 3D reconstruction and characterization of polycrystalline microstructures using a FIB–SEM system. Materials Characterization 57 (2006) 259–273.

[42] S. Zaefferer, S. Wright, and D. Raabe. Three-dimensional orientation microscopy in a focused ion beam–scanning electron microscope: A new dimension of microstructure characterization. Metallurgical and Materials Transactions A 39 (2008) 374–389.

[43] D. Rowenhorst, A. Lewis, and G. Spanos. Three-dimensional analysis of grain topology and interface curvature in a β-titanium alloy. Acta Materialia 58 (2010) 5511–5519.

[44] A. Ullah, G. Liu, J. Luan, W. Li, M. ur Rahman, and M. Ali. Three-dimensional visualization and quantitative characterization of grains in polycrystalline iron. Materials Characterization 91 (2014) 65–75.

[45] F. C. Hull. Plane section and spatial characteristics of equiaxed β-brass grains. Materials Science and Technology 4 (1988) 778–785.

[46] K. Matsuura, Y. Itoh, T. Ohmi, and K. Ishii. Evaluation of grain shape distribution in polycrystalline materials. Materials Transactions, JIM 35 (1994) 247–253.

[47] F. N. Rhines and B. R. Patterson. Effect of the degree of prior cold work on the grain volume distribution and the rate of grain growth of recrystallized aluminum. Metallurgical Transactions A 13 (1982) 985–993.

[48] M. Anderson, G. Grest, and D. Srolovitz. Computer simulation of normal grain growth in three dimensions. Philosophical Magazine B 59 (1989) 293–329.

[49] D. Weygand, Y. Brechet, J. Lepinoux, and W. Gust. Three-dimensional grain growth: A vertex dynamics simulation. Philosophical Magazine B 79 (1999) 703–716.

[50] F. Wakai, N. Enomoto, and H. Ogawa. Three-dimensional microstructural evolution in ideal grain growth—general statistics. Acta Materialia 48 (2000) 1297–1311.

[51] G. Liu, H. Yu, X. Song, and X. Qin. A new model of three-dimensional grain growth: theory and computer simulation of topology-dependency of individual grain growth rate. Materials & Design 22 (2001) 33–38.

[52] M. Elsey, S. Esedoglu, and P. Smereka. Large-scale simulation of normal grain growth via diffusion-generated motion. Proceedings of The Royal Society A 466 (2010).

[53] T. Keller, B. Cutler, E. A. Lazar, G. Yauney, and D. J. Lewis. Comparative grain topology. Acta Materialia 66 (2014) 414–423.

[54] V. Yadav and N. Moelans. Analysis of grain topology and volumetric growth rate relation in three-dimensional normal grain growth. Acta Materialia 156 (2018) 275–286.

[55] S. Bargmann, B. Klusemann, J. Markmann, J. E. Schnabel, K. Schneider, C. Soyarslan, and J. Wilmers. Generation of 3D representative volume elements for heterogeneous materials: A review. Progress in Materials Science 96 (2018) 322–384.

[56] K. Döbrich, C. Rau, and C. Krill. Quantitative characterization of the three-dimensional microstructure of polycrystalline Al-Sn using X-ray microtomography. Metallurgical and Materials Transactions A 35 (2004) 1953–1961.

[57] D. Bernard, D. Gendron, J.-M. Heintz, S. Bordere, and J. Etourneau. First direct 3D visualisation of microstructural evolutions during sintering through X-ray computed microtomography. Acta Materialia 53 (2005) 121–128.

[58] N. Limodin, L. Salvo, M. Suery, and M. DiMichiel. In situ investigation by x-ray tomography of the overall and local microstructural changes occurring during partial remelting of an Al-15.8 wt.% Cu alloy. Acta Materialia 55 (2007) 3177–3191.

[59] A. Vagnon, J. P. Riviere, J. M. Missiaen, D. Bellet, M. D. Michiel, C. Josserond, and D. Bouvard. 3D statistical analysis of a copper powder sintering observed in situ by synchrotron microtomography. Acta Materialia 56 (2008) 1084–1093.

[60] S. Terzi, L. Salvo, M. Suery, A. Dahle, and E. Boller. Coarsening mechanisms in a dendritic Al-10% Cu alloy. Acta Materialia 58 (2010) 20–30.

[61] R. Grupp, M. Nöthe, B. Kieback, and J. Banhart. Cooperative material transport during the early stage of sintering. Nature Communications 2 (2011) 298.

[62] T. Werz, M. Baumann, U. Wolfram, and C. E. Krill III. Particle tracking during Ostwald ripening using time-resolved laboratory X-ray microtomography. Materials Characterization 90 (2014) 185–195.

[63] K. M. Kareh, P. D. Lee, R. C. Atwood, T. Connolley, and C. M. Gourlay. Revealing the micromechanisms behind semi-solid metal deformation with time-resolved x-ray tomography. Nature Communications 5 (2014) 1–7.

[64] H. F. Poulsen, S. Garbe, T. Lorentzen, D. J. Jensen, F. W. Poulsen, N. H. Andersen, T. Frello, R. Feidenhans'l, and H. Graafsma. Applications of High-Energy Synchrotron Radiation for Structural Studies of Polycrystalline Materials. Journal of Synchrotron Radiation 4 (1997) 147–154.

[65] H. F. Poulsen, S. F. Nielsen, E. M. Lauridsen, S. Schmidt, R. M. Suter, U. Lienert, L. Margulies, T. Lorentzen, and D. J. Jensen. Three-dimensional maps of grain boundaries and the stress state of individual grains in polycrystals and powders. Journal of Applied Crystallography 34 (2001) 751–756.

[66] H. F. Poulsen. Three-dimensional x-ray diffraction microscopy. In *Springer Tracts in Modern Physics*, volume 205. Springer, 2004.

[67] S. Schmidt, S. F. Nielsen, C. Gundlach, L. Margulies, X. Huang, and D. J. Jensen. Watching the growth of bulk grains during recrystallization of deformed metals. Science 305 (2004) 229–232.

[68] H. Poulsen, L. Margulies, S. Schmidt, and G. Winther. Lattice rotations of individual bulk grains. Part I: 3D X-ray characterization. Acta Mater 51 (2003) 3821–3830.

[69] G. Winther, L. Margulies, S. Schmidt, and H. F. Poulsen. Lattice rotations of individual bulk grains Part II: correlation with initial orientation and model comparison. Acta Materialia 52 (2004) 2863–2872.

[70] R. Pokharel, J. Lind, S. F. Li, P. Kenesei, R. A. Lebensohn, R. M. Suter, and A. D. Rollett. In-situ observation of bulk 3D grain evolution during plastic deformation in polycrystalline Cu. International Journal of Plasticity 67 (2015) 217–234.

[71] S. Poulsen, E. Lauridsen, A. Lyckegaard, J. Oddershede, C. Gundlach, C. Curfs, and D. Juul Jensen. In situ measurements of growth rates and grain-averaged activation energies of individual grains during recrystallization of 50% cold-rolled aluminium. Scripta Materialia 64 (2011) 1003–1006.

[72] S. Schmidt, U. L. Olsen, H. F. Poulsen, H. O. Sørensen, E. M. Lauridsen, L. Margulies, C. Maurice, and D. Juul Jensen. Direct observation of 3-D grain growth in Al–0.1% Mn. Scripta Materialia 59 (2008) 491–494.

[73] J. Zhang, Y. Zhang, W. Ludwig, D. Rowenhorst, P. W. Voorhees, and H. F. Poulsen. Three-dimensional grain growth in pure iron. Part I. statistics on the grain level. Acta Materialia 156 (2018) 76–85.

[74] J. Oddershede, B. Camin, S. Schmidt, L. P. Mikkelsen, H. O. Sørensen, U. Lienert, H. F. Poulsen, and W. Reimers. Measuring the stress field around an evolving crack in tensile deformed Mg AZ31 using three-dimensional X-ray diffraction. Acta Materialia 60 (2012) 3570–3580.

[75] A. King, G. Johnson, D. Engelberg, W. Ludwig, and J. Marrow. Observations of intergranular stress corrosion cracking in a grain-mapped polycrystal. Science 321 (2008) 382.

[76] J. E. Daniels, M. Majkut, Q. Cao, S. Schmidt, J. Wright, W. Jo, and J. Oddershede. Heterogeneous grain-scale response in ferroic polycrystals under electric field. Scientific Reports 6 (2016) 22820.

[77] H. F. Poulsen, W. Ludwig, E. M. Lauridsen, S. Schmidt, W. Pantleon, U. L. Olsen, J. Oddershede, P. Reischig, A. Lyckegaard, and J. Wright. 4D characterization of metals by 3DXRD. In *Proceedings of the Risø International Symposium on Materials Science*, volume 31, pages 101–119. Risø National Laboratory, 2010.

[78] H. O. Sørensen, S. Schmidt, J. P. Wright, G. B. M. Vaughan, S. Techert, E. F. Garman, J. Oddershede, J. Davaasambuu, K. S. Paithankar, C. Gundlach, and H. F. Poulsen. Multigrain crystallography. Zeitschrift fur Kristallographie 227 (2011) 63–78.

[79] H. F. Poulsen. An introduction to three-dimensional x-ray diffraction microscopy. Journal of Applied Crystallography 45 (2012) 1084–1097.

[80] P. Reischig, A. King, L. Nervo, N. Vigano, Y. Guilhem, W. J. Palenstijn, K. J. Batenburg, M. Preuss, and W. Ludwig. Advances in x-ray diffraction contrast tomography: flexibility in the setup geometry and application to multiphase materials. Journal of Applied Crystallography 46 (2013) 297–311.

[81] R. Pokharel. *Materials Discovery and Design: By Means of Data Science and Optimal Learning*, volume 280, chapter Overview of High-Energy X-Ray Diffraction Microscopy (HEDM) for Mesoscale Material Characterization in Three-Dimensions, pages 167–201. Springer International Publishing, 2018.

[82] O. Engler, L. Löchte, and J. Hirsch. Through-process simulation of texture and properties during the thermomechanical processing of aluminium sheets. Acta Materialia 55 (2007) 5449–5463.

[83] P. D. Lee. Modelling of light metals: from the atomic scale to the processing of automotive and aerospace components. Journal of Light Metals 2 (2002) 113.

[84] C. E. Krill III. Personal communication, 2013.

[85] G. Herrmann, H. Gleiter, and G. Bäro. Investigation of low energy grain boundaries in metals by a sintering technique. Acta Metallurgica 24 (1976) 353–359.

[86] T. C. Hales. A Proof of the Kepler Conjecture. Annals of Mathematics 162 (2005) 1065–1185.

[87] A. Morawiec. *Orientations and Rotations*. Springer-Verlag Berlin Heidelberg GmbH, 2004.

[88] O. Engler and V. Randle. *Introduction to Texture Analysis: Macrotexture, Microtexture, and Orientation Mapping*. CRC Press, 2010.

[89] F. Frank. Orientation mapping. Metall Trans A 19 (1988) 403–408.

[90] P. Neumann. Representation of orientations of symmetrical objects by rodrigues vectors. Textures and Microstructures 14 (1991) 53–58.

[91] A. Morawiec and D. P. Field. Rodrigues parameterization for orientation and misorientation distributions. Philosophical Magazine A 73 (1996) 1113–1130.

[92] J. Hirsch, C. Leroy, and A. Green. Alumatter, a new interactive e-learning tool. In *Aluminium Alloys 2006 - ICAA10*, volume 519 of *Materials Science Forum*, pages 1209–1214. Trans Tech Publications, 7 2006.

[93] J. K. Mackenzie. Second paper on statistics associated with the random disorientation of cubes. Biometrika 45 (1958) 229–240.

[94] A. P. Sutton and R. W. Balluffi. Overview no. 61: On geometric criteria for low interfacial energy. Acta Metallurgica 35 (1987) 2177–2201.

[95] G. S. Rohrer. Grain boundary energy anisotropy: A review. Journal of Materials Science 46 (2011) 5881–5895.

[96] D. Wolf. Correlation between structure, energy, and ideal cleavage fracture for symmetrical grain boundaries in fcc metals. Journal of Materials Research 5 (1990) 1708–1730.

[97] D. M. Saylor, A. Morawiec, B. L. Adams, and G. S. Rohrer. Misorientation dependence of the grain boundary energy in magnesia. Interface Science 8 (2000) 131–140.

[98] M. Takashima, A. Rollett, and P. Wynblatt. A representation method for grain-boundary character. Philosophical Magazine A 80 (2000) 2457–2465.

[99] D. M. Saylor, A. Morawiec, and G. S. Rohrer. Distribution of grain boundaries in magnesia as a function of five macroscopic parameters. Acta Materialia 51 (2003) 3663–3674.

[100] D. M. Saylor, B. S. El Dasher, A. D. Rollett, and G. S. Rohrer. Distribution of grain boundaries in aluminum as a function of five macroscopic parameters. Acta Materialia 52 (2004) 3649–3655.

[101] D. M. Saylor, A. Morawiec, and G. S. Rohrer. The relative free energies of grain boundaries in magnesia as a function of five macroscopic parameters. Acta Materialia 51 (2003) 3675–3686.

[102] J. M. Burgers. Geometrical considerations concerning the structural irregularities to be assumed in a crystal. Proceedings of the Physical Society 52 (1940) 23.

[103] W. L. Bragg. Discussion. Part I. Proceedings of the Physical Society 52 (1940) 54.

[104] W. T. Read and W. Shockley. Dislocation models of crystal grain boundaries. Physical Review 78 (1950) 275–289.

[105] W. Read. *Dislocations in Crystals*. McGraw-Hill, New York, 1953.

[106] H. Gleiter. Chapter 9 - Microstructure. In R. W. Cahn and P. Haasen, editors, *Physical Metallurgy*, pages 843–942. North-Holland, Oxford, 4th edition, 1996.

[107] C. Shen, J. Li, and Y. Wang. Predicting structure and energy of dislocations and grain boundaries. Acta Materialia 74 (2014) 125–131.

[108] E. Holm, G. Hassold, and M. Miodownik. On misorientation distribution evolution during anisotropic grain growth. Acta Materialia 49 (2001) 2981–2991.

[109] M. Winning and A. D. Rollett. Transition between low and high angle grain boundaries. Acta Materialia 53 (2005) 2901–2907.

[110] L. E. Murr. *Interfacial Phenomena in Metals and Alloys.* Addison-Wesley, Reading, MA, 1975.

[111] N. M. Rosengaard and H. L. Skriver. Calculated stacking-fault energies of elemental metals. Physical Review B 47 (1993) 12865–12873.

[112] E. A. Holm, G. S. Rohrer, S. M. Foiles, A. D. Rollett, H. M. Miller, and D. L. Olmsted. Validating computed grain boundary energies in fcc metals using the grain boundary character distribution. Acta Materialia 59 (2011) 5250–5256.

[113] H. Hallberg. Influence of anisotropic grain boundary properties on the evolution of grain boundary character distribution during grain growth—a 2D level set study. Modelling and Simulation in Materials Science and Engineering 22 (2014) 085005.

[114] S. Ranganathan. On the geometry of coincidence-site lattices. Acta Crystallographica 21 (1966) 197–199.

[115] J. M. Howe. *Interfaces in Materials: Atomic Structure, Thermodynamics and Kinetics of Solid-Vapor, Solid-Liquid and Solid-Solid Interfaces.* A Wiley-Interscience publication. Wiley, 1997.

[116] D. L. Olmsted, S. M. Foiles, and E. A. Holm. Survey of computed grain boundary properties in face-centered cubic metals: I. Grain boundary energy. Acta Materialia 57 (2009) 3694–3703.

[117] D. L. Olmsted, E. A. Holm, and S. M. Foiles. Survey of computed grain boundary properties in face-centered cubic metals—ii: Grain boundary mobility. Acta Materialia 57 (2009) 3704–3713.

[118] V. V. Bulatov, B. W. Reed, and M. Kumar. Grain boundary energy function for fcc metals. Acta Materialia 65 (2014) 161–175.

[119] E. R. Homer, S. Patala, and J. L. Priedeman. Grain boundary plane orientation fundamental zones and structure-property relationships. Scientific Reports 5 (2015) 15476.

[120] G. Hasson and C. Goux. Interfacial energies of tilt boundaries in aluminium. Experimental and theoretical determination. Scripta Metallurgica 5 (1971) 889–894.

[121] G. Hasson, J.-Y. Boos, I. Herbeuval, M. Biscondi, and C. Goux. Theoretical and experimental determinations of grain boundary structures and energies: Correlation with various experimental results. Surface Science 31 (1972) 115–137.

[122] G. Rohrer, J. Li, S. Lee, A. Rollett, M. Groeber, and M. Uchic. Deriving grain boundary character distributions and relative grain boundary energies from three-dimensional EBSD data. Materials Science and Technology 26 (2010) 661–669.

[123] G. S. Rohrer. Measuring and Interpreting the Structure of Grain-Boundary Networks. Journal of the American Ceramic Society 94 (2011) 633–646.

[124] S. Zaefferer and N. Chen. The goss texture formation in silicon steels–growth selection or oriented nucleation. Solid State Phenomena 105 (2005) 29–36.

[125] K. Lücke and K. Detert. A quantitative theory of grain-boundary motion and recrystallization in metals in the presence of impurities. Acta Metallurgica 5 (1957) 628–637.

[126] J. W. Cahn. The impurity-drag effect in grain boundary motion. Acta Metallurgica 10 (1962) 789–798.

[127] C. S. Smith. Introduction to grains, phases, and interfaces: An interpretation of microstructure. Trans. AIME 175 (1948) 15–51.

[128] D. L. Olmsted, S. M. Foiles, and E. A. Holm. Grain boundary interface roughening transition and its effect on grain boundary mobility for non-faceting boundaries. Scripta Materialia 57 (2007) 1161–1164.

[129] S. I. Bae and S. Baik. Sintering and grain growth of ultrapure alumina. Journal of Materials Science 28 (1993) 4197–4204.

[130] O. S. Kwon, S. H. Hong, J. H. Lee, U. J. Chung, D. Y. Kim, and N. M. Hwang. Microstructural evolution during sintering of TiO2/SiO2-doped alumina: mechanism of anisotropic abnormal grain growth. Acta Materialia 50 (2002) 4865–4872.

[131] J. Dennis, P. S. Bate, and F. J. Humphreys. Abnormal grain growth in metals. Materials Science Forum 558-559 (2007) 717–722.

[132] M. Ames, J. Markmann, R. Karos, A. Michels, A. Tschöpe, and R. Birringer. Unraveling the nature of room temperature grain growth in nanocrystalline materials. Acta Materialia 56 (2008) 4255–4266.

[133] J. M. Dake and C. E. Krill III. Sudden loss of thermal stability in Fe-based nanocrystalline alloys. Scripta Materialia 66 (2012) 390–393.

[134] P. R. Cantwell, M. Tang, S. J. Dillon, J. Luo, G. S. Rohrer, and M. P. Harmer. Grain boundary complexions. Acta Materialia 62 (2014) 1–48.

[135] C.-S. Park, H.-K. Park, H.-S. Shim, T.-W. Na, C.-H. Han, and N.-M. Hwang. New understanding of the role of coincidence site lattice boundaries in abnormal grain growth of aluminium alloy. Philosophical Magazine Letters 95 (2015) 1–9.

[136] A. Lawrence, J. Rickman, M. Harmer, and A. Rollett. Parsing abnormal grain growth. Acta Materialia 103 (2016) 681–687.

[137] C. Braun, J. M. Dake, C. E. Krill, and R. Birringer. Abnormal grain growth mediated by fractal boundary migration at the nanoscale. Scientific Reports 8 (2018) 1592.

[138] S.-J. L. Kang. *Sintering - Densification, Grain Growth, and Microstructure*. Elsevier, 2005.

[139] A. D. Rollett, A. P. Brahme, and C. G. Roberts. An overview of accomplishments and challenges in recrystallization and grain growth. Materials Science Forum 558-559 (2007) 33–42.

[140] E. Starke Jr. and J. Staley. Application of modern aluminum alloys to aircraft. Progress in Aerospace Sciences 32 (1996) 131–172.

[141] P. Krajewski, L. Hector Jr., Y. Qi, R. Mishra, A. Sachdev, A. Bower, and W. Curtin. Atoms to autos: A multi-scale approach to modeling aluminum deformation. JOM 63 (2011) 24–32.

[142] J. Dennis, P. Bate, and F. Humphreys. Abnormal grain growth in Al-3.5Cu. Acta Materialia 57 (2009) 4539–4547.

[143] C. V. Thompson, H. J. Frost, and F. Spaepen. The relative rates of secondary and normal grain growth. Acta Metallurgica 35 (1987) 887–890.

[144] U. Kunaver and D. Kolar. Three-dimensional computer simulation of anisotropic grain growth in ceramics. Acta Materialia 46 (1998) 4629–4640.

[145] N. O. Hwang. Simulation of the effect of anisotropic grain boundary mobility and energy on abnormal grain growth. Journal of Materials Science 33 (1998) 5625–5629.

[146] N. M. Hwang, S. B. Lee, and D.-Y. Kim. Abnormal grain growth by solid-state wetting along grain boundary or triple junction. Scripta Materialia 44 (2001) 1153–1160.

[147] Y. Suwa, Y. Saito, and H. Onodera. Three-dimensional phase field simulation of the effect of anisotropy in grain-boundary mobility on growth kinetics and morphology of grain structure. Computational Materials Science 40 (2007) 40–50.

[148] D.-K. Lee, B.-J. Lee, K.-J. Ko, and N.-M. Hwang. Comparison of the Advantages Conferred by Mobility and Energy of the Grain Boundary in Inducing Abnormal Grain Growth Using Monte Carlo Simulations. Materials Transactions 50 (2009) 2521–2525.

[149] M. Wang. Simulation of abnormal grain growth in nanomaterials. Master's thesis, Ulm University, 2013.

[150] W. E. Frazier, G. S. Rohrer, and A. D. Rollett. Abnormal grain growth in the Potts model incorporating grain boundary complexion transitions that increase the mobility of individual boundaries . Acta Materialia 96 (2015) 390–398.

[151] B. L. DeCost and E. A. Holm. Phenomenology of abnormal grain growth in systems with nonuniform grain boundary mobility. Metallurgical and Materials Transactions A 48 (2017) 2771–2780.

[152] C. Dunn and J. Walter. Secondary recrystallization. In *Recrystallization, Grain Growth and Textures*, pages 461–521. American Society for Metals, 1966.

[153] P. A. Beck and H. Hu. Annealing textures in rolled face-centered cubic metals. Trans. AIME 194 (1952) 83–90.

[154] F. J. Humphreys. A unified theory of recovery, recrystallization and grain growth, based on the stability and growth of cellular microstructures–I. The basic model. Acta Materialia 45 (1997) 4231–4240.

[155] Y. Huang, F. Humphreys, and M. Ferry. The annealing behaviour of deformed cube-oriented aluminium single crystals. Acta Materialia 48 (2000) 2543–2556.

[156] O. M. Ivasishin, S. V. Shevchenko, and S. L. Semiatin. Modeling of abnormal grain growth in textured materials. Scripta Materialia 50 (2004) 1241–1245.

[157] Y. Hayakawa and M. Kurosawa. Orientation relationship between primary and secondary recrystallized texture in electrical steel. Acta Materialia 50 (2002) 4527–4534.

[158] Y. Hayakawa and J. Szpunar. The role of grain boundary character distribution in secondary recrystallization of electrical steels. Acta Materialia 45 (1997) 1285–1295.

[159] Y. Yoshitomi, Y. Ushigami, J. Harase, T. Nakayama, H. Masui, and N. Takahashi. Coincidence grain boundary and role of primary recrystallized grain growth on secondary recrystallization texture evolution in Fe-3% Si alloy. Acta Metallurgica et Materialia 42 (1994) 2593–2602.

[160] P. R. Rios and G. Gottstein. Texture evolution during normal and abnormal grain growth in an Al-1 wt% Mn alloy. Acta Materialia 49 (2001) 2511–2518.

[161] H. Park, D.-Y. Kim, N.-M. Hwang, Y.-C. Joo, C. H. Han, and J.-K. Kim. Microstructural evidence of abnormal grain growth by solid-state wetting in Fe-3%Si steel. Journal of Applied Physics 95 (2004) 5515–5521.

[162] A. Morawiec. On abnormal growth of goss grains in grain-oriented silicon steel. Scripta Materialia 64 (2011) 466–469.

[163] F. Ma, J.-M. Zhang, and K.-W. Xu. Surface-energy-driven abnormal grain growth in Cu and Ag films. Applied Surface Science 242 (2005) 55–61.

[164] R. D. Doherty and J. W. Martin. The effect of a dispersed second phase on the recrystallisation of aluminum-copper alloys. Journal of the Institute of Metals 91 (1962) 332.

[165] T. Gladman. The theory and inhibition of abnormal grain growth in steels. JOM 44 (1992) 21–24.

[166] I. Andersen, Ø. Grong, and N. Ryum. Analytical modelling of grain growth in metals and alloys in the presence of growing and dissolving precipitates–II. abnormal grain growth. Acta Metallurgica et Materialia 43 (1995) 2689–2700.

[167] G. Wang, D. Xu, E. Payton, N. Ma, R. Yang, M. Mills, and Y. Wang. Mean-field statistical simulation of grain coarsening in the presence of stable and unstable pinning particles. Acta Materialia 59 (2011) 4587–4594.

[168] A. Morawiec. Grain misorientations in theories of abnormal grain growth in silicon steel. Scripta Materialia 43 (2000) 275–278.

[169] H. Homma and B. Hutchinson. Orientation dependence of secondary recrystallisation in silicon–iron. Acta Materialia 51 (2003) 3795–3805.

[170] W. Ostwald. Über die vermeintliche Isomerie des roten und gelben Quecksilberoxyds und die Oberflächenspannung fester Körper. Zeitschrift fur Physikalische Chemie 34 (1900) 495–503.

[171] F. Yang, P. Kollias, R. A. Shaw, and A. M. Vogelmann. Cloud droplet size distribution broadening during diffusional growth: ripening amplified by deactivation and reactivation. Atmospheric Chemistry and Physics 18 (2018) 7313–7328.

[172] C. Clarke. *The Science of Ice Cream.* Royal Society of Chemistry, 2012.

[173] J. Martin. *Micromechanisms in Particle-Hardened Alloys.* Cambridge Solid State Science Series. Cambridge University Press, 1980.

[174] P. W. Voorhees. The theory of Ostwald ripening. Journal Of Statistical Physics 38 (1985) 231–252.

[175] S. Hardy and P. Voorhees. Ostwald ripening in a system with a high volume fraction of coarsening phase. Metallurgical and Materials Transactions A 19 (1988) 2713–2721.

[176] T. Courtney. Microstructural evolution during liquid phase sintering: Part II. Microstructural coarsening. Metallurgical Transactions A 8 (1977) 685–689.

[177] L. Ratke and P. Voorhees. *Growth and Coarsening: Ostwald Ripening in Material Processing*. Engineering Materials and Processes. Springer, 2002.

[178] I. M. Lifshitz and V. V. Slyozov. The kinetics of precipitation from supersaturated solid solutions. Journal of Physics and Chemistry of Solids 19 (1961) 35–50.

[179] C. Wagner. Theorie der Alterung von Niederschlägen durch Umlösen (Ostwald-Reifung). Zeitschrift für Elektrochemie, Berichte der Bunsengesellschaft für physikalische Chemie 65 65 (1961) 581–591.

[180] P. Voorhees and M. Glicksman. Ostwald ripening during liquid phase sintering—effect of volume fraction on coarsening kinetics. Metallurgical Transactions A 15 (1984) 1081–1088.

[181] P. W. Voorhees. Ostwald ripening of two-phase mixtures. Annual Review Of Materials Research 22 (1992) 197–215.

[182] T. Werz. *Ostwaldreifung bei hohen und ultra-hohen Volumenfraktionen: Eine 3-dimensionale Untersuchung mittels röntgenbasierender Computertomographie*. PhD thesis, Universität Ulm, 2016.

[183] A. Assmus. Early history of x rays. online, 1995. Accessed: 2015-05-21.

[184] The nobel prize in physics 1901. `https://www.nobelprize.org/prizes/physics/1901/rontgen/biographical/`. Accessed: 2019-05-26.

[185] B. Cullity. *Elements of X-ray Diffraction*. Pearson education. Prentice Hall, 2nd edition, 1978.

[186] M. O. Krause. Atomic radiative and radiationless yields for K and L shells. Journal of Physical and Chemical Reference Data 8 (1979) 307–327.

[187] D. Brandon and W. Kaplan. *Microstructural characterization of materials*. Quantitative software engineering series. John Wiley, Chichester, England, 2nd edition, 2008.

[188] J. P. Blewett. Synchrotron Radiation – Early History. Journal of Synchrotron Radiation 5 (1998) 135–139.

[189] M. S. Livingston and J. P. Blewett. *Particle Accelerators*. McGraw-Hill, 1962.

[190] I. V. Veksler. A new method of the acceleration of relativistic particles. Doklady Akad. Nauk SSSR 43 (1944) 329–331.

[191] E. M. McMillan. The Synchrotron—A Proposed High Energy Particle Accelerator. Physical Review 68 (1945) 143–144.

[192] F. K. Goward and D. E. Barnes. Experimental 8 mev. synchrotron for electron acceleration. Nature 158 (1946) 413.

[193] F. R. Elder, A. M. Gurewitsch, R. V. Langmuir, and H. C. Pollock. Radiation from Electrons in a Synchrotron. Physical Review 71 (1947) 829–830.

[194] H. Wiedemann. *Synchrotron Radiation*. Springer, 2003.

[195] J. Schwinger. On the classical radiation of accelerated electrons. Physical Review 75 (1949) 1912–1925.

[196] A. Liènard. L'ćlairage électrique (1898).

[197] E. Wiechert. Elektrodynamische elementargesetze. Annalen der Physik 309 (1901) 667–689.

[198] G. A. Schott. *Electromagnetic Radiation and the Mechanical Reactions Arising from It*. Cambridge University Press, 1912.

[199] Synchrotron light source. `https://en.wikipedia.org/wiki/Synchrotron_light_source`. Accessed: 2019-05-26.

[200] J. R. Helliwell. Synchrotron Radiation and Crystallography: the First 50 Years. Acta Crystallographica A A54 (1998) 738–749.

[201] H. Kamitsubo. Spring-8 program. Journal of Synchrotron Radiation 5 (1998) 162–167.

[202] M. Eckert. Max von Laue and the discovery of X-ray diffraction in 1912. Annalen der Physik 524 (2012) A83–A85.

[203] H. P. Klug and L. E. Alexander. *X-ray Diffraction Procedures for Polycrystalline and Amorphous Materials*. John Wiley and Sons, 1974.

[204] B. E. Warren. *X-Ray Diffraction*. Dover, New York, 1990.

[205] P. Scherrer. Bestimmung der Größe und der inneren Struktur von Kolloidteilchen mittels Röntgenstrahlen. Nachrichten von der Gesellschaft der Wissenschaften zu Göttingen, Mathematisch-Physikalische Klasse 1918 (1918) 98–100.

[206] C. E. Krill and R. Birringer. Estimating grain-size distributions in nanocrystalline materials from x-ray diffraction profile analysis. Philosophical Magazine A 77 (1998) 621–640.

[207] V. Gertsman and R. Birringer. On the room-temperature grain growth in nanocrystalline copper. Scripta Metallurgica et Materialia 30 (1994) 577–581.

[208] G. Hibbard, K. Aust, and U. Erb. Thermal stability of electrodeposited nanocrystalline Ni-Co alloys. Materials Science and Engineering: A 433 (2006) 195–202.

[209] K. Darling, B. VanLeeuwen, C. Koch, and R. Scattergood. Thermal stability of nanocrystalline Fe-Zr alloys. Materials Science and Engineering: A 527 (2010) 3572–3580.

[210] J. He, J. Ye, E. J. Lavernia, D. Matejczyk, C. Bampton, and J. M. Schoenung. Quantitative analysis of grain size in bimodal powders by x-ray diffraction and transmission electron microscopy. Journal of Materials Science 39 (2004) 6957–6964.

[211] S. Schmidt. GrainSpotter: a fast and robust polycrystalline indexing algorithm. Journal of Applied Crystallography 47 (2014) 276–284.

[212] S. Schmidt. Grainspotter. `https://sourceforge.net/p/fable/wiki/grainspotter/`, 2007. Accessed: 2019-05-26.

[213] H. Poulsen. *Three-Dimensional X-Ray Diffraction Microscopy: Mapping Polycrystals and Their Dynamics*. Number Nr. 205 in Springer Tracts in Modern Physics. Springer, 2004.

[214] H. F. Poulsen. A six-dimensional approach to microtexture analysis. Philosophical Magazine 83 (2003) 2761–2778.

[215] S. Schmidt. Grainsweeper. `https://anaconda.org/fable/grainsweeper`. Accessed: 2019-05-26.

[216] S. Schmidt. Personal communication, 2015.

[217] D. Rowenhorst, A. Gupta, C. Feng, and G. Spanos. 3D Crystallographic and morphological analysis of coarse martensite: Combining EBSD and serial sectioning. Scripta Materialia 55 (2006) 11–16.

[218] J. M. Dake, J. Oddershede, H. O. Sørensen, T. Werz, J. C. Shatto, K. Uesugi, S. Schmidt, and C. E. Krill. Direct observation of grain rotations during coarsening of a semisolid Al–Cu alloy. Proceedings of the National Academy of Sciences 113 (2016) E5998–E6006.

[219] MATLAB and Image Processing Toolbox Release 2014a. The MathWorks, Inc., Natick, Massachusetts, 2014.

[220] B. Lin, Y. Jin, C. Hefferan, S. Li, J. Lind, R. Suter, M. Bernacki, N. Bozzolo, A. Rollett, and G. Rohrer. Observation of annealing twin nucleation at triple lines in nickel during grain growth. Acta Materialia 99 (2015) 63–68.

[221] X.-M. Wei, J.-M. Zhang, and K.-W. Xu. Generalized stacking fault energy in FCC metals with MEAM. Applied Surface Science 254 (2007) 1489–1492.

[222] J. von Neumann. Discussion of C. S. Smith's "Grain Shapes and Other Metallurgical Applications of Topology". In C. Herring, editor, *Metal Interfaces*, pages 108–110. American Society for Metals, 1952.

[223] W. W. Mullins. Two-dimensional motion of idealized grain boundaries. Journal of Applied Physics 27 (1956) 900–904.

[224] P. A. Mulheran and J. H. Harding. A statistical theory of normal grain growth. Materials Science Forum 94–96 (1992) 367–372.

[225] R. D. MacPherson and D. J. Srolovitz. The von Neumann relation generalized to coarsening of three-dimensional microstructures. Nature 446 (2007) 1053–1055.

[226] J. Jeppsson, J. Agren, and M. Hillert. Modified mean field models of normal grain growth. Acta Materialia 56 (2008) 5188–5201.

[227] M. Syha and D. Weygand. A generalized vertex dynamics model for grain growth in three dimensions. Modelling and Simulation in Materials Science and Engineering 18 (2010) 015010.

[228] E. A. Holm and S. M. Foiles. How grain growth stops: A mechanism for grain-growth stagnation in pure materials. Science 328 (2010) 1138–1141.

[229] W. W. Mullins. The effect of thermal grooving on grain boundary motion. Acta Metallurgica 6 (1958) 414–427.

[230] G. Gottstein and L. Shvindlerman. On the true dependence of grain boundary migration rate on driving force. Scripta Metallurgica et Materialia 27 (1992) 1521–1526.

[231] J. L. Murray. The Al−Mg (aluminum−magnesium) system. Journal of Phase Equilibria 3 (1982) 60.

[232] D. Altenpohl. *Aluminium und Aluminiumlegierungen.* Reine und angewandte Metallkunde in Einzeldarstellungen. Springer-Verlag, 1965.

[233] BL20XU. Online `http://www.spring8.or.jp/wkg/BL20XU/instrument/lang-en/INS-0000000286/instrument_summary_view`. Accessed: 2019-05-27.

[234] J. Oddershede, S. Schmidt, M. K. A. Koker, and D. S. Dale. *Near-field mapping with box beam using FABLE and GrainSweeper.3D.* Technical manual from: DTU Physics and Cornell High Energy Synchrotron Source, 2016.

[235] C. E. Krill III, L. Helfen, D. Michels, H. Natter, A. Fitch, O. Masson, and R. Birringer. Size-Dependent Grain-Growth Kinetics Observed in Nanocrystalline Fe. Physical Review Letters 86 (2001) 842–845.

[236] W. B. Jiang, Q. P. Kong, D. A. Molodov, and G. Gottstein. Compensation effect in grain boundary internal friction. Acta Materialia 57 (2009) 3327–3331.

[237] J. K. Mason, E. A. Lazar, R. D. MacPherson, and D. J. Srolovitz. Geometric and topological properties of the canonical grain-growth microstructure. Physical Review E 92 (2015) 063308.

[238] G. Liu, H. Yu, and X. Qin. Three-dimensional grain topology—size relationships in a real metallic polycrystal compared with theoretical models. Materials Science and Engineering: A 326 (2002) 276–281.

[239] S. G. Kim, D. I. Kim, W. T. Kim, and Y. B. Park. Computer simulations of two-dimensional and three-dimensional ideal grain growth. Physical Review E 74 (2006) 061605.

[240] K. Chang, C. E. Krill III, Q. Du, and L.-Q. Chen. Evaluating microstructural parameters of three-dimensional grains generated by phase-field simulation or other voxel-based techniques. Modelling and Simulation in Materials Science and Engineering 20 (2012) 075009.

[241] J. Gruber, H. Miller, T. Hoffmann, G. Rohrer, and A. Rollett. Misorientation texture development during grain growth. Part I: Simulation and experiment. Acta Materialia 57 (2009) 6102–6112.

[242] D. Aboav. The arrangement of grains in a polycrystal. Metallography 3 (1970) 383–390.

[243] D. Weaire. Some remarks on the arrangement of grains in a polycrystal. Metallography 7 (1974) 157–160.

[244] J. K. Mason, R. Ehrenborg, and E. A. Lazar. A geometric formulation of the law of Aboav–Weaire in two and three dimensions. Journal of Physics A 45 (2012) 065001.

[245] P. Rios. On the relationship between time exponent and quasi stationary grain size distribution. Acta Metallurgica et Materialia 40 (1992) 873–875.

[246] J. Hirsch and K. Lücke. Overview no. 76. Acta Metallurgica 36 (1988) 2863–2882.

[247] H.-C. Kim, C.-G. Kang, M.-Y. Huh, and O. Engler. Effect of primary recrystallization texture on abnormal grain growth in an aluminum alloy. Scripta Materialia 57 (2007) 325–327.

[248] S. Suwas and R. K. Ray. *Crystallographic Texture of Materials*. Springer, London, 2014.

[249] J. J. Sidor, R. H. Petrov, and L. A. Kestens. Modeling the crystallographic texture changes in aluminum alloys during recrystallization. Acta Materialia 59 (2011) 5735–5748.

[250] F. Bachmann, R. Hielscher, and H. Schaeben. Texture Analysis with MTEX – Free and Open Source Software Toolbox. In *Texture and Anisotropy of Polycrystals III*, volume 160 of *Solid State Phenomena*, pages 63–68. Trans Tech Publications Ltd, 3 2010.

[251] O. Engler and J. Hirsch. Texture control by thermomechanical processing of AA6xxx Al-Mg-Si sheet alloys for automotive applications—a review. Materials Science and Engineering: A 336 (2002) 249–262.

[252] M. Miodownik, A. Godfrey, E. Holm, and D. Hughes. On boundary misorientation distribution functions and how to incorporate them into three-dimensional models of microstructural evolution. Acta Materialia 47 (1999) 2661–2668.

[253] V. Randle. Twinning-related grain boundary engineering. Acta Materialia 52 (2004) 4067–4081.

[254] H.-K. Park, H.-G. Kang, C.-S. Park, M.-Y. Huh, and N.-M. Hwang. Observation of microstructure evolution during abnormal grain growth in aluminum alloy. Metallurgical and Materials Transactions A (2012) 1–6.

[255] A. Garbacz and M. Grabski. The relationship between texture and CSL boundaries distribution in polycrystalline materials—II. Analysis of the relationship between texture and coincidence grain boundary distribution. Acta Metallurgica et Materialia 41 (1993) 475–483.

[256] E. A. Holm, M. A. Miodownik, and A. D. Rollett. On abnormal subgrain growth and the origin of recrystallization nuclei. Acta Materialia 51 (2003) 2701–2716.

[257] R. Doherty, D. Hughes, F. Humphreys, J. Jonas, D. Juul Jensen, M. Kassner, W. King, T. McNelley, H. McQueen, and A. Rollett. Current issues in recrystallization: A review. Materials Science and Engineering A 238 (1997) 219–274.

[258] P. G. Shewmon. Energy and structure of grain boundaries. In *Recrystallization, Grain Growth and Textures*, pages 165–203. American Society for Metals, Materials Park, OH, 1966.

[259] S.-W. Chan and R. W. Balluffi. Study of energy vs misorientation for grain boundaries in gold by crystallite rotation method—I. [001] Twist boundaries. Acta Metallurgica 33 (1985) 1113–1119.

[260] S.-W. Chan and R. W. Balluffi. Study of energy vs misorientation for grain boundaries in gold by crystallite rotation method—II. Tilt boundaries and mixed boundaries. Acta Metallurgica 34 (1986) 2191–2199.

[261] M. Ziehmer, A. Tschöpe, R. Birringer, and J. Markmann. Examination of the energy phase space of mixed copper grain boundaries by EBSD and the sphere-on-a-plate method. Acta Materialia 61 (2013) 5586–5594.

[262] W. M. Williams and C. S. Smith. A study of grain shape in an aluminum alloy and other applications of stereoscopic microradiography. Journal of Metals 167 (1952) 755–765.

[263] D. Rowenhorst, J. Kuang, K. Thornton, and P. Voorhees. Three-dimensional analysis of particle coarsening in high volume fraction solid-liquid mixtures. Acta Materialia 54 (2006) 2027–2039.

[264] R. Warren. Microstructural development during the liquid-phase sintering of two-phase alloys, with special reference to the NbC/Co system. Journal of Materials Science 3 (1968) 471–485.

[265] R. Watanabe and Y. Masuda. The growth of solid particles in some two-phase alloys during sintering in the presence of a liquid phase. In G. Kuczynski, editor, *Sintering and Catalysis*, volume 10 of *Materials Science Research*, pages 389–398. Springer US, 1975.

[266] R. German, A. Bose, and S. Mani. Sintering time and atmosphere influences on the microstructure and mechanical properties of tungsten heavy alloys. Metallurgical Transactions A 23 (1992) 211–219.

[267] G. Petzow and H. E. Exner. Particle Rearrangement in Solid State Sintering. Zeitschrift für Metallkunde 67 (1976) 611–618.

[268] H. Exner. *Principles of Single Phase Sintering*. Reviews on powder metallurgy and physical ceramics. Freund Publishing House, 1979.

[269] O. Lame, D. Bellet, M. Di Michiel, and D. Bouvard. Bulk observation of metal powder sintering by x-ray synchrotron microtomography. Acta Materialia 52 (2004) 977–984.

[270] A. N. Niemi and T. H. Courtney. Microstructural development and evolution in liquid-phase sintered Fe-Cu alloys. Journal of Materials Science 16 (1981) 226–236.

[271] R. Lumley. *Fundamentals of Aluminium Metallurgy: Production, Processing and Applications*. Woodhead Publishing Series in Metals and Surface Engineering. Elsevier Science, 2010.

[272] J. M. Martin and F. Castro. Liquid phase sintering of P/M aluminium alloys: effect of processing conditions. Journal of Materials Processing Technology 143–144 (2003) 814–821.

[273] J. M. Torralba, C. E. da Costa, and F. Velasco. P/M aluminum matrix composites: an overview. Journal of Materials Processing Technology 133 (2003) 203–206.

[274] G. Schaffer, T. Sercombe, and R. Lumley. Liquid phase sintering of aluminium alloys. Mater Chem Phys 67 (2001) 85–91.

[275] R. German. *Sintering: From Empirical Observations to Scientific Principles*. Butterworth-Heinemann, Oxford, 2014.

[276] R. Abbaschian and R. Reed-Hill. *Physical Metallurgy Principles*. Cengage Learning, 1991.

[277] T. B. Massalski. *Binary Alloy Phase Diagrams*, volume 1, chapter Al-Cu Phase Diagram, pages 141–143. ASM International, Materials Park, Ohio, 3rd edition, 1996.

[278] R. German. *Liquid Phase Sintering*. Springer, 1985.

[279] K. Wang, M. E. Glicksman, and C. Lou. Correlations and fluctuations in phase coarsening. Physical Review E 73 (2006) 061502.

[280] K. E. Harris, V. V. Singh, and A. H. King. Grain rotation in thin films of gold. Acta Materialia 46 (1998) 2623–2633.

[281] L. Wang, J. Teng, P. Liu, A. Hirata, E. Ma, Z. Zhang, M. Chen, and X. Han. Grain rotation mediated by grain boundary dislocations in nanocrystalline platinum. Nature Communications 5 (2014) 4402.

[282] D. Wolf and S. Phillpot. Role of the densest lattice planes in the stability of crystalline interfaces: A computer simulation study. Materials Science and Engineering A 107 (1989) 3–14.

[283] G. S. Rohrer, E. A. Holm, A. D. Rollett, S. M. Foiles, J. Li, and D. L. Olmsted. Comparing calculated and measured grain boundary energies in nickel. Acta Materialia 58 (2010) 5063–5069.

[284] S. E. Restrepo, S. T. Giraldo, and B. J. Thijsse. Using artificial neural networks to predict grain boundary energies. Computational Materials Science 86 (2014) 170–173.

[285] S. Ratanaphan, D. L. Olmsted, V. V. Bulatov, E. A. Holm, A. D. Rollett, and G. S. Rohrer. Grain boundary energies in body-centered cubic metals. Acta Materialia 88 (2015) 346–354.

[286] D. Freedman, R. Pisani, and R. Purves. *Statistics*. W.W. Norton & Company, 2007.

[287] D. Moldovan, D. Wolf, and S. R. Phillpot. Theory of diffusion-accommodated grain rotation in columnar polycrystalline microstructures. Acta Materialia 49 (2001) 3521–3532.

[288] K.-P. Wieters, I. J. Boiko, and W. Schatt. The mechanism of the rotation of single-crystal spheres during sintering. Crystal Research and Technology 19 (1984) 1195–1200.

[289] E. Brandes and G. Brook, editors. *Smithells Metals Reference Book*. Butterworth Heinemann, 7th edition, 1992.

[290] W. D. Kingery. Densification during sintering in the presence of a liquid phase. I. Theory. Journal of Applied Physics 30 (1959) 301–306.

[291] R. M. German, P. Suri, and S. Park. Review: Liquid phase sintering. Journal of Materials Science 44 (2009) 1–39.

[292] J. Liu and R. German. Rearrangement densification in liquid-phase sintering. Metallurgical and Materials Transactions A 32 (2001) 3125–3131.

[293] D. N. Yoon and W. J. Huppmann. Grain growth and densification during liquid phase sintering of W-Ni. Acta Metallurgica 27 (1979) 693–698.

[294] T. Courtney. Densification and structural development in liquid phase sintering. Metallurgical Transactions A 15 (1984) 1065–1074.

[295] R. M. German, A. Griffo, and Y. Liu. Gravitational effects on grain coarsening during liquid-phase sintering. Metallurgical and Materials Transactions A 28 (1997) 215–221.

[296] S. Ganesan and D. R. Poirier. Densities of Aluminum-Rich Aluminum-Copper Alloys during Solidification. Metallurgical Transactions A 18 (1987) 721–723.

[297] J. Perrin. *Brownian movement and molecular reality.* Taylor and Francis, London, 1910.

[298] R. Mazo. *Brownian Motion: Fluctuations, Dynamics, and Applications.* Oxford University Press, 2002.

[299] M. D. Haw. Colloidal suspensions, Brownian motion, molecular reality: a short history. Journal of Physics: Condensed Matter 14 (2002) 7769.

[300] T. Courtney. Microstructural evolution during liquid phase sintering: Part I. Development of microstructure. Metallurgical Transactions A 8 (1977) 679–684.

[301] R. Huang, I. Chavez, K. M. Taute, B. Lukic, S. Jeney, M. G. Raizen, and E.-L. Florin. Direct observation of the full transition from ballistic to diffusive Brownian motion in a liquid. Nature Physics 7 (2011) 576–580.

[302] S. Ganesan, R. Speiser, and D. Poirier. Viscosities of Aluminum-Rich Al-Cu Liquid Alloys. Metallurgical Transactions B 18 (1987) 421–424.

[303] J.-P. Kruth, G. Levy, F. Klocke, and T. Childs. Consolidation phenomena in laser and powder-bed based layered manufacturing. CIRP annals 56 (2007) 730–759.

[304] D. L. Bourell and J. J. Beaman. Powder material principles applied to additive manufacturing. In *141st Annual Meeting and Exhibition, TMS 2012*, pages 537–544. Minerals, Metals and Materials Society, 2012.

[305] B. C. H. Steele and A. Heinzel. Materials for fuel-cell technologies. Nature 414 (2001) 345–352.

[306] S.-Y. Chung, J. T. Bloking, and Y.-M. Chiang. Electronically conductive phospho-olivines as lithium storage electrodes. Nature Materials 1 (2002) 123–128.

[307] H. Föll. Iron, steel and swords. `https://www.tf.uni-kiel.de/matwis/amat/iss/index.html`. Accessed: 2019-05-27.

[308] J. C. Shatto. Spatial and Orientation Tracking of Coarsening in Semisolid Al-Cu by 3DXRD Microscopy. Master's thesis, Ulm University, 2014.

[309] P. A. Manohar, M. Ferry, and T. Chandra. Five decades of the zener equation. ISIJ International 38 (1998) 913–924.

[310] H. Simons, A. King, W. Ludwig, C. Detlefs, W. Pantleon, S. Schmidt, I. Snigireva, A. Snigirev, and H. F. Poulsen. Dark-field X-ray microscopy for multiscale structural characterization. Nature Communications 6 (2015) 6098.

[311] V. Yadav and N. Moelans. Investigation on the existence of a hillert regime in normal grain growth. Scripta Materialia 142 (2018) 148–152.

[312] A. Manin. Simulation and modeling of grain growth using a misorientation-dependent phase field model. Master's thesis, Ulm University, 2015.

[313] M. Wang, J. Dake, A. Manin, and C. E. Krill III. Probing texture-induced abnormal grain growth in polycrystalline materials in 4D. In *Verhandlungen der Deutschen Physikalischen Gesellschaft e.V.*, 2016. MM 15: Poster session I.

[314] J. Lambert, R. Mokso, I. Cantat, P. Cloetens, J. A. Glazier, F. Graner, and R. Delannay. Coarsening Foams Robustly Reach a Self-Similar Growth Regime. Physical Review Letters 104 (2010) 248304.

[315] B. E. Publishing and K. Kuiper. *The Britannica Guide to Theories and Ideas That Changed the Modern World*. Turning Points in History. Rosen Publishing Group, 2009.

List of Author's Publications

C. Braun, J. M. Dake, C. E. Krill III and R. Birringer, Abnormal grain growth mediated by fractal boundary migration at the nanoscale, *Scientific Reports* 8 (2018) 1592.

O. Sedivy, J. M. Dake, C. E. Krill III, V. Schmidt and A. Jäger, Description of the 3D morphology of grain boundaries in aluminum alloys using tessellation models generated by ellipsoids, *Image Analysis and Stereology* 36 (2017) 5–13.

J. M. Dake, J. Oddershede, H. O. Sørensen, T. Werz, J. C. Shatto K. Uesugi, S. Schmidt and C. E. Krill III, Direct observation of grain rotations during coarsening of a semisolid Al–Cu alloy, *PNAS* 113 (2016) E5998–E6006.

J. M. Dake and C. E. Krill III. Abnormal grain growth in nanocrystalline materials. *Materials Science Forum* 753 (2013) 317–320.

Dana Zöllner, J. M. Dake and C. E. Krill III, Simulation der Korngrenzenmigration in polykristallinem Graphen, *Praktische Metallographie* 45 (2013) 247–252.

J. M. Dake and C. E. Krill III, Sudden loss of thermal stability in Fe-based nanocrystalline alloys, *Scripta Materialia* 66 (2012) 390–393.

N. Kheradmand, J. M. Dake, A. Barnoush and H. Vehoff, Novel methods for micromechanical examination of hydrogen and grain boundary effects on dislocations, *Philosophical Magazine* 92 (2012) 3216–3230.

A. Barnoush, J. Dake, N. Kheradmand and H. Vehoff. Examination of hydrogen embrittlement in FeAl by means of in situ electrochemical micropillar compression and nanoindentation techniques. *Intermetallics* 18 (2010) 1385–1389.

Acknowledgments

This thesis was the culmination of a long and challenging but also very rewarding journey. Looking back now, I am filled with a great sense of gratitude for the love, encouragement and support that I received from many people along the way.

The first time I heard the German word "Doktorvater" I thought that it sounded quite odd, but I have since come to appreciate the term. I entered the doctoral program at Ulm University barely capable of tying my academic shoes and left with not only the ability to conduct quality research but also the skills necessary to present the results in an intelligible and conclusive manner. I am certain that my training as a scientist was not always an easy undertaking and am very grateful to my supervisor, Professor Carl Krill, for his constant and patient support, pointed critique and general availability. When struggling with a problem, I could always get an answer or helpful suggestion, often even well after midnight. Carl found the right mixture of challenge, motivation and support to help me excel.

I am also very grateful to Professor Greg Rohrer for his contribution as my second referee. It was an honor to have him travel all the way to Ulm and serve on my defense committee. Although our interaction was limited, his feedback was nevertheless invaluable.

The academic, technical and administrative support provided by the permanent staff of the former Institute for Micro and Nanomaterials was second to none. I am especially grateful to Helga Faißt, who made the process of filling out countless applications, contracts and expense reports absolutely painless—almost even pleasant. I would also like to thank Professors Hans-Jörg Fecht and Ulrich Herr, along with Dr. Kai Brühne, for their feedback and assistance in preparing exercises, seminars and conference talks.

I had the exciting opportunity to travel to Japan three times with a brilliant team of Danish scientists: Søren Schmidt, Henning Sørensen and Jette Oddershede. Sleep deprivation and the excess consumption of a particular sugary caffeinated beverage may have impaired my synaptic transmissions, but it was during these beamtimes that I made many of my fondest memories as a doctoral student. I am also indebted to Søren and especially Jette for teaching me the ins and outs of reconstructing 3DXRD data. This in-depth training took place over three visits to DTU, and each time I was housed and fed by Pia Buchwaldt and her family, to whom I am very grateful for their warm welcome and hospitality.

Regardless of whether I was running experiments, analyzing data, preparing lab courses or correcting exams, it was always fun when working with other PhD students. This camaraderie and mutual support among doctoral students made life at the university special. I will never forget how Mike Haddad spent all weekend working late into the night with me to help prepare samples for my first trip to Japan. Mike and I also shared an office for many years with Barat Kurbanjan, a great experimentalist and friend from whom I

learned as much about life as I did about science. My favorite task as a doctoral student was supervising undergraduates. One of my best students was Mingyan Wang, and later we became colleagues and good friends. We spent many long days and nights together developing efficient algorithms to analyze the mountains of 3D data that we had collected.

Friendships and relationships such as these are what I miss and cherish most from my time at Ulm University. Irene Helzel, née Fleischer, was my neighbor at the university and at home. I fondly remember our many rides to work together. Irene motivated me to get up early and work hard, but she also reminded me of the importance of having a beer in the sun from time to time. I often referred to Thomas Werz as my "Doktorbruder," and I am very thankful that we got to experience the highs and lows of PhD life together during this intense and influential period of our lives. Our late-night philosophical discussions expanded my views on a wide range of topics. A chance encounter on a seemingly ordinary day at the university was the beginning of my friendship with Chris Williams. He and I were able to relate on many different levels, because, like me, he was an American doing his PhD in Germany, married and raising three kids. I am extremely grateful for his motivation and encouragement, especially near the end, where things were most difficult. Chris has a special gift of helping people realize their goals and how to achieve them.

My children were my greatest source of strength and inspiration, but once I left the university it was extremely challenging to balance work and family life while still working to complete my thesis. I am so very grateful to friends like Ruth and Eddy Luft, Nadja and Sascha Menges, Heike and Joachim Selig, and Susanne and Martin Grimmeiß for watching the kids and taking them on many fun outings so I could write on weekends and holidays.

Finally, I would like to thank my family. Without their support and many sacrifices, I would not have been able to finish. Despite the distance between us, my family in the US provided constant encouragement through frequent phone calls and visits. Explaining my research to my sister, Satin Brennan, helped me to keep the motivation and big picture in mind, and planning milestones with my brother, Monny Dake, kept me moving forward. At the same time, I was extremely blessed to be living close to my wife's family in Ulm. My in-laws, Cornelia and Michael Leibinger, took me in as their own son and gave me a base of wholehearted love and day-to-day support that all too often goes unnoticed, but for which I am infinitely grateful. You were and remain for me an example of how great family can be.

To my three wonderful children, Johanna, Michael and Magdalena: Thank you for your unlimited love and patience, for your nightly prayers and for always understanding when dad could not come out and play or join you on vacation. You were absolutely the best kids a stressed out PhD candidate could ask for. I look forward to having even more fun and exciting adventures with you now that I am finished. To my lovely wife Caroline: I cannot thank you enough for your unwavering belief in me and our family and for your unconditional love. We did it!